

**Investigation of the luminescent properties of metal quinolates (Mq<sub>x</sub>)  
for use in OLED devices.**

*by*

**Mart-Mari Duvenhage  
(M.Sc)**

*A thesis submitted in fulfillment of the requirements for the degree*

**PHILOSOPHIAE DOCTOR**

*in the*

**Faculty of Natural and Agricultural Sciences  
Department of Physics**

*at the*

**University of the Free State  
Republic of South Africa**

**Promoter: Prof H.C. Swart  
Co-promoter: Prof O.M. Ntwaeaborwa**

January 2014

“If you can’t explain it **simply**,  
you don’t understand it well enough.”

– Albert Einstein

## Acknowledgements

- Prof H.C. Swart for being my supervisor and giving me the freedom to do my own project. For learning with me all the wonderful aspects about organic phosphors; for making my visit to the USA possible and also ensuring that I had enough money for my stay there; for listening to all my frustrations about systems and students and always offering to help.
- Prof O.M. Ntwaeaborwa for being my co-supervisor.
- Prof J.J. Terblans for his interest in my project and helping me with some of the (basic) maths that I had to do.
- Prof H.G. Visser for making some samples for me to characterize and use in my project; for growing single crystals and supplying me with XRD standards and for all his inputs and discussions about the papers we wrote together.
- Dr E. Coetzee-Higo for helping me with XPS measurements and also for giving me training on the XPS system.
- Prof J.C. Swarts and Pieter Swarts for doing cyclic voltammetry measurements and helping me to interpret the results.
- Hanlie Grobler and Prof van Wyk for assisting with SEM and microscope work.
- Edward Wreznieski for welcoming me into his lab and helping me to fabricate and characterize my own OLED devices.
- Prof Holloway and his family who welcomed me to the USA and made me feel at home there; for taking me around Florida to experience all the wonderful sights and taking me to the FLAVS conference at their expense.
- To Dawie van Jaarsveldt for showing me that there are some big things out there as well.
- Personnel and students at the Physics Department for discussions and encouragements.
- To my family for encouraging me to pursue my dreams.
- Thanks to my husband, Giel, for listening to all my practice runs of presentations for conferences, for bringing me food when I had to work late, struggling with systems not working, and then helping to fix them and for listening to all my explanations about the work I am doing – pretending to understand. I love you!
- I would also like to thank the National Research Foundation (NRF) and the cluster program of the University of the Free State for financial support.

## Abstract

Since Tang and VanSlyke developed the first organic light emitting diode (OLED) in the late 80's using tris-(8-hydroxyquinoline) aluminium ( $\text{Alq}_3$ ) as both the emissive and electron transporting layer, a lot of research has been done on  $\text{Alq}_3$  and other metal quinolates ( $\text{Mq}_x$ ). The optical, morphological and electrical properties of these  $\text{Mq}_x$  have been studied extensively.  $\text{Alq}_3$  has, however, a disadvantage as it tends to degrade when stored under atmospheric conditions. These degraded products are non-luminescent and lead to poor device performance. A good understanding of what happens during the degradation process and ways of eliminating this process are needed. In this study different  $\text{Mq}_x$  compounds were synthesized and their degradation behavior was studied to see what effect it has on their luminescent properties.

One way to tune the emissive colour of  $\text{Alq}_3$  is to introduce electron-withdrawing or electron-donating groups (EWG and EDG) onto the hydroxyquinoline ligands. These groups have an effect on the energy gap between the highest occupied molecular orbital and the lowest unoccupied molecular orbital. In this study  $\text{Alq}_3$  powders were synthesized with an EDG ( $-\text{CH}_3$ ) substituted at position 5 and 7 ((5,7-dimethyl-8-hydroxyquinoline) aluminium) ( $5,7\text{Me-Alq}_3$ ) and EWG ( $-\text{Cl}$ ) at position 5 ((5-chloro-8-hydroxyquinoline) aluminium) ( $5\text{Cl-Alq}_3$ ). A broad absorption band at  $\sim 380$  nm was observed for un-substituted  $\text{Alq}_3$ . The bands of the substituted samples were red shifted. The un-substituted  $\text{Alq}_3$  showed a high intensity emission peak at 500 nm. The  $5\text{Cl-Alq}_3$  and  $5,7\text{Me-Alq}_3$  samples showed a red shift of 33 and 56 nm respectively. Optical absorption and cyclic voltammetry measurements were done on the samples. The optical band gap was determined from these measurements. The band gap did not vary with more than 0.2 eV from the theoretical value of  $\text{Alq}_3$ . The photon degradation of the samples was also investigated and the  $5,7\text{Me-Alq}_3$  sample showed the least degradation to the UV irradiation over the 24 h of continuous irradiation.

By encapsulating the  $\text{Alq}_3$  molecule with glass ( $\text{SiO}_2$ ) or a polymer-like polymethyl methacrylate (PMMA), the oxygen and moisture responsible for degradation have a lesser effect on the degradation of the  $\text{Alq}_3$  molecule. The as prepared  $\text{SiO}_2\text{-Alq}_3$  sample's emission was blue shifted by 10 nm from that of  $\text{Alq}_3$ . The sample was subjected to UV irradiation and after 24 hours, no

luminescence intensity was detected. According to literature the  $\text{SiO}_2$  will decompose into Si and O species under UV irradiation. These O species have reacted with the  $\text{Alq}_3$  to form non-luminescent products. The  $\text{Alq}_3$ :PMMA samples showed a maximum emission at 515 nm. There was a decrease in luminescence intensity when the sample was irradiated with UV photons. This was due to the decomposition of PMMA into elemental species and the O again reacted with the  $\text{Alq}_3$  molecule to form non-luminescent products. However, the intensity stabilized after 100 h of irradiation.

X-ray photoelectron spectroscopy (XPS) and infra red (IR) measurements were done on the as-prepared and degraded  $\text{Alq}_3$  samples. It revealed that the Al-O and Al-N bonds stayed intact, but C-O and C=O bonds formed during degradation, indicating that the phenoxide ring ruptures during degradation. It is known that the luminescent centre of the molecule is located on the quinoline rings and the rupturing of one of these rings will destroy this centre, leading to a decrease in luminescence intensity. When the  $\text{Al}^{3+}$  ion was replaced with a  $\text{Zn}^{2+}$  ion to form  $\text{Znq}_2$ , it showed higher emission intensity and, compared to  $\text{Alq}_3$ , did not degrade as fast. This might be due to the fact that  $\text{Znq}_2$  only has two quinoline rings.

The effect of solvent molecules, in the solid state crystal lattice, on the photoluminescence properties of synthesized *mer*- $[\text{In}(\text{qn})_3]\cdot\text{H}_2\text{O}$ . 0.5  $\text{CH}_3\text{OH}$  was studied. Single crystals were obtained through a recrystallization process and single crystal x-ray diffraction (XRD) was performed to obtain the unit cell structure. The main absorption peaks were assigned to ligand centered electronic transitions, while the solid state photoluminescence excitation peak at 440 nm was assigned to the 0-0 vibronic state of  $\text{In}(\text{qn})_3$ . Broad emission at 510 nm was observed and was ascribed to the relaxation of an excited electron from the  $S_1$ - $S_0$  level. A powder sample was annealed at 130 °C for two hours. A decrease in intensity was observed and could possibly be assigned to a loss of solvent species. To study the photon degradation, the sample was irradiated with an UV lamp for ~ 15 hours. The emission data was collected and the change in photoluminescence intensity with time was monitored. High resolution XPS scans of the O-1s peak revealed that after annealing, the binding energy shifted to lower energies indicating a possible loss of the  $\text{H}_2\text{O}$  and  $\text{CH}_3\text{OH}$  present in the crystal. The O-1s peak of the degraded

sample indicated the possible formation of C=O (~ 532.5 eV), C-O-H and O=C-O-H (~ 530.5 eV) on the phenoxide ring.

Commercial Alq<sub>3</sub> is normally used in the fabrication of OLEDs. In this study Alq<sub>3</sub> was synthesized using a co-precipitation method and it was purified using temperature gradient sublimation. The Alq<sub>3</sub> was then used to fabricate a simple two layer OLED with a device structure: ITO/NPB/Alq<sub>3</sub>/Cs<sub>2</sub>CO<sub>3</sub>:Al. The electroluminescence (EL) spectrum of the device consisted of a broad band with a maximum at ~520 nm and was similar to the photoluminescence (PL) spectrum observed from the synthesized Alq<sub>3</sub> powder. The luminance (*L*)–current density (*J*)–voltage (*V*) characteristics of the device showed a turn on voltage of ~ 2 V, which was lower than the current density of the device fabricated using the commercial Alq<sub>3</sub>. The external quantum efficiency ( $\eta_{EQE}$ ) and the power conversion efficiency ( $\eta_P$ ) of the device were 1% and 2 lm/W, respectively.

## **Keywords**

Metal quinolates

Alq<sub>3</sub>

Organic light emitting diodes

Photoluminescence

Absorption

Optical band gap

Electron donating group

Electron withdrawing group

Cyclic voltammetry

X-ray diffraction

Morphology

Degradation

UV irradiation

X-ray photoelectron spectroscopy

Electroluminescence

# Contents

<b>CHAPTER 1</b> .....	<b>11</b>
INTRODUCTION TO ORGANIC LIGHT EMITTING DIODES (OLEDs).....	11
1. Demand for high efficiency light emitting devices. ....	11
2. Advantages of organic light emitting devices.....	14
3. Applications of organic light emitting devices. ....	16
3.1 Solid-state lighting (SSL) .....	16
3.2 Flat panel displays.....	17
4. Demand for a stable emissive and electron transporting layer in OLED devices. ....	20
5. Layout of the thesis .....	22
References: .....	23
<b>CHAPTER 2</b> .....	<b>25</b>
PHOTO-PHYSICAL PROPERTIES OF ORGANIC SEMICONDUCTORS.....	25
1. Introduction .....	25
2. Electronic structures.....	26
3. Charge transport .....	28
3.1 Band transport.....	29
3.2 Hopping transport .....	29
4. Transport bandgap vs. optical bandgap.....	31
5. Excitons .....	31
5.1 Exciton formation .....	31
5.2 Multiplicity of excitons.....	32
5.3 Metal-ligand charge transfer exciton .....	33
6. Intra-molecular energy transfer .....	34
6.1 Absorption.....	35
6.2 Fluorescence .....	35
6.3 Intersystem crossing.....	36
6.4 Phosphorescence .....	36
6.5 Frank-Condon shift .....	36
7. Inter-molecular energy transfer .....	37
7.1 Dexter energy transfer.....	38
7.2 Förster energy transfer .....	39
References.....	40
<b>CHAPTER 3</b> .....	<b>42</b>
THE EFFECT OF SUBSTITUENTS ON THE OPTICAL PROPERTIES OF MQ <sub>3</sub> .....	42
1. Introduction .....	42
2. Synthesis .....	43

3. <i>Results and discussion</i> .....	44
3.1 Effect of substituents on the luminescence and morphology of Alq <sub>3</sub> .....	44
3.2. Effect of Al <sup>3+</sup> , Ga <sup>3+</sup> and In <sup>3+</sup> and substituents on the optical properties of Mq <sub>3</sub> . ....	48
3.3 Effect of excitation wavelength on the emission of Mq <sub>3</sub> .....	51
5. <i>Conclusion</i> .....	52
<i>References</i> .....	54
<b>CHAPTER 4</b> .....	<b>55</b>
THE INFLUENCE OF SUBSTITUENTS ON THE OPTICAL BAND GAP OF ALQ <sub>3</sub> . ....	55
2. <i>Cyclic voltammetry</i> .....	56
2.1 Technique overview.....	56
2.2 Experimental setup.....	60
2.3 Results.....	61
3. <i>Optical absorption</i> .....	64
3.1 Technique overview.....	64
3.2 Beer's Law.....	66
3.3 Tauc's relation.....	66
3.4 Experimental setup.....	68
3.5 Results.....	69
3.5.1 Determination of n.....	69
4. <i>Conclusion</i> .....	74
<i>References</i> .....	75
<b>CHAPTER 5</b> .....	<b>77</b>
SYNTHESIS AND CHARACTERIZATION OF ALQ <sub>3</sub> , ALQ <sub>3</sub> :SiO <sub>2</sub> , ALQ <sub>3</sub> :PMMA AND ALQ <sub>3</sub> :PS.....	77
1. <i>Introduction</i> .....	77
2. <i>Synthesis</i> .....	78
2.1 Synthesis of Alq <sub>3</sub> .....	78
2.2 Synthesis of SiO <sub>2</sub> -Alq <sub>3</sub> .....	78
2.3 Synthesis of Alq <sub>3</sub> :PMMA.....	79
3. <i>Results</i> .....	80
3.1 Alq <sub>3</sub> .....	80
3.2 SiO <sub>2</sub> -Alq <sub>3</sub> .....	82
3.3 Alq <sub>3</sub> :PMMA.....	84
3.4 Alq <sub>3</sub> :PS.....	88
4. <i>XPS of PMMA and Alq<sub>3</sub>:PMMA</i> .....	90
4.1 PMMA powder.....	90
4.2 PMMA films.....	91
4.3 Alq <sub>3</sub> :PMMA films.....	94
4. <i>Conclusion</i> .....	97
<i>References</i> .....	98

**CHAPTER 6..... 99**

PHOTON DEGRADATION..... 99

1. Introduction ..... 99
2. Photon degradation of Alq<sub>3</sub>..... 100
  - 2.1 Effect on photoluminescence intensity ..... 100
  - 2.2 FTIR analysis ..... 104
  - 2.3 XPS analysis ..... 105
3. Photon degradation of Znq<sub>2</sub> ..... 113
  - 3.1 General characterization of Znq<sub>2</sub> ..... 113
  - 3.2 UV exposure ..... 115
  - 3.3 XPS measurements. .... 116
4. The effect of SiO<sub>2</sub> encapsulation on the degradation of Alq<sub>3</sub>. .... 128
5. Effect of PMMA on the degradation of Alq<sub>3</sub>..... 128
6. Effect of substituents on the phenoxide ring on the photon degradation. .... 132
7. Conclusion ..... 133
- References..... 135

**CHAPTER 7 ..... 137**

SYNTHESIS, CRYSTAL STRUCTURE, LUMINESCENT PROPERTIES AND PHOTON DEGRADATION OF MER-TRIS(8-HYDROXY-QUINOLINATO-N, O)-INDIUM(III) HYDRATE 0.5 METHANOL SOLVATE.\*

..... 137

1. Introduction ..... 137
2. Synthesis of mer-[In(qn)<sub>3</sub>].H<sub>2</sub>O. 0.5 CH<sub>3</sub>OH (compound 1)..... 138
3. Results..... 138
  - 3.1 Crystal structure and x-ray crystallography..... 138
    - 3.1.1 Experimental and calculations ..... 138
    - 3.1.2 Crystal structure ..... 139
    - 3.1.3 X-ray crystallography..... 141
  - 3.2 Luminescent properties and photon degradation ..... 142
4. Conclusion ..... 149
- References..... 150

**CHAPTER 8 ..... 152**

BASIC PRINCIPLES OF ORGANIC LIGHT EMITTING DIODES AND THEIR FABRICATION..... 152

1. Introduction ..... 152
2. OLED..... 153
3. OLED Materials ..... 154
  - 3.1 Anode and hole-injection materials ..... 155
  - 3.2 Hole-transport materials..... 156
  - 3.3 Electron-transport and host emitting materials ..... 157
  - 3.4 Cathode ..... 158

3.4.1 Elemental metals .....	158
3.4.2 Alkali metal compounds/Al .....	158
3.4.3 LiF .....	159
4. <i>Purification of OLED materials.</i> .....	159
4.1 Temperature gradient sublimation. ....	159
5. <i>OLED fabrication</i> .....	160
<i>References:</i> .....	163
<b>CHAPTER 9 .....</b>	<b>164</b>
THE EFFECT OF SYNTHESISED ALQ <sub>3</sub> ON THE EXTERNAL QUANTUM AND POWER CONVERSION EFFICIENCIES OF OLEDs. ....	164
1. <i>Introduction</i> .....	164
2. <i>Experimental</i> .....	165
2.1 Purification of Alq <sub>3</sub> .....	165
2.2 Fabrication of OLEDs.....	166
2.3 Characterization .....	169
3. <i>Results</i> .....	170
4. <i>Conclusion</i> .....	175
<i>References</i> .....	176
<b>CHAPTER 10 .....</b>	<b>177</b>
CONCLUSION AND FUTURE WORK.....	177
1. <i>Conclusion</i> .....	177
2. <i>Future work:</i> .....	181
<b>APPENDIX A .....</b>	<b>183</b>
<i>PUBLICATIONS</i> .....	183
<i>CONFERENCES</i> .....	186

# Chapter 1

## Introduction to organic light emitting diodes (OLEDs).

### 1. Demand for high efficiency light emitting devices.

The total energy consumption worldwide is growing every year, especially with the recent increase in the use of small mobile electronic devices. In order to satisfy both the environmental clean energy issue and the limited energy resource problem, there have been continuous efforts to harvest natural energy sources such as wind, water and sunlight. Fuel and solar cells and high energy efficient rechargeable batteries such as Li-ion batteries are intensively under investigation to meet the modern sustainable energy initiatives [1-5]. The demands on the power grid might also be reduced by using low-electrical power-consuming electronic devices. Research into high efficiency and low power consuming electronics is currently a high research priority.

It is reported that approximately 17% of the total energy consumed in South Africa is transformed into lighting [6]. The common incandescent light bulb (figure 1 (a)), which works by heating a filament to over 3000 °C, has a power conversion efficiency (PCE) of 5 % (that is 95 % of the electricity used is lost as heat). A 60 W bulb will consume 525.6 KWh/yr. A compact fluorescence lamp (CFL) (figure 1 (b)), which excites a coated phosphor by discharging gas, has a better PCE of up to 20 % and a 13-15 W bulb will only consume 131.4 KWh/yr. However, it is very sensitive to low and high temperatures and will stop working at temperatures below -20 °C and above 50 °C. It also contains 1 - 5 mg of mercury per bulb, which is an environmentally hazardous material [7].

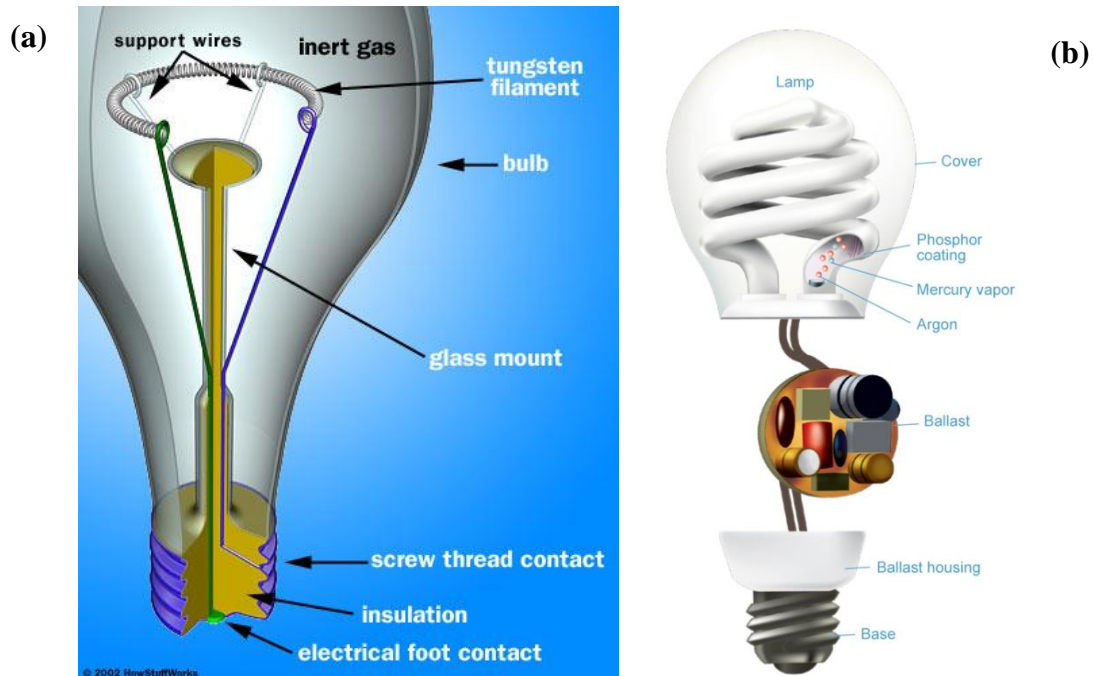


**Figure 1: Schematic diagram of (a) an incandescent light bulb [8] and (b) a compact fluorescent lamp [9].**

Solid-state lighting (SSL) comprises highly energy-efficient light emitting devices (LEDs) based on semi-conducting materials (figure 2). Inorganic semiconductors, mostly group III-nitride, which have direct band gaps, converting electrical energy directly into visible light with less indirect energy losses, are used for conventional LEDs. Although almost 100 % internal quantum efficiency could be achieved using inorganic LEDs [10], there are still a few issues such as low colour rendering index (CRI) for white light sources, device scalability and high material and fabrication cost. Nevertheless, the inorganic LED market has been increasing at an enormous rate in the last decade [11].

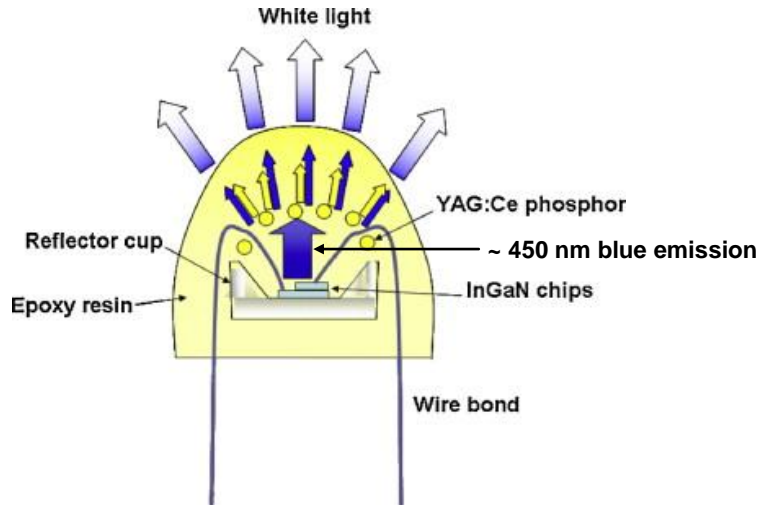


**Figure 2: Schematic structure of a dichromatic pc white LED [12].**

Organic light emitting diodes (OLEDs) convert electrical power into light by using organic semiconductors such as polymers and small molecules. Since their first introduction by Tang and Vanslyke in the late 80's at Eastman Kodak [13], extensive research has been conducted in academia and industry to achieve high efficiency and stable OLEDs. Compared to inorganic LEDs, OLEDs can be easily scalable, cheaper and even tunable in electrical/optical properties, suggesting an excellent next-generation light source for either SSL or flat panel displays (FPDs). However, device stability and low efficiency are the most important issues for OLEDs in order to replace most existing light sources in the world. The classic power efficiencies and current progress of several white light sources including inorganic and organic LEDs are shown in figure 3.

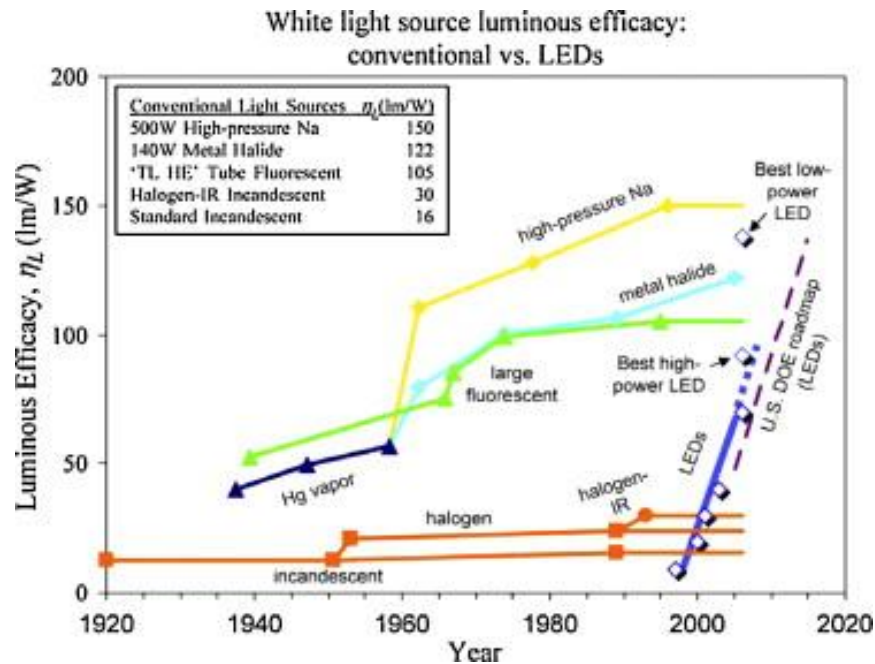


**Figure 3: Evolution of luminous efficacy performance of white light sources. Commercially available high-power LED performance is indicated by the points along the solid blue curve [12].**

## 2. Advantages of organic light emitting devices.

There are many advantages to organic semi-conducting materials. First of all, organic materials are more cost effective than inorganic semiconductors due to the thinner film thickness, typically  $\sim 100$  nm and the nearly unlimited synthetic abundance of organic materials. Secondly, organic thin films can be easily deposited using various simple fabrication methods such as vacuum thermal evaporation (VTE) [14], spin-coating [15], inkjet printing [16] and even roll-to-roll process [17], compared to the more expensive inorganic thin film growth methods such as chemical vapour deposition (CVD) [18], molecular beam epitaxy (MBE) [19] and pulsed laser deposition (PLD) [20]. Thirdly, the extremely thin film thickness and flexibility of organic materials make OLEDs suitable for flexible device applications as shown in figure 4.



**Figure 4: Examples of flexible OLED displays [21, 22].**

Furthermore, the optical and electrical properties of organic materials can be tuned via chemical structure modification of organic molecules. For example, different visible emission spectra can be represented by tuning the chemical structure of cyclometalated iridium(III) complexes as shown in figure 5 [23].

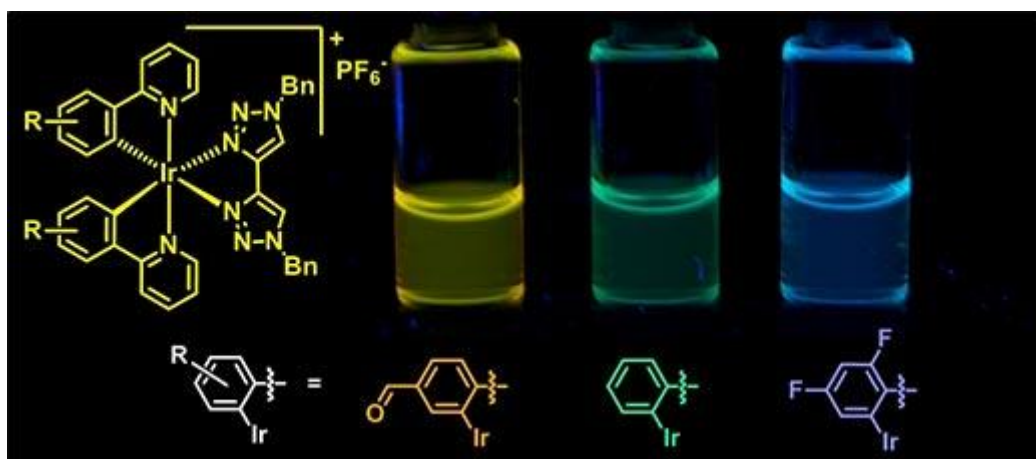


**Figure 5: Luminescent cyclometalated iridium(III) complexes used in light emitting device application [23].**

Also, if compared to their main competitor, liquid crystal displays (LCDs), OLEDs have excellent display performances such as a wide viewing angle, low power consumption, a fast response time and high contrast.

### **3. Applications of organic light emitting devices.**

There are two major application areas in OLEDs, namely the next generation SSL source which could ultimately replace fluorescent tubes and the flat panel display device where OLEDs compete with LCDs. Both of these applications can currently be found in the commercial consumer market.

#### **3.1 Solid-state lighting (SSL)**

Figure 6 shows various OLED lighting products introduced by Armstrong, General Electric, Konica, Novald and Osram. The OLED lighting market is not yet as large as the display market, but has picked up significantly since 2011 [24]. The requirements for the white light sources is somewhat different than that for displays, higher brightness conditions (luminance,  $L = 1000$   $\text{cd/m}^2$  for lighting versus  $L = 100$   $\text{cd/m}^2$  for displays), good colour rendering index (CRI) of at least 70, matching of Commission Internationale de l'Eclairage (CIE) coordinates similar to that of a black body radiator, which is on the Planckian locus, and a correlated colour temperature (CCT) between 2500 K and 6000 K [25]. The adjustment of these various light-emitting properties for an efficient white light source can be easily tailored by selectively choosing different light emitting organic molecules and optimizing the device structure of the OLEDs, consequently resulting in a wide range of white light emissions such as cool or warm.



**Figure 6: Various OLED lighting applications (sources from: Armstrong, General Electric, Konica, Novaled and Osram).**

### 3.2 Flat panel displays

There have been many types of display devices such as the cathode ray tube (CRT), the plasma display panel (PDP) and the LCD. The LCD has been the most prevalent display device up to now, but the demand for OLED displays is growing tremendously due to the excellent light emitting qualities, compared with the LCD. The short radiative lifetime (typically in the range of nanoseconds [26]) of organic materials can provide much faster response time, compared to the slow response time of the LCD, which typically takes milliseconds to rotate the liquid crystal cells [27]. The OLED can therefore be a better display device for watching sport and videos. The wide viewing angle (nearly 180°) of OLEDs, which is one of the most important requirements for mobile display devices, is also another advantage [28].

The first commercialized 11” OLED display, XEL-1, was released by Sony in 2007 [29], while the first passive matrix OLED (PMOLED) screens were used in mobile phones since 2001 and replaced by active matrix OLED (AMOLED) in 2006 [30]. Nowadays all the leading companies are using OLED screens in some of their products with Samsung being the market leader in the mobile phone displays and Samsung and LG in TV displays. LG has a 55” display that weighs only 3.5 kg with a thickness of 4 mm [28]. In the next 3-5 years, we'll start seeing bendable, flexible and rollable displays. Kyocera has a concept phone that uses a foldable OLED and LG is working on a 60” 4K rollable TV for 2017.



**Figure 7: (a) First OLED screen released by Sony in 2007, (b) first PMOLED mobile phone by Motorola, (c) a Samsung Louvre B7610 using an AMOLED screen, (d) LG's full HD flat panel TV, (e) Kyocera concept mobile phone using foldable OLEDs and (f) a concept kit of a rollable OLED TV.**

#### **4. Demand for a stable emissive and electron transporting layer in OLED devices.**

Since the late 80's Alq<sub>3</sub> has been used as both the green emissive layer and electron transporting layer in OLED devices [13]. Although Alq<sub>3</sub> emits bright green light in the wavelength range 500 – 520 nm, it gives poor device efficiency and degrades to non-radiative by-products when stored under atmospheric conditions [31]. This leads to high manufacturing costs as all the processes must be done under vacuum conditions.

A need arises to understand this degradation of Alq<sub>3</sub>. By subjecting Alq<sub>3</sub> to UV irradiation under atmospheric conditions, this degradation process is enhanced and the degraded products can be studied after just a few days of degradation. By knowing what products form during degradation, measures can be taken to prevent these products from forming and thus yielding a stable organic phosphor.

Although Alq<sub>3</sub> is widely used in OLED devices, other metal quinolates (Mq<sub>x</sub>) might have better optical and electrical properties. Changing from a 3+ ion to a 2+ ion as the metal centre decreases the number of quinoline ligands and might decrease the formation of non-radiative products. These new Mq<sub>x</sub> might be more stable than the traditional Alq<sub>3</sub> that is being used at the moment.

**This leads to the aim of this study.** To synthesize stable Mq<sub>x</sub> by substituting the Al<sup>3+</sup> metal centre with other group 3 metals such as Ga and In or transition metals such as Zn. The morphology of these new Mq<sub>x</sub> samples will be characterized by x-ray diffraction (XRD) and scanning electron microscopy (SEM). These techniques will give information about the crystal and particle size of the synthesized materials. The optical properties of these samples must be studied in great detail. Absorption and photoluminescent (PL) studies will be done to determine the absorption, excitation and emission wavelengths of the various materials. These wavelengths must also be assigned to their respective transitions. Determining the optical band gap and the positions of the highest occupied molecular orbital (HOMO) and lowest unoccupied molecular orbital (LUMO) is of utmost importance as this will show if the material is suitable for use in OLED devices. The optical band gap can be determined from the absorption onset of the

materials and the positions of the HOMO and LUMO levels can be determined by cyclic voltammetry. By adding substituents to the quinoline ligand, more stable products might be achieved. The effect of these substituents on the morphology and optical properties must, however, be studied carefully in order to know if they will be suitable to use in OLED devices. Solvents left in the crystal structure after synthesis might influence the optical properties of the materials. By doing single crystal XRD, the composition of the unit cell of the specific material can be determined to see if and where solvent molecules are located. The optical properties of these new materials can again be studied by absorption and PL measurements to see if they enhance the emission intensity of the material. By doing x-ray photoelectron spectroscopy (XPS), the effect of solvent molecules can also be studied.  $Mq_x$  might become more stable if it is encapsulated with a protective layer that prevents oxygen and moisture in the atmosphere from reacting with the molecule and forming non-radiative products. By using polymers such as polymethyl methacrylate (PMMA) and polystyrene (PS) or glasses like  $SiO_2$ ,  $Mq_x$  might become more stable and degrade much more slowly. By studying the PL lifetimes of the samples, the effect of these protective layers on the degradation can be studied. By doing XPS studies on the as-prepared and degraded products, the chemical change in the molecules can be determined. It is also important to first understand the basic principles of OLED devices and their fabrication before fabricating OLED devices. By using synthesized  $Alq_3$  powder to fabricate a simple OLED device and compare the optical and electrical properties with a device fabricated with commercial  $Alq_3$ , the effect of particle size and impurity levels on the device's performance can be studied.

## 5. Layout of the thesis

*Chapter 1* presents the introduction and aim of this study. It is followed by an explanation of the basic principles involved in organic semiconductors in *chapter 2*. *Chapter 3* gives insight into the morphological and luminescent properties of the Alq<sub>3</sub> samples. It also determines the effect of electron withdrawing (EWG) and electron donating groups (EDG) on the optical properties of Alq<sub>3</sub>. In *chapter 4* CV and absorption measurements are used to determine the optical band gap of Alq<sub>3</sub>, and the effect of EDG and EWG on the band gap is also investigated. In *chapter 5* Alq<sub>3</sub> powder is mixed with SiO<sub>2</sub>, PMMA and PS to see what effect these protective layers might have on the luminescent properties of Alq<sub>3</sub>. *Chapter 6* focuses on the photon degradation of the different samples under prolonged UV exposure and what effect EDG and EWG have on the degradation. A mechanism explaining the degradation is also provided. *Chapter 7* investigates the effect of solvents, which are left in the crystal structure of Inq<sub>3</sub>, on the morphological and optical properties of the sample. The sample is heated to evaporate the solvents to see the difference they have on the luminescence. X-ray photoelectron spectroscopy (XPS) is also done on the samples to see if there were any changes to their chemical environments during annealing. *Chapter 8* gives an overview of the theoretical aspects of OLED device fabrication and *Chapter 9* shows what the effect of nano sized Alq<sub>3</sub> will be on the device performance of simple OLED devices. In *Chapter 10*, a conclusion and planned future work are given.

## References:

- [1] M. Lenzen, *Energies* **3** (2010) 462-591.
- [2] S.S. Dhrab and K. Sopian, *Renew. Energ.* **35** (2010) 1303-1307.
- [3] J. Brouwer, *Curr. Appl. Phys.* **10** (2010) S9-S17.
- [4] J. Paska, P. Biczal and M. Klos, *Renew. Energ.* **34** (2009) 2414-2421.
- [5] C.J. Lawn, *Proc. Mech. Eng. Sci.* **223** (2009) 2717-2742.
- [6] How to save electricity in your home; accessed from:  
<http://www.homemakersonline.co.za/features/31/> (27/08/2013).
- [7] Comparison Chart LED Light vs. Incandescent Light Bulbs vs. CFLs; accessed from:  
<http://www.designrecycleinc.com/led%20comp%20chart.html> (27/08/2013).
- [8] How Light Bulbs Work; accessed from: <http://home.howstuffworks.com/light-bulb1.htm> (29/08/2013).
- [9] Learn about CFLs; accessed from:  
[http://www.energystar.gov/index.cfm?c=cfls.pr\\_cfls\\_about](http://www.energystar.gov/index.cfm?c=cfls.pr_cfls_about) (29/08/2013).
- [10] E. Dupont, H.C. Liu, M. Buchanan, S. Chiu and M. Gao, *Appl. Phys. Lett.* **76** (2000) 4-6.
- [11] C.J. Humphreys, *MRS Bull.* **33** (2008) 459-470.
- [12] S. Ye, F. Xiao, Y.X. Pan, Y.Y. Ma and Q.Y. Zhang, *Mat. Sci. Eng. R.* **71** (2010) 1-34.3
- [13] C.W. Tang and S.A. Vanslyke, *Appl. Phys. Lett.* **51** (1987) 913-915.
- [14] M. Long, J.M. Grace, D.R. Freeman, N.P. Redden. B.E. Koppe and R.C. Brost, *Sid. Int. Symp. Dig. Tec.* **37** (2006) 1474-1476.
- [15] J.L. Gugat, A. Pradana, M. Radler, J. Mikat and M. Gerken, *IEEE Photonic Tech. L.* **24** (2012) 912-914.
- [16] M. Singh, H.M. Haverinen, P. Dhagat and G.E. Jabbour, *Adv. Mater.* **22** (2010) 673-685.
- [17] J. Hast, M. Tuamikoski, R. Suhonen, K.L. Vaisanen, M. Valimaki, T. Maaninen, P. Apilo, A. Alastalo and A. Maanineny, *Sid. Int. Symp. Dig. Tec.* **44** (2013) 192-195.
- [18] K. Okano, S. Koizumi, S. Ravi, P. Silva, A. Gehan and J. Amaratunga, *Nature* **381** (1996) 140-141.
- [19] B.A. Joyce, *Rep. Prog. Phys.* **48** (1985) 1637.
- [20] D.B. Crisey and G.K. Hubler, *Pulsed Laser Deposition of Thin Films*, Wiley-VCH (2003) 648.

- [21] Say Goodbye To Shattered Screens! Next iPhone Will Feature Flexible OLED Display [Rumour]; accessed from: <http://www.cultofmac.com/167086/say-goodbye-to-shattered-screens-next-iphone-will-feature-flexible-oled-display-rumor/> (29/08/2013).
- [22] [LG Showcases 5" Flexible OLED Technology at SID 2013](http://www.dailytech.com/LG+Showcases+5+Flexible+OLED+Technology+at+SID+2013/article31581.htm); accessed from: <http://www.dailytech.com/LG+Showcases+5+Flexible+OLED+Technology+at+SID+2013/article31581.htm> (29/08/2013).
- [23] The Materials Chemistry Research Group – Projects; accessed from: <http://www.hud.ac.uk/research/researchcentres/mcrg/projects/> (02/09/2013).
- [24] OLED lighting to take off in 2011; accessed from: [http://www.displaysearch.com/cps/rde/xchg/displaysearch/hs.xsl/090312\\_oled\\_lighting\\_to\\_take\\_off\\_in\\_2011.asp](http://www.displaysearch.com/cps/rde/xchg/displaysearch/hs.xsl/090312_oled_lighting_to_take_off_in_2011.asp) (05/09/2013).
- [25] Light Emitting Diodes; accessed from <http://www.ecse.rpi.edu/~schubert/Light-Emitting-Diodes-dot-org/chap18/F18-03%20Chromaticity%20diagram%20-%20planckian.jpg> (03/09/2013).
- [26] N. S. Christ, S.W. Kettlitz, S. Valouch, S. Züfle, C. Gärtner, M. Punke and U. Lemmer, *J. Appl. Phys.* **105** (2009) 104513-104522.
- [27] LCD Response Time and Motion Blur; accessed from: [http://www.displaymate.com/LCD\\_Response\\_Time\\_ShootOut.htm](http://www.displaymate.com/LCD_Response_Time_ShootOut.htm) (05/09/2013).
- [28] OLED TV; accessed from: <http://www.oled-info.com/oled-tv> (05/09/2013).
- [29] Sony Launches World's First OLED TV; accessed from: <http://www.sony.net/SonyInfo/News/Press/200710/07-1001E/> (03/09/2013).
- [30] OLED in mobile phones; accessed from: <http://www.oled-info.com/oled-mobile-phones> (06/09/2013).
- [31] F.P. Rosseli, W.G. Quirino, C. Legnani, V.L. Calil, K.C. Teixeira, A.A. Leitao, R.B. Capaz, M. Cremona and C.A. Achete, *Org. Electron.* **10** (2009) 1417-1423.

# Chapter 2

## Photo-physical properties of organic semiconductors.

### 1. Introduction

Organic compounds are defined by the presence of carbon atoms, most often arranged as conjugated aromatic hydrocarbons. Three main categories of organic materials exist namely: small molecules, polymers and biological compounds (figure 1). Small molecules, or monomers, have a well-defined molecular weight. Polymers on the other hand, are long-chain molecules comprised of a varying number of repeated units and the weight of each polymer molecule differs from the other. Biological molecules are on the extreme end of the complexity scale and they have yet to find a clear application in optical or electronic systems.

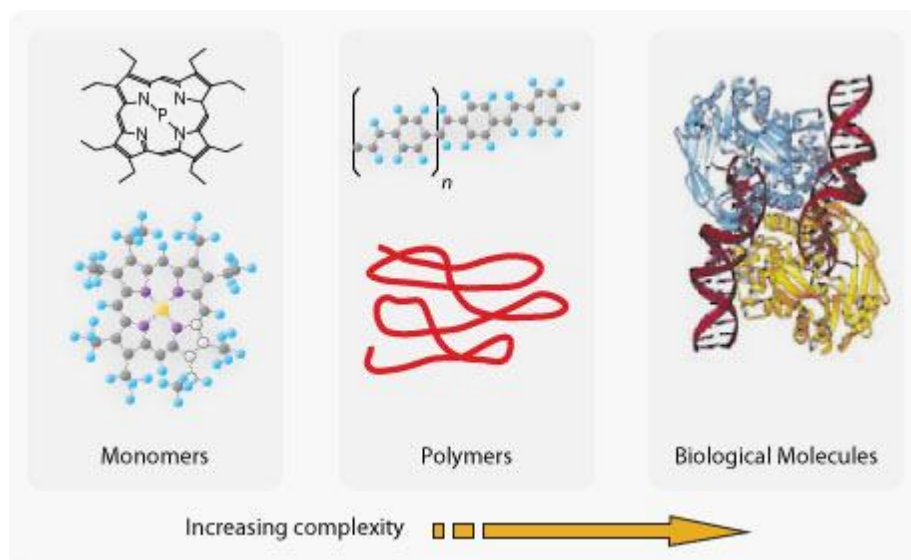


**Figure 1: Representative molecular structures of organic semiconductors depend on the complexity of hydrocarbon conjugation length [1].**

There are four different types of bonding in solids namely: covalent bond, ionic bond, metallic bond and van der Waals (VDW) bond (figure 2). Organic solids are composed of discrete molecules held together by VDW forces. It is therefore expected that the photo-physical properties and the electronic structure of organic molecules will be different when compared

with inorganic solid materials. In this chapter, the basic properties of organic semiconductors will be described.

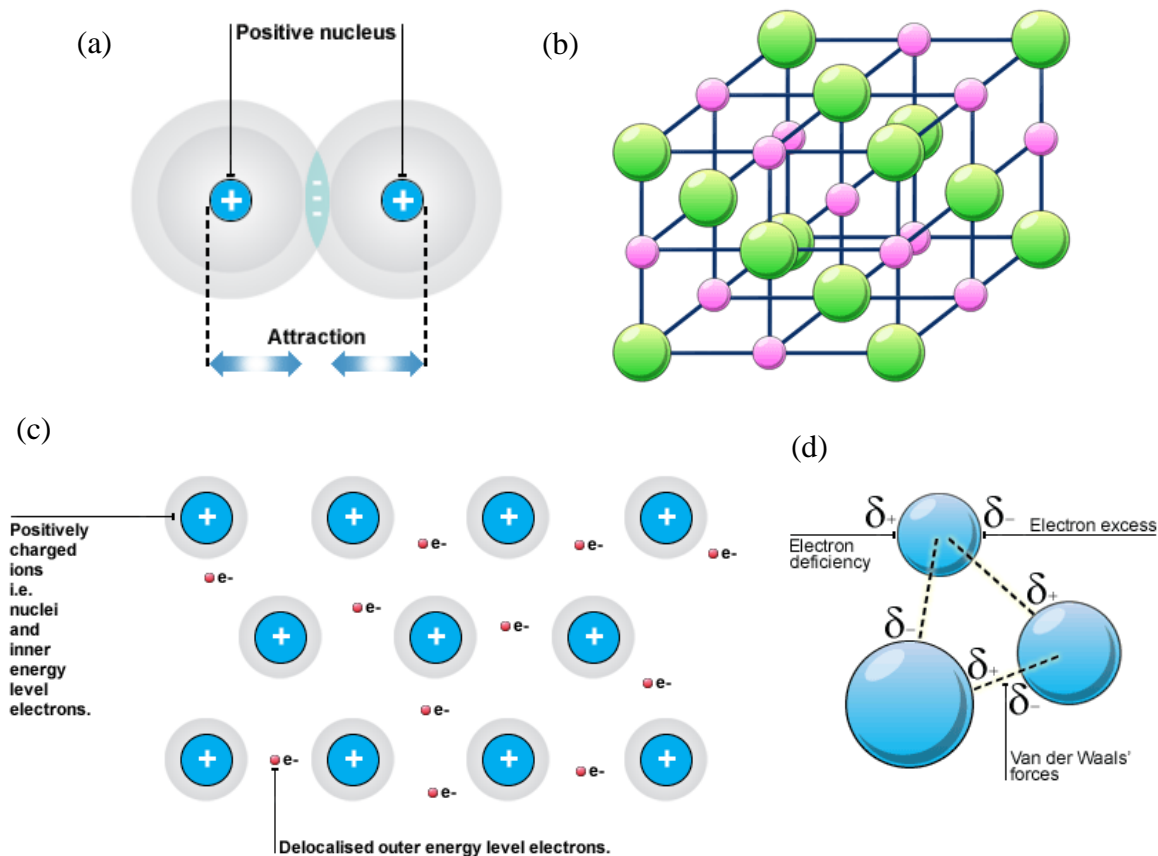


**Figure 2: (a) Covalent bond, (b) ionic bond, (c) metallic bond and (d) van der Waals bond [2].**

## 2. Electronic structures

An organic semiconductor is defined as a highly conductive organic compound. Monomers and polymers form the two major classes of organic semiconductors. Both have in common a conjugated  $\pi$ -electron system. Strong bonding between conjugated carbon atoms forms  $sp^2$ -hybridized orbitals ( $\sigma$ -bonds) and loosely connected  $p_z$ -orbitals which are perpendicular to the plane containing all the carbon atoms. Overlapping between the neighboring  $p_z$ -electrons of the carbon atoms form the so-called  $\pi$ -bonds shown in figure 3. The  $\sigma$ -bonds form the backbone of the molecule while the  $\pi$ -bonds are significantly weaker.

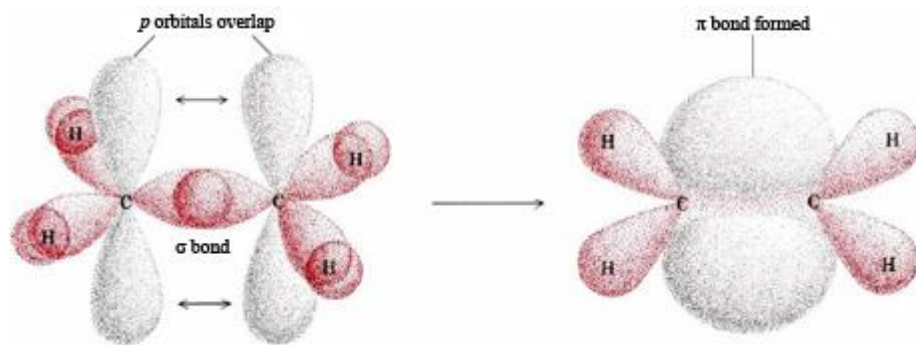


**Figure 3: The electronic states of organic semiconductors.  $sp^2$  hybridization generates strong  $\sigma$ -bonds and loosely connected  $\pi$ -orbitals [3].**

The delocalized  $\pi$ -electrons are free to move within the molecule enabling charge transport in organic materials. While inorganic semiconductors have a valence band (VB) and conduction band (CB), organic semiconductors have a highest occupied molecular orbital (HOMO) and a lowest unoccupied molecular orbital (LUMO). The gap between the HOMO and LUMO is decided by the interactions between the  $\sigma$  and  $\pi$ -electrons within the molecule, while the optical properties of organic semiconductors are decided by the  $\pi$ - $\pi^*$  transition (figure 4). These transitions have an energy gap typically between 1.5 and 3 eV, leading to light absorption or emission in the visible spectral range. When a large number of electrons are involved, the energy levels may form a continuous band like the VB and CB of an inorganic semiconductor. The band gap of the molecule is also strongly affected by the degree of conjugation. Larger molecules will therefore have smaller band gaps. By controlling the degree of conjugation in a molecule, there is a wide range of possibilities to tune the optoelectronic properties of organic semiconductor materials [4, 5].

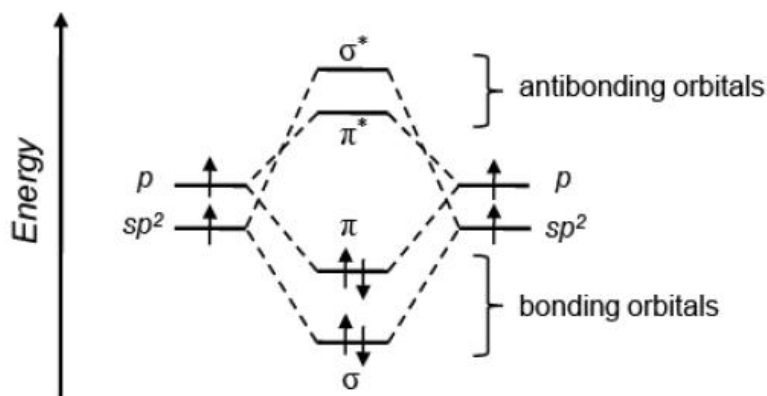


Figure 4: Splitting of energy levels by strong interaction between two molecules [5].

### 3. Charge transport

In inorganic semiconductors such as silicon or germanium, the strong coupling between the constituting atoms and the long-range order lead to the delocalization of the electronic states and the formation of allowed valence and conduction bands, separated by a forbidden gap (energy gap). By photo-excitation or thermal activation, free carriers are generated in the conduction band, leaving behind positively charged holes in the valence band. The transport of these carriers is described in quantum mechanical terms by dispersion relations, Bloch functions and wave-space [6].

Charge transport in organic molecules should be considered as a pair of electron and hole forming from a neutral molecule. In organic solids, interactions are mainly covalent, but intermolecular interactions are due to much weaker London and VDW forces. These organic semiconductors typically have narrow energy bands and the HOMO and the LUMO can easily be disrupted by disorder. Therefore, even in crystals, the concept of allowed energy band is of limited validity and excitations and interactions localized on individual molecules play a predominant role. Compared to a single molecule in the gas phase, ionized electron and hole pairs in the solid crystal lower the band gap due to the polarization energy (figure 5). In amorphous solids the charge transport sites have a Gaussian distribution of energies and are localized [5, 6]. The shape of the density of states (DOS) is suggested to be Gaussian based on the observed shape of the optical spectra [7]. Depending on the degree of order, the charge

carrier transport mechanism in organic semiconductors can fall between two extreme cases: band or hopping transport.

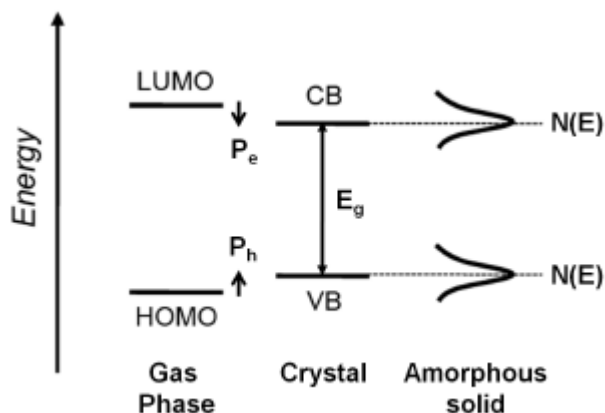


**Figure 5: Different energy level diagrams of a single molecule in gas phase, ionized electron and hole pairs in the solid crystal, and a disordered Gaussian density of states in an amorphous solid [4].**

### 3.1 Band transport

Band transport will typically be observed in highly purified molecular crystals at not too high temperatures. The bandwidth is small as compared to inorganic semiconductors (a few  $kT$  at 25 °C) since the electronic delocalization is weak. Room temperature mobilities in molecular crystals will therefore reach only values in the range of 1 to 10  $\text{cm}^2/\text{Vs}$ . As a characteristic feature of band transport the temperature dependence follows a power law behavior [4]

$$\mu \propto T^{-n} \quad \text{with } n = 1 \dots 3 \quad (1)$$

upon going to lower temperature. In the presence of traps significant deviations from such behavior are observed.

### 3.2 Hopping transport

Most organic thin films are in an amorphous solid state and weak VDW interactions throughout the amorphous structure cannot provide a continuous band transporting path. The motion of carriers is therefore typically described by hopping transport, which is a phonon-assisted tunneling mechanism from site to site (figure 6). Many hopping models are based on the Miller-

Abrahams equation [8]. In this model, hopping from a localized state  $i$  to a state  $j$  takes place at frequency  $\nu_o$ , corrected for a tunneling probability to absorb a phonon for hops upwards in energy:

$$\omega_{ij} = \nu_o \begin{cases} \exp\left(-2\alpha R_{ij} - \frac{E_j - E_i}{k_B T}\right) & : E_j - E_i \geq 0 \\ \exp -2\alpha R_{ij} & : E_j - E_i \leq 0 \end{cases} \quad (2)$$

Here  $\alpha$  is the inverse localization length,  $R_{ij}$  the distance between the localized states,  $E_i$  the energy at the state  $i$  and  $\nu_o$  the attempt-to-escape frequency. Since the hopping probability depends on both the spatial and energetic difference between the hopping sites, it is natural to describe the hopping processes in a four-dimensional hopping space, which is spanned by three spatial and one energy coordinate.

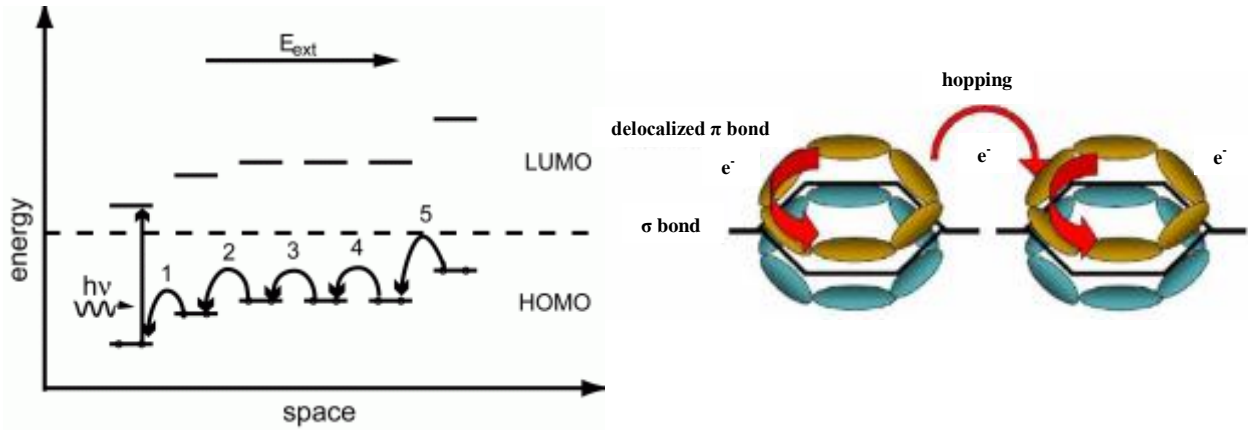


**Figure 6: Hopping of charge carriers in molecules [5, 9].**

The typical charge carrier mobility ( $\mu$ ) of amorphous organic semiconductors is in the range of  $10^{-3} \sim 10^{-10} \text{ cm}^2/\text{Vs}$ . The mobility can be expressed as a function of the electric field and temperature [10]:

$$\mu_{F,T} \propto \exp\left(\frac{-\Delta E}{kT}\right) \cdot \exp\left(\frac{\beta\sqrt{F}}{kT}\right) \quad (3)$$

where  $F$  is the electric field,  $T$  is the temperature,  $\Delta E$  is the activation energy for intermolecular hopping,  $k$  is Boltzmann's constant and  $\beta$  is a constant value.

## 4. Transport bandgap vs. optical bandgap

For inorganic semiconductors, there is a negligible difference ( $\sim$ meV) between the optical band gap ( $E_{opt}$ ) and the transport band gap ( $E_{tr}$ ) due to the small exciton binding energy in delocalized energy states. In organic semiconductors, the  $E_{opt}$  and  $E_{tr}$  should be classified due to the strong exciton binding energy ( $\sim$ eV) in the localized organic molecule. The relationship between  $E_{opt}$  and  $E_{tr}$  for an organic semiconductor can be defined as [11]:

$$E_{opt} = (E_{gap} - E_p) - E_{ex} = E_{tr} - E_{ex} \quad (4)$$

where  $E_{gap}$  is the energy level difference between the HOMO and LUMO in a single molecule,  $E_p$  is the energy loss due to polarization and  $E_{ex}$  is the exciton binding energy.

## 5. Excitons

### 5.1 Exciton formation

An exciton is defined as a bound state of an electron-hole pair which is attracted to each other by the electrostatic coulombic interaction. It is an electrically neutral or charge-less quasi-particle that is found in semiconductors, insulators and also in some liquids. It is capable of diffusion and can therefore transport energy without transporting net electric charge [12]. Two major types of excitons can be found and they are classified by their binding energy. The loosely-bound Wannier exciton is found in inorganic semiconductors, while the tightly-bound Frenkel exciton can be found in organic semiconductors (figure 7). The delocalized Wannier exciton has a large radius of  $\sim 100 \text{ \AA}$  with a weak binding energy of  $\sim 10 \text{ meV}$ . The Frenkel exciton, on the other hand, is typically localized within one or two molecules ( $\sim 10 \text{ \AA}$ ) and has a strong binding energy of  $\sim 1 \text{ eV}$ . There is also a third type of exciton known as the charge-transfer (CT) exciton. It has a binding energy between that of the Wannier and Frenkel excitons and the electron-hole pairs can therefore reside up to a few intermolecular distances.

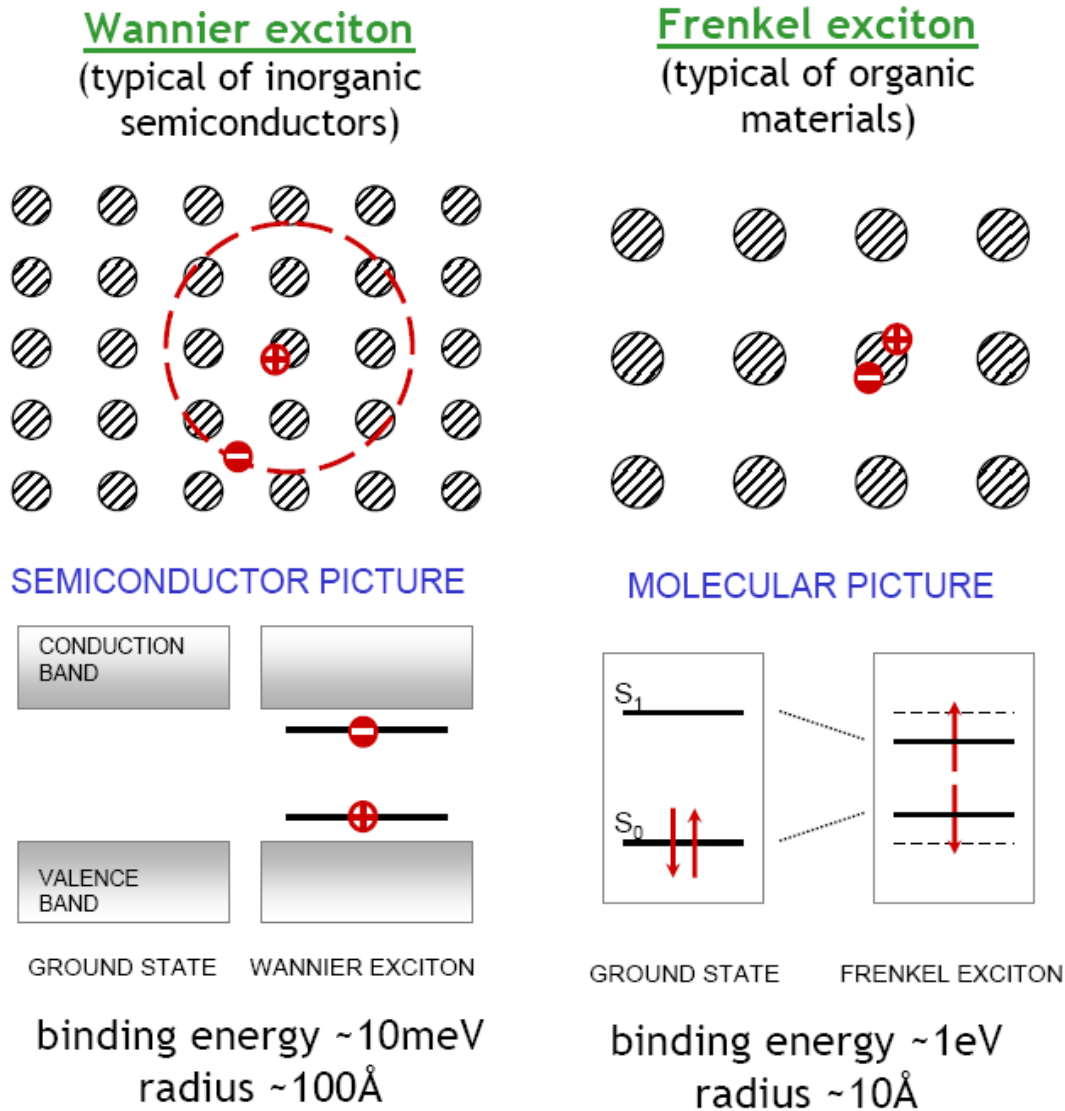


**Figure 7: Schematic illustration of the two major types of excitons: (left) loosely bounded Wannier exciton and (right) the tightly bounded Frenkel exciton [13].**

## 5.2 Multiplicity of excitons

The exciton has four possible spin states (two spin states in each charge). The total wave function of a two-electron system must be anti-symmetric with the interchange of the particles based on Pauli's exclusion principle. ( $\Psi_s$  and  $\Psi_a$ ), based on the possible spin statistics of the excited electrons, can be expressed as

$$\begin{aligned}
 \Psi_s &= X_1(\uparrow) X_2(\uparrow) \\
 \Psi_s &= X_1(\downarrow) X_2(\downarrow) \\
 \Psi_s &= X_1(\uparrow) X_2(\downarrow) + X_1(\downarrow) X_2(\uparrow) \\
 \Psi_a &= X_1(\uparrow) X_2(\downarrow) - X_1(\downarrow) X_2(\uparrow)
 \end{aligned}
 \left. \vphantom{\begin{aligned} \Psi_s \\ \Psi_s \\ \Psi_s \\ \Psi_a \end{aligned}} \right\} \begin{array}{l} \text{Symmetric states (spin = 1, triplet)} \\ \text{Anti-symmetric state (spin = 0, singlet)} \end{array} \quad (5)$$

where  $X_n$  ( $n = 1,2$ ) is a spin function and ( $\uparrow$ ) or ( $\downarrow$ ) represents the possible spin states of each electron [14]. The radiative relaxation processes using singlet and triplet excitations are shown in figure 8. The singlet state has higher energy than that of the triplet state because of the difference in spatial symmetry. The triplet exciton has smaller electron-electron repulsion and this leads to less potential energy. A very fast lifetime of  $\sim 1$  ns is also observed for fluorescence due to the symmetry conservation in the singlet exciton. In the case of phosphorescence a slow relaxation time of  $\sim 1$  ms is observed. This is due to the fact that the triplet exciton transition to the ground state is not preferable.

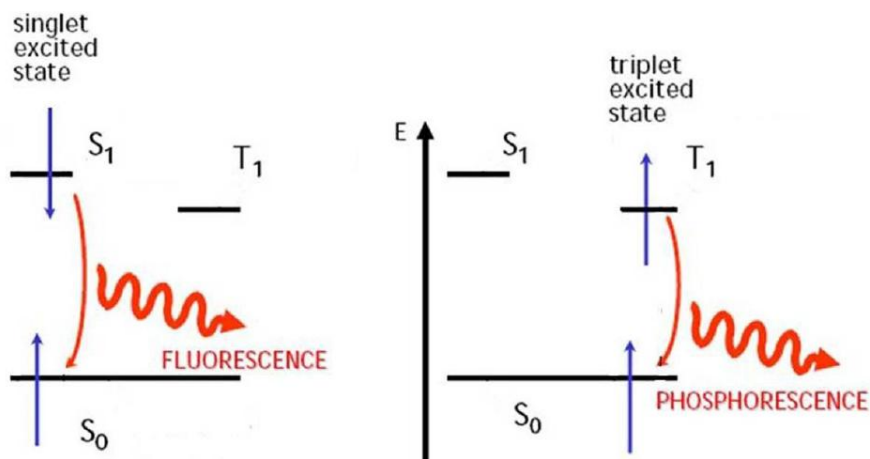


**Figure 8: Fluorescence from the singlet exciton (left) and phosphorescence from the triplet exciton (right) [5].**

### 5.3 Metal-ligand charge transfer exciton

Organometallic compounds that are based on heavy metals such as iridium, platinum, osmium and ruthenium can exploit singlet as well as triplet excitons. This is due to the very strong spin-

orbit coupling and it is proportional to the atomic number ( $Z$ ) [15]. Strong spin-orbit coupling based on heavier metals such as iridium can effectively mix the singlet and triplet states and generate emissive metal-ligand charge transfer (MLCT) excitons (figure 9). Therefore, in theory, it would be possible to convert all the singlet and triplet excitons to phosphorescence and this will lead to a 100% photon conversion efficiency using these organometallic compounds as emitters [16].

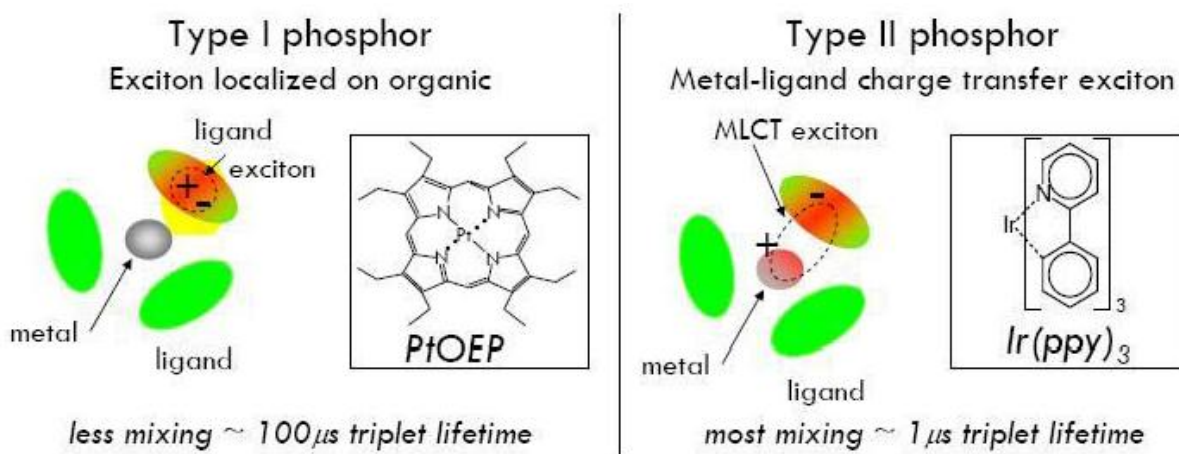


**Figure 9: Schematic illustration of two organometallic compounds that are composed of a heavy metal atom in the core and organic molecules (ligands) surrounding it.**

## 6. Intra-molecular energy transfer

The Jablonski energy diagram (figure 10) illustrates various photo-physical processes in a typical molecule. The absorption process is from the ground state ( $S_0$ ) to the excited state ( $S_{1,2}$ ) and non-radiative transitions like vibrational relaxation, inter-system crossing, quenching and internal conversion can take place before the radiative processes like fluorescence ( $S_1 \rightarrow S_0$ ) or phosphorescence ( $T_1 \rightarrow S_0$ ) occur.

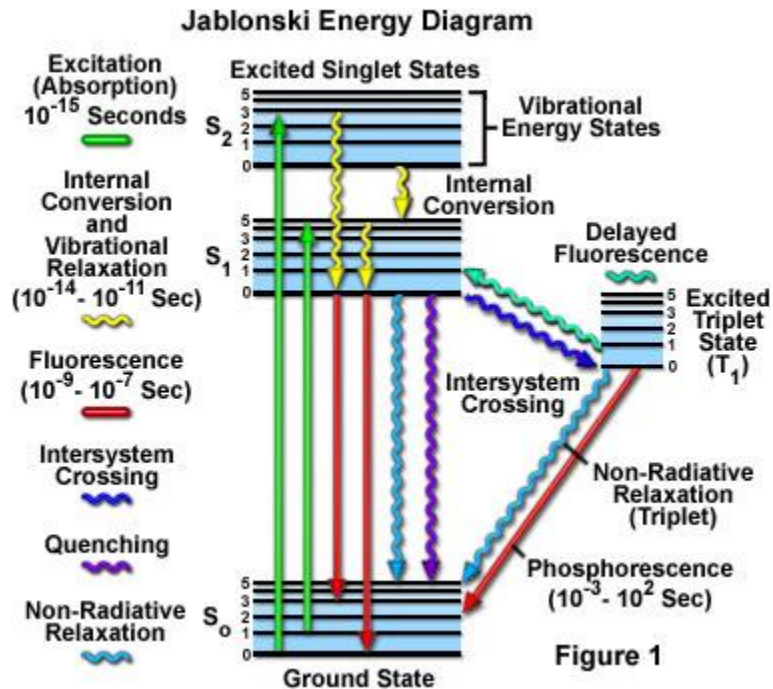


Figure 10: The Jablonski energy diagram illustrating the different intra-molecular energy transfer processes [17].

## 6.1 Absorption

Absorption occurs when the excitation energy is larger than the bandgap energy ( $E_b=hc/\lambda$ ). An absorption transition occurs from a vibrational energy level of the ground state to a higher vibrational level in the excited state (green arrows in figure 10). The electronic absorption spectrum is generally a broad band, rather than just a single line.

## 6.2 Fluorescence

Once generated, excitons will quickly relax to the lowest vibrational level of an excited singlet state via internal conversion and vibrational relaxation processes. Excitons will then relax to the ground state and emit a photon in the process ( $S_1 \rightarrow S_0$ ). This process is called fluorescence and it can only exploit the singlet excitons (25%) and also has a very short radiative lifetime ( $\sim 10^{-9}$  to  $10^{-7}$  s).

### 6.3 Intersystem crossing

A direct absorption from the ground state to the triplet state is not preferable, but a significant amount of energy can be transferred from the lowest excited singlet state to the excited triplet state ( $S_1 \rightarrow T_1$ ). This process is known as intersystem crossing. The mechanism for intersystem crossing involves vibrational coupling between the excited singlet state and triplet state.

### 6.4 Phosphorescence

When an intersystem crossing has occurred, the exciton will undergo an internal conversion process and relaxes to the lowest vibrational level of the triplet state. Since the difference in energy between the lowest vibrational level of the triplet state and the lowest vibrational level of the singlet state is large compared to the thermal energy, backward energy transfer from the triplet to the singlet state is highly improbable. The transition from the lowest vibrational level of the triplet state to the ground state ( $T_1 \rightarrow S_0$ ) is possible (typically forbidden process) only when the spin-orbit coupling breaks the selection rule. Therefore the molecules are only able to emit weakly and the radiative lifetime of a triplet exciton (75%) is  $\sim 10^{-4}$  to 1 s.

### 6.5 Frank-Condon shift

Most of the absorption and emission processes in organic molecules involve the vibrational modes. An electronically excited molecule releases its energy very quickly towards a stable energy state through either photon generation (fluorescence or phosphorescence) and/or phonon vibration (heat loss). Figure 11 shows the configurational diagram of the ground and excited states in a molecule. Absorption occurs by a transition from the zero order vibrational level of the ground state to a higher order vibrational level of the excited state ( $v'' = 0 \rightarrow v' = 2$ ). The exciton then experiences a fast vibrational relaxation by releasing heat to the zero order level ( $v' = 2 \rightarrow v' = 0$ ). Emission will occur from a transition of the zero order vibrational level of the excited state to various vibrational levels of the ground state ( $v' = 0 \rightarrow v'' = 2$ ). This Frank-Condon shift (or Stokes shift) leads to the red shifted emission peak compared to the absorption peak [11].

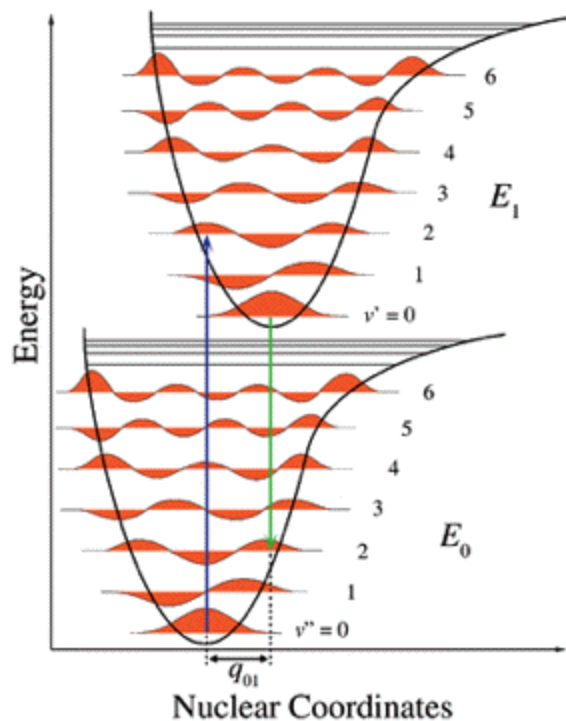


**Figure 11: The configurational diagram of ground ( $S_0$ ) and excited ( $S_1$ ) states of a molecule, respectively. So called “Frank-Condon shift” or “Stokes shift” happens in a molecule due to the fast and nonradiative vibrational relaxations.**

## 7. Inter-molecular energy transfer

Inter-molecular energy transfer is a non-radiative process between molecules and it can be divided into two types, depending on the range of the transitions. The short range transition ( $\sim 10 \text{ \AA}$ ) is called the Dexter transfer [18] and the long range transition ( $\sim 100 \text{ \AA}$ ) is called the Förster transfer [19]. Figure 12 illustrates the mechanism of Dexter and Förster transitions.

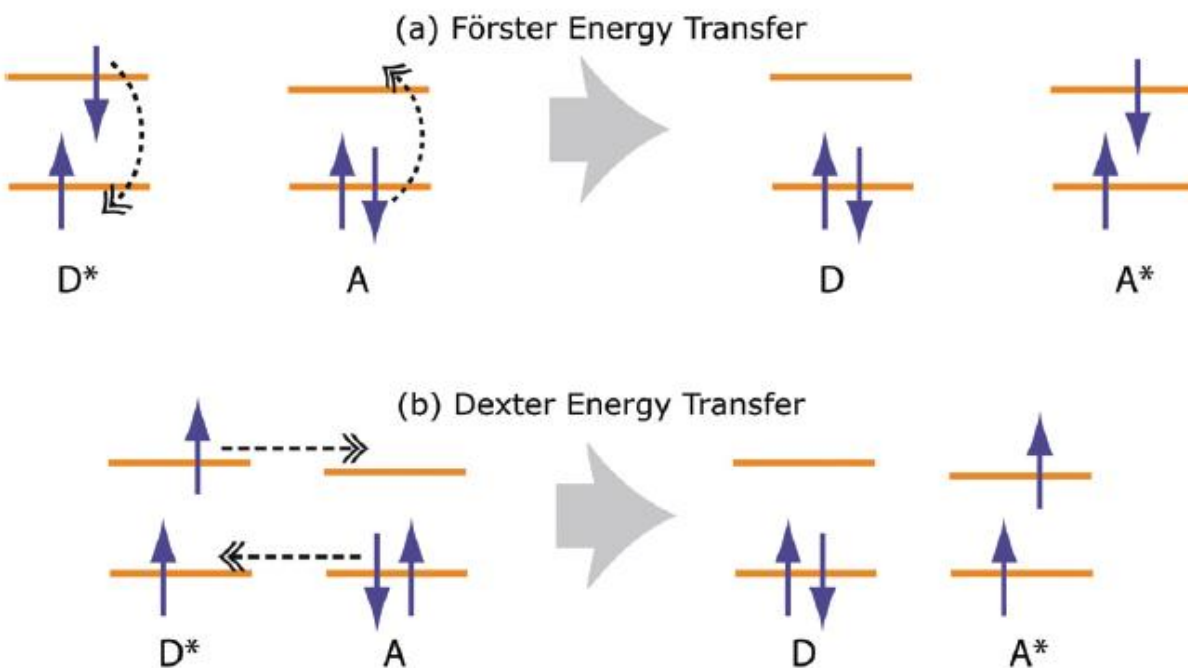


**Figure 12: (a) Förster energy transfer and (b) Dexter energy transfer. The horizontal lines are the HOMO and LUMO energy levels of the donor (D) and acceptor (A) molecules; the asterisk denotes the excited states [20].**

## 7.1 Dexter energy transfer

Dexter energy transfer takes place through a double electron exchange mechanism within the molecular orbitals of the donor and acceptor and is known as through-bond energy transfer. Significant orbital overlap is required for the electron coupling leading to the energy transfer. Close interaction between the excited donor and the acceptor ground state is therefore necessary. The rate constant of Dexter energy transfer,  $k_{ET}(Dexter)$ , is given by [21]

$$k_{ET}(Dexter) = KJ e^{-2R_{DA}/L} \quad (6)$$

where  $R_{DA}$  is the distance between donor (D) and acceptor (A) relative to their van der Waals radii  $L$ ,  $K$  is related to the specific orbital interactions and  $J$  is the normalized spectral overlap integral. The Dexter transfer rate is therefore affected by both the separation distance between D and A and also the spectral overlap.

## 7.2 Förster energy transfer

The Förster energy transfer is also known as the dipole-dipole or through-space energy transfer. It involves the long-range coupling of the donor and acceptor dipoles. The presence of intervening solvent dipoles facilitates the resonance between the donor dipole moment and the acceptor dipole moment. This kind of energy transfer, according to Förster, is mainly affected by three factors: (1) the orientation of the dipoles of the donor and acceptor molecules and the intervening medium; (2) the spectral overlap between the absorption spectrum of the acceptor and the fluorescence spectrum of the donor; and (3) the distance between donor and acceptor since both dipole-dipole interaction energy and resonance are distance dependent. Förster energy transfer is favored when the donor and acceptor are rigidly held in good alignment, because resonance is maximized when the oscillating dipole, the excited donor and the transition dipole of the acceptor ground state are aligned. The energy transfer rate,  $k_{ET}(Förster)$ , is given by [21]

$$k_{ET}(Förster) = k \frac{\kappa^2 k_D^0}{R_{DA}^6} J \quad (7)$$

where  $k$  is a constant determined by experimental conditions such as concentration and solvent index of refraction.  $\kappa^2$  is related to the interaction between the oscillating donor dipole and the acceptor dipole, which depends on the square of the transition dipole moments for the donor and the acceptor and the orientation of the dipoles in space.  $k_D^0$  is the pure radiative rate of the donor,  $J$  is the spectral overlap integral and  $R_{DA}$  is the distance between the donor and acceptor.

## References

1. Organic Semiconductors and Organic Photovoltaics; accessed from: <http://www.globalphotonic.com/Technology.aspx> (02/03/2012).
2. Bonding, structures and properties; accessed from: [http://www.bbc.co.uk/scotland/learning/bitesize/higher/chemistry/energy/bsp\\_rev3.shtml](http://www.bbc.co.uk/scotland/learning/bitesize/higher/chemistry/energy/bsp_rev3.shtml) (02/03/2012).
3. Sigma and Pi Bonds; accessed from: <http://chemed.chem.wisc.edu/chempaths/GenChem-Textbook/Sigma-and-Pi-Bonds-858.html> (29-03-2012).
4. W. Brütting, "Physics of Organic Semiconductors", (WILEY-VCH, 2005).
5. S.H. Eom "High efficiency blue and white phosphorescent organic light emitting devices" (PhD thesis, University of Florida, 2010)
6. Organic Semiconductor Physics; accessed from: <http://www.iue.tuwien.ac.at/phd/li/node10.html> (29/02/2012).
7. H. Bassler, *Phys. Stat. Sol.(b)*, **175** (1993) 15-56.
8. A. Miller and E. Abrahams, *Phys. Rev.*, **120** no. 3 (1960) 745-755.
9. Composition of electro optic polymers; accessed from: [http://www.uni-muenster.de/Physik.AP/Denz/en/Forschung/Forschungsaktivitaeten/FunktionaleMaterialien/elektrooptische\\_polymere.html](http://www.uni-muenster.de/Physik.AP/Denz/en/Forschung/Forschungsaktivitaeten/FunktionaleMaterialien/elektrooptische_polymere.html) (03/03/2012).
10. J. D. Wright, "Molecular Crystals", 2nd Ed. (Cambridge University Press, 1995).
11. M. Pope and C.E. Swenberg, "Electronic Processes in Organic Crystals and Polymers", 2nd Ed. (Oxford University Press, Oxford, 1999).
12. Exciton; accessed from: <http://www.princeton.edu/~achaney/tmve/wiki100k/docs/Exciton.html> (08/01/2013)
13. Excitons – Types, Energy Transfer; accessed from: <http://ocw.mit.edu/courses/electrical-engineering-and-computer-science/6-973-organic-optoelectronics-spring-2003/lecture-notes/7.pdf> (09/01/2013).
14. Symmetric and anti-symmetric wave functions; accessed from: <http://faculty.uaeu.ac.ae/~maamar/modphys2/73.html> (09/01/2013).
15. J. Paska, P. Biczal, and M. Klos, *Renew. Energ.* **34** (2009) 2414-2421.

16. C. Adachi, M. A. Baldo, M. E. Thompson, and S. R. Forrest, *J. Appl. Phys.* **90** (2001) 5048-5051.
17. Jablonski energy diagram; accessed from:  
<http://www.olympusmicro.com/primer/java/jablonski/jabintro/index.html> (10/01/2013).
18. D. L. Dexter, *J. Chem. Phys.* **21** (1953) 836-850.
19. T. Förster, *Discuss. Faraday Soc.* **27** (1959) 7-17.
20. O.V. Mikhnenko “Singlet and Triplet Excitons in Organic Semiconductors” (PhD thesis, University of Groningen, 2012).
21. N.S. Allen “Photochemistry and Photophysics of Polymeric Materials” (John Wiley and Sons, 2010).

# Chapter 3

## The effect of substituents on the optical properties of $Mq_3$ .

### 1. Introduction

Tang and VanSlyke developed the first efficient multi-layered organic light emitting diode (OLED) in 1987 [1]. They used tris-(8-hydroxyquinoline) aluminium ( $Alq_3$ ) as both the electron transporting and emitting layer. Since then substantial progress has been made in the field, leading to more and more commercial OLED products (screens for cell phones, mp3 players and cameras).  $Alq_3$  is still used in these devices due to its high fluorescent efficiency, relatively good electron mobility and thermal stability [2]. It has been widely reported [3 - 5] that the emission color of  $Alq_3$  can be chemically tuned. The emission of  $Alq_3$  originates from the ligand's electronic  $\pi$ - $\pi^*$  transitions. This is from the highest occupied molecular orbital (HOMO) that is mainly situated on the phenoxide ring to the lowest unoccupied molecular orbital (LUMO) situated on the pyridyl ring [2]. The highest electron density of the HOMO of  $Alq_3$  is located on the C-5, C-7 and C-8 positions of the phenoxide oxygen and for the LUMO on the C-2 and C-4 positions of pyridyl nitrogen [2]. It is predicted that electron donating groups (EDG) and electron withdrawing groups (EWG) at these positions can lead to either a blue-shift or red-shift of the absorption and emission spectra.

In this study the effect of EDG and EWG on the morphology and optical properties were investigated.  $Alq_3$  powders were synthesized with an EDG ( $-CH_3$ ) substituted at position 5 and 7 ((5,7-dimethyl-8-hydroxyquinoline) aluminium (5,7Me- $Alq_3$ )) and EWG ( $-Cl$ ) at position 5 ((5-chloro-8-hydroxyquinoline) aluminium (5Cl- $Alq_3$ )).  $Al^{3+}$  was substituted with  $Ga^{3+}$  and  $In^{3+}$  and the effect of the different metals on the luminescent properties was investigated. The effect of excitation wavelength on the emission maxima of  $Mq_3$  was also investigated.

## 2. Synthesis

A methanol solution (20 ml) of the preferred 8-hydroxyquinoline (8-hydroxyquinoline, 5-chloro-8-hydroxyquinoline or 5,7-dimethyl-8-hydroxyquinoline (purchased from Sigma Aldrich and used without further purification)) (1.36 mmol) was slowly added to a water solution (20 ml) of the preferred trichloride ( $\text{AlCl}_3$ ,  $\text{GaCl}_3$  or  $\text{InCl}_3$ ) (0.1 g, 0.45 mmol) with stirring at room temperature. Stirring was continued overnight and a yellow precipitate was filtered out and washed with cold methanol to remove excess 8-hydroxyquinoline. The filtrate was recrystallized in a water/methanol mixture (10:90 %) by slow evaporation at room temperature. Yellow crystalline powder was obtained after one week of drying at room temperature. Yield: 0.228 g (87 % based on In). Figure 1 shows the molecular structure of the metal complexes synthesized with the EWG and EDG.

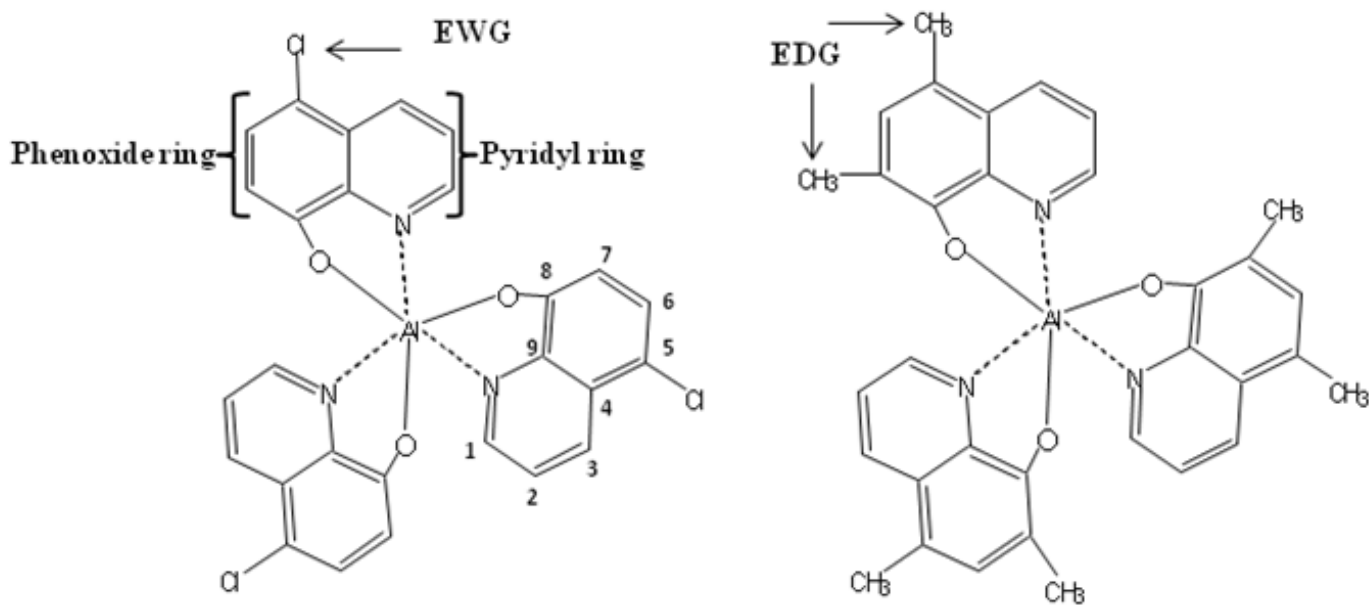


**Figure 1: The two metal complexes that were synthesized with the EWG ( $5\text{Cl-Alq}_3$ ) and EDG ( $5,7\text{Me-Alq}_3$ ).**

### 3. Results and discussion

#### 3.1 Effect of substituents on the luminescence and morphology of Alq<sub>3</sub>.

Figure 2(a) shows the absorption spectra for the three Alq<sub>3</sub> samples dissolved in ethanol. The spectrum of Alq<sub>3</sub> is dominated by an intense absorption band at 383 nm. In addition to this intense band, there are 2 weak absorption bands at 317 and 332 nm. The broad band at 383 nm is reported to be a ligand centered electronic transitions [6]. The band at 383 nm has multiple electronic origins and is a superposition of two or more electronic transitions. Burrows et al. [7] calculated the three lowest-energy transitions of the meridional isomer and found it to be at wavelengths of 377, 369 and 362 nm respectively. The absorption maximum for Alq<sub>3</sub> in solution is at 383 nm, which is close to the average of 372 nm for the three bands. The absorption band is broad enough (FWHM = 80 nm), so it is not expected that these nearly degenerate energy transitions will be resolved at room temperature. The three lowest-energy electronic transitions are effectively donor-acceptor transitions, from a phenoxide donor to a pyridyl acceptor. The two bands at 317 and 332 nm are assigned to the vibronic progression due to the ring deformation mode of an electronic transition at 346 nm [6]. The main bands of 5,7Me-Alq<sub>3</sub> and 5Cl-Alq<sub>3</sub> are both red-shifted by 27 and 11 nm respectively.

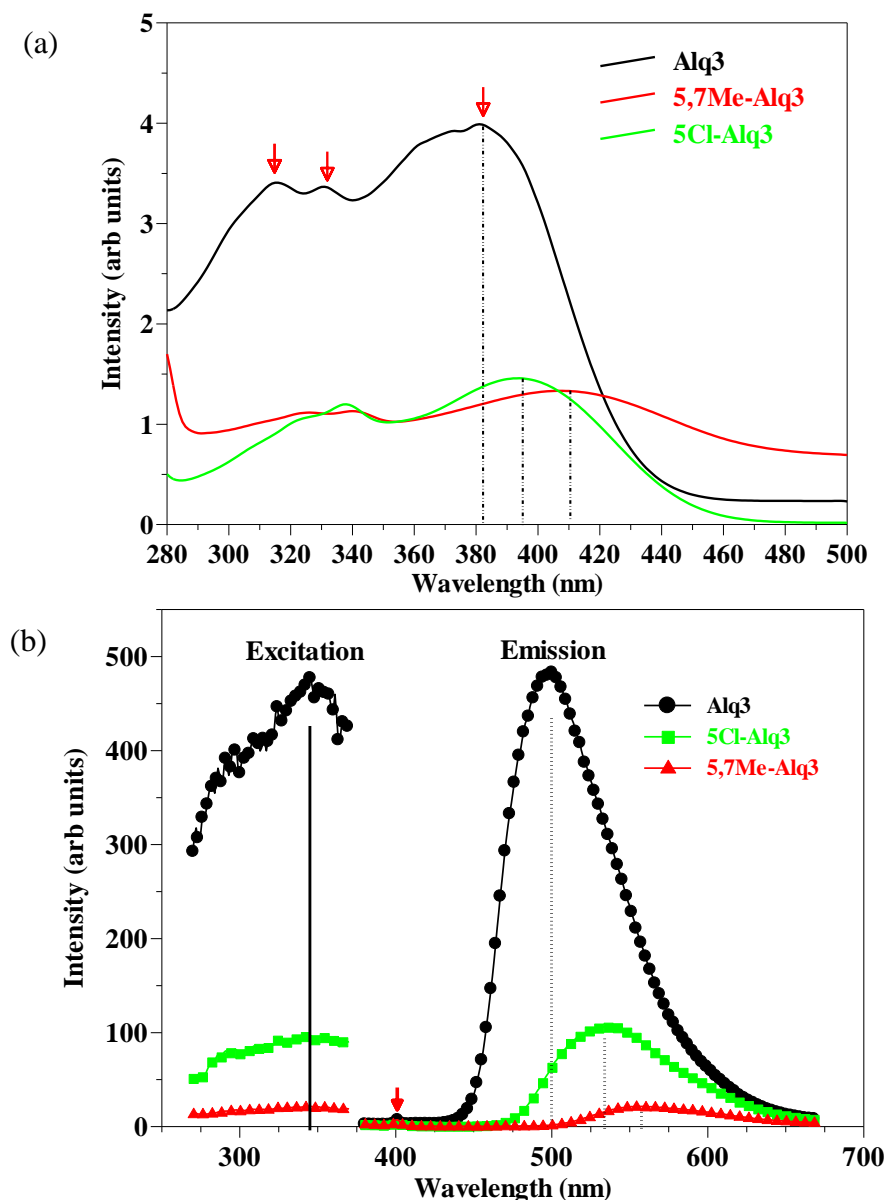


**Figure 2: (a) The absorption and (b) the excitation (left side of graph) and emission spectra (right side of graph) of the various Alq<sub>3</sub> derivatives. The solid black line indicates the excitation maximum and the dashed black lines indicate the emission maxima.**

Figure 2(b) shows the solid state emission spectra of the three Alq<sub>3</sub> derivatives. All the samples were excited at a wavelength of 345 nm. This wavelength correlates with a higher energy electronic transition (S<sub>4</sub> and above) [6, 8]. The Alq<sub>3</sub> sample has an emission peak at 500 nm with a FWHM of 80 nm. The emission spectrum is red shifted by ~ 0.4 eV from the excitation spectra. This can be interpreted as the Franck-Condon (or Stokes) shift, which results from large

conformational energy changes upon optical excitation. The broadness of the peak can also be attributed to these conformational changes, due to strong exciton-phonon coupling [7]. Alq<sub>3</sub> is known to be a singlet emitter [9]. The emission is due to the relaxation of an excited electron from the S<sub>1</sub>-S<sub>0</sub> level. The small peak at 400 nm corresponds to the emission of 8-hydroxyquinoline. This is an indication that a small amount of unreacted 8-hydroxyquinoline is still present in the powder samples.

The 5,7Me-Alq<sub>3</sub> sample shows a red shift of ~ 56 nm to 556 nm. Singh et al. [10] found a similar shift in 5,7-dimethyl-8-hydroxyquinoline zinc to 560 nm. The shift is due to the decrease in the band gap of the material. Qin et al. [4] reported that electron-donating groups and groups capable of extended  $\pi$  conjugation at the 5-position of the phenoxide ring should lead to higher HOMO levels and smaller HOMO-LUMO gaps, thus resulting in a red shift.

The highest electron density of Alq<sub>3</sub>'s HOMO is located at the C-5, C-7 and C-8 positions of the phenoxide oxygen. It is predicted that an electron-withdrawing group at these positions will lead to a blue shift in the absorption and emission spectra. In the case of 5Cl-Alq<sub>3</sub>, a red shift of ~ 33 nm to 533 nm was observed. Shi et al. [5] found that in the case of 5F-Alq<sub>3</sub> the lone electron pair on the F atom and the high electron density at the C-5 position will cause the F group to take part in forming the HOMO of Alq<sub>3</sub> through a conjugation effect, giving rise to the higher HOMO energy level of 5F-Alq<sub>3</sub>. The higher HOMO level will lead to a narrowed HOMO-LUMO gap and a red shift of the emission peaks. Cl also contains a lone electron pair that will cause the HOMO level to be higher leading to the observed red shift.

The above explanation also applies to the red shift observed in the absorption spectra of 5,7Me-Alq<sub>3</sub> and 5Cl-Alq<sub>3</sub>.

There was a significant decrease in the absorption and PL intensity of 5,7Me-Alq<sub>3</sub> and 5Cl-Alq<sub>3</sub> compared to that of Alq<sub>3</sub>. Sapochak et al. suggested that the stronger coupling of the metal-ligand stretching coordinating to the electronic transition in Alq<sub>3</sub> may provide additional paths for non radiative decay [11]. The decrease in the absorption and PL intensity is therefore

reasonable because the conjugated effect makes the coupling of the metal-ligand stronger which will lead to an increase in the energy loss in the excited state vibration [5].

Figure 3 shows the SEM images of the different Alq<sub>3</sub> derivatives. The Alq<sub>3</sub> sample image, figure 3 (a), shows smooth, big rod-like crystals with lengths between 4 and 16 μm and widths between 2 and 3 μm. The 5Cl-Alq<sub>3</sub> sample, figure 3 (b), formed agglomerated rods, encrusted with semi-spherical particles. The lengths and widths of these rods ranged from 1-1.5 μm respectively. Similarly, agglomerated rod-like structures, encrusted with semi spherical particles, were observed for the 5,7Me-Alq<sub>3</sub> samples, figure 3 (c). These rods have varying lengths generally shorter than the rods of fig 3 (a) and (b). It therefore shows that adding EWD and EDG into the Alq<sub>3</sub> clearly has an effect on the morphology of the samples.

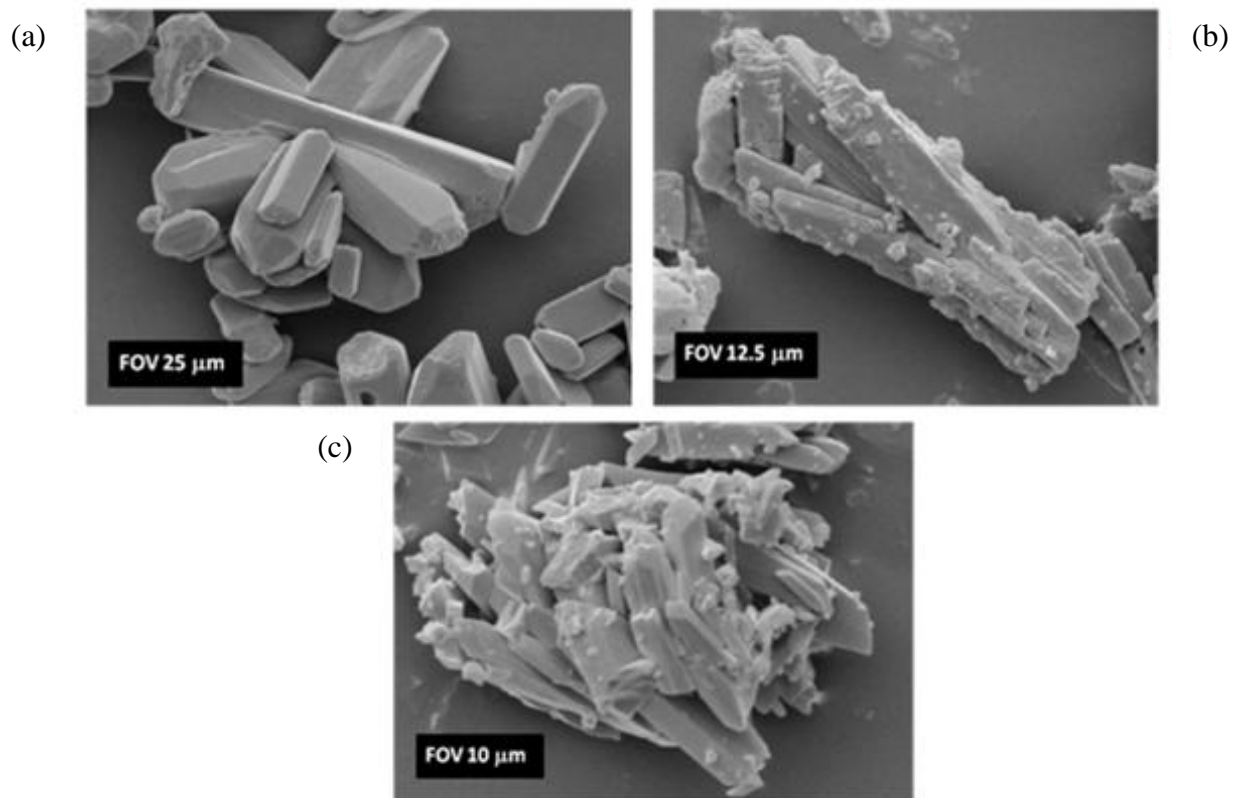


**Figure 3: SEM images of (a) Alq<sub>3</sub> – (FOV 25 μm) (b) 5Cl-Alq<sub>3</sub> – (FOV 12.5 μm) and (c) 5,7Me-Alq<sub>3</sub> – (FOV 10 μm).**

### 3.2. Effect of Al<sup>3+</sup>, Ga<sup>3+</sup> and In<sup>3+</sup> and substituents on the optical properties of Mq<sub>3</sub>.

It is known that the emission of Mq<sub>3</sub> compounds originates from the ligand's electronic  $\pi$ - $\pi^*$  transitions. This is from the highest occupied molecular orbital (HOMO) that is mainly situated on the phenoxide ring to the lowest unoccupied molecular orbital (LUMO) situated on the pyridyl ring [2]. The nature of the metal ion has, however, been shown to influence the emission color, stability, efficiency and evaporation of the metal complex [12]. Not all metals can be coordinated with the 8-hydroxyquinoline ligand and still be used as fluorescent materials. A few general rules which govern the fluorescence of metal chelates of 8-hydroxyquinoline have been formulated:

- Chelates with metal ions that are paramagnetic are essentially non-fluorescent due to a high rate of intersystem crossing from the singlet to triplet state (e.g. Cr, Ni).
- Fluorescence is reduced with increasing atomic number of the metal ion, also caused by an increase in the rate of intersystem crossing, known as the heavy atom effect. For example, Alq<sub>3</sub> will be more fluorescent than Gaq<sub>3</sub> which, in turn, is more fluorescent than Inq<sub>3</sub>.
- As the covalent nature of the metal-ligand bonding (primarily metal-nitrogen) is increased, the emission shifts to longer wavelengths. For example, the chelates formed by In will emit at longer wavelengths than those formed by Al. On the other hand, more ionic-metal-ligand bonding results in a blue shift. For example, Mgq<sub>2</sub> will emit at a shorter wavelength compared to Znq<sub>2</sub>.

The effect that Al<sup>3+</sup>, Ga<sup>3+</sup> and In<sup>3+</sup> have on the luminescent properties of Mq<sub>3</sub> was investigated. Figure 4 shows the absorption and emission spectra of the three Mq<sub>3</sub> samples. Three absorption bands were observed for all the samples. The main band for Alq<sub>3</sub> was at 383 nm while it was shifted by 2 nm to 385 nm for the other two samples. Two weaker bands were observed at 332 and 317 nm for Alq<sub>3</sub> and were shifted by 1 nm for the other two samples. These bands were assigned in the same way as in figure 2 (a). A broad emission peak was observed for all three samples excited at 345 nm. The peaks of Gaq<sub>3</sub> and Inq<sub>3</sub> were red shifted by 18 nm and 12 nm respectively. The peak was due to singlet emission. Although it had been expected that the Inq<sub>3</sub>

peak should be shifted to longer wavelengths [12], impurities trapped in the crystal might have caused the shift in luminescence to be less than expected. The fluorescence of Gaq<sub>3</sub> and Inq<sub>3</sub> was reduced with respect to Alq<sub>3</sub>. It had been expected that fluorescence should decrease with an increase in atomic number [12], but impurities might again have caused the enhancement in fluorescence intensity in the Inq<sub>3</sub> (see chapter 7).

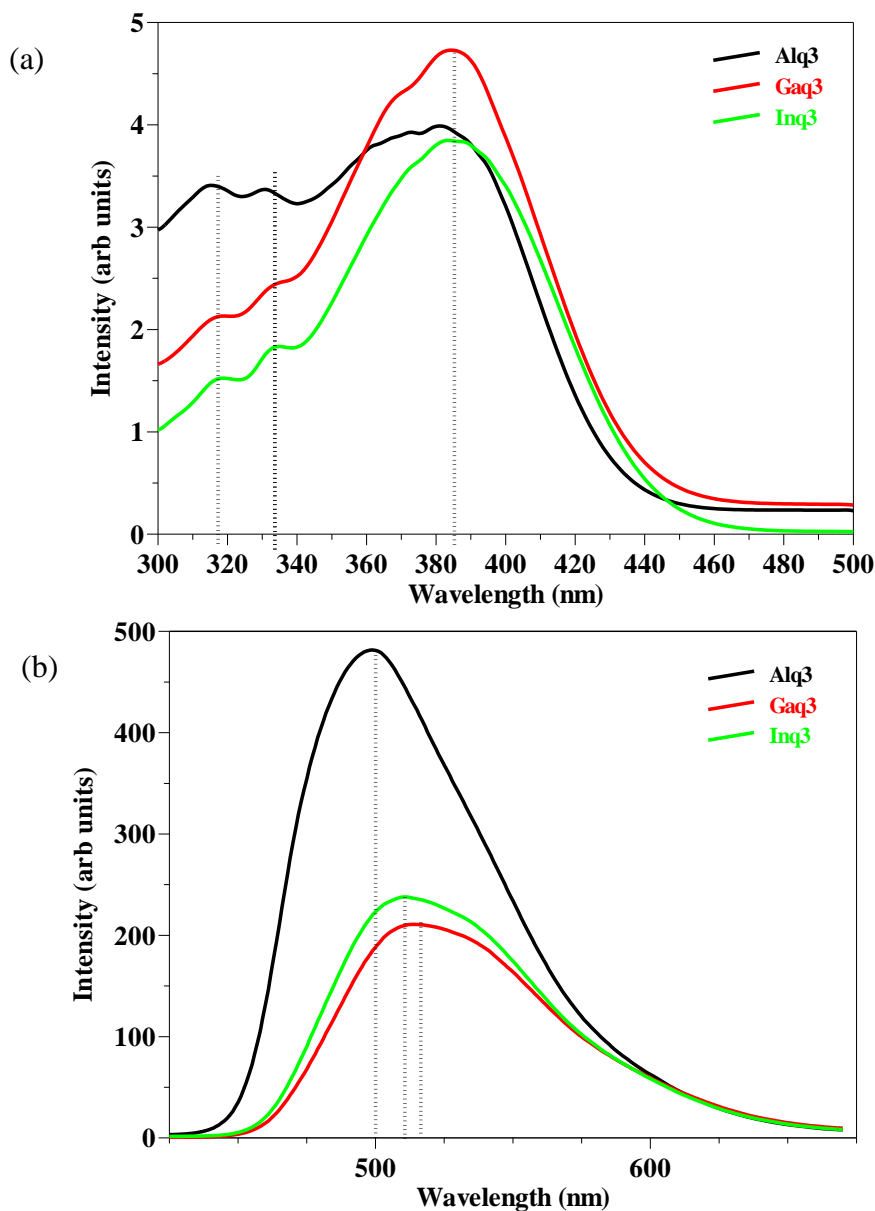


**Figure 4: (a) The absorption and (b) emission spectra of the various Mq<sub>3</sub> derivatives. The dashed black lines indicate the absorption and emission peaks.**

The effect of substituents on the absorption and emission spectra of the various  $Mq_3$  derivatives were also investigated. Zhang et al. [13] reports that the luminescence of the ligand is strongly affected by the electron cloud overlapping between the ligand and metal ion. Regardless of the direction of energy transfer (metal to ligand (fluorescence) or ligand to metal (phosphorescence)), the electron cloud between the metal and ligand strongly determines the efficiency of intramolecular transfer. By attaching substituents to the quinoline ligand the electron cloud of the ligand is altered and should lead to a change in emission wavelength. The absorption and emission spectra of 5Cl- $Mq_3$  and 5,7Me- $Mq_3$  are shown in figure 5. The absorption spectra show a broad absorption band and two weaker bands at lower wavelengths. The main band for the 5Cl samples is at  $\sim 402$  nm, with the 5Cl-Al $q_3$  sample's band at 394 nm. The two weaker bands are located at  $\sim 340$  nm and 320 nm. The band at 340 nm is more prominent than the one at 320 nm. The 5,7Me samples also show three absorption bands. The main band is red shifted by  $\sim 15$  nm from that of the 5Cl samples, while the two weaker bands are almost at the same position. The 5Cl and 5,7Me samples all have one broad emission peak. In the case of the 5Cl samples, 5Cl-Al $q_3$  has the highest intensity with a maximum at 535 nm. The Ga sample is red shifted by 10 nm and the In sample by 18 nm. The intensity has decreased and is red shifted by an increase in atomic number of the central metal ion. For the 5,7Me samples the emission intensity is much lower than that of the un-substituted samples. This is due to non-radiative decays [11]. The Al and In samples show emission at a maximum of 555 nm while the Ga sample is slightly blue shifted by 3 nm. From both the absorption and emission spectra, it can be seen that substituents play a big role on the electron cloud between the metal and ligand, and has a marked effect on the luminescence on the samples. By choosing different substituents, it will be possible to tune the color of the  $Mq_3$  samples from blue all the way to red.

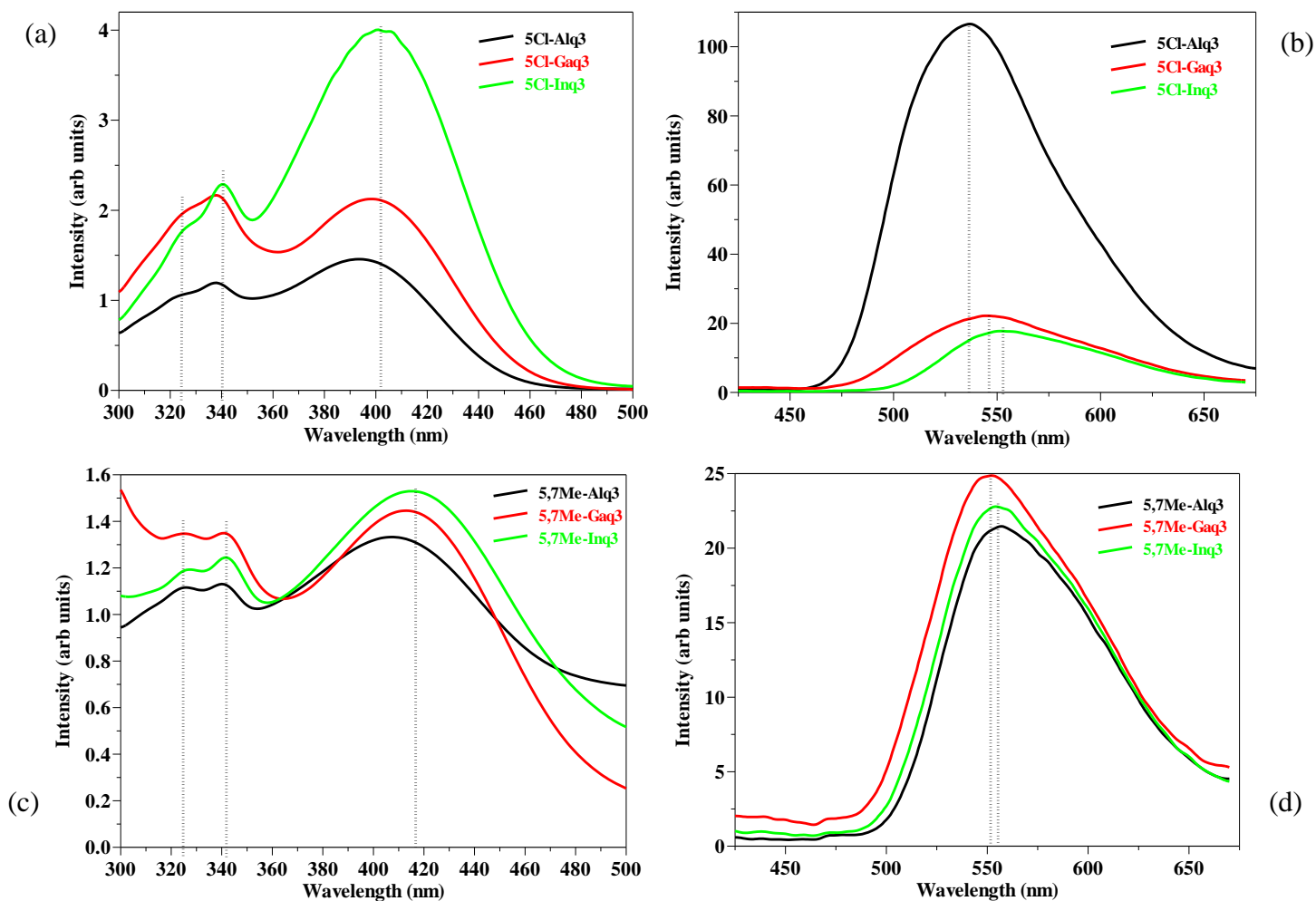


**Figure 5: The absorption (a) and (c) and the emission spectra (b) and (d) of 5Cl-Mq<sub>3</sub> and 5,7Me-Mq<sub>3</sub>. The dashed black lines indicate the absorption and emission peaks.**

### 3.3 Effect of excitation wavelength on the emission of Mq<sub>3</sub>.

The effect of the emission wavelength on the emission spectra of Mq<sub>3</sub> was investigated. Many different excitation wavelengths have been reported for Mq<sub>3</sub> samples [13, 14] ranging from 240 nm – 450 nm. Heiskanen et al. [15] and Levichkova et al. [16] reported that the PL emission of Alq<sub>3</sub> is independent of the excitation wavelength. The excitation spectra (PLE) of the three Mq<sub>3</sub> samples were determined from the emission maxima. All three samples has a PLE ranging from 200 nm – 450 nm, with a maximum at 345 nm (figure 6 (a-c)). The samples were excited at different wavelengths and the emission spectra were recorded (figure 6 (a-c)). The emission

maxima stayed the same for all the excitation wavelengths, but the emission intensity varied according to the intensity of the excitation wavelength.

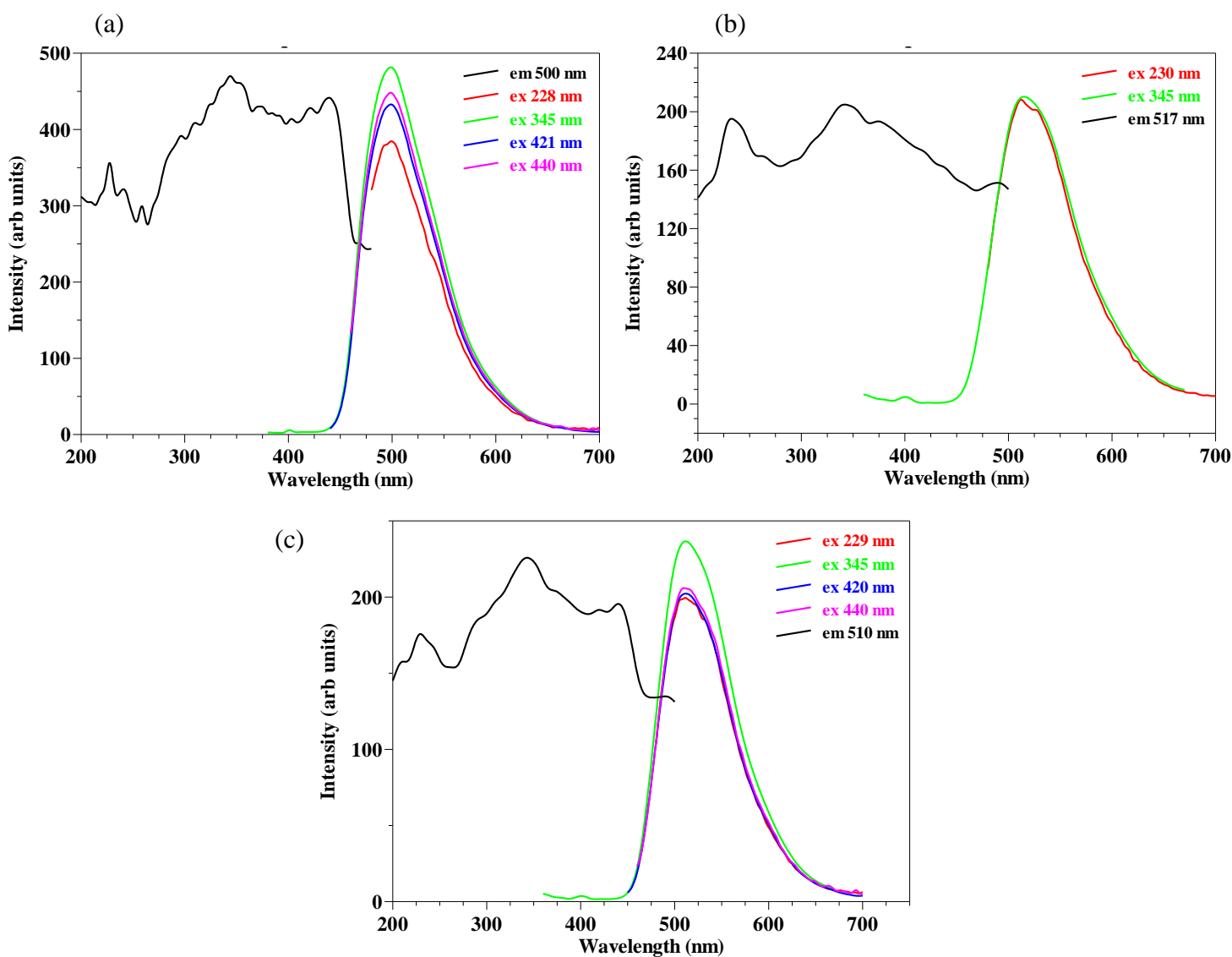


Figure 6. PLE and emission spectra of (a) Alq<sub>3</sub> (b) Gaq<sub>3</sub> and (c) Inq<sub>3</sub>.

## 5. Conclusion

Alq<sub>3</sub>, Gaq<sub>3</sub> and Inq<sub>3</sub> with CH<sub>3</sub> and Cl substituents were successfully synthesized. The Alq<sub>3</sub> has a main absorption band at 383 nm which was assigned to ligand centered electronic transitions. Two weak bands at 317 and 332 nm were assigned to vibronic progressions. The absorption spectra of 5,7Me-Alq<sub>3</sub> and 5Cl-Alq<sub>3</sub> were red shifted by 27 and 11 nm respectively. The

emission peak of Alq<sub>3</sub> was at 500 nm with a FWHM of 80 nm. The emission was due to the relaxation of an excited electron from the S<sub>1</sub>-S<sub>0</sub> level. The emission peak of 5,7Me-Alq<sub>3</sub> was red shifted by 56 nm and that of 5Cl-Alq<sub>3</sub> by 33 nm. The PL intensity of both the samples decreased significantly due to prolonged photon irradiation. The SEM micrographs showed rod-like structures for all the samples. In the case of Alq<sub>3</sub>, the big smooth rods formed, but for the other two samples the rods were agglomerated and encrusted with smaller particles, and varied much more in size. The difference in morphology between the samples may also play a role in the significant decrease in the absorption and emission intensities that was observed.

It was proposed that the emission intensity of Mq<sub>3</sub> samples will decrease and red shift with an increase in atomic number of the centre metal ion. Alq<sub>3</sub> showed the highest PL intensity, with the intensity of Gaq<sub>3</sub> and Inq<sub>3</sub> significantly lower and red shifted with respect to Alq<sub>3</sub>. The electron cloud between the centre metal and ligands would influence the luminescence. Mq<sub>3</sub> samples substituted with Cl and CH<sub>3</sub> showed a change in luminescence intensity and peak maximum. It was also shown that the emission maxima of the Mq<sub>3</sub> samples were independent of the emission wavelength.

## References

- [1] C.W. Tang and S.A. Vanslyke, *Appl. Phys. Lett.* **51** (1987) 913-915.
- [2] M.M. Shi, J.J. Lin, Y.W. Shi, M. Ouyang, M. Wang and H.Z. Chen, *Mater. Chem. Phys.* **115** (2009) 841-845.
- [3] A. Irfan, R. Cui, J. Zhang and L. Hao, *Chem. Phys.* **364** (2009) 39-45.
- [4] Y. Qin, I. Kiburu, S. Shah and F. Jakle, *Org. Lett.* **8** (2006) 5227-5230.
- [5] Y.W. Shi, M.M. Shi, J.C. Haung, H.Z. Chen, M. Wang, X.D. Liu, Y.G. Ma, H. Xu and B. Yang, *Chem. Commun.* (2006) 1941-1943.
- [6] V.V.N. Ravi Kishore, A. Aziz, K.L. Narasimhan, N. Periasamy, P.S. Meenakshi and S. Wategaonkar. *Synth. Met.* **126** (2002) 199-205.
- [7] P.E. Burrows, Z. Shen, V. Bulovic, D.M. McCarty and S.R. Forrest, *J. Appl. Phys.* **79** (1996) 7991-8006.
- [8] W. Stampor, J.Kalinowski, G. Marconi, P. Di Marco, V Fattori and G. Giro, *Chem. Phys. Lett.* **283** (1998) 373-380.
- [9] A.D. Walser, R. Priestley and R. Dorsinville. *Synth. Met.* **102** (1999) 1552-1553.
- [10] K. Singh, A. Kumar, R. Srivastava, P.S. Kadyan, M.N. Kamalasanan and I. Singh, *Opt. Mater.* **34** (2011) 221-227.
- [11] L.S. Sapochak, A. Padmaperuma, N. Washton, F. Endrino, G.T. Schmett, J. Marshall, D. Fogerty, P.E. Burrows and S.R. Forrest, *J. Am. Chem. Soc.* **123** (2001) 6300-6307.
- [12] C.H. Chen and J. Shi, *Coord. Chem. Rev.* **171** (1998) 161-174.
- [13] S.A. Bhagat, *Int. Ref. Res. J.* **20** (2011) 54-55.
- [14] D.Z. Garbuzov, V. Bulovic, P.E. Burrows and S.R. Forrest, *Chem. Phys. Lett.* **248** (1996) 433-437.
- [15] J.P. Heiskanen, A.E. Tolkki, H.J. Lemmetyinen and O.E.O. Hormi, *J. Mater. Chem.* **21** (2011) 14766-14775.
- [16] M. M. Levichkova, J. J. Assa, H. Fröb, and K. Leo, *Appl. Phys. Lett.* **88** (2006) 201912-1-201912-3

# Chapter 4

## The influence of substituents on the optical band gap of Alq<sub>3</sub>.

### 1. Introduction

Organic materials such as small molecules and polymers have unique properties that open up new approaches for the fabrication of plastic electronic devices rather than conventional inorganic materials, such as Si and Ge devices. Organic light emitting diodes (OLEDs) are a promising energy alternative for the future and are therefore one of the most interesting organic devices. These devices can be used for potential low cost lighting as well as flexible devices. The first step in the fabrication of these devices is the selection of the emissive layers, which form the heart of the OLED device and generate the desired photons when a current is applied. In the preparation of OLEDs, emissive layers are needed that fit in the band diagram to fulfil the energy requirements to generate photons [1]. The optical band gap ( $E_g$ ) is a necessary parameter to be considered. The value of  $E_g$  defines the fundamental light absorption edge. Light with enough energy can promote electrons from the highest occupied molecular orbital (HOMO) to the lowest unoccupied molecular orbital (LUMO). Therefore, tuning the optical band gap into the desired value for applications is of great importance.

In OLED devices the matching of the HOMO and LUMO energy levels of the emissive materials with the work functions of the electrodes as well as their optical, chemical and electrical stabilities are of uttermost importance. The electronic energy levels (HOMOs and LUMOs) of the materials determine the OLED device structure and selection of electrodes and charge transfer materials [2].

By introducing substituents to the Alq<sub>3</sub> molecule, the optical properties of the material will change, because these substituents take part in the formation of the HOMO and LUMO levels [3]. An accurate way of determining the HOMO and LUMO levels of these new materials is needed in order to see if they are suitable replacements for the emissive layer in OLED devices. Generally the ionization potential ( $I_p$ ) of the organic molecules is measured by ultraviolet

photoelectron spectroscopy (UPS), while the electron affinity ( $E_a$ ) is determined from the difference of the ionization potential and the optical band gap, from optical absorption spectra [2]. But this is not a direct measurement technique to determine the position of the HOMO and LUMO energy levels.

The electrochemical processes are similar to the charge injection and transport in the OLED devices. Cyclic Voltammetry (CV) has therefore been recognized as an easy and effective approach to evaluate the position of both the HOMO and LUMO energy levels and the optical band gap of the organic materials. It has also been used to determine the reversibility, reproducibility and stability of organic films on the electrodes.

In this chapter CV measurements were done on Alq<sub>3</sub>, as well as Alq<sub>3</sub> substituted with chloride in the 5 position (5Cl-Alq<sub>3</sub>) or methyl groups in the 5 and 7 positions (5,7Me-Alq<sub>3</sub>) in dichloromethane (DCM). Optical absorption was also done on these 3 samples in DCM. The  $I_p$ ,  $E_a$  (HOMO and LUMO energy levels) and  $E_g$  were determined from the CV and absorption measurements.

## **2. Cyclic voltammetry**

### **2.1 Technique overview**

Cyclic voltammetry (CV) is a very important analytical characterization tool in the field of electrochemistry. Any process that includes electron transfer can be investigated by this technique. Analyzing the stoichiometry of complex compound, the investigation of catalytic reactions and determining the band gap of photovoltaic material are just some of the aspects that can be analyzed using CV [4].

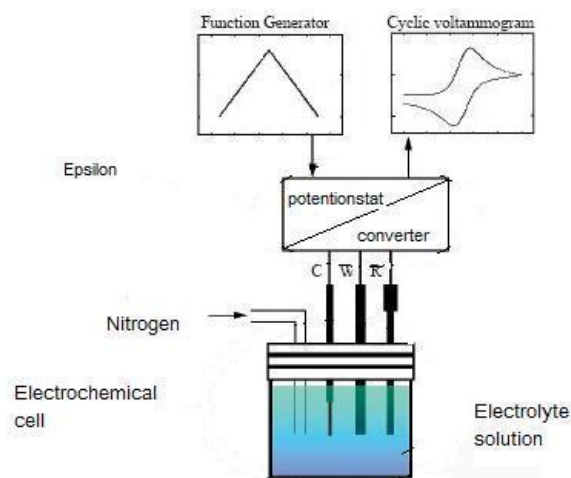


**Figure 1: Components of cyclic voltammetry systems [4].**

Figure 1 shows the different components of a cyclic voltammetry system. The different components will be briefly discussed:

- The epsilon includes the current-voltage converter and the potentiostat. The current is measured with the current-voltage converter and the potentiostat is used to control the applied potential.
- The input system is a basic function generator. The different parameters, such as scan range and scan rate, can be changed in this part. The output part is normally a computer screen that displays the curves and data directly to the operator.
- Oxygen and water in the atmosphere may dissolve in the electrolyte solution and the solution will be oxidized or deoxidized when a potential is applied. The data will therefore be less accurate. Bubbling of an inert gas (like nitrogen or argon) through the solution will prevent this from happening.
- The key component of the CV system is the electrochemical cell which is connected to the epsilon part. The electrochemical cell contains three electrodes: the working electrode (W), the counter electrode (C) and the reference electrode (R). All of the above must be immersed in an electrolyte solution when working.
- The counter electrode (C) is a high surface area electrode and is non-reactive. The platinum gauze is a common choice.

- The working electrode (W) has a well defined area and is commonly an inlaid disc electrode (Au, Pt, graphite, etc.). Other geometries may be used such as a cylinder, array, dropping or hanging mercury hemisphere, band or grid electrode.
- For the reference electrode (R), a calomel or aqueous Ag/AgCl half cell is commonly used. A simple platinum or silver wire might also be used in conjunction with an internal potential reference that is provided by ferrocene. Ferrocene will undergo a one-electron oxidation at a low potential, around 0.5 V versus a saturated calomel electrode (SCE). It can also be used as a standard in electrochemistry as  $F_c^+/F_c = 0.64$  V versus a normal hydrogen electrode (NHE).

In cyclic voltammetry the current that flows between the electrode of interest (whose potential is monitored with respect to a reference electrode) and a counter electrode is measured under the control of a potentiostat. The potentials at which different electrochemical processes will occur are determined by the voltammogram. The working electrode is subjected to a triangular potential sweep (see Figure 1). The potential rises from a start value  $E_i$  to a final value  $E_f$ ; then returns to the start potential at a constant potential sweep rate. The applied sweep rate can vary from a few millivolts per second to a hundred volts per second. The peak width and height for a specific process may depend on the electrolyte concentration and the electrode material as well as the sweep rate [5].

Cyclic voltammetry can be used to estimate the HOMO and LUMO energy levels of the emissive layers in OLEDs. CV gives direct information of the oxidation and reduction potentials of the materials. The oxidation process corresponds to the removal of electrons from the HOMO energy level and the reduction process corresponds to electron addition in the LUMO energy level of the materials (figure 2) [2]. The current will arise from the transfer of electrons between the energy level of the working electrode and the molecular energy levels of the materials under study.

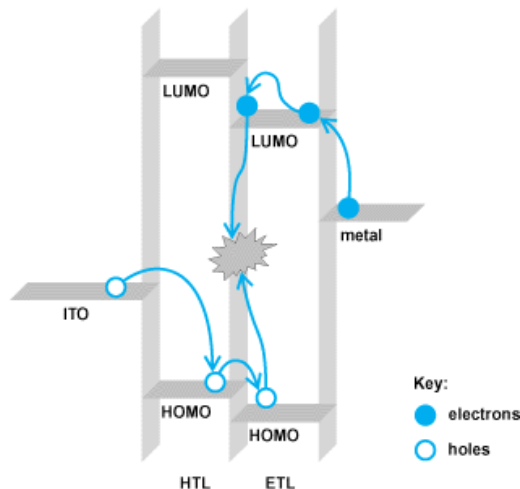


**Figure 2: Simplified energy diagram showing electrons and holes in the process of generating light near the organic/organic interface [6].**

The onset potentials of oxidation and reduction of a material can be correlated to the ionization potential ( $I_p$ ) and electron affinity ( $E_a$ ) according to the empirical relationship proposed by Bredas et al. [7] on the basis of a detailed comparison between valence effective Hamiltonian calculations and experimental electrochemical measurements. The correlation can be expressed as:

$$I_p = E_{ox} + 4.4 \text{ eV} \quad (1)$$

$$E_a = E_{red} + 4.4 \text{ eV} \quad (2)$$

$$\text{and } E_g = I_p - E_a \quad (3)$$

where  $E_{ox}$  and  $E_{red}$  are the onset potentials of oxidation and reduction, respectively, while  $E_g$  is the optical band gap of the material. The 4.4 eV constant in the relation between  $I_p$ ,  $E_a$  and the redox potentials arises from the difference in gas-phase ionization potentials and electrochemical oxidation potentials of solid films and the solid-state polarization energy [8]. The onset potentials are determined from the intersection of the two tangents drawn at the rising current and baseline charging current of the CV traces.

By using the onset potentials rather than the oxidation and reduction peaks gives values that represent the minimum  $I_p$  and maximum  $E_a$  for the inhomogeneous ensemble of polymer chains present in a typical sample. These values would generally arise for the longest polymer chain

segments with most extended conjugation and are thus most representative of the ideal polymer structure free from conjugation limiting defects [9].

## 2.2 Experimental setup

Cyclic voltammograms of the samples were recorded with a PARSTAT 2273 model potentiostat utilising a three-electrode electrochemical cell at a constant scan rate of 100 mV/s. The samples were dissolved in DCM (0.5 mM) or CH<sub>3</sub>CN (0.5mM) and 0.2M of [<sup>n</sup>Bu<sub>4</sub>N][B(C<sub>6</sub>F<sub>5</sub>)<sub>4</sub>] was used as the electrolyte because this solvent-electrolyte combination is known to minimize substrate-solvent and substrate-electrolyte interactions after generating charged species during oxidation or reduction [10 ,11]. Glassy carbon (3.14 mm<sup>2</sup>) was used as the working electrode and Pt was used as both the auxiliary and pseudo reference electrode. Free ferrocene with redox potential for the FcH/FcH<sup>+</sup> coupled assigned as 0 V was used as internal reference standard. The experiment was done in a glove box under Ar atmosphere at 25 °C.

## 2.3 Results

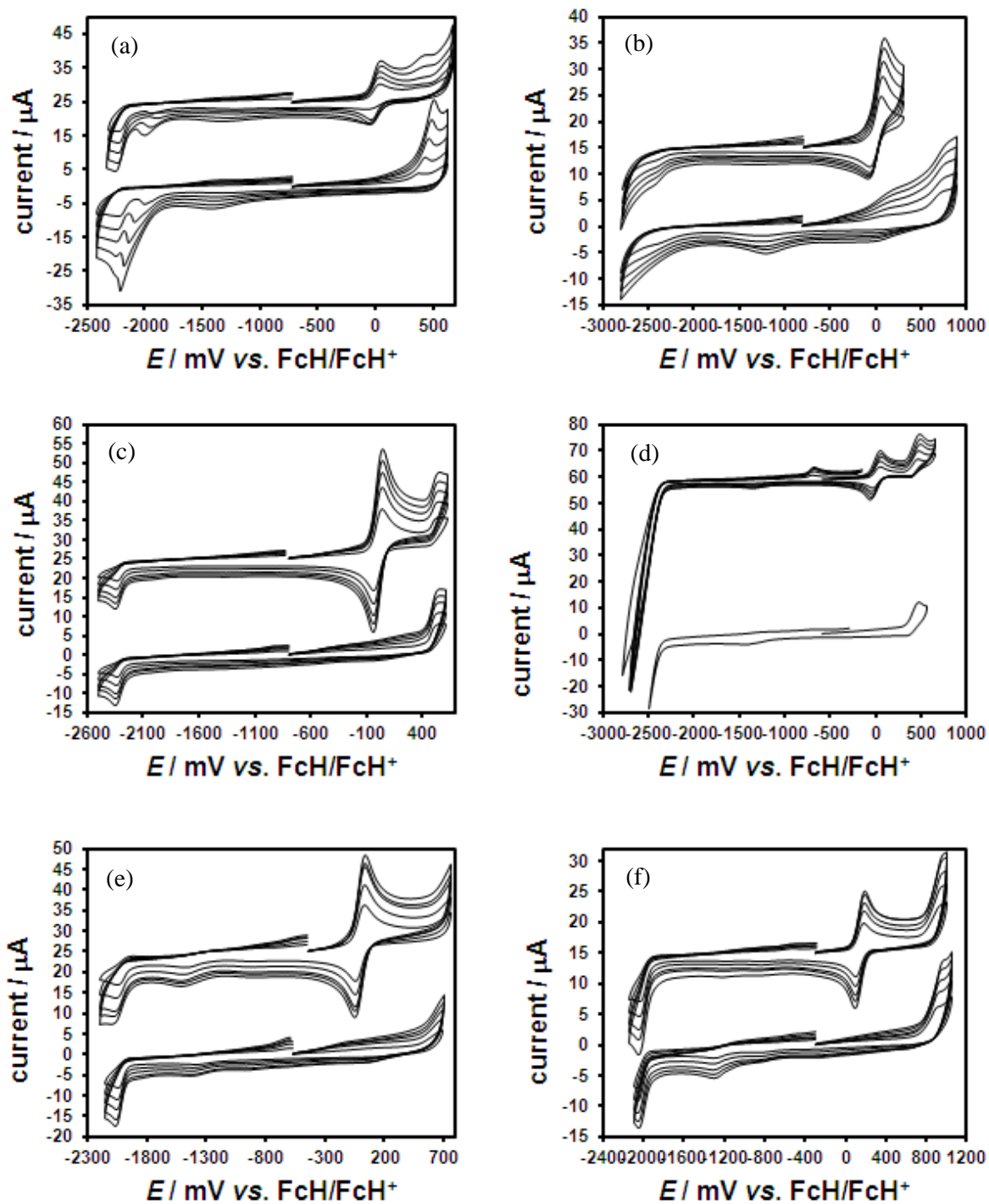


**Figure 3:** Cyclic voltammograms of (a) and (b)  $\text{Alq}_3$  (0.5 mM) (c) and (d)  $5,7\text{Me-Alq}_3$  (0.5 mM) and (e) and (f)  $5\text{Cl-Alq}_3$  (0.5 mM) in  $\text{CH}_3\text{CN}$  (left) and  $\text{DCM}$  (right) containing 0.2 M  $\text{NBu}_4\text{PF}_6$  at 25 °C in glove box at scan rates of 100 (smallest currents), 200, 300, 400 and 500  $\text{mV s}^{-1}$  in the presence of ferrocene as internal standard (top) and in the absence of ferrocene (bottom).

Figure 3 shows the cyclic voltammograms of the three compounds in CH<sub>3</sub>CN (left) and DCM (right). The top graphs are in the presence of ferrocene as internal standard and the bottom ones are in the absence of ferrocene. The scan rates for all the samples were 100 (showing the smallest currents), 200, 300, 400 and 500 mVs<sup>-1</sup>. No change was observed for the oxidation and reduction onset at the different scan rates.

Figure 4 and 5 shows the cyclic voltammograms for the three samples in DCM and CH<sub>3</sub>CN respectively. The oxidation and reduction onsets are shown on the graphs and summarized in table 1 and 2.

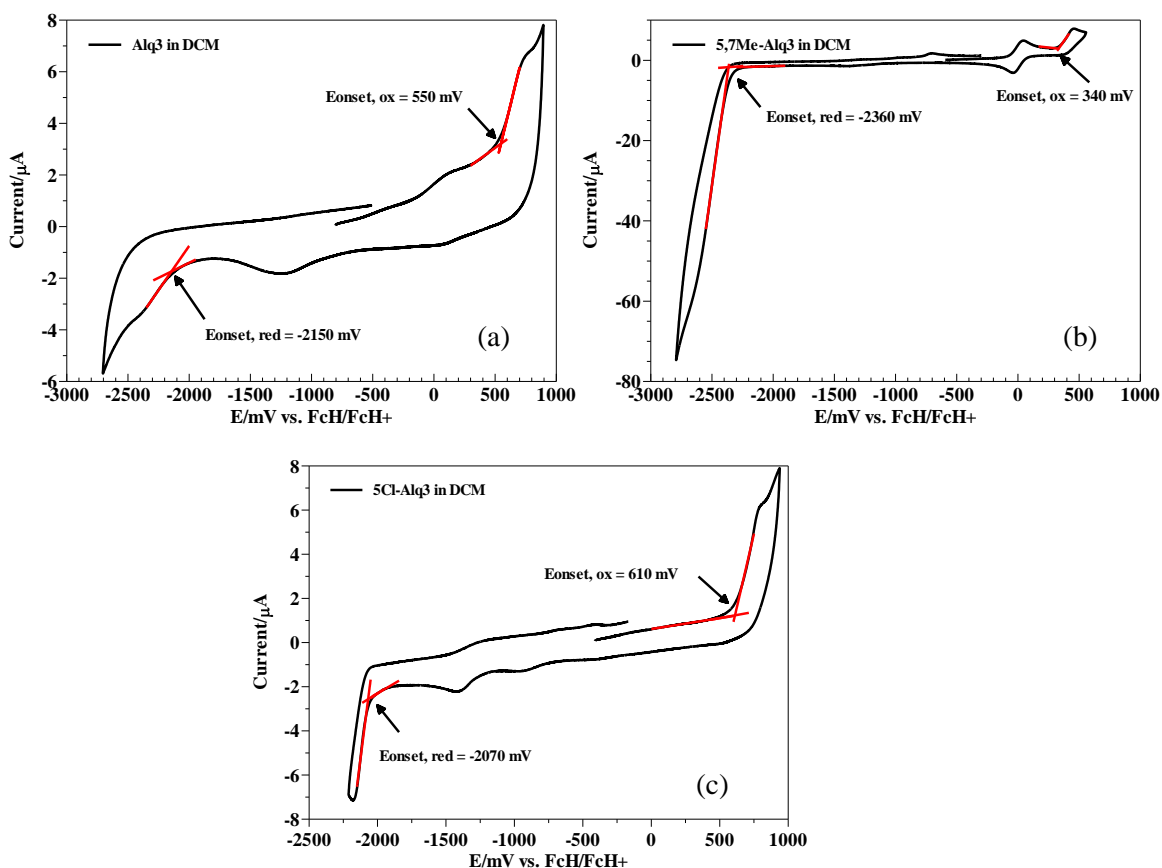


**Figure 4: Cyclic voltammograms of (a) Alq<sub>3</sub> (b) 5,7Me-Alq<sub>3</sub> and (c) 5Cl-Alq<sub>3</sub> in DCM (100 mV/sec scan rate).**

**Table 1: Electrochemical data for the three samples in DCM.**

	$E_{\text{red}}$ (mV)	$E_{\text{ox}}$ (mV)	$I_p$ (HOMO) (eV)	$E_a$ (LUMO) (eV)	Electrochemical band gap (eV)
$\text{Alq}_3$	-2150	550	4.95	2.25	2.70
$5,7\text{Me-Alq}_3$	-2360	340	4.74	2.04	2.70
$5\text{Cl-Alq}_3$	-2070	610	5.01	2.33	2.68

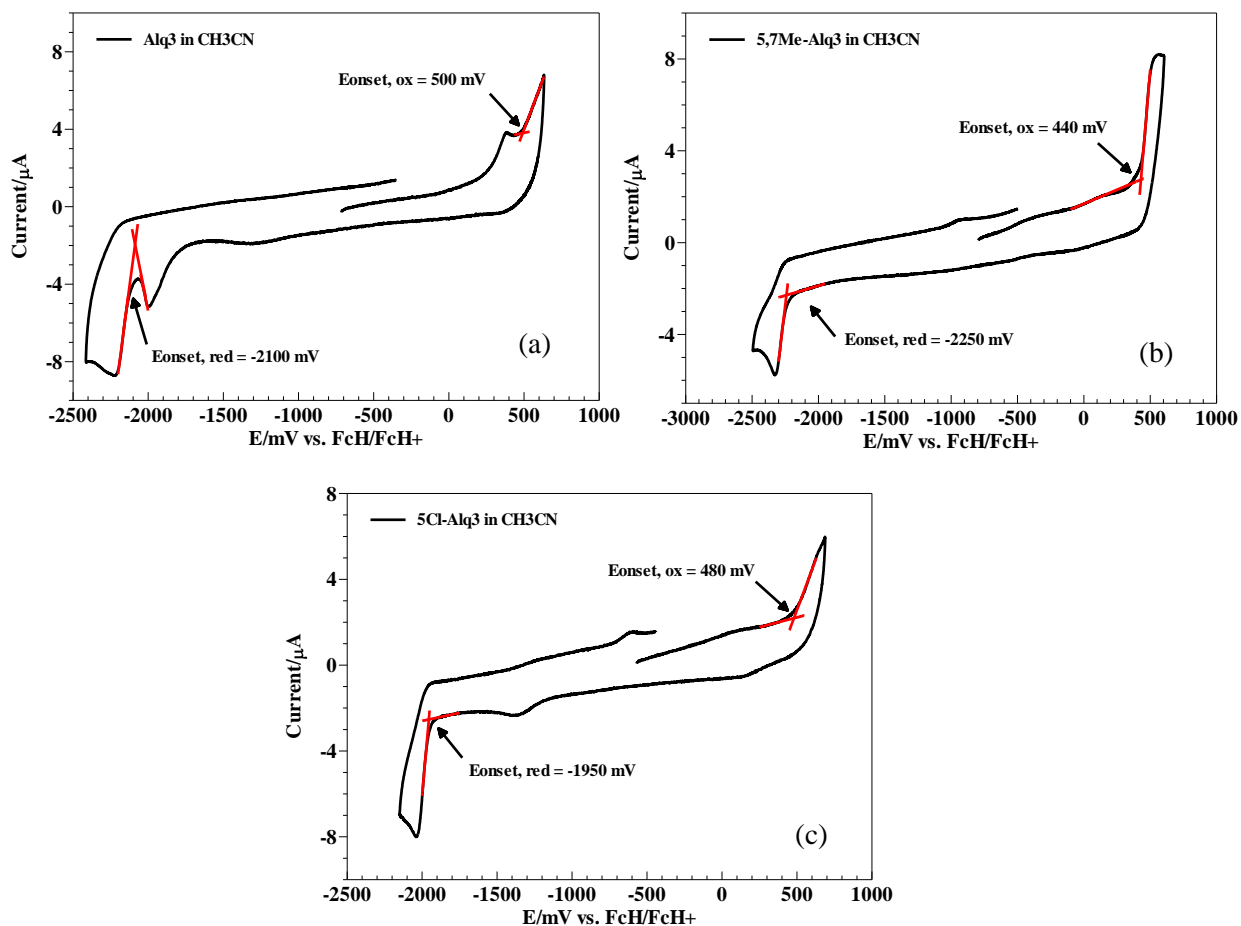


**Figure 5: Cyclic voltammograms of (a)  $\text{Alq}_3$  (b)  $5,7\text{Me-Alq}_3$  and (c)  $5\text{Cl-Alq}_3$  in  $\text{CH}_3\text{CN}$  (100 mV/sec scan rate).**

**Table 2: Electrochemical data for the three samples in CH<sub>3</sub>CN.**

	$E_{\text{red}}$ (mV)	$E_{\text{ox}}$ (mV)	$I_p$ (HOMO) (eV)	$E_a$ (LUMO) (eV)	Electrochemical band gap (eV)
<b>Alq<sub>3</sub></b>	-2100	500	4.90	2.30	2.60
<b>5,7Me-Alq<sub>3</sub></b>	-2250	440	4.84	2.15	2.69
<b>5Cl-Alq<sub>3</sub></b>	-1950	480	4.88	2.45	2.43

The theoretical value of the optical band gap of solid state Alq<sub>3</sub> is 2.80 eV [1]. The value obtained from CV measurements is ~ 0.1 eV lower in the case of DCM and ~ 0.2 eV lower in the case of CH<sub>3</sub>CN. The values will differ from the theoretical value of Alq<sub>3</sub> because the band gap was determined by a technique where the samples are dissolved and it is known that solvents play a role on the values of the band gap [12]. The EWG and EDG do not have a big influence on the band gap and it does not vary more than ~ 0.3 eV from the theoretical value of Alq<sub>3</sub>. The HOMO and LUMO levels are ~ 0.8 eV lower than the theoretical values for Alq<sub>3</sub> (LUMO = ~ 3.1 eV and HOMO = ~ 5.7 eV [13]). When using these samples as die electron transporting or emissive layer care should be taken in the design of the device architecture. The band gap obtained from the CV measurements should however be more meaningful [2] as it corresponds directly to an electron being excited from the HOMO to the LUMO level.

### 3. Optical absorption

#### 3.1 Technique overview

Several processes are possible when a sample is stimulated by the application of an external electromagnetic radiation source. The radiation can for example be reflected or scattered. What is important is that some of the radiation can be absorbed and promote some of the sample into the excited state (Figure 6). In absorption spectroscopy the amount of light that is absorbed is measured as a function of wavelength. Both qualitative and quantitative information can be obtained from the sample using this method.

Every molecular species is capable of absorbing its own characteristic frequencies of electromagnetic radiation. In this process energy is transferred to the molecule and results in a decrease in the intensity of the electromagnetic radiation that is incident on the sample. The radiation is thus attenuated because of absorption. The Beer-Lambert law or just Beer's law (absorption law) is quantitatively giving how the amount of attenuation depends on the concentration of the absorbing molecule as well as the path length over which the absorption occurs. When light traverses through a medium that contains an absorbing analyte, intensity decreases will occur when the analyte becomes excited. For a sample with a certain concentration, the longer the path length of the light (length of the medium through which the light passes), the more absorbers will be in the path and the greater the attenuation. Also, for a given path length, the higher the concentration of the absorbers the stronger the attenuation of the light beam.

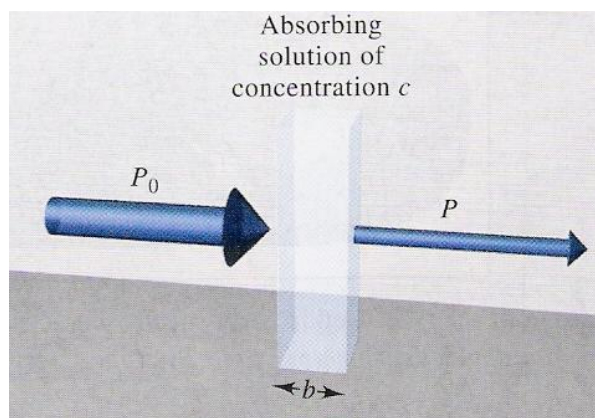


**Figure 6: Attenuation of a beam of radiation by an absorbing solution. The larger arrow on the incident beam signifies a higher radiant power than is transmitted by the solution. The path length of the solution is  $b$ , and the concentration is  $c$  [13].**

Figure 6 is a schematic diagram showing the attenuation of a parallel beam of monochromatic radiation passing through an absorbing solution of thickness  $b$  centimetres and a concentration of  $c$  moles per litre. The interactions between the photons and absorbing particles cause the radiant power of the beam to decrease from  $P_0$  to  $P$ . The fraction of incident radiation transmitted by the solution is the transmittance  $T$  of the solution, as shown in equation 4. Transmittance is often expressed as a percentage called the percent transmittance.

$$T = \frac{P}{P_0} \quad (4)$$

The absorbance  $A$  of a solution is translated to the transmittance in a logarithmic manner, as shown in equation 5. When the absorbance of a solution increases the transmittance will decrease.

$$\begin{aligned} A &= -\log T \\ &= \log \frac{P_0}{P} \end{aligned} \quad (5)$$

### 3.2 Beer's Law

Absorbance is directly proportional to the concentration of the absorbing species  $c$  and to the path length  $b$  of the absorbing medium, according to Beer's law. This is expressed by equation 6.

$$\begin{aligned} A &= \log \frac{P_0}{P} \\ &= abc \end{aligned} \quad (6)$$

with  $a$  a proportionally constant called the absorptivity. Absorbance is a unit less quantity so the units of the absorptivity must cancel the units of  $b$  and  $c$ . If  $b$  has the units of cm and  $c$  have the units of  $\text{g L}^{-1}$ , then absorptivity must have the units of  $\text{L g}^{-1} \text{cm}^{-1}$ . When  $b$  is expressed in cm and the concentration in moles per litre, the proportionality is called the molar absorptivity and is given the special symbol,  $\epsilon$ . Thus

$$A = \epsilon bc \quad (7)$$

where  $\epsilon$  has the units of  $\text{L mol}^{-1} \text{cm}^{-1}$  [14].

### 3.3 Tauc's relation

The band gap of the powder samples can be determined using Tauc's relation [15]. This is a direct relation between the measured energy and the band gap. Figure 7 shows a schematic diagram of the absorption process that takes place in a double beam UV-Vis spectrophotometer.

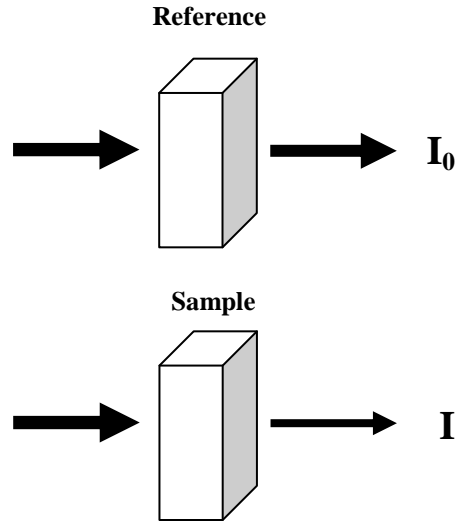


**Figure 7: Schematic diagram of the absorption process.**

In Figure 7 the intensity of the beam that is measured after it had passed through the reference is referred to as  $I_0$  and the measured intensity of the beam passing through the sample is  $I$ . The relation between  $I$  and  $I_0$  is given by equation 8

$$I = I_0 e^{-\alpha x t} \quad (8)$$

where  $\alpha$  is the absorption coefficient,  $x$  is the concentration and  $t$  is the path length of the cuvette (10 mm in this case). Equation 8 can be rewritten in this form

$$\frac{I}{I_0} = e^{-\alpha x t} \quad (9)$$

By taken logs on both sides of equation 8 it can be rewritten as

$$\log\left(\frac{I}{I_0}\right) = -\alpha x t \quad (10)$$

and by making  $\alpha$  the subject of the formula a relation for the absorption coefficient can be found in terms of known parameters. This relation is given in equation 11

$$\begin{aligned} \alpha &= -\frac{1}{x t} \log\left(\frac{I}{I_0}\right) \\ &= \frac{1}{x t} \log\left(\frac{I_0}{I}\right) \end{aligned} \quad (11)$$

The absorbance that is measured with the equipment is equal to  $\frac{1}{xt} \log\left(\frac{I_0}{I}\right)$ . It is also equal to the absorption coefficient, so the absorption coefficient is therefore equal to the measured absorbance and can be used directly in Tauc's relation without any conversion.

Tauc's relation [15] is given by

$$\begin{aligned} \alpha h\nu &\approx (h\nu - E_g)^n \\ \alpha h\nu^{1/n} &\approx h\nu - E_g \end{aligned} \quad (12)$$

where  $\alpha$  is the absorption coefficient,  $h\nu$  is the photon energy and  $E_g$  is the band gap of the material.  $n$  indicates the type of transition. The value of  $n$  for allowed direct, allowed indirect, forbidden direct and forbidden indirect transitions are  $1/2$ ,  $2$ ,  $3/2$ , and  $3$  [16]. When  $\alpha h\nu^{1/n} \approx 0$  then  $0 \approx h\nu - E_g$  and this means that  $h\nu \approx E_g$ . From this it can be seen that by extrapolating the linear portion of the graph and making  $\alpha h\nu^{1/n} \approx 0$  the band gap of the material can be obtained.

### 3.4 Experimental setup

The absorption spectra of the samples were recorded with a Perkin Elmer Lambda 950 UV-VIS-NIR spectrophotometer (figure 8). Ethanol, DCM and  $\text{CH}_3\text{CN}$  were used as solvents.



**Figure 8: The Perkin Elmer Lambda 950 UV-VIS-NIR spectrophotometer.**

## 3.5 Results

### 3.5.1 Determination of $n$

When using Tauc's relation (equation 11) it is important to know the value of  $n$ . A few reports used  $n = 1/2$  (direct allowed transitions) [18], but Wojdyla et al. used  $n = 2$  (indirect allowed transitions) [21]. By taking the natural logarithms and derivation of equation 12 the equation can be rearrange as [19], [22]

$$\frac{d \ln \alpha h\nu}{dh\nu} = \frac{n}{h\nu - E_g} \quad (13)$$

According to equation 13, a peak in the curve of  $d \ln \alpha h\nu / dh\nu$  versus  $h\nu$  should be observed at a point nearly where  $h\nu = E_g$ . The left hand side of figure 9, 10 and 11 shows the plot of  $d \ln \alpha h\nu / dh\nu$  versus  $h\nu$  for the three different samples in the different solvents. The peak at a particular energy value gives approximately the value of  $E_g$ . By utilizing this initial value of  $E_g$ , a graph of  $\ln \alpha h\nu$  versus  $\ln h\nu - E_g$  was plotted to determine the value of  $n$ . By determining the slope of the curves (right hand side of figure 9, 10 and 11) an estimate value for  $n$  can be determine [19], [22]. A value of  $\sim 0.5$  was determined for  $n \sim 0.5$ , for all the samples. Interestingly, this estimation evidences the presence of a direct gap between the intermolecular energy bands in these organometallic materials.

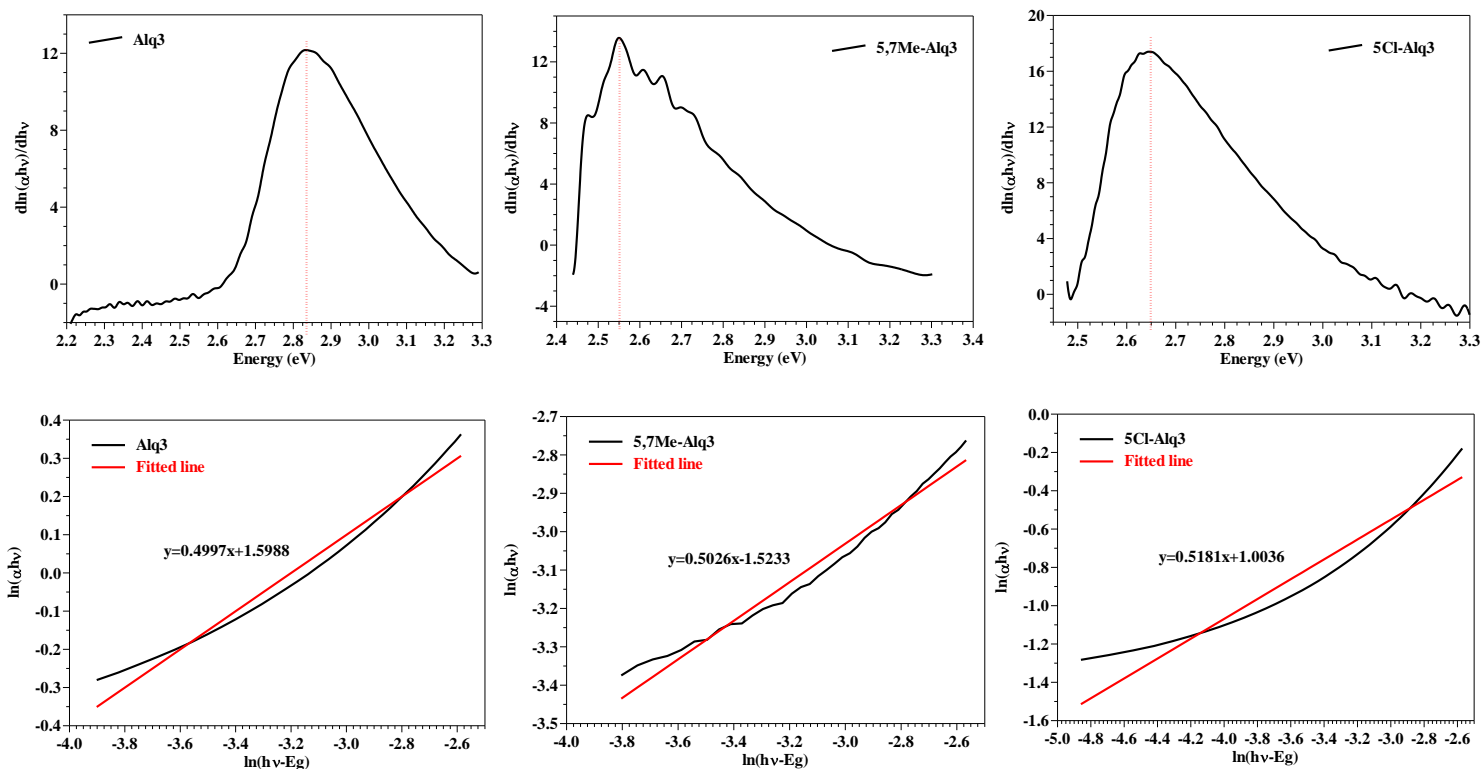


Figure 9: Determining  $n$  for the three samples in ethanol.

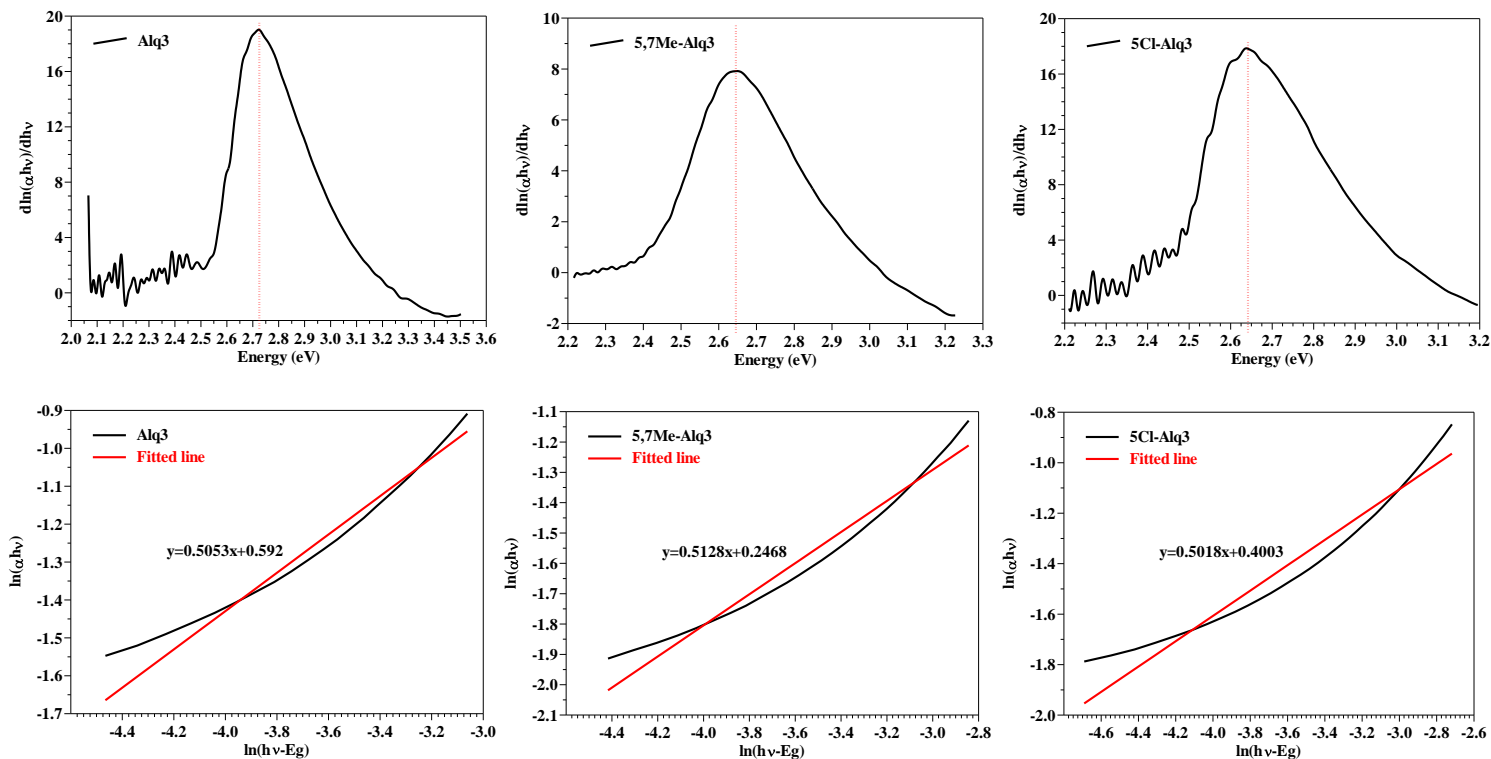
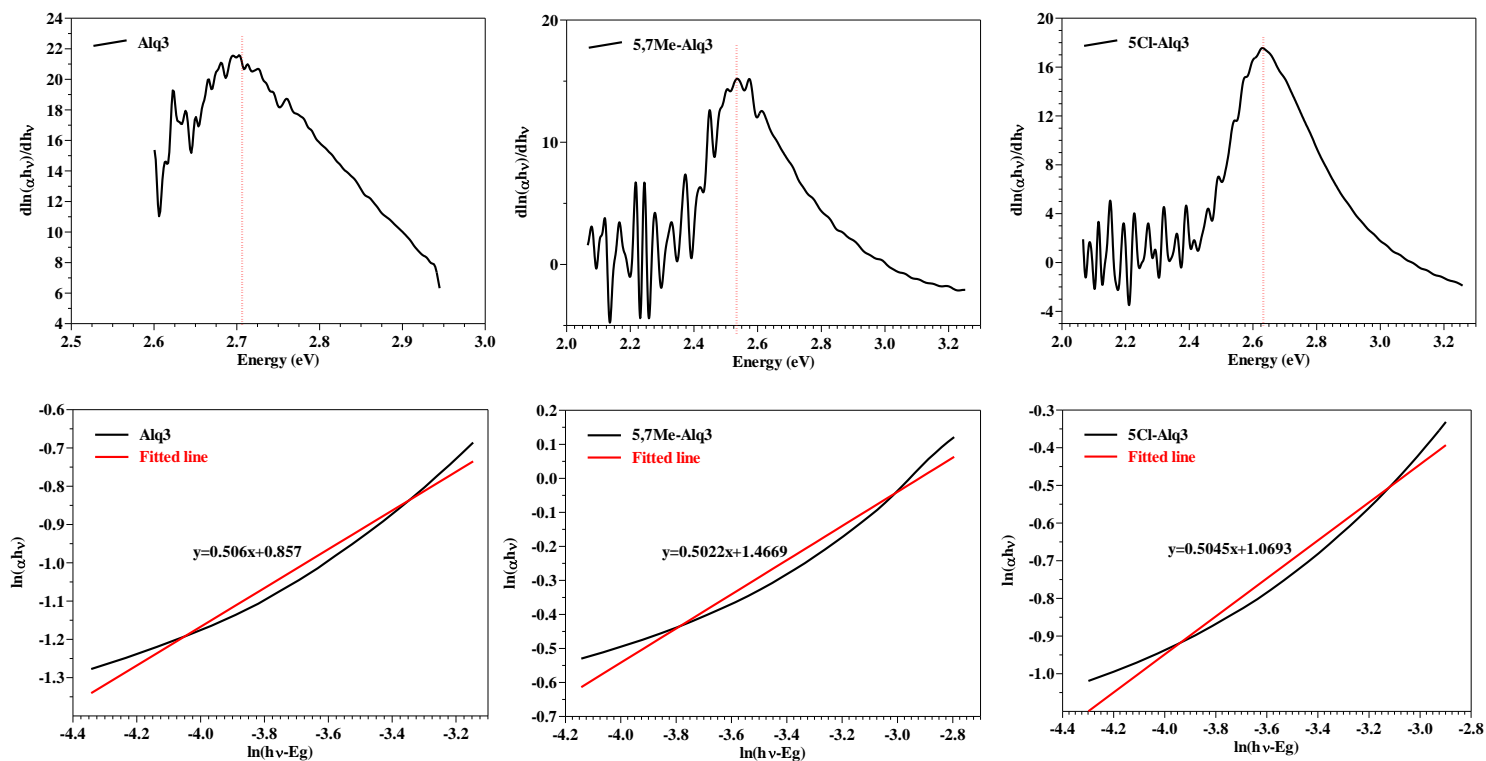
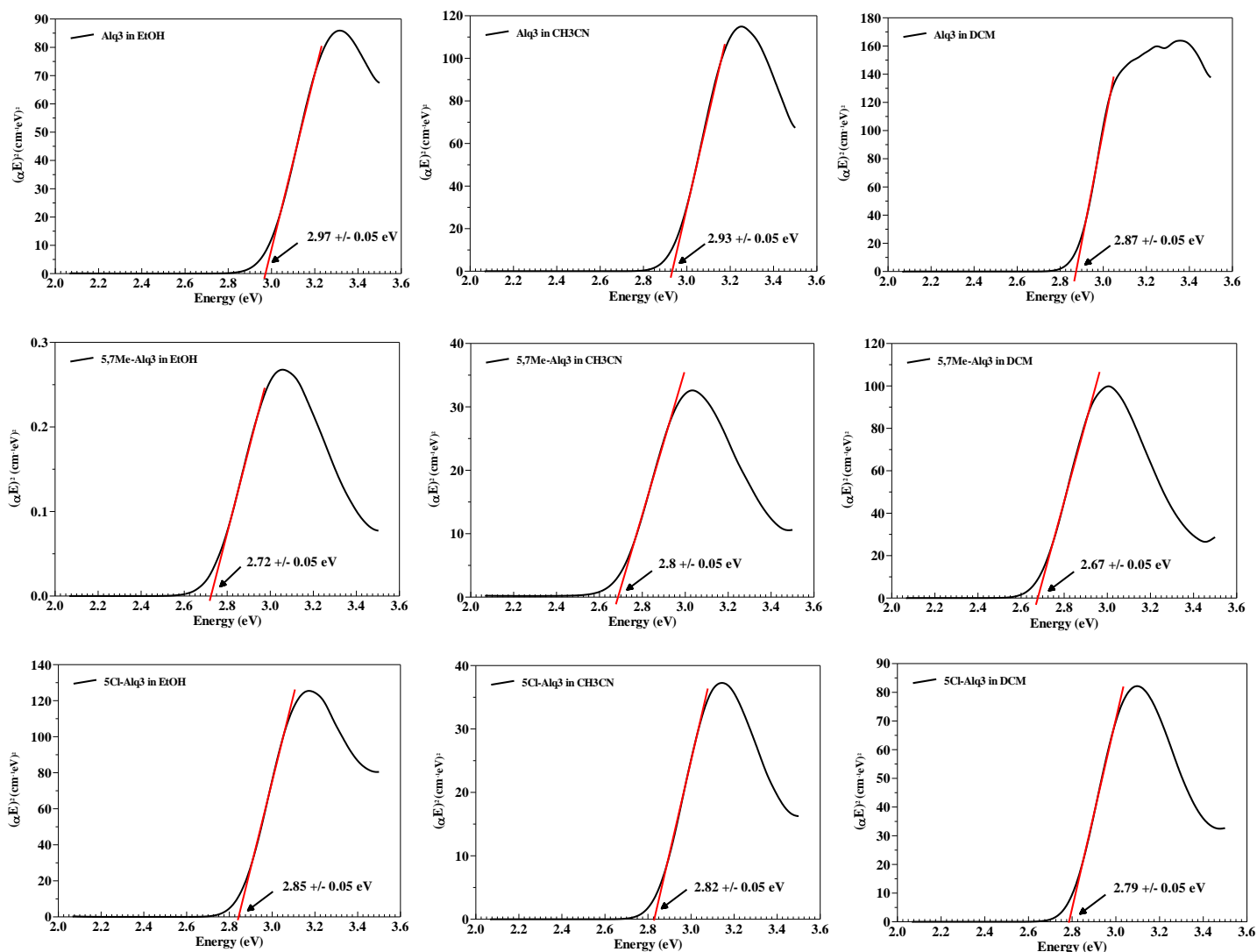


Figure 10: Determining  $n$  for the three samples in  $\text{CH}_3\text{CN}$ .



**Figure 11: Determining  $n$  for the three samples in DCM.**

In order to determine the precise value of the energy gap, graphs of  $\alpha h\nu^2$  against  $h\nu$  were plotted for the three samples in the different solvents, as shown in figure 12. Extrapolation of this plot for  $\alpha h\nu^2 = 0$  gives the energy gap,  $E_g$ . The values are given in table 3. The accuracy of these values was calculated to be  $\pm 0.05$  eV. Only one possible fit were performed and it must be noted that this might not be a unique solution.



**Figure 12: Determining the band gap by using Tauc's relation.**

**Table 3: Determined energy gaps for the three sample in the different solvents.**

	<b>Alq<sub>3</sub></b>	<b>5,7Me-Alq<sub>3</sub></b>	<b>5Cl-Alq<sub>3</sub></b>
<b>EtOH</b>	2.97 eV	2.72 eV	2.85 eV
<b>CH<sub>3</sub>CN</b>	2.93 eV	2.80 eV	2.82 eV
<b>DCM</b>	2.87 eV	2.67 eV	2.79 eV

The obtained value for the optical band gap for Alq<sub>3</sub> is ~ 0.1 eV higher than the one reported in literature [1] for all three the solvents. The band gap of 5,7Me-Alq<sub>3</sub> en 5Cl-Alq<sub>3</sub> is smaller than

that of Alq<sub>3</sub>. This is expected because of the red shift in the absorption spectra that was observed for these two samples. The effect that the different solvents have on the optical band gap can clearly be seen from these results.

The optical band gap of the samples was also determined from the absorption onset. The corrected base line of the absorption spectra was drawn horizontally. In order to determine the absorption edge a straight line was fitted to the right hand side of the maximum peak (located at ~380 nm for Alq<sub>3</sub> in DCM) and its intersection with the corrected baseline was determined [23].

The obtained values are given in table 4.

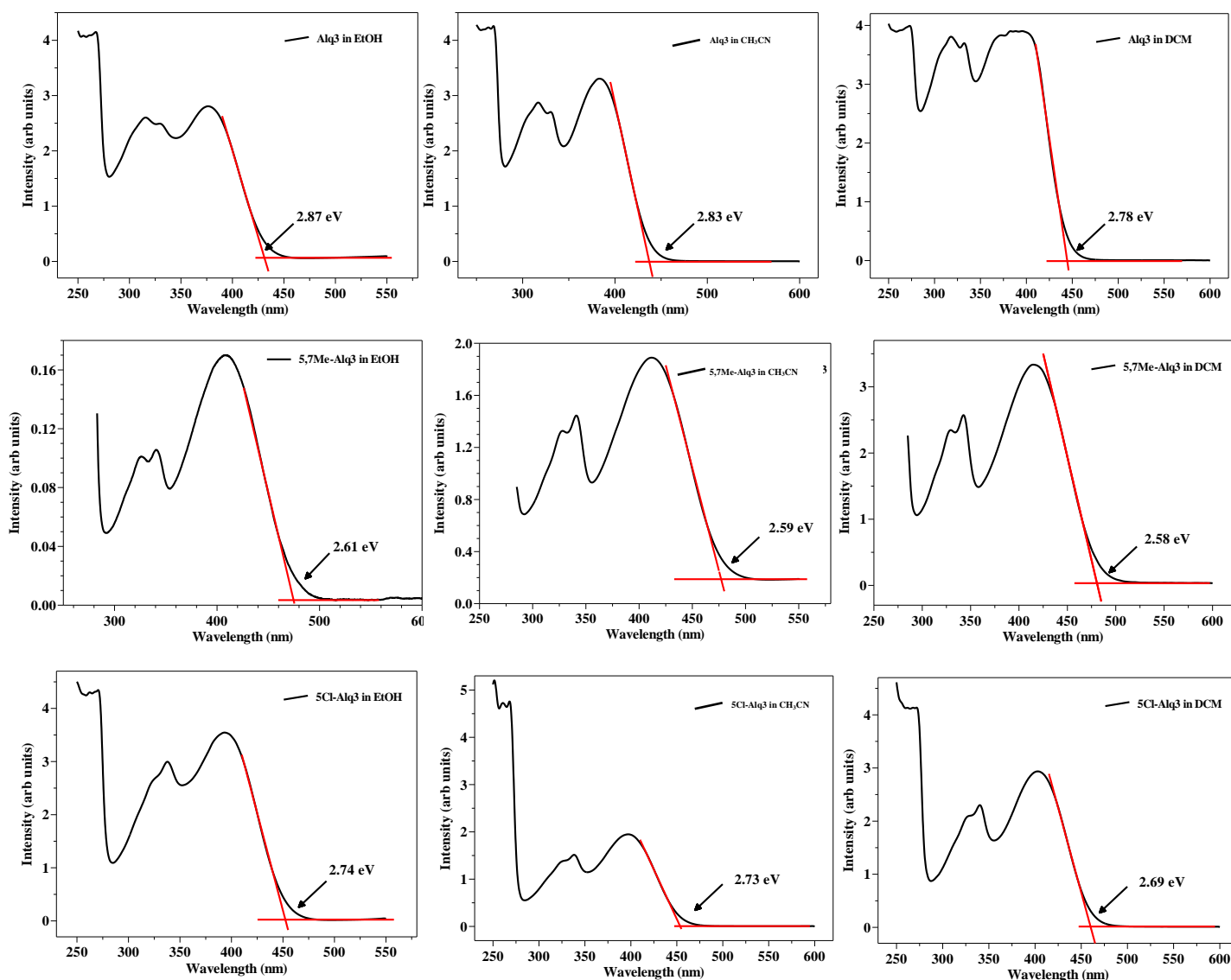


**Figure 13: Determining the band gap by using the absorption onset.**

**Table 4:**

	<b>Alq<sub>3</sub></b>	<b>5,7Me-Alq<sub>3</sub></b>	<b>5Cl-Alq<sub>3</sub></b>
<b>EtOH</b>	<b>2.87 eV</b>	<b>2.61 eV</b>	<b>2.74 eV</b>
<b>CH<sub>3</sub>CN</b>	<b>2.83 eV</b>	<b>2.59 eV</b>	<b>2.73 eV</b>
<b>DCM</b>	<b>2.78 eV</b>	<b>2.58 eV</b>	<b>2.69 eV</b>

The obtained optical band gap for Alq<sub>3</sub> corresponds well to the value reported in literature [1]. The values of 5,7Me-Alq<sub>3</sub> and 5Cl-Alq<sub>3</sub> are again lower than that of Alq<sub>3</sub> as expected from the red shift observed in the absorption spectra of these two samples.

#### **4. Conclusion**

The optical band gap of Alq<sub>3</sub>, 5,7Me-Alq<sub>3</sub> and 5Cl-Alq<sub>3</sub> was determined by cyclic voltammetry, Tauc's relation and the absorption onset. The band gap obtained for Alq<sub>3</sub> with the three techniques was within ~ 0.2 eV from the theoretical value. The theoretical value is for solid state Alq<sub>3</sub> and the band gap determined by the three techniques was for dissolved Alq<sub>3</sub>. The difference in the value might be attributed to the solvents playing a role in the formation of the band gap. The values of the optical band gap of 5,7Me-Alq<sub>3</sub> and 5Cl-Alq<sub>3</sub> were lower than that of Alq<sub>3</sub>. This was expected because of the red shift observed in the absorption spectra of these two samples. Although the band gap for the three samples was in good agreement with the theoretical value, the HOMO and LUMO values were ~ 0.8 eV lower than the theoretical values. If these samples were used to fabricate OLED devices, care should be taken in the design of their device architecture.

## References

- [1] A Shafiee, M.M. Salleh and M. Yahaya, *Sains Malaysiana* **40** (2011) 173-176.
- [2] A Misra, P Kumar, R Srivastava, S.K. Dhawan, M.N. Kamalasanan and S. Chandra, *Indian J. Pure Ap. Phy.* **43** (2005) 921-925.
- [3] Y.W. Shi, M.M. Shi, J.C. Haung, H.Z. Chen, M Wang, X.D. Liu, Y.G. Ma, H Xu and B Yang, *Chem. Commun.* (2006) 1941-1945.
- [4] Introduction to Cyclic Voltammetry Measurements; accessed from: <http://cnx.org/content/m34669/latest> accessed (18/06/2013).
- [5] Cyclic voltammetry: Some theoretical aspects; accessed from: [http://uqu.edu.sa/files2/tiny\\_mce/plugins/filemanager/files/27/02\\_Chapter\\_Two.pdf](http://uqu.edu.sa/files2/tiny_mce/plugins/filemanager/files/27/02_Chapter_Two.pdf) accessed (18/06/2013).
- [6] Organic light emitting devices; accessed from: <http://www.accessscience.com/overflow.aspx?SearchInputText=Organic+light-emitting+devices&ContentTypeSelect=10&term=Organic+light-emitting+devices&rootID=795407> (19/06/2013).
- [7] J.L. Bredas, R Silbey, D.X. Boudreaux and R.R. Chance, *J. Am. Chem. Soc.* **105** (1983) 6555-6559.
- [8] C.J. Yang and S.A. Jenekhe, *Macromolecules* **28** (1995) 1180-1196.
- [9] S. Janietz, D.D.C. Bradley, M. Grell, C. Giebeler, M. Inbasekaran, and E. P. Woo, *Appl. Phys. Lett.* **73**, (1998) 2453-2455.
- [10] K.C. Kemp, E Fourie, J Conradie and J.C. Swarts, *Organomet.* **27** (2008) 353-362.
- [11] M.J. Cook, I Chambrier, G.F. White, E Fourie and J.C. Swarts, *Dalton Trans.* (2009) 1136-1144.
- [12] B Su, M Zhang, Y Shao and H.H. Girault, *J. Phys. Chem.* **110** (2006) 21460-21466.
- [13] T. Mori, T. Ogawa, D.C. Cho and T. Mizutani, *Appl. Surf. Sci.* **212-213** (2003) 458-463.
- [14] D.A. Skoog, D.M. West, F.J. Holler and S.R. Crouch, *Fundamentals of Analytical Chemistry* 8th edition, Brooks/Cole – Thomson Learning, USA, (2004) p. 715 - 720.
- [15] J. Tauc, R. Grigorovici and A. Vancu, *Phys. Status Solidi* **15** (1966) 627-637.
- [16] V. Kumar, R. Kumar, S.P. Lochab and N. Singh, *Nucl. Instr. and Meth. in Phys. Res. B* **262** (2007) 194-197.

- [17] R. Sarkar, C.S. Tiwary, P. Kumbhakar, S. Basu and A.K. Mitra, *Physica E* **40** (2008) 3115-3120.
- [18] F.F. Muhammad and K. Sulaiman, *Sains Malaysiana* **40** (2011) 17-20.
- [19] F.F. Muhammad, A.I.A. Hapip and K. Sulaiman, *J. Organomet. Chem.* **695** (2010) 2526 - 2531
- [20] P. Dalasinki, Z. Lukasiak, M. Wojdyla, M Rebarz and W. Bala. *Opt. Mat.* **28** (2006) 98 – 101
- [21] O.G. Gardens, Trends in Optical Materials. Nova Science Publishers, New York, (2007) p. 32 – 41.
- [22] Z.A. Rahman, K. Sulaiman, A. Shuhaimi and M. Rusop, *Adv. Mat. Res.* **501** (2012) 252 - 256.
- [23] R Schlaf, P.G. Schroeder, M.W. Nelson, B.A. Parkinson, C.D. Merritt, L.A. Crisafulli, H Murata and Z.H. Kafafi, *Surf. Sci.* **450** (2000) 142-152.

# Chapter 5

## Synthesis and characterization of Alq<sub>3</sub>, Alq<sub>3</sub>:SiO<sub>2</sub>, Alq<sub>3</sub>:PMMA and Alq<sub>3</sub>:PS.

### 1. Introduction

Although Alq<sub>3</sub> is used in OLED devices [1] it tends to degrade with time leading to a decrease in device performance and efficiency. The current trend during the fabrication of OLEDs is to use solution-processing. However, with this technique Alq<sub>3</sub> must be vacuum deposited [2]. A possible solution to this problem is to dope different polymers with Alq<sub>3</sub>. These polymers should contain the optical properties of Alq<sub>3</sub> while the processability of a polymer is maintained. This will allow for low cost manufacturing techniques such as ink-jet printing and solution processing [3]. Another solution is to encapsulate the Alq<sub>3</sub> molecule with SiO<sub>2</sub> to prevent atmospheric gasses like oxygen and hydrogen to react with the molecule and create non luminescent products. A good understanding of the chemical interactions between Alq<sub>3</sub> and the polymers or SiO<sub>2</sub> is needed in order to know if these new materials will still be suitable for use in OLED devices.

In this chapter Alq<sub>3</sub> powder was synthesized using a co-precipitation method and the morphological and optical properties of the powder were investigated. The synthesized powder was then encapsulated with SiO<sub>2</sub> to form Alq<sub>3</sub>:SiO<sub>2</sub>, and the effect on the optical properties of Alq<sub>3</sub> was investigated. Polymethyl methacrylate (PMMA) and polystyrene (PS) were doped with different mol percentages of Alq<sub>3</sub> ranging from 0.5 - 5 mol %. The effects of Alq<sub>3</sub> concentration on the photoluminescence (PL) intensity and emission wavelength were investigated. The surface morphology and structure of the blended films were studied to evaluate their effects on the PL intensity. XPS studies were also done on commercial PMMA powder, PMMA thin films and Alq<sub>3</sub>:PMMA thin films in order to get a better understanding of the chemical interactions between the Alq<sub>3</sub> molecule and the PMMA.

## 2. Synthesis

### 2.1 Synthesis of Alq<sub>3</sub>

The different phosphor powders were synthesized using a co-precipitation method explained in ref. [4]. A schematic diagram is shown in figure 1 for the synthesis of the Alq<sub>3</sub>.

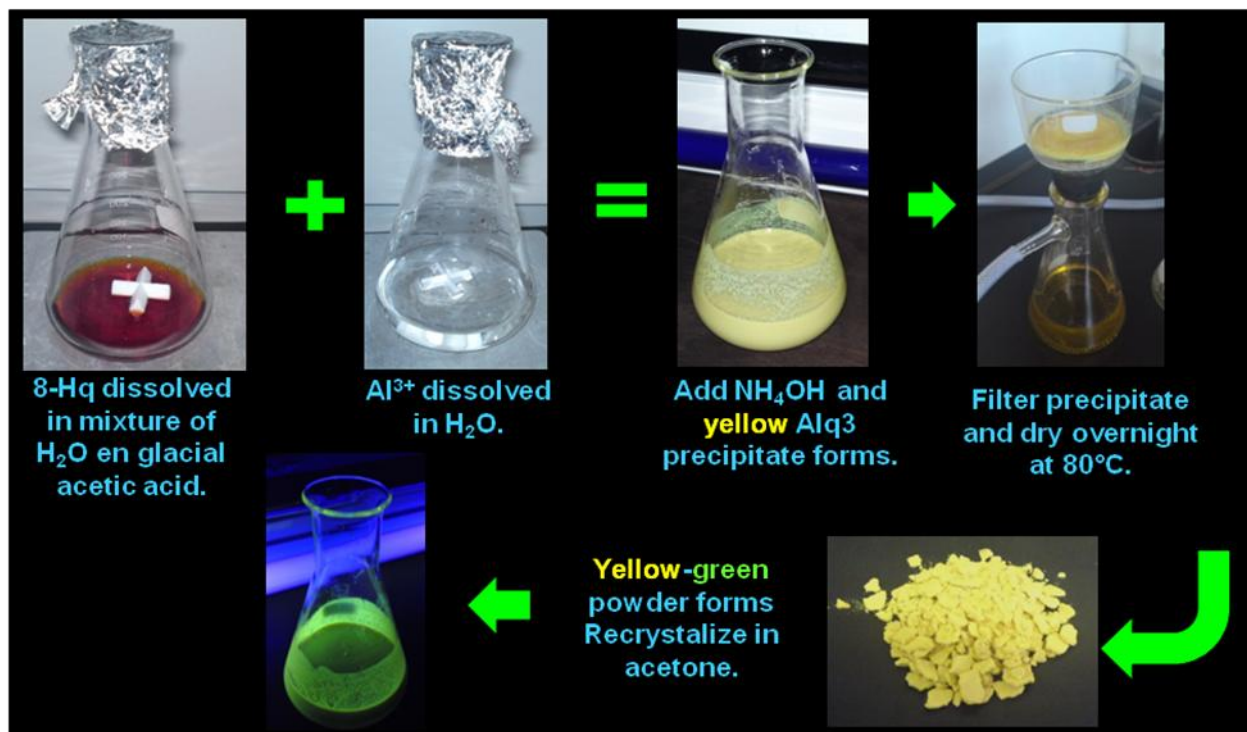
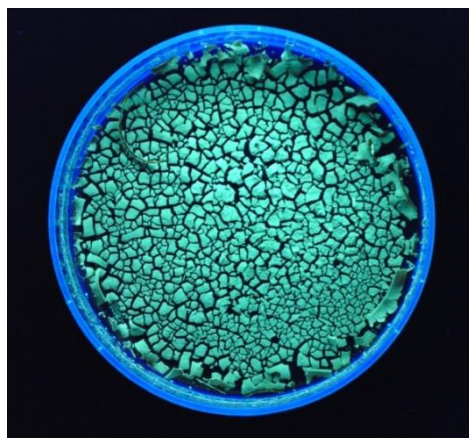


Figure 1: Schematic diagram of the synthesis of Alq<sub>3</sub>.

### 2.2 Synthesis of SiO<sub>2</sub>-Alq<sub>3</sub>

SiO<sub>2</sub> sols were prepared by using the method described by Ntwaeaborwa et al. [5], 5 ml of TEOS was added to 10 ml distilled water and stirred at the boiling temperature (77 °C) for two hours to ensure complete hydrolysis of the reaction. 0.103g (1 mol%) of the prepared Alq<sub>3</sub> powder was dissolved in 10 ml ethanol and added to the solution. It was stirred for another three hours and annealed at 150 °C in air. The yellow brown product was ground to obtain a fine powder.



**Figure 2: SiO<sub>2</sub>-Alq<sub>3</sub> powder (before grinding) under UV irradiation.**

### **2.3 Synthesis of Alq<sub>3</sub>:PMMA**

A blended thin film of Alq<sub>3</sub>:PMMA at a concentration ratio of 1% Alq<sub>3</sub> was obtained in the following way: 2 g of PMMA was dissolved in 25 ml of chloroform. A solution of 0.026 g Alq<sub>3</sub> in 15 ml of chloroform was added to the PMMA solution. The blend was stirred and poured into a stainless steel dish and was left to dry in air for 24 hours. The films were then cut into 1x1 cm pieces for further characterization. The blended thin films of Alq<sub>3</sub>:PMMA at concentration ratios of 0.5% - 5% were obtained in a similar way.

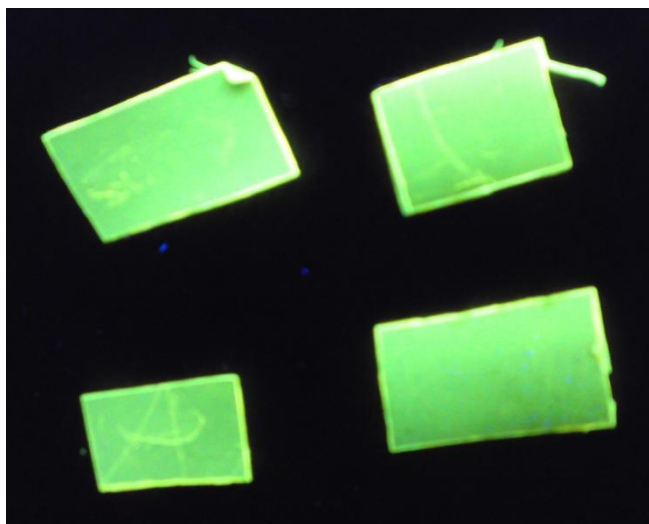
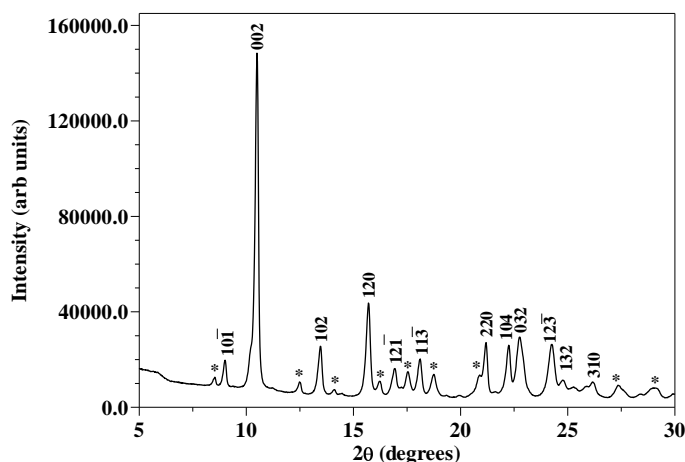


**Figure 3: Alq<sub>3</sub>:PMMA films under UV irradiation.**

### 3. Results

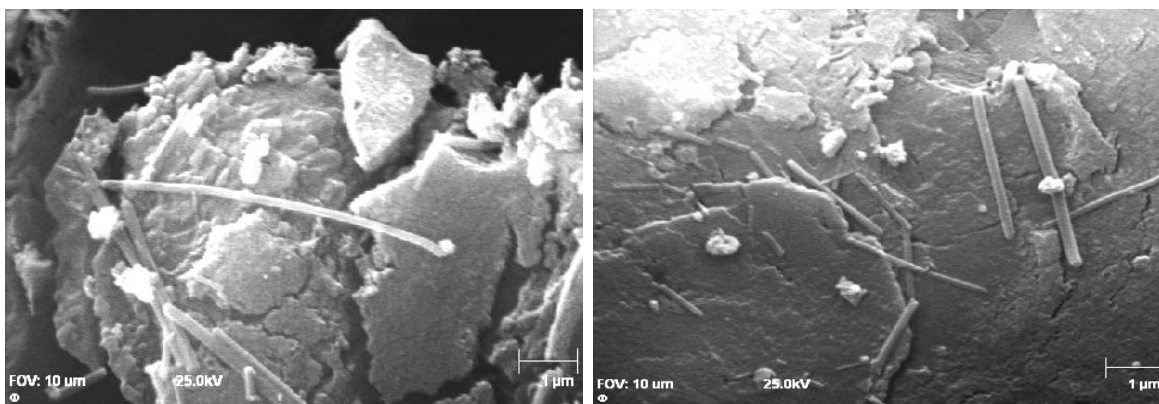
#### 3.1 Alq<sub>3</sub>

The crystallinity of the Alq<sub>3</sub> powders was determined by XRD and is shown in figure 4. The peaks are in agreement with data reported by Mao et al. [6], confirming that the chemical compound that has formed is indeed Alq<sub>3</sub>. The standard data available on various XRD databases for Alq<sub>3</sub> does not match with all the peaks in the sample. Upon investigation it was found that the standard data, taken by Taylor et al. [7] in 1973, was for tris(quinolin-8-olato)titanium(III) (Tiq<sub>3</sub>) and not for Alq<sub>3</sub>, resulting in a mismatch of the standard data with the prepared Alq<sub>3</sub> powder sample. Peaks marked with a \* are not yet identified at present. The average particle size was determined by using Scherrer's equation and was found to be 40 ± 4 nm.

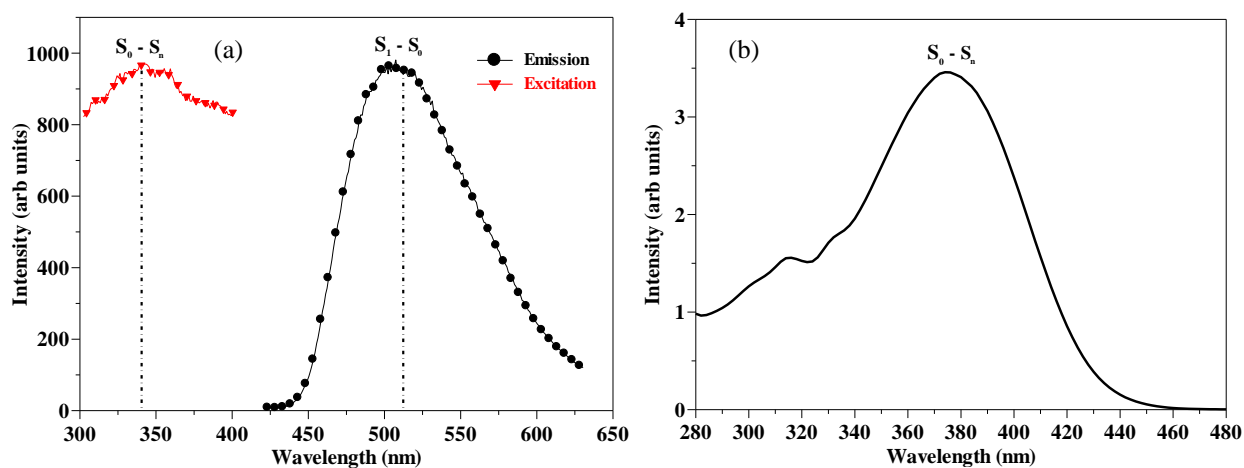


**Figure 4: XRD spectra of Alq<sub>3</sub> after recrystallization in acetone.**

The SEM image in figure 5 shows that some needle like crystals had formed during recrystallization in acetone. These needles are 5-10 μm in length. Although the XRD clearly indicates the formation of nanoparticles, a small part of the Alq<sub>3</sub> has formed crystals. The rest of the sample is composed of big agglomerated particles. It is suggested that an increase in recrystallization time would lead to an increase in the number and length of the needle like crystals.

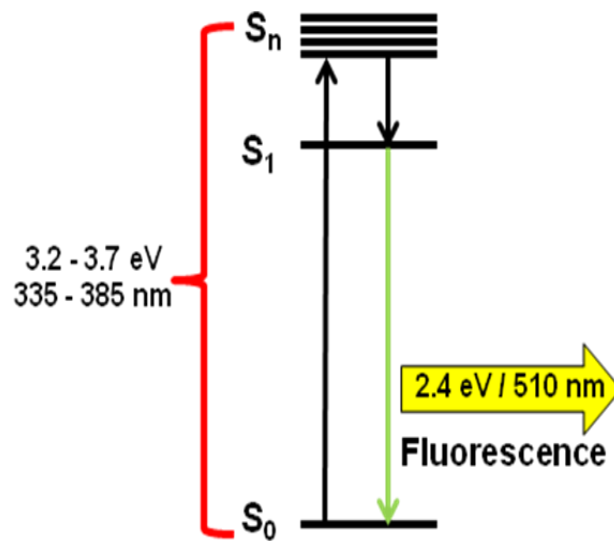


**Figure 5: SEM images of Alq<sub>3</sub> after recrystallization in acetone.**



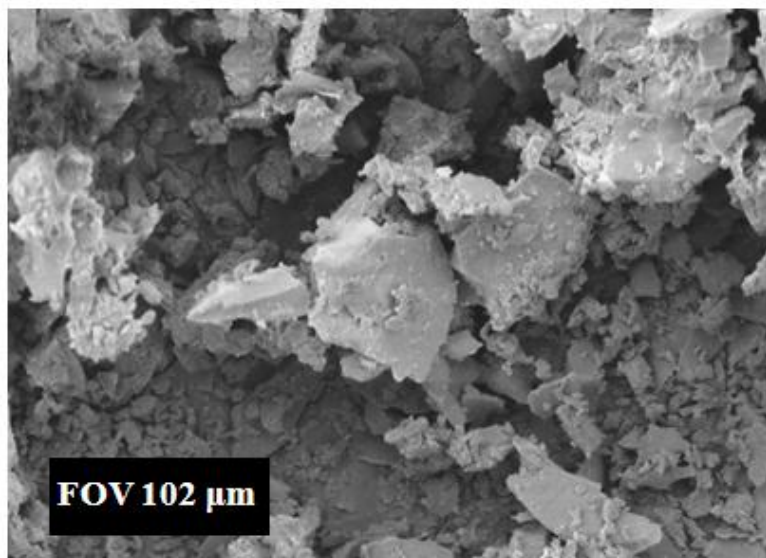
**Figure 6: (a) Excitation and emission spectra of Alq<sub>3</sub> and (b) absorption spectrum of Alq<sub>3</sub>.**

Figure 6(a) shows the excitation and emission spectra of Alq<sub>3</sub> ( $\lambda_{\text{ex}} = 335 \text{ nm}$ ). The emission wavelength for Alq<sub>3</sub> is at 510 nm. Alq<sub>3</sub> is known to be a singlet emitter [8]. The emission is due to the relaxation of an excited electron from the  $S_1$ - $S_0$  level (Figure 7). The excitation and absorption spectra both display broad peaks. This suggests that excitation can take place from  $\sim 320 - 390 \text{ nm}$ . Figure 7 shows a schematic diagram of the energy levels [9] found in Alq<sub>3</sub>. The reason for the broad excitation and emission spectra is the existence of a lot of  $S_n$  levels above the  $S_1$  level. An electron can be excited to any of these levels before relaxing non-radiatively to the  $S_1$  level.



**Figure 7: Schematic diagram of the energy levels in Alq<sub>3</sub> and the excitation and emission process taking place in Alq<sub>3</sub>.**

### 3.2 SiO<sub>2</sub>-Alq<sub>3</sub>



**Figure 8: SEM image of SiO<sub>2</sub>-Alq<sub>3</sub> (FOV 102 μm).**

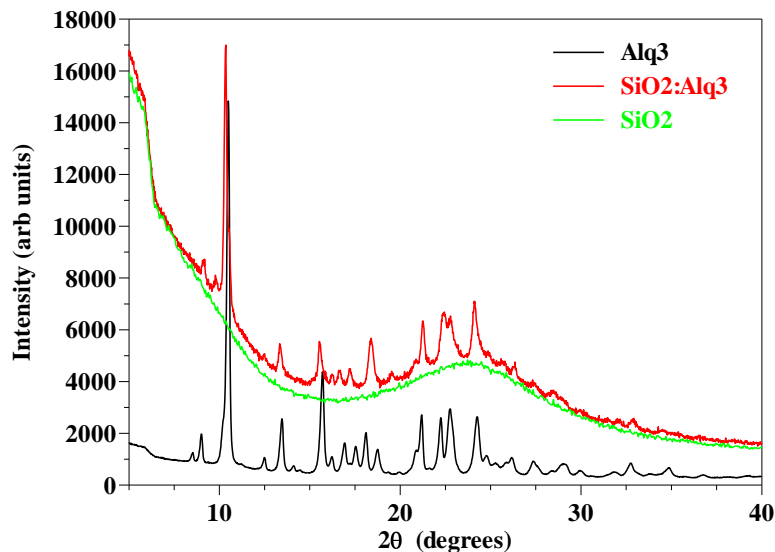
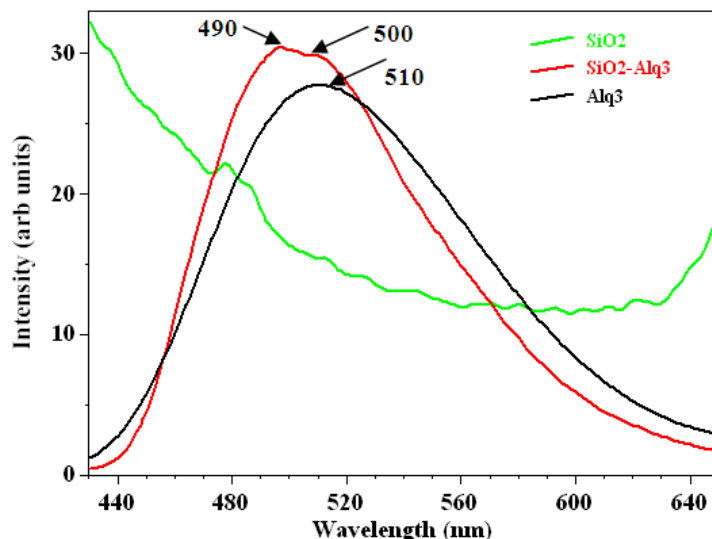


**Figure 9: XRD spectra of Alq<sub>3</sub> powder, SiO<sub>2</sub> and SiO<sub>2</sub>-Alq<sub>3</sub>.**

Figure 8 shows the SEM image of SiO<sub>2</sub>-Alq<sub>3</sub>. The particles are irregularly shaped as a result of the grinding process. Figure 9 shows the XRD spectra of Alq<sub>3</sub> powder, SiO<sub>2</sub> and SiO<sub>2</sub>-Alq<sub>3</sub>. It can be seen that the SiO<sub>2</sub> is amorphous which is expected from SiO<sub>2</sub> prepared by a sol-gel method [10]. The SiO<sub>2</sub>-Alq<sub>3</sub> sample shows peaks on top of the amorphous background. The peaks correspond to the peaks observed for Alq<sub>3</sub> powder. There is a slight shift in the peaks indicating that the SiO<sub>2</sub> matrix slightly distorts the crystal structure of Alq<sub>3</sub>.

Figure 10 shows the PL spectra of pure SiO<sub>2</sub>, Alq<sub>3</sub> powder and SiO<sub>2</sub>-Alq<sub>3</sub> 1 mol% powder. All the samples were excited at 350 nm. It can be seen that SiO<sub>2</sub> does not contribute to the emission. The high background can be ascribed to reflections of the Xenon lamp by the white SiO<sub>2</sub> powder. Alq<sub>3</sub> shows a broad emission peak with a maximum at 510 nm which is due to singlet emission [11]. There is a blue shift of ~ 10 nm when Alq<sub>3</sub> is encapsulated by SiO<sub>2</sub>. The Alq<sub>3</sub> molecule will interact with the encapsulating material and the interactions are reflected by the molecular orbitals being perturbed. This will lead to the formation of new energy states. The blue shift can therefore be explained by assuming both the absence of interactions among Alq<sub>3</sub> molecules and the onset of new interactions of Alq<sub>3</sub> with the SiO<sub>2</sub> material. Minor positive or negative contributions can be made by the matrix materials (SiO<sub>2</sub>), which will also leave their mark on the observable structures of the emission bands. The shoulder observed at 490 nm might

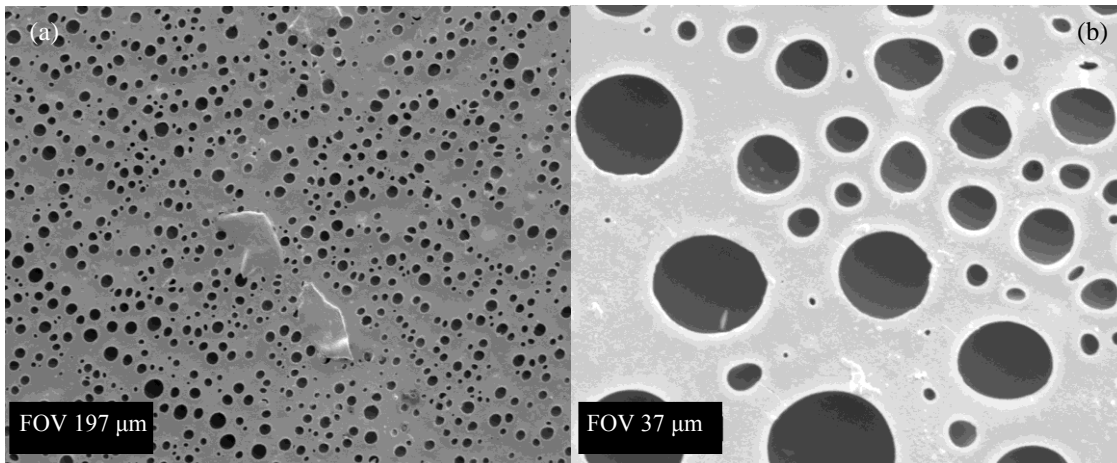
be due to inhomogeneous broadening that is common in glasses, meaning that each molecule acquires a slightly different position [12].



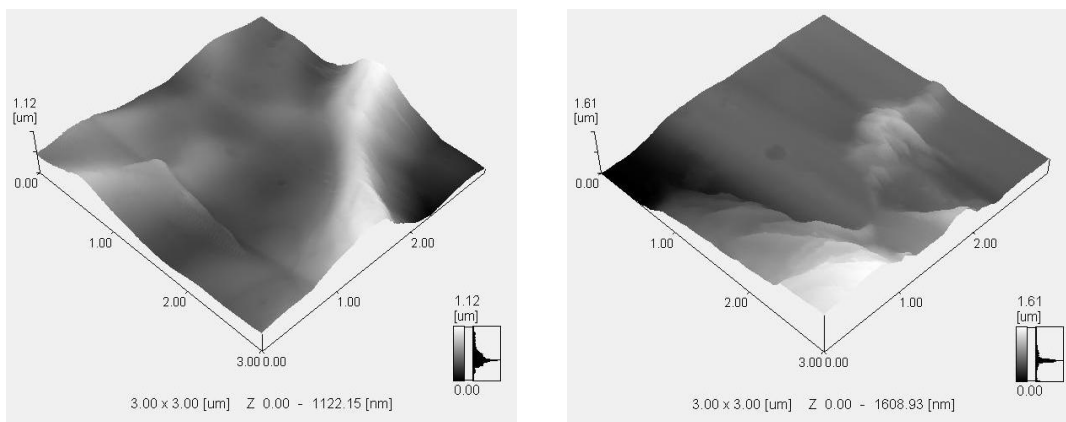
**Figure 10: PL spectra of pure SiO<sub>2</sub>, Alq<sub>3</sub> powder and SiO<sub>2</sub>-Alq<sub>3</sub> 1 mol% powder.**

### 3.3 Alq<sub>3</sub>:PMMA

Figure 11 shows the SEM images of the Alq<sub>3</sub>:PMMA (Alq<sub>3</sub> = 1 mol%) blended thin film with an FOV of 197  $\mu\text{m}$  and 37  $\mu\text{m}$ . The surface was smooth with small holes scattered all over the film. These holes were formed when gasses escaped during evaporation of chloroform (the solvent). At higher magnifications it can be seen that the holes are not all the same size. Bigger holes were probably formed early in the solidification process due to rapid rate of evaporation of the solvent, while small holes were probably formed toward the end when there was less solvent and the rate of evaporation was slow.

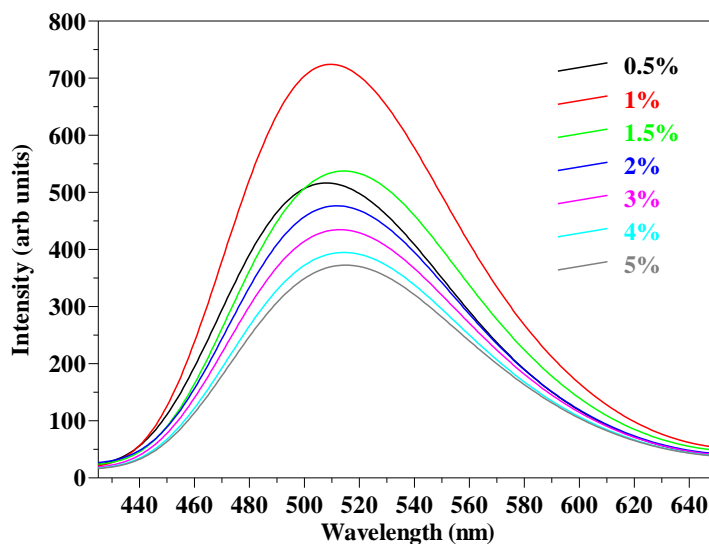


**Figure 11: SEM images of 1% Alq<sub>3</sub>:PMMA at a FOV of (a) 197 μm and (b) 37 μm. Holes that had formed during the evaporation of the solvent can clearly be seen.**



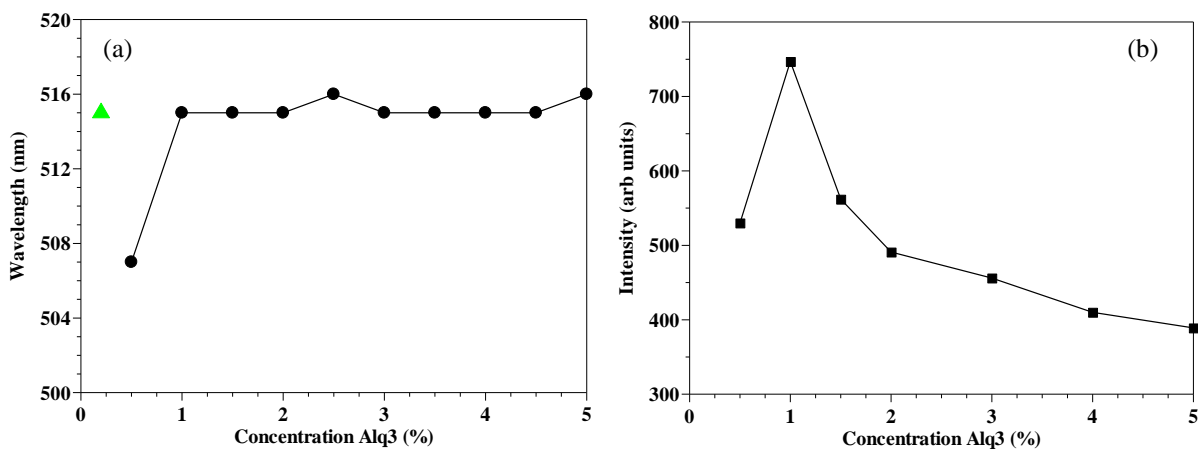
**Figure 12: AFM images of two different spots on the Alq<sub>3</sub>:PMMA (Alq<sub>3</sub> = 1 mol%) film.**

Figure 12 shows the AFM images of two different spots on the Alq<sub>3</sub>:PMMA film. From the images, it can be seen that the surface of the film is not as smooth as the SEM image suggests. Outcrops can be seen ranging between 1-2 μm in height. No distinct particles can be seen, confirming that the Alq<sub>3</sub> powder was completely mixed with the PMMA.



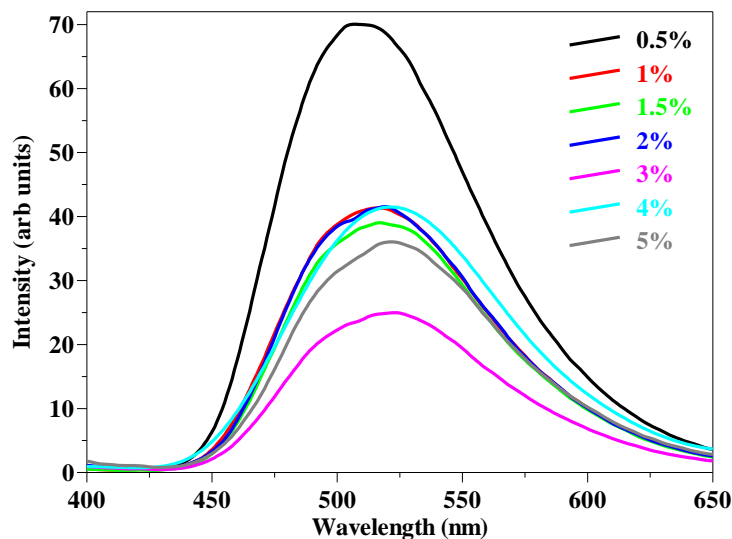
**Figure 13: PL spectra of different concentrations of Alq<sub>3</sub> in a PMMA matrix, just after synthesis.**

Figure 13 shows the PL spectra of different concentrations of Alq<sub>3</sub> in a PMMA matrix just after preparation of the films. The films were excited at 355 nm. All the peaks showed a broad spectrum with a maximum intensity at around 515 nm (figure 14(a)) which is red shifted by 5 nm from that of the powder sample. This corresponds to the emission of Alq<sub>3</sub> in the solid state [13]. This emission is again associated with the S<sub>1</sub>→S<sub>0</sub> transition localized on the a-quinolate ligand [11].



**Figure 14: (a) A plot of the emission wavelength at maximum intensity as function of the Alq<sub>3</sub> concentration. The triangle represents the emission of Alq<sub>3</sub> in the solid state. (b) Plot of PL maximum intensity as a function of concentration of Alq<sub>3</sub>.**

The peak of the 0.5 mol% sample is blue-shifted by 8 nm (figure 14(a)). Previous reports by Cölle et al. [13] and Levichkova et al. [14] attributed the blue-shift to either the formation of the  $\delta$ -phase of Alq<sub>3</sub> or the transformation of the meridional form of Alq<sub>3</sub> to the facial form. Cölle and co-workers obtained the  $\delta$ -phase of Alq<sub>3</sub> by thermal sublimation in a horizontal glass at high temperature (410 °C) [13] and Katakura et al. [15] reported that the facial form of Alq<sub>3</sub> has a very short lifetime in solution. In this study neither annealing nor sublimation at high temperatures was performed. Shukla and Kumar [16] attributed the blue shift in Alq<sub>3</sub> thin films to the change from the 3D to 2D excitonic states with decreasing film thickness. Although the film thicknesses were not evaluated, it can be possible that the blue-shift of the Alq<sub>3</sub> film in this study was due to the change in excitonic states. The emission of solid state Alq<sub>3</sub> is due to the relaxation of an excited electron from the S<sub>1</sub>-S<sub>0</sub> level. Several S<sub>n</sub> levels exist above the S<sub>1</sub> level. At low concentrations the emission is most probably due to relaxation from the S<sub>n</sub>-S<sub>0</sub> level causing a blue shift. Figure 14(b) shows that the sample doped with 1 mol% of Alq<sub>3</sub> has the highest intensity. The intensity then decreases with an increase in concentration. This same decrease in intensity was reported by Meyers and Weck [2]. The decrease (or quenching) of luminescence at higher concentrations is due to concentration quenching effects. This is the result of clustering or cross relaxation [17].



**Figure 15: PL spectra of different concentrations of Alq<sub>3</sub> in a PMMA matrix, after 30 months of storage.**

Figure 15 shows the PL spectra of different concentrations of Alq<sub>3</sub> in a PMMA matrix after 30 months of storage. The films were again excited at 355 nm. When compared to figure 13 it can be seen that the films still have 10 % of their initial luminescence intensity. These films were stored under atmospheric conditions in the dark. The 0.5 % sample has the highest intensity and this is ascribed to the fact that this sample has the least amount of Alq<sub>3</sub> and therefore atmospheric conditions will have the smallest effect on this sample.

### 3.4 Alq<sub>3</sub>:PS

An Alq<sub>3</sub>:PS sample (10 mol % Alq<sub>3</sub>) was synthesized in the same way as the Alq<sub>3</sub>:PMMA samples. Figure 16 shows the PL spectra of Alq<sub>3</sub>:PS, Alq<sub>3</sub>:PMMA and Alq<sub>3</sub> powder with  $\lambda_{\text{ex}} = 350$  nm. The PS sample shows the lowest PL intensity.

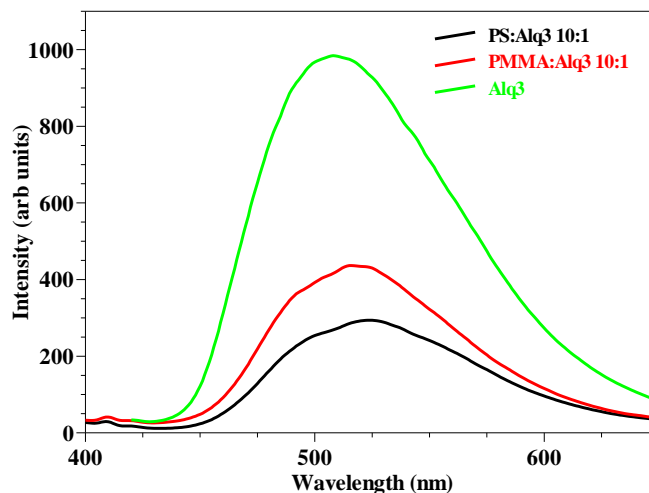
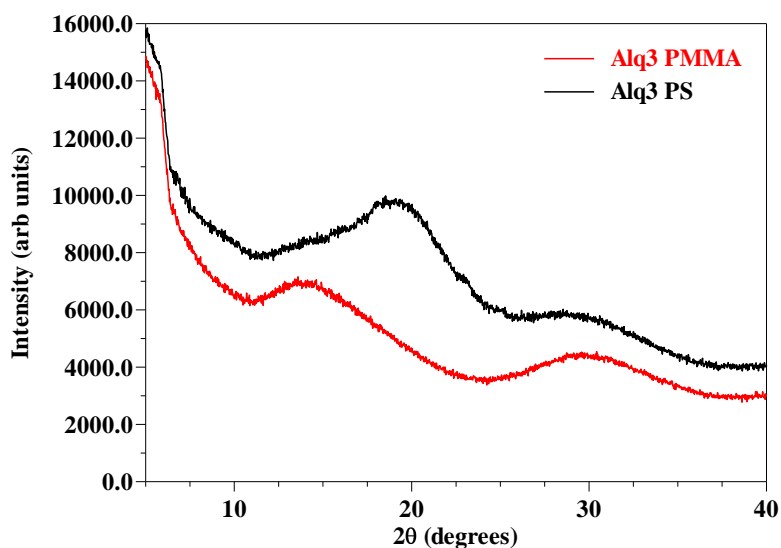
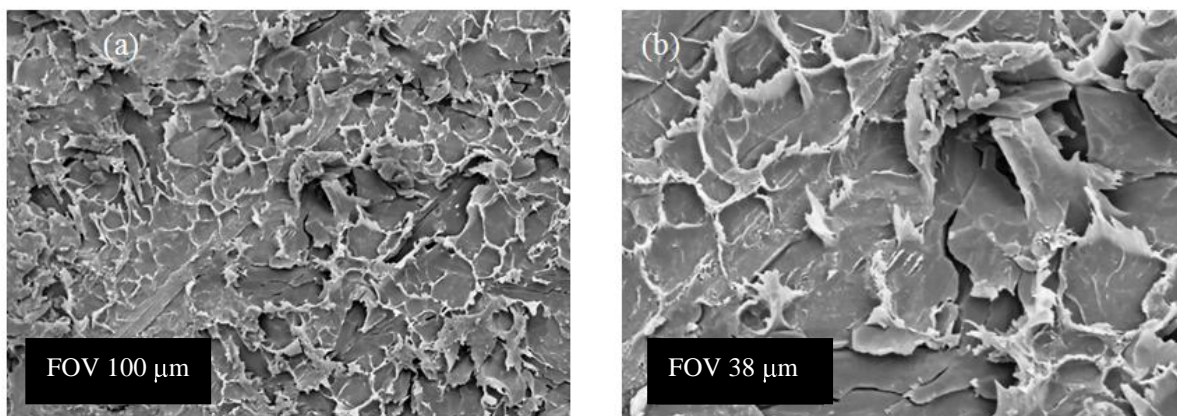


Figure 16: PL spectra of Alq<sub>3</sub>:PS, Alq<sub>3</sub>:PMMA and Alq<sub>3</sub> powder ( $\lambda_{\text{ex}} = 350$  nm).



**Figure 17: XRD spectrum of Alq<sub>3</sub>:PS and Alq<sub>3</sub>:PMMA films.**



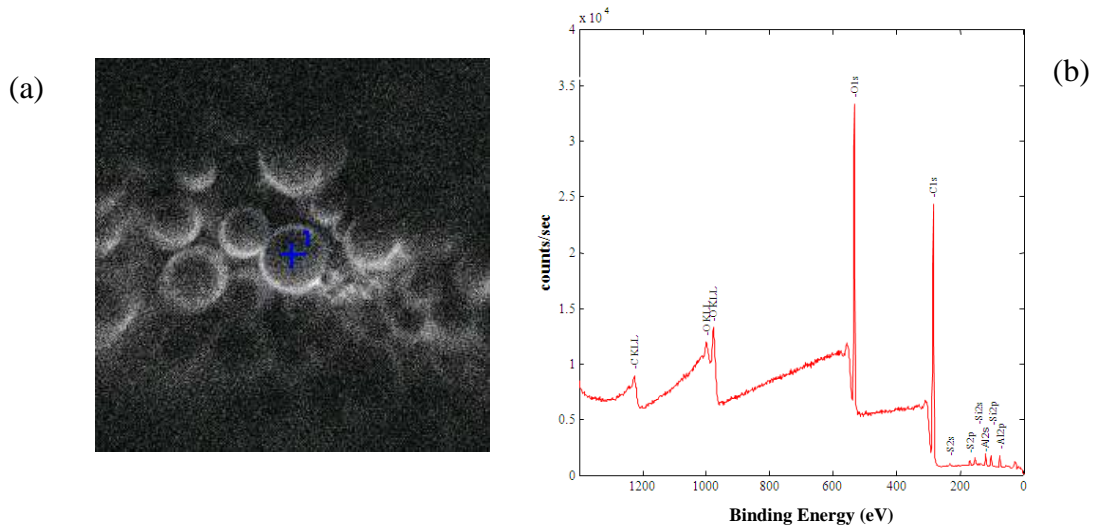
**Figure 18: SEM images of 10% Alq<sub>3</sub>:PS at a FOV of (a) 100 μm and (b) 38 μm.**

Figure 17 shows the XRD spectra of the Alq<sub>3</sub>:PS and Alq<sub>3</sub>:PMMA films. Both the films are amorphous with no Alq<sub>3</sub> peaks present. The SEM micrographs are shown in figure 18. The micro structure displays tear marks. It was very difficult to remove the films from the stainless steel container, which resulted in the tear marks. This also made the Alq<sub>3</sub>:PS impractical to work with.

## 4. XPS of PMMA and Alq<sub>3</sub>:PMMA

### 4.1 PMMA powder

Figure 19 (a) shows the secondary x-ray images of commercial PMMA powder (Sigma Aldrich) and figure 19 (b) shows the XPS survey scan. The main peaks for O1s and C1s are observed as well as some small peaks for S2s, S2p, Si2s, Si2p, Al2s and Al2p. These small peaks are attributed to contamination during the fabrication of the powder. Figure 20 shows the high resolution scans for O1s and C1s (pass energy of 11.8 eV and 50 cycles) , as well as S2p, Si2p and Al2p (pass energy of 23.5 eV and 100 cycles).



**Figure 19: (a) SXI and (b) XPS survey scan of PMMA powder.**

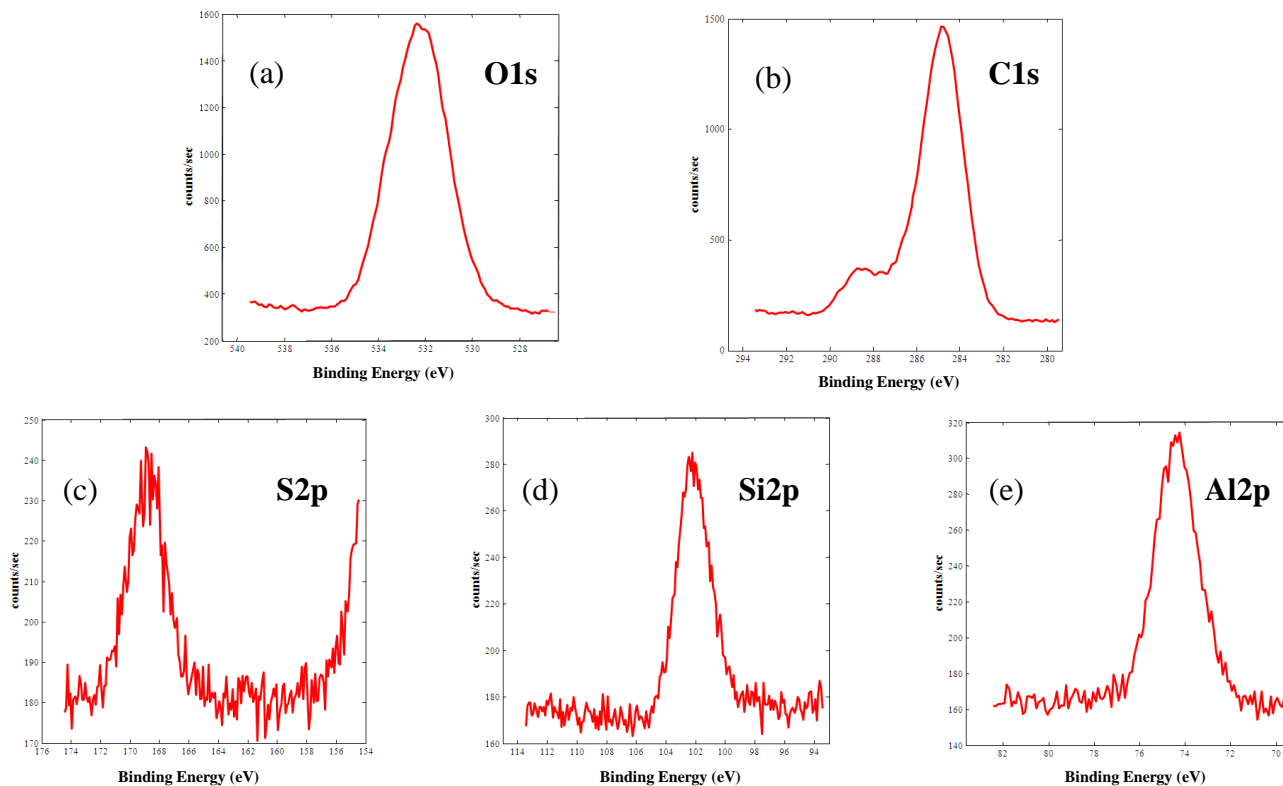


**Figure 20: High resolution XPS peaks of PMMA powder.**

## 4.2 PMMA films

Figure 21 shows the XPS survey scan of the prepared PMMA films. The same peaks as in figure 19 (b) are observed, but small peaks of Cl2s and Cl2p are also present. These peaks are due to solvent (chloroform) still trapped inside the film. The increase in the C1s peak's counts is also attributed to solvent effects. Figure 22 shows the high resolution scans for O1s and C1s (pass energy of 11.8 eV and 50 cycles), as well as S2p, Si2p, Cl2p and Al2p (pass energy of 23.5 eV and 100 cycles). Please note that a complete explanation of the high resolution XPS peaks of the Alq<sub>3</sub> powder samples are discussed in chapter 6.

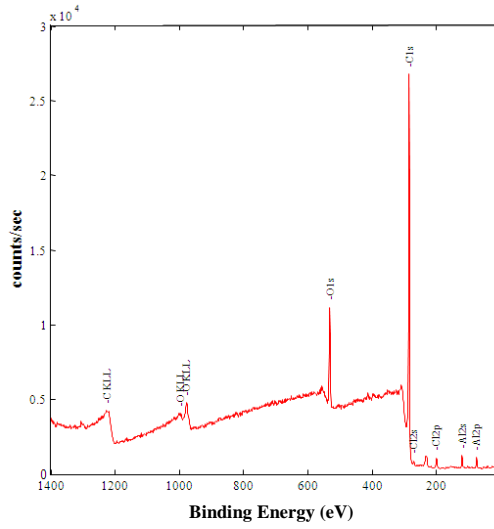


**Figure 21: XPS survey scan of PMMA film.**

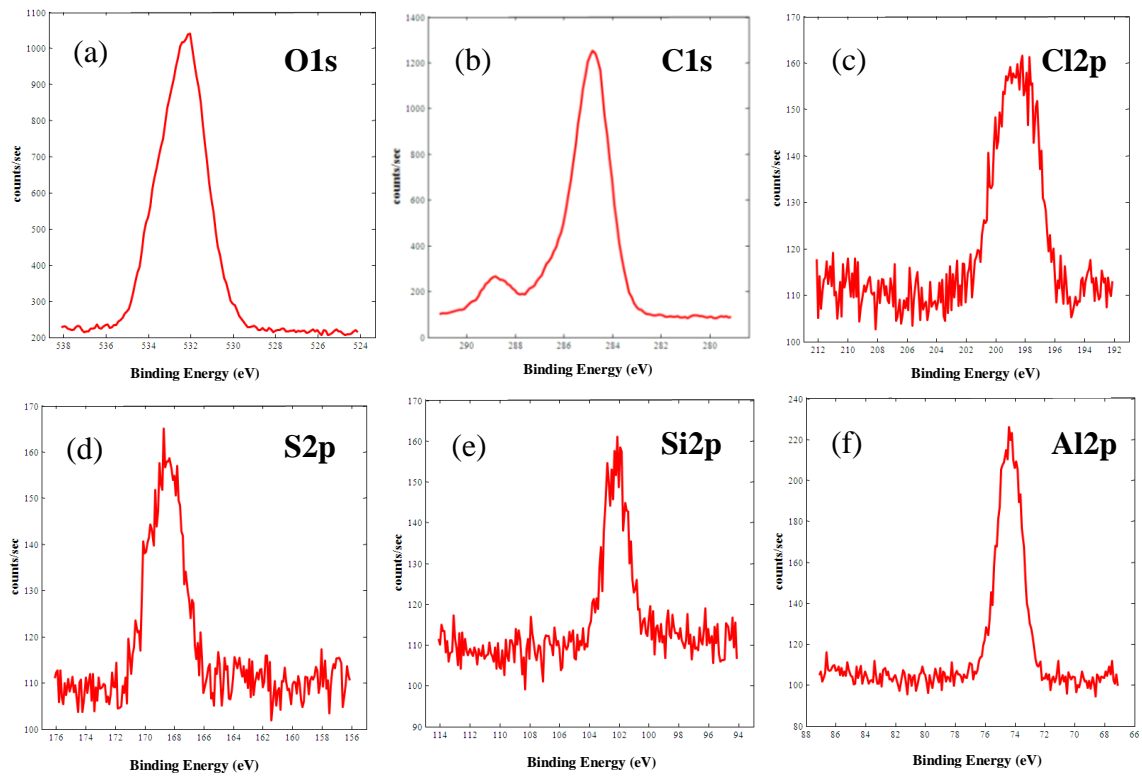


**Figure 22: High resolution XPS peaks of PMMA film.**

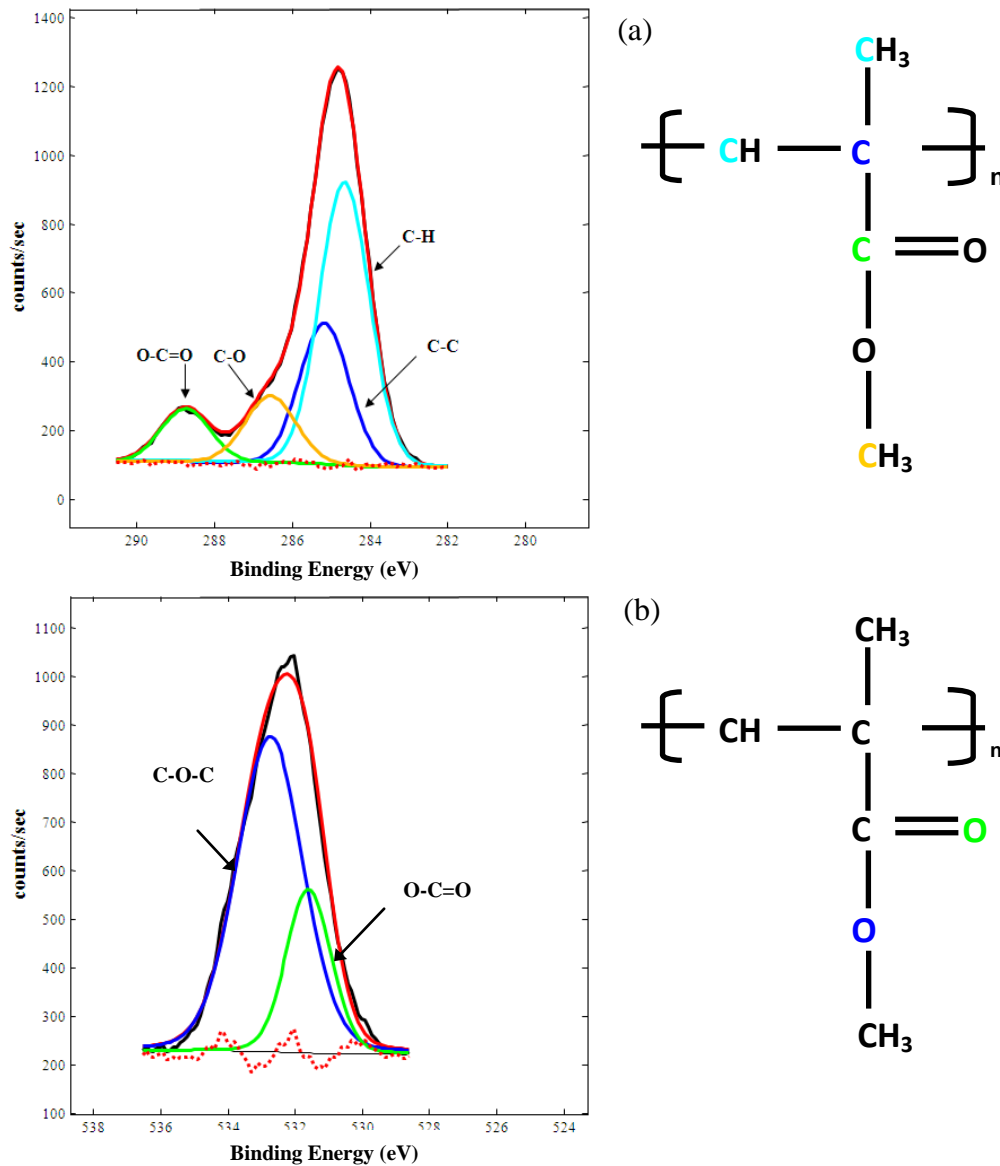


**Figure 23: Fitted peaks for (a) C1s and (b) O1s of the PMMA film.**

Figure 23 (a) and (b) show the fitted peaks for the C1s and O1s peaks. The peak at 284.7 eV is assigned to  $-\text{CH}_3$  and  $-\text{CH}_2$ . The peak at 285.8 eV is due to the quaternary carbon of PMMA. The peak at 286.6 eV is due to  $-\text{C}-\text{O}-$  species, while the peak at 288.75 is assigned to the carbonyl C 1s electrons. Two peaks are fitted for the O1s peak. The one at 532.1 eV is due to carbonyl O1s electrons, while the peak at 533.6 eV is due to the methoxy O1s species [18].

### 4.3 Alq<sub>3</sub>:PMMA films

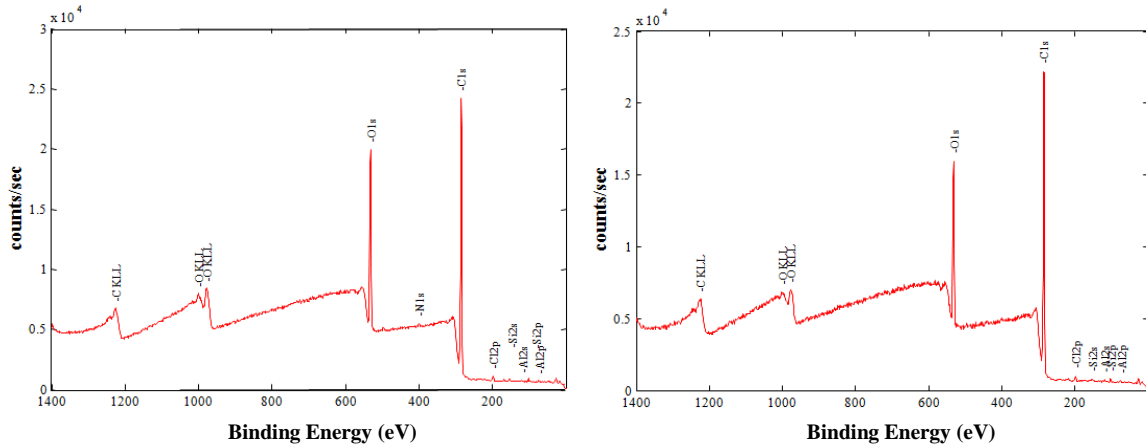


**Figure 24: XPS survey scan of Alq<sub>3</sub>:PMMA film on two different areas before sputter.**

Figure 24 shows the XPS survey scan of Alq<sub>3</sub>:PMMA film on two different areas on the film. The main peaks of O1s and C1s are observed that are characteristic of PMMA. Small peaks for N1s, Si2s, Si2p, Al2s, Al2p and C12p are observed on the surface of the film. The Si2s, Si2p, Al2s and Al2p peaks are attributed to contamination during the fabrication of the PMMA powder used to produce the films. The C12p peak is again assigned to solvent trapped inside the film. The Alq<sub>3</sub> present in the film can contribute to the Al2s, Al2p, N1s, O1s and C1s peaks. Figure 25 shows the high resolution peaks of O1s and C1s (pass energy of 11.8 eV and 50 cycles), as well as Si2p, C12p, N1s and Al2p (pass energy of 23.5 eV and 100 cycles) before sputter (red) and after 31.5 sec sputter (blue). The sample was sputtered with an Ar<sup>+</sup> – ion beam, 2 kV, 2 μA, 2x2 mm, with a sputter rate of about 8.5 nm/min. The depth profile is shown in figure 26. The change in peaks is attributed to the breaking of the molecular bonds under ion bombardment.

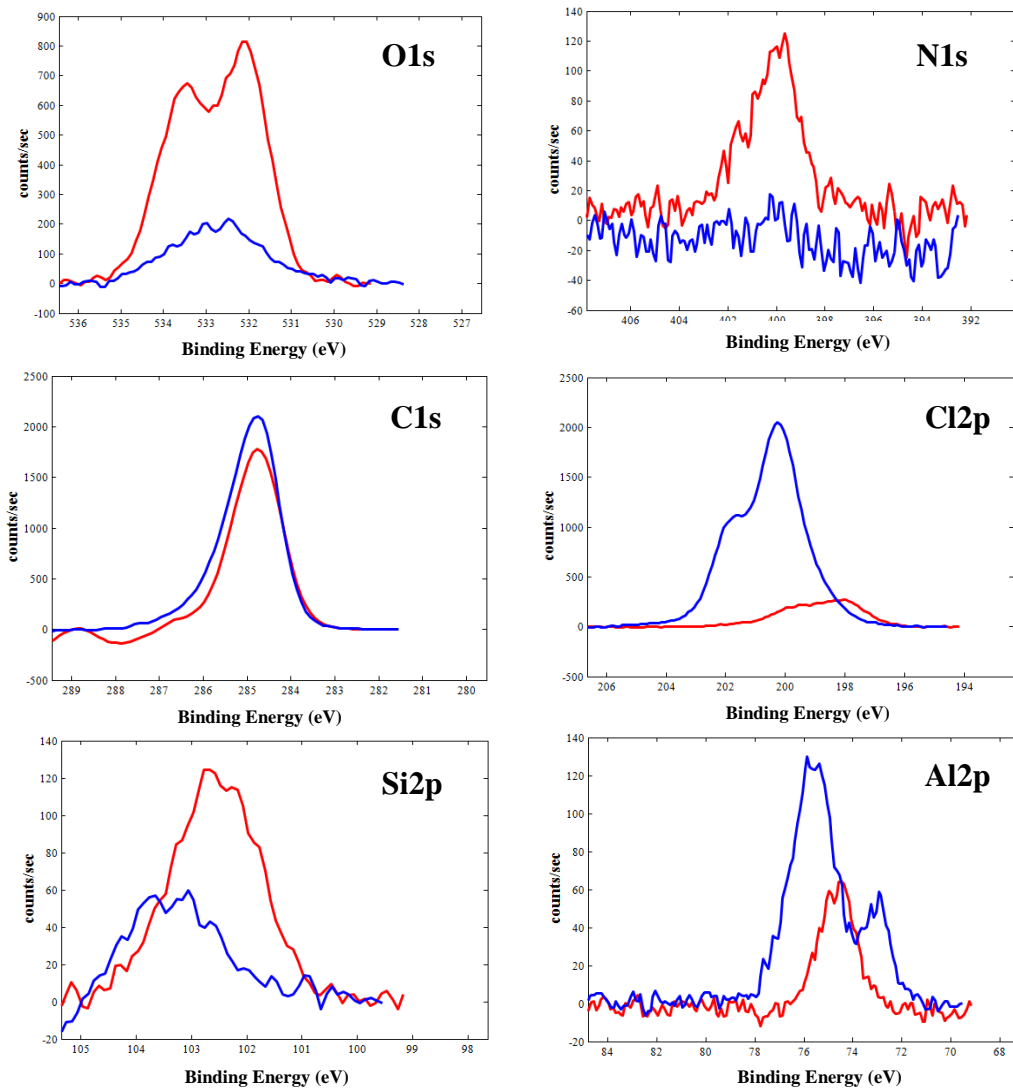


**Figure 25: High resolution XPS scans of the Alq<sub>3</sub>:PMMA film (red before Ar-sputter and blue after Ar-sputter).**

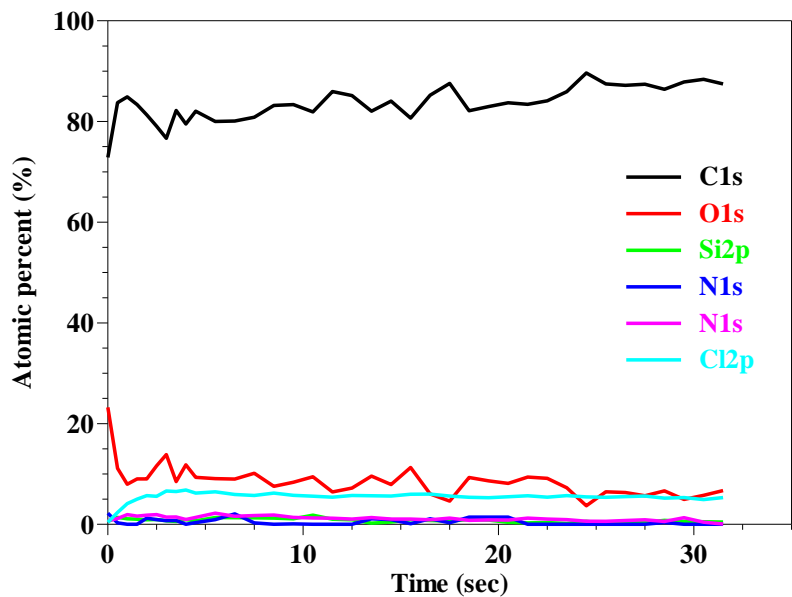


**Figure 26: XPS depth profile of the Alq<sub>3</sub>:PMMA film.**

Figure 27 shows the fitted peaks of C1s and O1s before Ar-sputtering. The same peaks are fitted as for the PMMA film.

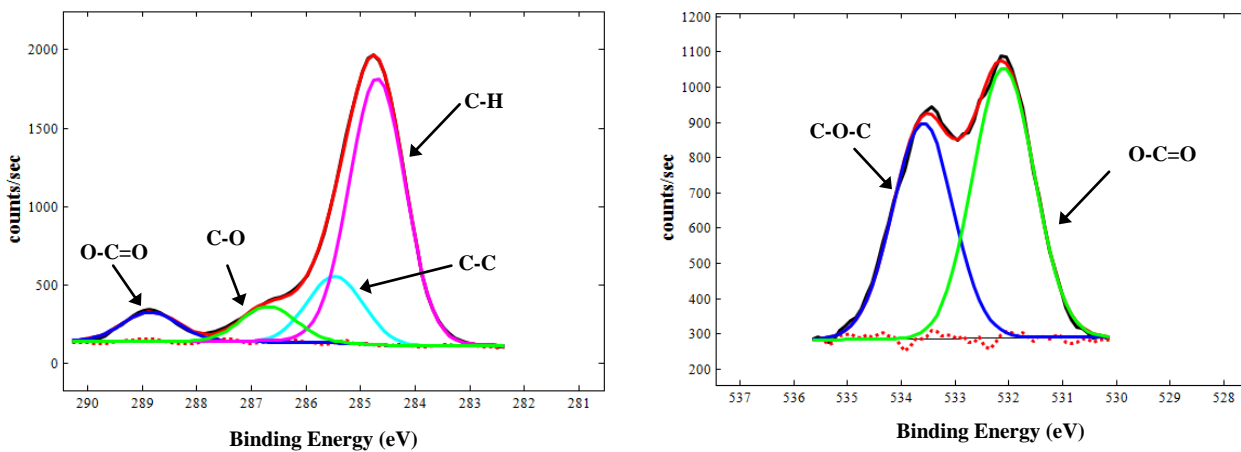


**Figure 27: Fitted XPS peaks of C1s and O1s before Ar-sputtering.**

## 4. Conclusion

Alq<sub>3</sub> powder, Alq<sub>3</sub>:SiO<sub>2</sub>, Alq<sub>3</sub>:PMMA and Alq<sub>3</sub>:PS were successfully synthesized. Alq<sub>3</sub> powder showed broad emission at 510 nm. The emission is due to the relaxation of an excited electron from the S<sub>1</sub>-S<sub>0</sub> level. The Alq<sub>3</sub>:SiO<sub>2</sub> samples showed a slight increase in PL intensity with a blue shift of 10 nm. The blue shift could therefore be explained by assuming both the absence of interactions among Alq<sub>3</sub> molecules and the onset of new interactions of Alq<sub>3</sub> with the SiO<sub>2</sub> material. Blended thin films of Alq<sub>3</sub>:PMMA were successfully synthesized. The morphology and structure measurements of the films showed that the surface contained a lot of holes. The AFM images showed that the surface of the films was not smooth, but rather rough with a lot of “hills and valleys”. This rough surface contributed to the high luminescence intensity that was observed due to less internal reflection that occurred within the film. A broad emission band was observed, with its maximum at 515 nm when excited with 355 nm photons. This is consistent with emissions of Alq<sub>3</sub> in the solid state. A blue shift in the emission was observed for the 0.5 mol % sample and it was attributed to change in excitonic states. The 1 mol % sample showed the highest intensity and the intensity then decreased with an increase in doping concentration due to concentration quenching effects. Alq<sub>3</sub>:PS films had a lower PL intensity than the Alq<sub>3</sub>:PMMA films. XPS results for commercial PMMA powder showed that Al, Si and S were also present in the sample. The O1s and C1s peaks corresponded to reports in literature. The PMMA film had some Cl present and this was due to solvent (chloroform) trapped inside the film. The Alq<sub>3</sub>:PMMA film showed the same peaks as the PMMA film.

## References

- [1] C.W. Tang and S.A. Vanslyke, *Appl. Phys. Lett.* **51** (1987) 913-915.
- [2] A. Meyers and M. Weck, *Macromolecules* **36** (2003) 1766-1768.
- [3] R.H. Friend, R.W. Gymer, A.B. Holmes, J.H. Burroughes, R.N. Marks, C. Taliani, D.D.C. Bradley, D.A. Dos Santos, J.L. Brédas, M. Lögdlund and W.R. Salaneck, *Nature* **397** (1999) 121-128.
- [4] J.G. Mahakhode, B.M. Bahirwar, S.J. Dhoble and S.V. Moharil, *Proc. Of ASID.* (2006) 237-239.
- [5] O.M. Ntwaeaborwa, H.C. Swart, R.E. Kroon, P.H. Holloway and J.R. Botha, *J. Phys. Chem. Sol.* **67** (2006) 1749-1753.
- [6] C.J. Mao, D.C. Wang, H.C. Pan and J.J. Zhu, *Ultrason. Sonochem.* **18** (2011) 473-476.
- [7] F. Taylor and J. Wilkins, *Chem. Soc. Dalton Trans.* **1** (1973) 87-90.
- [8] A.D. Walser, R. Priestley and R. Dorsinville. *Synth. Met.* **102** (1999) 1552-1553.
- [9] S. Watanabe, A. Furube and R. Katoh, *J. Phys. Chem. A.* **110** (2006) 10173-10178.
- [10] M.D. Halls and H.B. Schlegel, *Chem. Mater.* **13** (2001) 2632-2640.
- [11] G. Baldacchini, P. Chiacchiaretta, R. Reisfeld and E. Zigansky, *J. Lumin.* **129** (2009) 1849-1852.
- [12] V.K. Shukla, S. Kumar and D. Deva, *Synth. Met.* **156** (2006) 387-391.
- [13] M. Colle, J. Gmeiner, W. Milius, H. Hillebrecht and W. Brutting, *Adv. Func. Mat.* **13** (2003) 108-112.
- [14] M.M. Levichkova, J.J. Assa, H. Fröb and K. Leo, *Appl. Phys. Lett.* **88** (2006) 201912-201914.
- [15] R Katakura and Y Koide, *Inorg. Chem.* **45** (2006) 5730-5732.
- [16] V.K. Shukla and S. Kumar, *Synthetic Metals* **160** (2010) 450-454.
- [17] Blasse G and Grabmaier B C 1994 *Luminescent Materials* Springer Verlag ISBN 3-540-58019-0 New York.
- [18] L.P. Buchwalter and G. Czornyj, *J. Vac. Sci. Technol. A*, **8** (1990) 781-784.

# Chapter 6

## Photon degradation

### 1. Introduction

Tris-(8-hydroxyquinoline) aluminium ( $\text{Alq}_3$ ) is widely used in organic light emitting diodes (OLEDs) as a light emitting material and also as an electron transporting layer.  $\text{Alq}_3$  is, however, very sensitive to the atmospheric environment and the performance of  $\text{Alq}_3$  is affected by oxygen, moisture and light exposure [1], [2]. Light exposure leads to the formation of non-emissive regions, or “dark spots”. F.P. Rosselli et al. [3] propose two degradation products that may form: the first is the rupture of one of the Al-O bonds which leads to the rupture of the benzene ring on one 8-hydroxyquinoline unit. This rupture is a result of reduction. In the second case the Al-O bond stays intact and breaking of the phenoxide ring occurs. These changes result from oxidation. The breaking of the phenoxide ring leads to the forming of a carboxylate group that is bound to the Al. The formation of the different degradation species was investigated by analysis with infra red (IR) and x-ray photoelectron spectroscopy (XPS). These degradation species tend to decrease the luminescence intensity of the  $\text{Alq}_3$  sample. They can either act as quenchers or they may be non-luminescent themselves [4].

In this chapter the photon degradation, caused by exposure to UV light, of  $\text{Alq}_3$  was investigated. The effect of oxygenation and ozonolysis, as well as moisture in the atmosphere, on the luminescence intensity of the  $\text{Alq}_3$  sample were monitored to see if it is in agreement with the theoretical report by Rosselli et al [3]. The rate of degradation was also monitored and the effect of the rate of formation of quenchers is discussed. IR and XPS measurements were performed on the as-prepared and degraded samples to determine the change in their chemical states.

By altering the molecule itself, the effect of degradation might be minimized. The following changes were made to the molecule and the effect of degradation on these new species was investigated:

- The Al in  $\text{Alq}_3$  was replaced by Zn to form  $\text{Znq}_2$ .

- The Alq<sub>3</sub> was encapsulated with SiO<sub>2</sub> and PMMA to form Alq<sub>3</sub>:SiO<sub>2</sub> and Alq<sub>3</sub>:PMMA.
- The effect of substituents on the phenoxide ring of Alq<sub>3</sub>.

## 2. Photon degradation of Alq<sub>3</sub>

Alq<sub>3</sub> was synthesized with the co-precipitation method described in chapter 5. The powder sample of Alq<sub>3</sub> obtained was exposed to prolonged UV radiation in air and the photoluminescence (PL) decrease in intensity as function of exposure time was recorded. To study the photon degradation, the sample was irradiated with an 8W Matelec UV lamp. The emission data was collected by a HR4000CG-UV-NIR Ocean Optics spectrometer.

### 2.1 Effect on photoluminescence intensity

Figure 1 (a) shows the evolution of the emission band during the ~330 hours of UV exposure, resulting in a decrease in intensity. A decrease of ~ 90% was observed. This result is in correlation with results previously reported by Baldacchini et al. [2] and Popovic et al. [4]. From Figure 1 (b) it can be seen that the luminescence intensity decreases very fast at the beginning and reaches one-half of its original value after about 24 hours and the decreasing rate then slows down for longer exposure times.

The powder was placed in a round aluminium sample holder with an area of 346 mm<sup>2</sup> and a depth of 2.5 mm. The sample can be described as being composed of molecules on the surface and molecules making up the bulk of the sample. By using geometrical calculations it was found that 2% of the powder was on the surface and was therefore left completely unprotected against atmospheric agents, while molecules inside the volume of the sample were better protected by the upper layer and the sides of the sample holder. The molecules on the surface were fully exposed to oxygen and moisture in the open air, which are known to destroy the molecular structure [3].

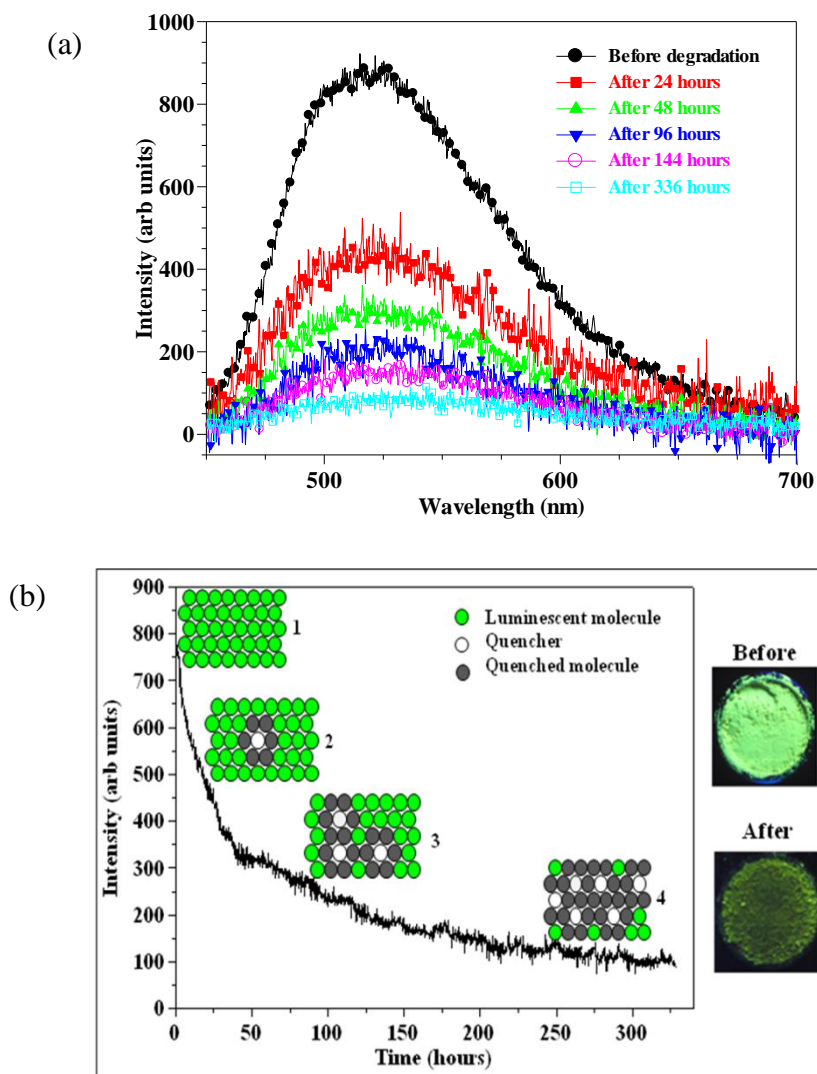


**Figure 1: Degradation of Alq<sub>3</sub> under UV exposure ( $\lambda = 365$  nm). (a) Evolution of the emission band with time. (b) Quenching of luminescence with time.**

According to Rosselli et al. [3] the phenoxide ring can break as a result of oxidation (figure 2). In this case oxidation is very likely to occur since measurements are carried out in air. It is well known that when high energy UV rays interact with molecules of ordinary oxygen (O<sub>2</sub>), it will split into two single oxygen atoms. These free oxygen atoms can combine with O<sub>2</sub> molecules to form ozone (O<sub>3</sub>) molecules [5]. It is therefore important to consider that degradation can occur in the presence of both O<sub>2</sub> and O<sub>3</sub> and both oxygenation and ozonolysis reactions must be considered. These degraded products can decrease the PL intensity in two ways [4]. In the first case they can act as fluorescence quenchers. Only a relatively few degraded Alq<sub>3</sub> molecules are

sufficient to effectively quench the luminescence of the surrounding molecules. Secondly the degraded products do not act as fluorescence quenchers, but are themselves not luminescent. In this case a much larger amount of degraded Alq<sub>3</sub> molecules is needed to achieve a similar decrease in PL intensity. Because the PL intensity decreased very fast over the first 24 hours it is more likely that the degraded products act as luminescence quenchers, because only a few molecules are needed to rapidly decrease the intensity. Figure 1 (b) shows how the quenchers decrease the luminescence intensity. At the start all the molecules on the surface are luminescent (1). The degraded products start acting as quenchers (2) and the rate of degradation is very fast over the first 24 hours, because a small amount of quenchers is needed to quench a large number of molecules. The rate of degradation will slow down with time because the amount of quenchers will increase on the surface, while the amount of molecules that can be quenched will decrease (3). In the end quenchers will be surrounded by quenchers (4) and the degradation rate of the molecules on the surface will slow down.

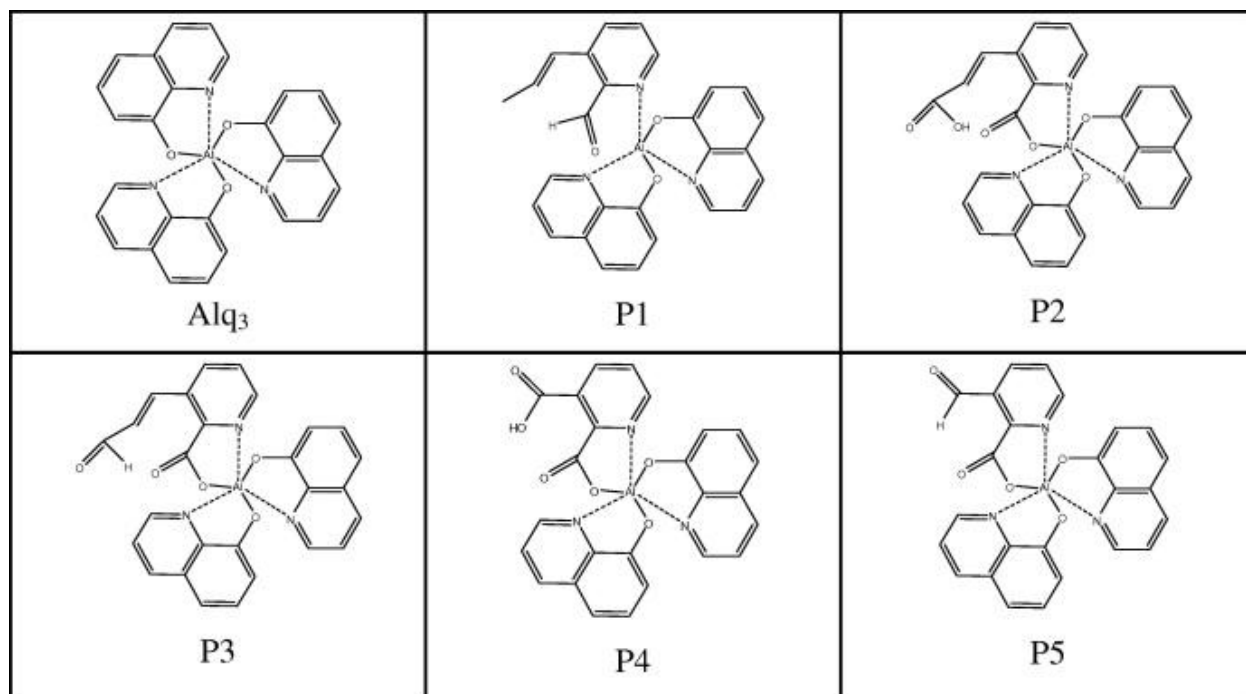


**Figure 2: Some of the products that might form when the phenoxide ring breaks during oxidation of the sample [3].**

Moisture ( $\text{H}_2\text{O}$ ) also contributes to the decrease in luminescence intensity. When  $\text{Alq}_3$  reacts with  $\text{H}_2\text{O}$  a dark brown product forms. According to Papadimitrakopoulos et al. [6]  $\text{Alq}_3$  will form 8-Hq and two stable by-products in the presence of  $\text{H}_2\text{O}$ , so the deep brown product that formed in this case should be 8-Hq. When 8-Hq reacts with  $\text{O}_2$  it will form  $\text{H}_2\text{O}$  and a dark, non emissive polymer.

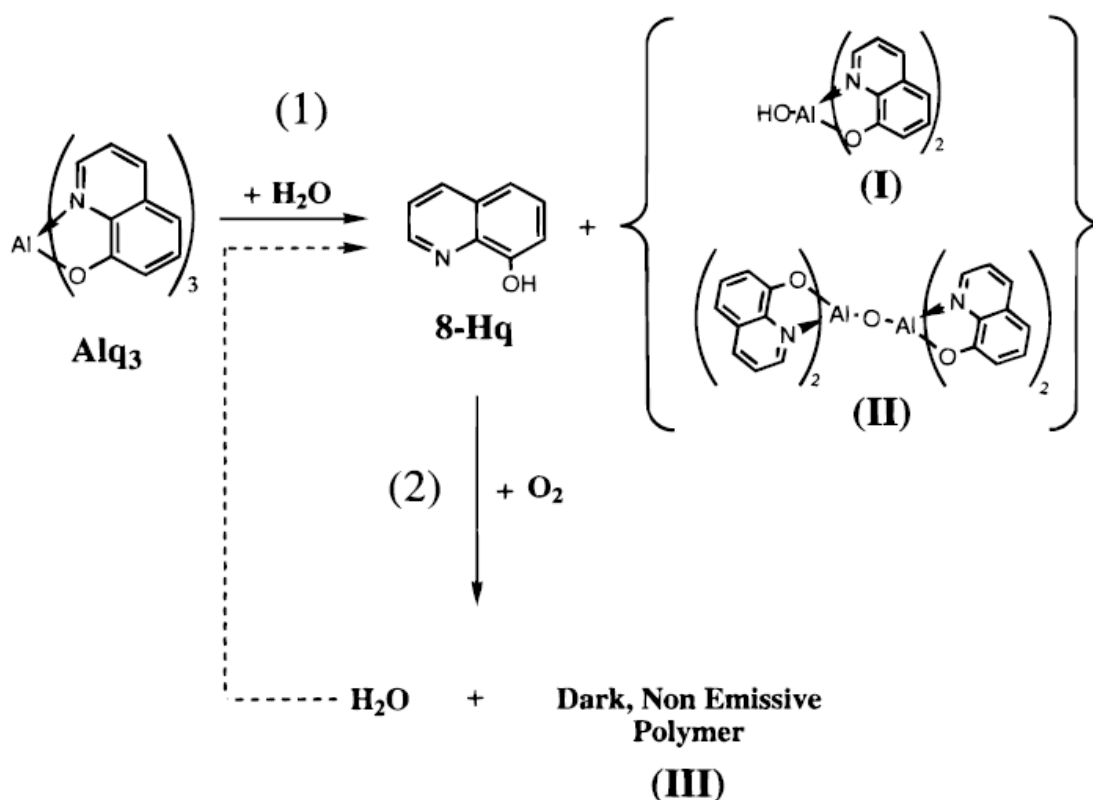


**Figure 3: The formation of 8-Hq and two stable by-products in the presence of  $\text{H}_2\text{O}$ .**

The dark spot observed on the degraded sample can therefore be attributed to two main degradation mechanisms. In the first case oxygenation and ozonolysis cause quenchers to form and with time these quenchers will cover the whole surface. Secondly the  $\text{Alq}_3$  will react with  $\text{H}_2\text{O}$  to form 8-Hq. The 8-Hq will then further react with  $\text{O}_2$  to form  $\text{H}_2\text{O}$  and a dark, non emissive polymer. The oxygenation and ozonolysis are most probably responsible for the fast degradation at the beginning, while exposure to moisture will result in slower degradation rates with time, causing the whole sample (surface and bulk) to become non-luminescent with time.

## 2.2 FTIR analysis

An FTIR analysis was done on the as-prepared and degraded samples. The spectra are shown in figure 4 in the range of 400 – 3500  $\text{cm}^{-1}$ . The characteristic peaks of  $\text{Alq}_3$  are the C-C stretching vibrations (1580, 1501, 1470, 1384 and 748  $\text{cm}^{-1}$ ), C-N stretching vibrations (1580, 1384, 1281 and 1229  $\text{cm}^{-1}$ ), C-C-H bending vibrations (1501, 1425, 1331, 1281 and 1116  $\text{cm}^{-1}$ ), C-O stretching vibrations (1470, 1331 and 1281  $\text{cm}^{-1}$ ), N-C-H bending vibrations (1384 and 1229  $\text{cm}^{-1}$ ), C-N-C bending vibrations (1116  $\text{cm}^{-1}$ ), C-C-C bending vibrations (806 and 748  $\text{cm}^{-1}$ ), C pyramidalization mode (825 and 789  $\text{cm}^{-1}$ ), N pyramidalization mode (789  $\text{cm}^{-1}$ ), C-C torsional mode (789  $\text{cm}^{-1}$ ), Al-O stretching vibration (748 and 523  $\text{cm}^{-1}$ ) and Al-N stretching vibration (419  $\text{cm}^{-1}$ ) [7]. The peak at  $\sim 3400 \text{ cm}^{-1}$  indicates the amount of moisture ( $\text{H}_2\text{O}$ ) present in the sample.

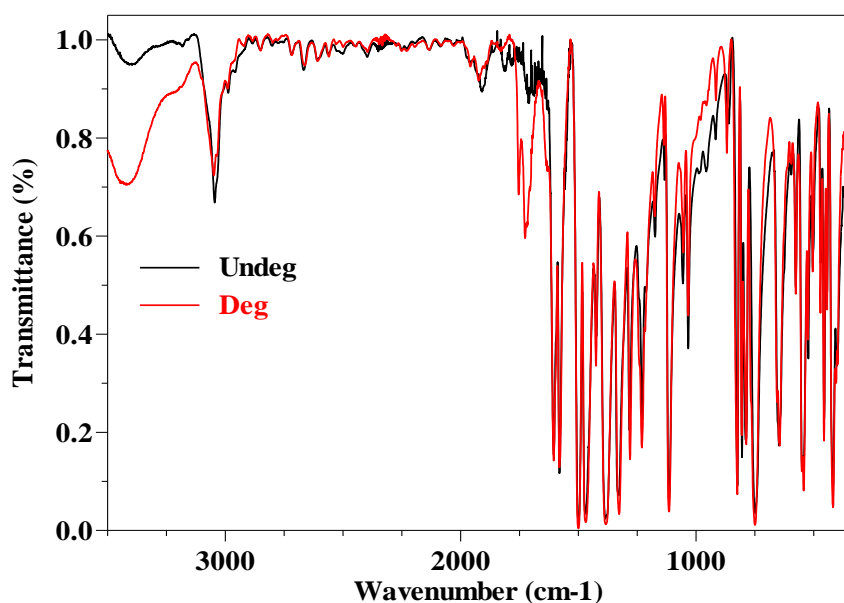


**Figure 4: FTIR spectra of as prepared (Undeg) and degraded (Deg)  $\text{Alq}_3$  samples.**

Figure 5 shows the high resolution scans of the (a)  $\text{H}_2\text{O}$ , (b) C=O, (c) Al-O and (d) Al-N peaks. The degraded sample contains more moisture than the as-prepared sample. This is an indication that the  $\text{Alq}_3$  molecule had degraded because of exposure to moisture (figure 3). There were also more C=O stretching vibrations present in the degraded sample indicating that the phenoxide ring had broken and C=O species had formed. This slight shift in the Al-O bond is due to the

breaking (deformation) of the phenoxide ring. The Al-N peak for both samples is the same. This indicates that the Al-O and Al-N bonds remain intact and only the phenoxide ring will break during degradation.

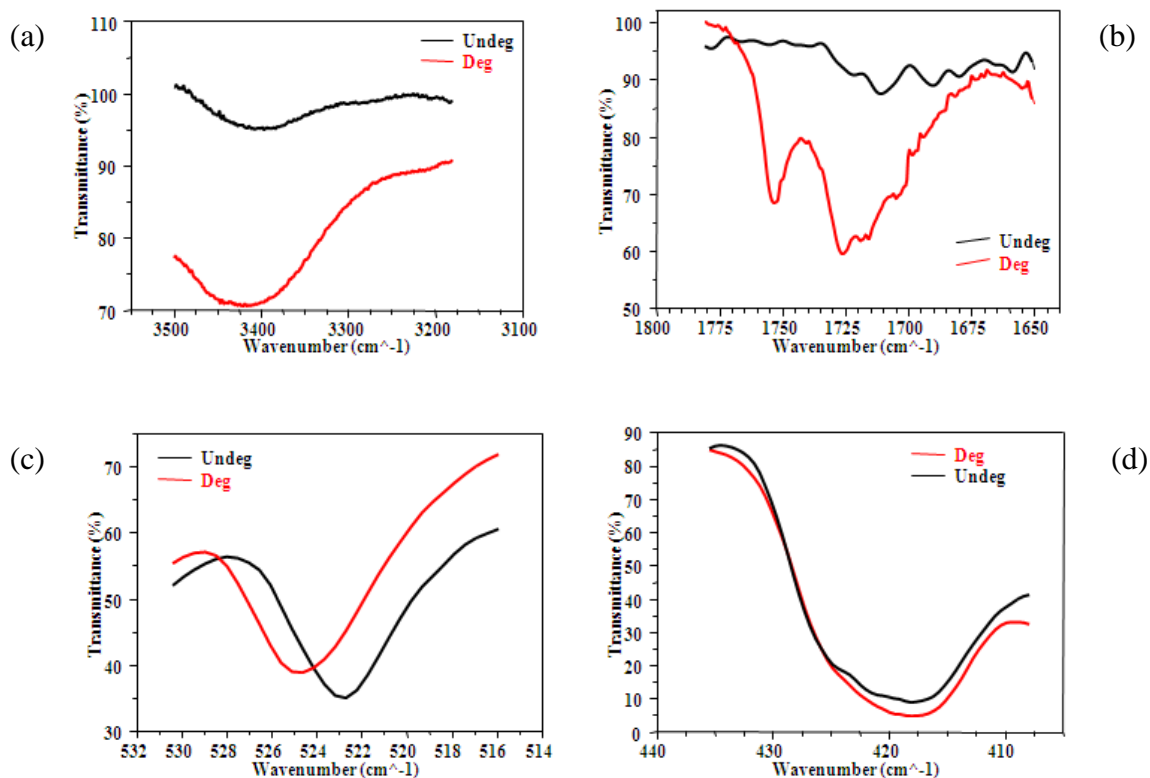
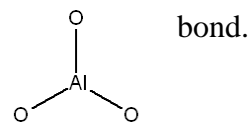


**Figure 5: High resolution IR scans of the (a) H<sub>2</sub>O, (b) C=O, (c) Al-O and (d) Al-N peaks.**

## 2.3 XPS analysis

XPS studies were done on the as-prepared and degraded samples. Figure 6 shows the high resolution peaks of the as-prepared sample. Two peaks were observed for the O1s peak. The peak at 530.7 eV is attributed to the C-O-Al bond and the one at 531.9 eV is attributed to chemisorbed species (such as CO<sub>3</sub>, NO, NO<sub>2</sub>, adsorbed H<sub>2</sub>O or O<sub>2</sub>) on the surface of Alq<sub>3</sub> [8].

The N1s peak consists of two peaks. The one at 399.2 eV is attributed to the C=N-C bond of Alq<sub>3</sub> and the small peak at 400.5 eV is due to chemisorbed NO and NO<sub>2</sub> species. The Al2p peak only consists of one peak at 73.6 eV. This peak is attributed to the



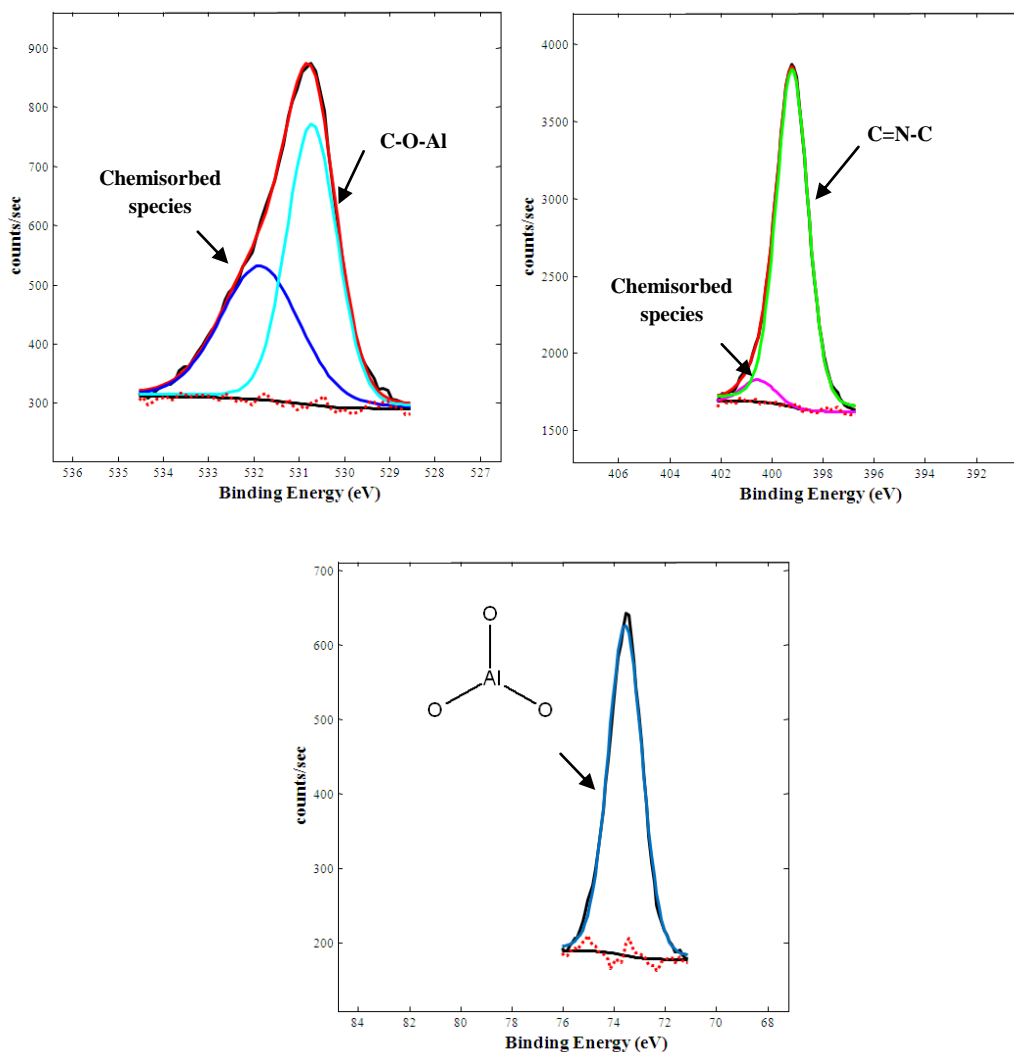


**Figure 6: High resolution XPS peaks of the as-prepared Alq<sub>3</sub> sample.**

Figure 7 (a) shows the high resolution C1s XPS peak of the as-prepared Alq<sub>3</sub> sample. Carbon appears in Alq<sub>3</sub> in five chemical environments (figure 7(b)) resulting in five identifiable binding energies for the C1s transition. Each chemical state and the proportions in which it occurs in are summarized in table 1. The sixth peak is attributed to chemisorbed species like CO<sub>2</sub>.

**Table 1: Carbon bonds for as-prepared Alq<sub>3</sub>.**

Bond number	Carbon bond	Number of bonds
1 (284.6 eV)	$\begin{array}{c} \text{HC} = \text{C} - \text{CH}_2 \\   \\ \text{O} \end{array}$	3
2 (284.8 eV)	$\begin{array}{c} \text{HC} = \text{C} - \text{C} \\   \\ \text{H} \end{array}$	15
3 (283.8 eV)	$\begin{array}{c} \text{HC} - \text{C} - \text{CH} \\    \\ \text{C} \end{array}$	3
4 (285.5 eV)	$\begin{array}{c} \text{HC} - \text{C} - \text{H} \\    \\ \text{N} \end{array}$	3
5 (285.8 eV)	$\begin{array}{c} \text{HC} = \text{C} - \text{N} \\   \\ \text{C} \end{array}$	3
6 (284.0 eV)	Chemisorbed C	

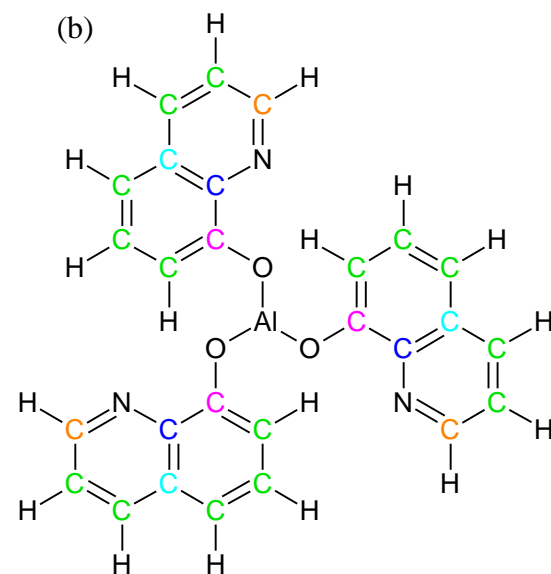
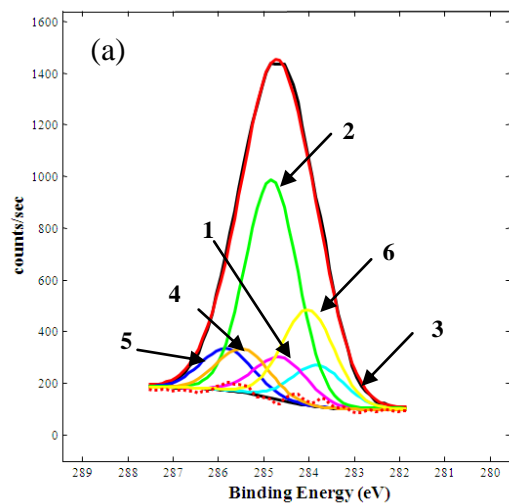


**Figure 7: (a) High resolution C1s XPS peak and (b) Alq<sub>3</sub> molecule showing the different carbon bonds.**

Figure 8 shows the high resolution XPS peaks for the degraded Alq<sub>3</sub> sample. The O1s peak consists of three peaks. The peak at 530.9 eV is attributed to the C-O-Al bond, indicating that the O-Al bond is still intact after degradation. The peak at 532.0 eV is attributed to chemisorbed species on the surface of Alq<sub>3</sub> [9]. An additional peak at 532.9 eV is present. This peak is attributed to the carbonyl and methoxy O1s species that are present in the degraded products [10]. This is an indication that the phenoxide ring broke during degradation. The N1s peak consists of two peaks. The one at 399.2 eV is attributed to the C=N-C bond of Alq<sub>3</sub> and the small peak at 400.3 eV is due to chemisorbed NO and NO<sub>2</sub> species. This indicates that the pyridyl ring is still intact after degradation. Only one peak is present for Al2p at 73.8 also indicating that the Al is still bonded to three O atoms.

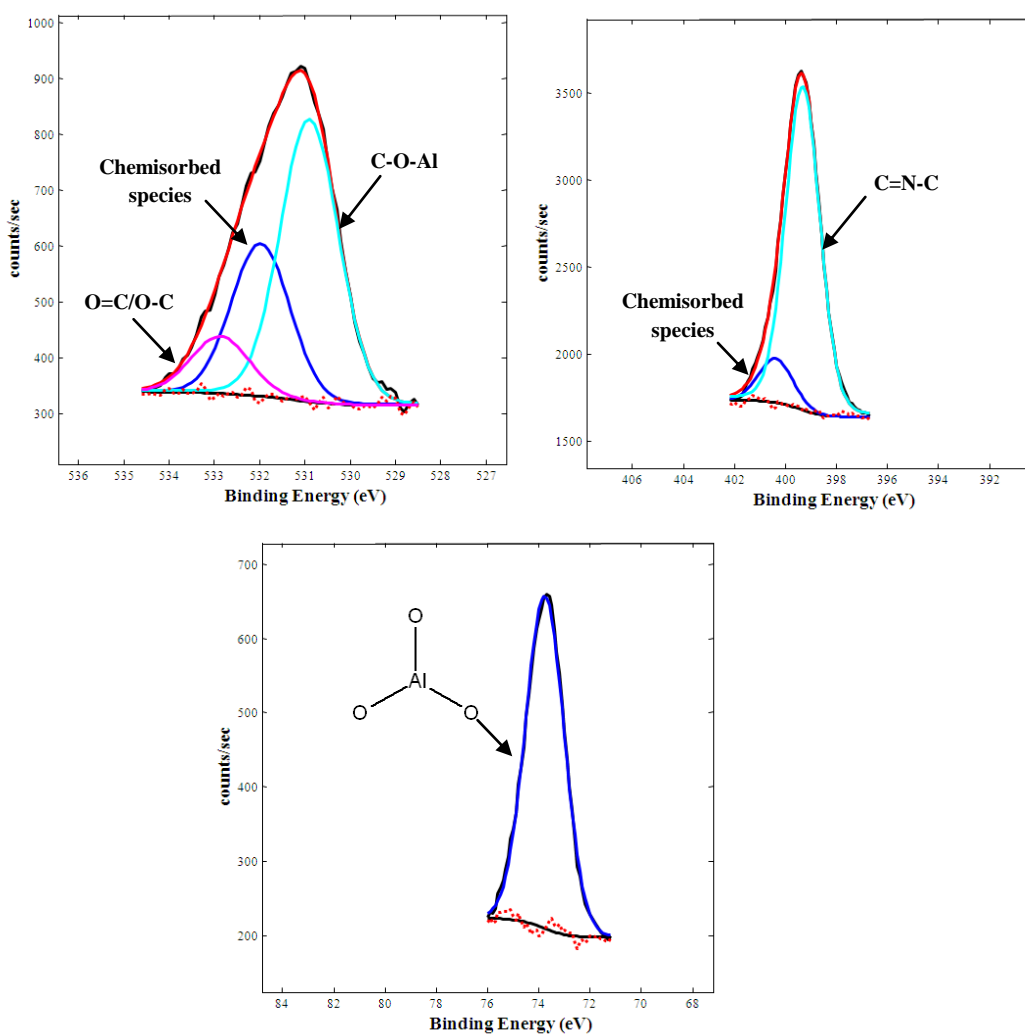


**Figure 8: High resolution XPS peaks of the degraded Alq<sub>3</sub> sample.**

Rosseli [3] proposed that four different products (P2 – P5) can form when the phenoxide ring ruptures during degradation (figure 2). Peak fittings were done on the C1s peak of the degraded sample for all four these products and are shown in figure 9-12. Each chemical state and the proportions in which it occurs in are summarized in table 2-5. This indicates that all four products can form during degradation.

**Table 2: Carbon bonds for degraded Alq<sub>3</sub> (P2)**

Bond number	Carbon bond	Number of bonds
1 (284.1 eV)	$\begin{array}{c} \text{O} = \text{C} - \text{C} \\   \\ \text{O} \end{array}$	6
2 (285.8 eV)	$\begin{array}{c} \text{HC} = \text{C} - \text{N} \\   \\ \text{C} \end{array}$	3
3 (283.8 eV)	$\begin{array}{c} \text{HC} - \text{C} - \text{CH} \\    \\ \text{C} \end{array}$	3
4 (285.0 eV)	$\begin{array}{c} \text{HC} = \text{C} - \text{C} \\   \\ \text{H} \end{array}$	12
5 (284.75 eV)	$\begin{array}{c} \text{HC} - \text{C} - \text{H} \\    \\ \text{N} \end{array}$	3

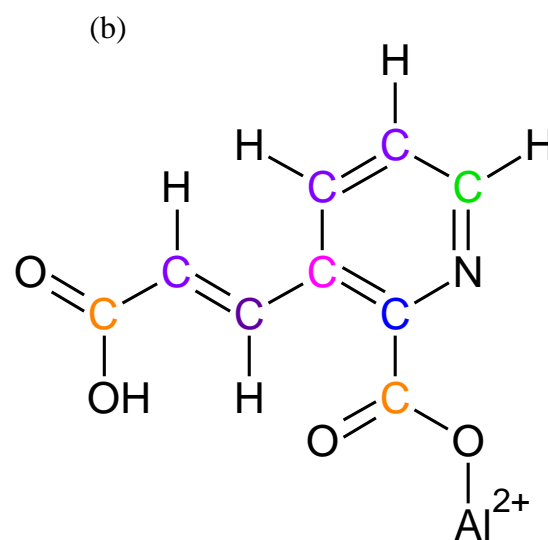
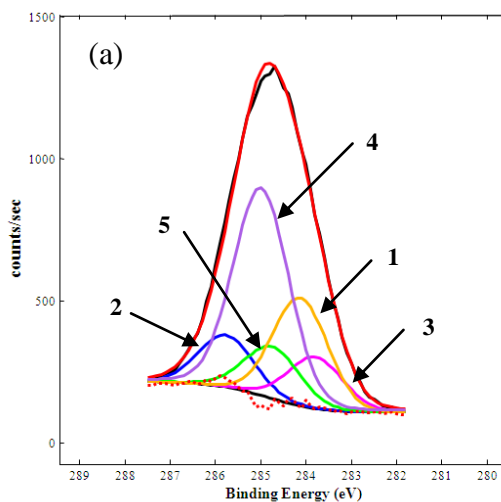


**Figure 9: (a) High resolution C1s XPS peak of P2 and (b) part of the degraded Alq<sub>3</sub> molecule (P2) showing the different carbon bonds.**

**Table 3: Carbon bonds for degraded Alq<sub>3</sub> (P3)**

Bond number	Carbon bond	Number of bonds
1 (284.2 eV)	$\begin{array}{c} \text{O} = \text{C} - \text{C} \\   \\ \text{H} \end{array}$	3
2 (285.0 eV)	$\begin{array}{c} \text{HC} = \text{C} - \text{C} \\   \\ \text{H} \end{array}$	12
3 (283.7 eV)	$\begin{array}{c} \text{HC} - \text{C} - \text{CH} \\    \\ \text{C} \end{array}$	3
4 (284.65 eV)	$\begin{array}{c} \text{HC} - \text{C} - \text{H} \\    \\ \text{N} \end{array}$	3
5 (285.8 eV)	$\begin{array}{c} \text{HC} = \text{C} - \text{N} \\   \\ \text{C} \end{array}$	3
6 (284.1 eV)	$\begin{array}{c} \text{O} = \text{C} - \text{C} \\   \\ \text{O} \end{array}$	3

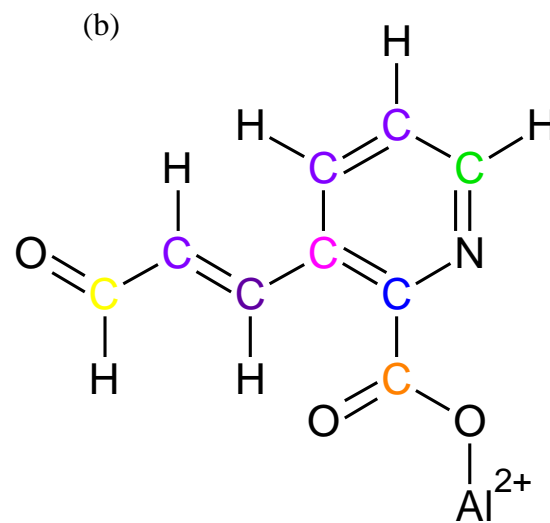
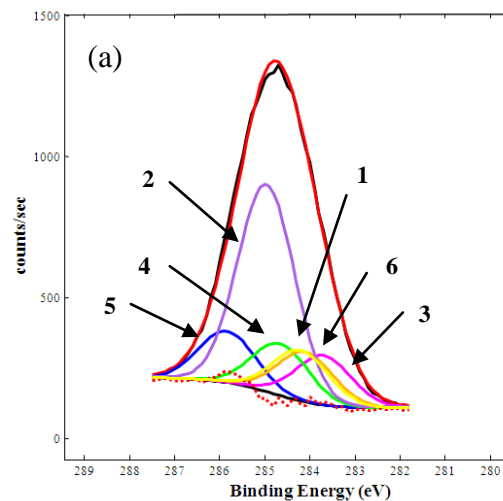


**Figure 10: (a) High resolution C1s XPS peak of P3 and (b) part of the degraded Alq<sub>3</sub> molecule (P3) showing the different carbon bonds.**

**Table 4: Carbon bonds for degraded Alq<sub>3</sub> (P4)**

Bond number	Carbon bond	Number of bonds
1 (284.3 eV)	$\begin{array}{c} \text{O} = \text{C} - \text{C} \\   \\ \text{O} \end{array}$	6
2 (285.8 eV)	$\begin{array}{c} \text{HC} = \text{C} - \text{N} \\   \\ \text{C} \end{array}$	3
3 (283.8 eV)	$\begin{array}{c} \text{HC} - \text{C} - \text{CH} \\    \\ \text{C} \end{array}$	3
4 (285.1 eV)	$\begin{array}{c} \text{HC} = \text{C} - \text{C} \\   \\ \text{H} \end{array}$	6
5 (284.7 eV)	$\begin{array}{c} \text{HC} - \text{C} - \text{H} \\    \\ \text{N} \end{array}$	3

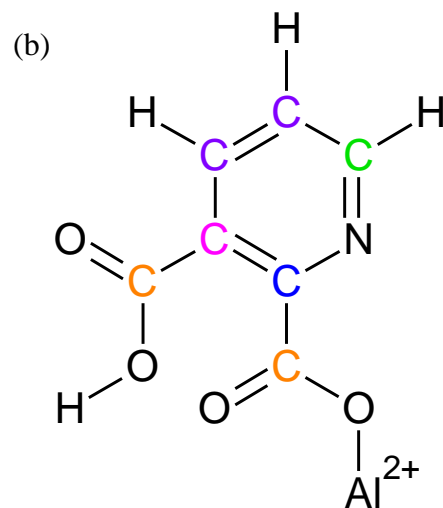
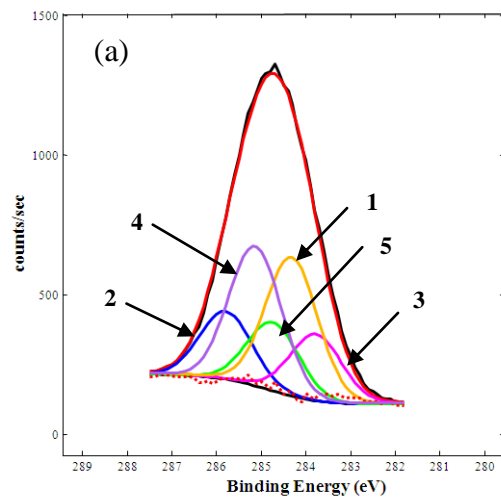
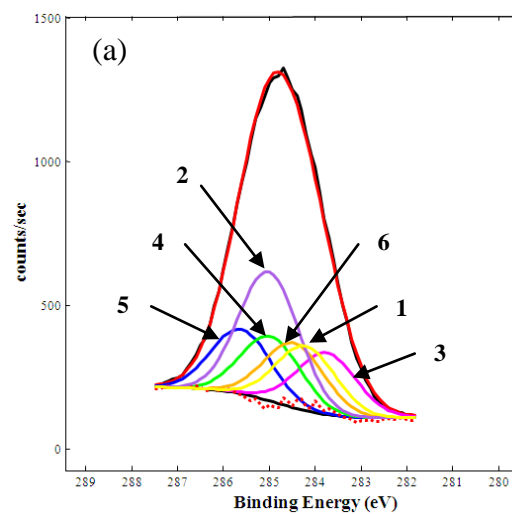


**Figure 11: (a) High resolution C1s XPS peak of P4 and (b) part of the degraded Alq<sub>3</sub> molecule (P4) showing the different carbon bonds.**

**Table 5: Carbon bonds for degraded Alq<sub>3</sub> (P5)**

Bond number	Carbon bond	Number of bonds
1 (284.2 eV)	$\begin{array}{c} \text{O} = \text{C} - \text{C} \\   \\ \text{H} \end{array}$	3
2 (285.0 eV)	$\begin{array}{c} \text{HC} = \text{C} - \text{C} \\   \\ \text{H} \end{array}$	6
3 (283.8 eV)	$\begin{array}{c} \text{HC} - \text{C} - \text{CH} \\    \\ \text{C} \end{array}$	3
4 (286.0 eV)	$\begin{array}{c} \text{HC} - \text{C} - \text{H} \\    \\ \text{N} \end{array}$	3
5 (285.6 eV)	$\begin{array}{c} \text{HC} = \text{C} - \text{N} \\   \\ \text{C} \end{array}$	3
6 (284.5 eV)	$\begin{array}{c} \text{O} = \text{C} - \text{C} \\   \\ \text{O} \end{array}$	3



(b)

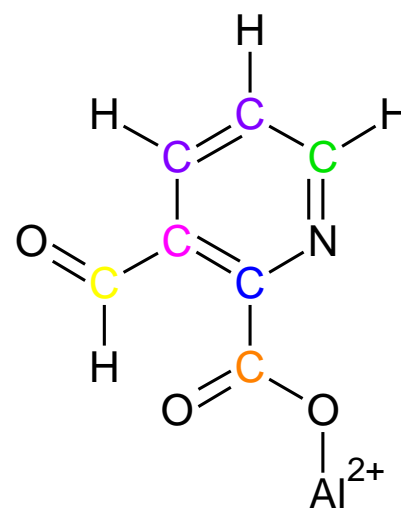


**Figure 12: (a) High resolution C1s XPS peak of P5 and (b) part of the degraded Alq<sub>3</sub> molecule (P5) showing the different carbon bonds.**

### 3. Photon degradation of Znq<sub>2</sub>

In this part of the study we have replaced the Al with Zn to form Znq<sub>2</sub>. It has been reported that Znq<sub>2</sub> has shown advantages over Alq<sub>3</sub> in electron transport and higher quantum yields in device performance which would result in lower operating voltages [11]. We investigated the effect of photon degradation on Znq<sub>2</sub> and compared it to Alq<sub>3</sub>.

#### 3.1 General characterization of Znq<sub>2</sub>

Znq<sub>2</sub> was prepared with the same method as Alq<sub>3</sub>, but the Al ion was substituted with Zn<sup>2+</sup> ions. The molecular structure of Znq<sub>2</sub> is shown in figure 13.

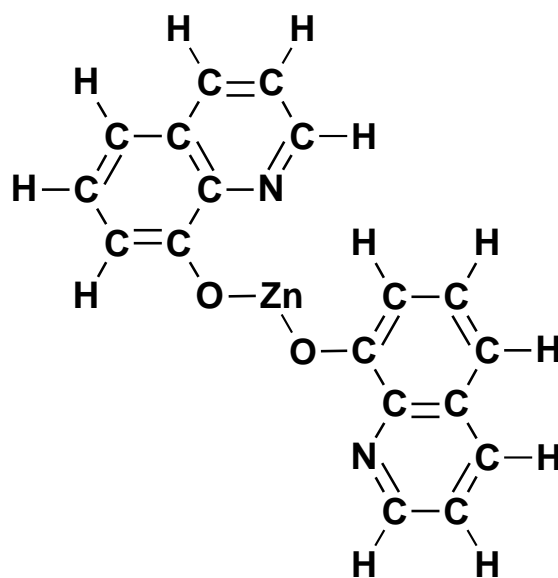
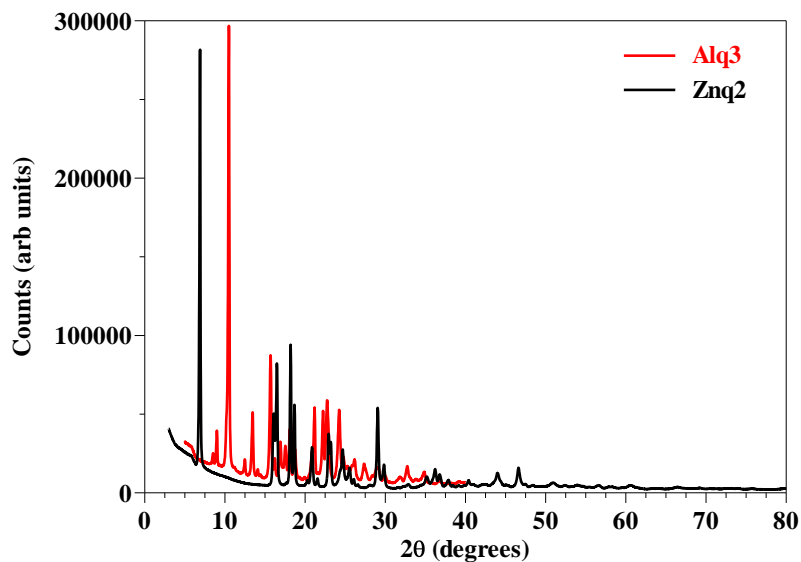


Figure 13: Molecular structure of Znq<sub>2</sub>.

XRD measurements were performed on the Znq<sub>2</sub> sample and the results were compared to that obtained for Alq<sub>3</sub> (figure 14). It can be seen that the crystal structure of the two samples are not the same. The main reason for this is that Znq<sub>2</sub> only has two quinoline rings compared to the three of Alq<sub>3</sub>. The main diffraction peaks of Znq<sub>2</sub> occurs at  $2\theta = 6.96^\circ$ ,  $16.5^\circ$ ,  $18.26^\circ$ ,  $21.0^\circ$ ,  $23.5^\circ$ , and  $28.96^\circ$ . The peaks can be indexed to be the Znq<sub>2</sub>.2H<sub>2</sub>O crystal form of bis(8-hydroxyquinoline) zinc [12,13].



**Figure 14: XRD spectrum of Alq<sub>3</sub> and Znq<sub>2</sub>.**

Figure 15 shows the PL spectra of Alq<sub>3</sub> and Znq<sub>2</sub> excited at 330 nm. According to Shukla et al. [13] Znq<sub>2</sub> will crystallize in two different forms. Znq<sub>2</sub>·2H<sub>2</sub>O will form at room temperature, while (Znq<sub>2</sub>)<sub>4</sub> will form at temperatures of 135 °C or higher. The PL spectrum of (Znq<sub>2</sub>)<sub>4</sub> shows a peak at 542 nm whereas the PL spectrum of Znq<sub>2</sub>·2H<sub>2</sub>O shows a PL peak at 506 nm. This indicates that the HOMO-LUMO gap in Znq<sub>2</sub>·2H<sub>2</sub>O is broader [13]. As can be seen from figure 15, the synthesized Znq<sub>2</sub> PL peak has a maximum at 506 nm, indicating that the Znq<sub>2</sub>·2H<sub>2</sub>O crystal form of Znq<sub>2</sub> formed during synthesis. The synthesis was also performed at room temperature, confirming that Znq<sub>2</sub>·2H<sub>2</sub>O had formed during synthesis. It is also noted that the PL intensity of Znq<sub>2</sub> is also 2 times higher than that of Alq<sub>3</sub>.

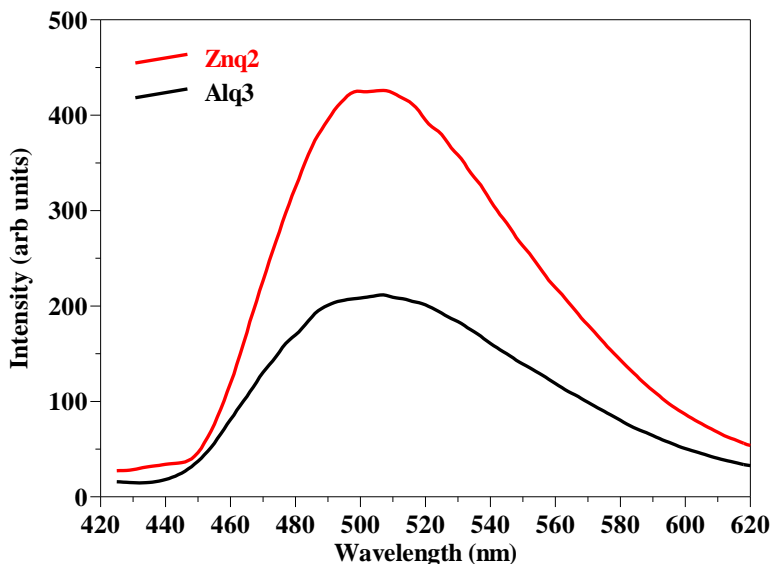


**Figure 15: PL spectra of Znq<sub>2</sub> and Alq<sub>3</sub>.**

### 3.2 UV exposure

Figure 16 (a) shows the normalized PL intensity of Znq<sub>2</sub> and Alq<sub>3</sub> during the ~ 400 hours of UV exposure. Both bands show a decrease in intensity with time. A decrease of ~ 80% is observed for the Alq<sub>3</sub> band while a decrease of only ~ 30% is observed for the Znq<sub>2</sub> band. This indicates that the Znq<sub>2</sub> sample is more stable during photon degradation. This might be due to the fact that Znq<sub>2</sub> only has two quinoline ligands compared to the three of Alq<sub>3</sub>. From figure 16 (b) it can be seen that the luminescence intensity decreases rapidly (~ 10%) in the first few hours after exposure, but slows down for longer exposure times.

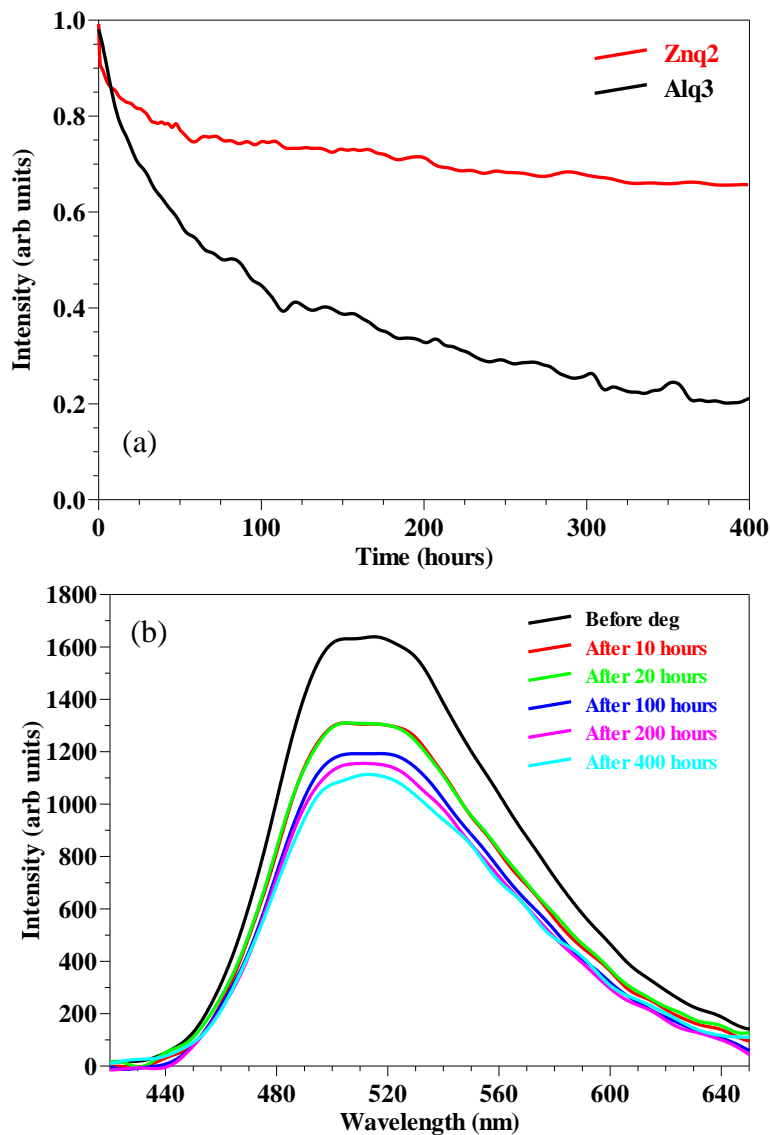


**Figure 16: Degradation of Znq<sub>2</sub> under UV exposure ( $\lambda = 365$  nm). (a) Quenching of luminescence with time and (b) evolution of the emission band with time.**

### 3.3 XPS measurements.

XPS measurements were done on the as-prepared and degraded samples of Znq<sub>2</sub>. Figure 17 shows the high resolution XPS spectra of the as-prepared sample. The Zn2p peak consists of two peaks at 1021.5 eV and 1044.6 eV. These peaks are attributed to the O-Zn-O bond. The O1s peak consists of two peaks. The one at 530.9 eV is attributed to the C-O-Zn bond and the one at 532.2 eV is attributed to chemisorbed species. Only one peak is observed for N1s at 399.3 eV and this peak is attributed to the C-N=N bond.

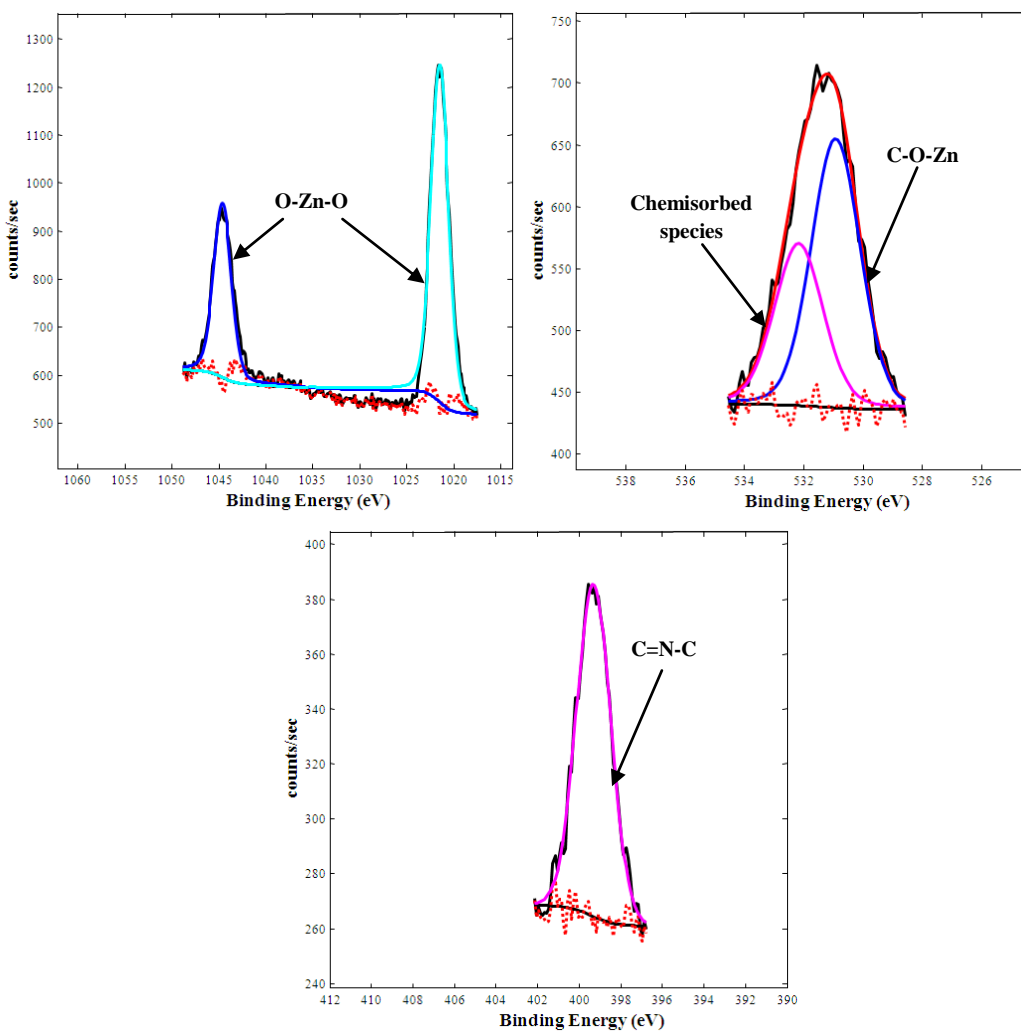


**Figure 17: High resolution XPS peaks of the as-prepared Znq<sub>2</sub> sample.**

Figure 18 (a) shows the high resolution C1s XPS peak of the as-prepared Znq<sub>2</sub> sample. Carbon appears in Znq<sub>2</sub> in five chemical environments (figure 18(b)) resulting in five identifiable binding energies for the C1s transition. Each chemical state and the proportions it occurs in are summarized in table 6. The sixth peak is attributed to chemisorbed species like CO and CO<sub>2</sub>.

**Table 6: Carbon bonds for as-prepared Znq<sub>2</sub>.**

Bond number	Carbon bond	Number of bonds
1 (284.7 eV)	$\begin{array}{c} \text{HC} = \text{C} - \text{CH}_2 \\   \\ \text{O} \end{array}$	2
2 (284.95 eV)	$\begin{array}{c} \text{HC} = \text{C} - \text{C} \\   \\ \text{H} \end{array}$	10
3 (283.4 eV)	$\begin{array}{c} \text{HC} - \text{C} - \text{CH} \\    \\ \text{C} \end{array}$	2
4 (285.3 eV)	$\begin{array}{c} \text{HC} - \text{C} - \text{H} \\    \\ \text{N} \end{array}$	2
5 (285.8 eV)	$\begin{array}{c} \text{HC} = \text{C} - \text{N} \\   \\ \text{C} \end{array}$	2
6 (284.1 eV)	Chemisorbed C	

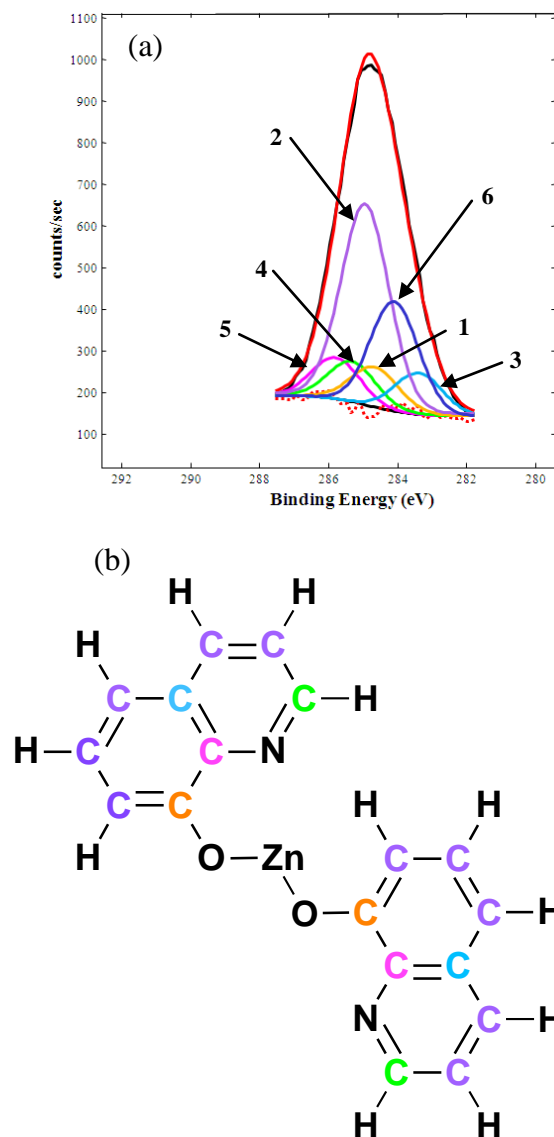


**Figure 18: (a) High resolution C1s XPS peak of as-prepared Znq<sub>2</sub> and (b) the as-prepared Znq<sub>2</sub> molecule showing the different carbon bonds.**

The as-prepared sample was sputtered for 2 minutes at a rate of 27 nm/min to remove any dirt (like C, O and N species) on the surface. High resolution XPS scans were done after sputtering. Figure 19 shows the difference in the high resolution peaks (red – before sputter and blue – after sputter). A slight shift and increase in intensity in the Zn2p peak was observed. The O1s peak's

intensity decreased and is not as broad as the peak before sputtering. No change was observed for the N1s peak. The C1s peak's intensity also increased and the peak was broader than the peak before sputtering.

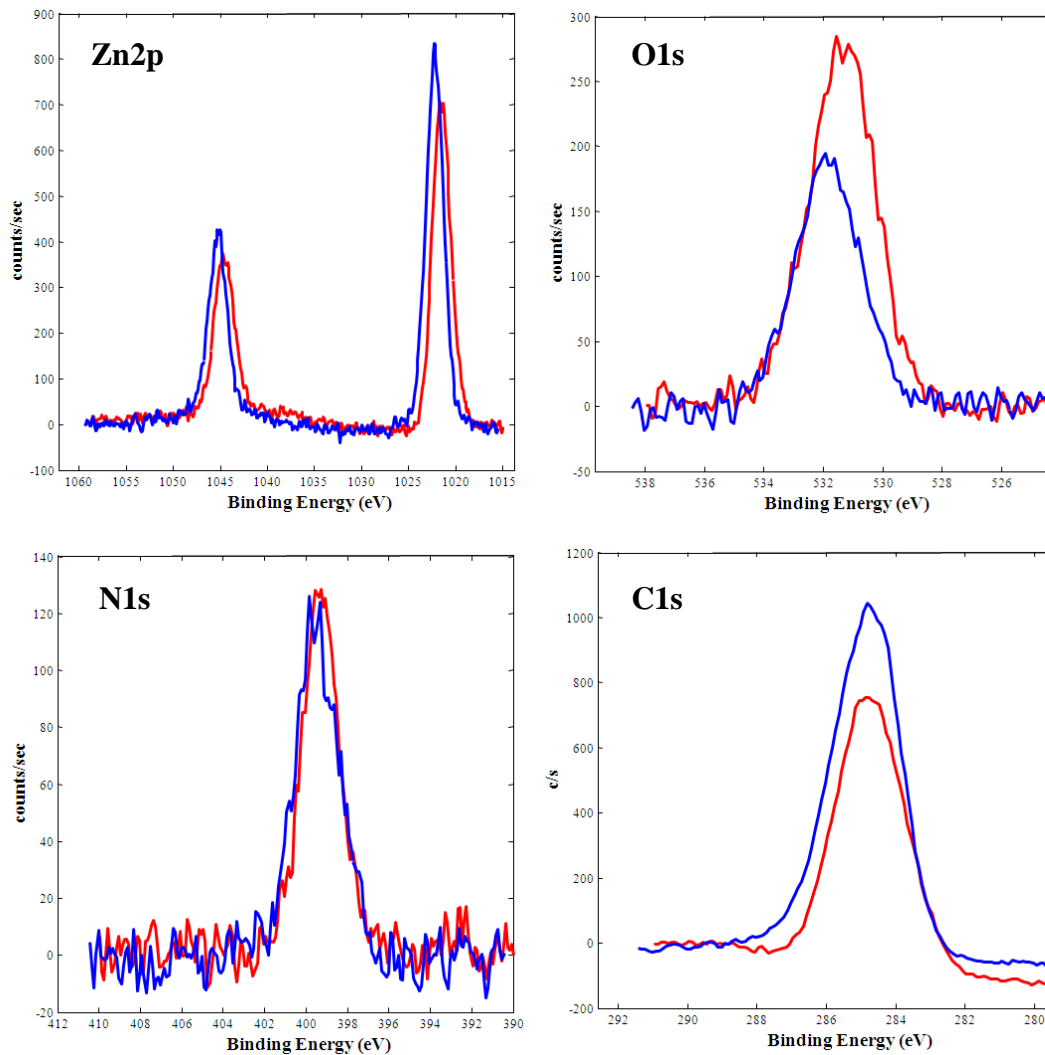


**Figure 19: Comparison of the high resolution XPS peaks of Znq<sub>2</sub> before (red) and after (blue) sputtering.**

Figure 20 shows the fitted high resolution peaks of the sputtered Znq<sub>2</sub> sample. The peaks fitted for the Zn2p peak at 1022.2 eV and 1045.3 eV is attributed to the O-Zn-O bond. Two peaks are fitted for the O1s peak. The peak at 531.2 eV is attributed to the C-O-Zn peak and the one at 532.3 is due to chemisorbed species. One peak is fitted for the N1s peak at 399.35 eV and is

attributed to the C-N=C bond. Carbon still appears in five chemical environments in the sputtered sample and is summarized in table 7. The amount of chemisorbed C species has decreased as is expected from a sputtered sample.

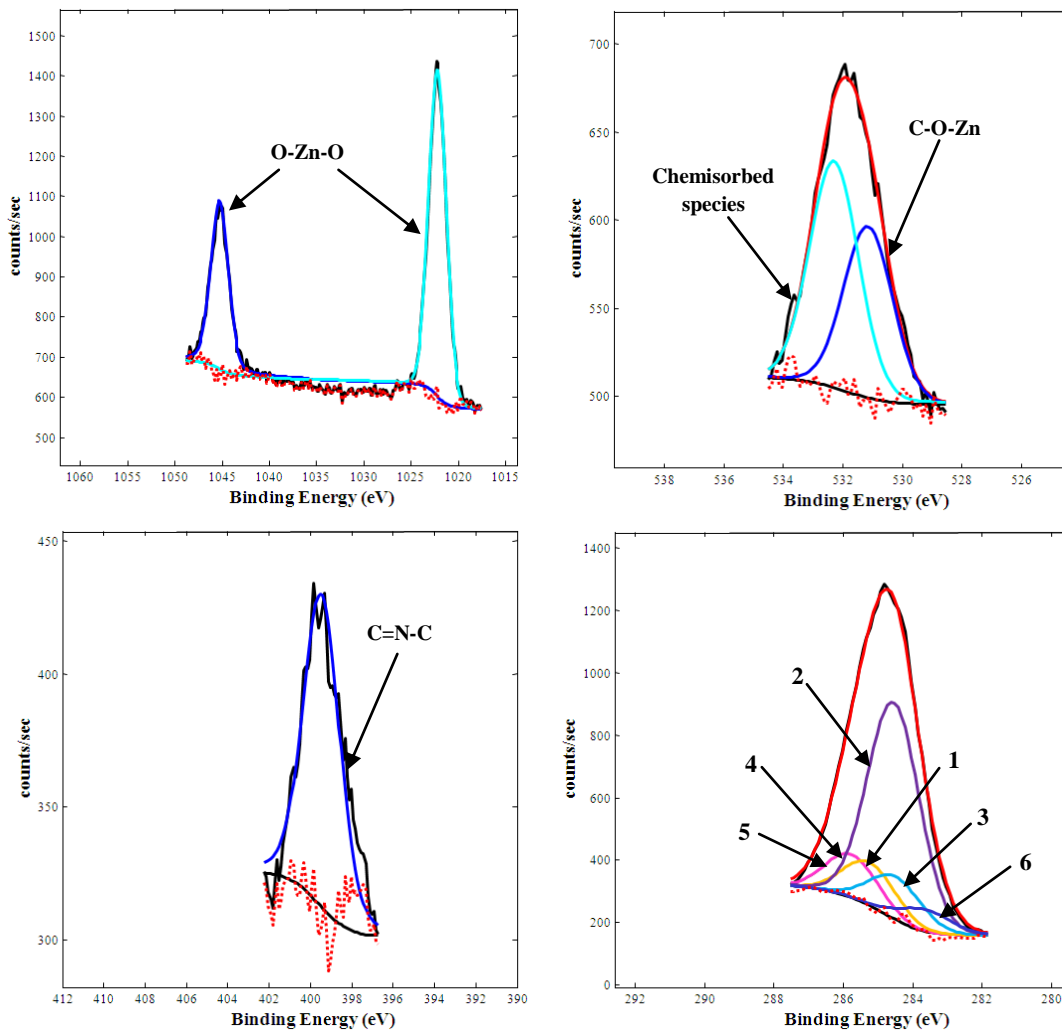


**Figure 20: High resolution XPS peaks of the sputtered as-prepared Znq<sub>2</sub> sample.**

**Table 7: Carbon bonds for sputtered as-prepared Znq<sub>2</sub>.**

Bond number	Carbon bond	Number of bonds
1 (285.2 eV)	$\text{HC} = \text{C} - \text{CH}_2$ $ $ $\text{O}$	2
2 (284.55 eV)	$\text{HC} = \text{C} - \text{C}$ $ $ $\text{H}$	10
3 (284.5 eV)	$\text{HC} - \text{C} - \text{CH}$ $  $ $\text{C}$	2
4 (285.7 eV)	$\text{HC} - \text{C} - \text{H}$ $  $ $\text{N}$	2
5 (285.8 eV)	$\text{HC} = \text{C} - \text{N}$ $ $ $\text{C}$	2
6 (283.6 eV)	Chemisorbed C	

Figure 21 shows the difference in the high resolution peaks of the as-prepared (red) and degraded (blue) Znq<sub>2</sub> samples. The Zn2p peaks show a slight increase in intensity, while the peak positions stay the same. The O1s peak has shifted toward lower energies and has also increased in intensity. The N1s peak has stayed at the same position, with an increase in intensity, while a slight shift can be observed in the C1s peak. The fact that there is almost no change in the Zn and

N peaks is an indication that the Zn-O and C-N=C bonds have stayed intact, while the change in the O and C peaks is an indication that the phenoxide ring broke during degradation.

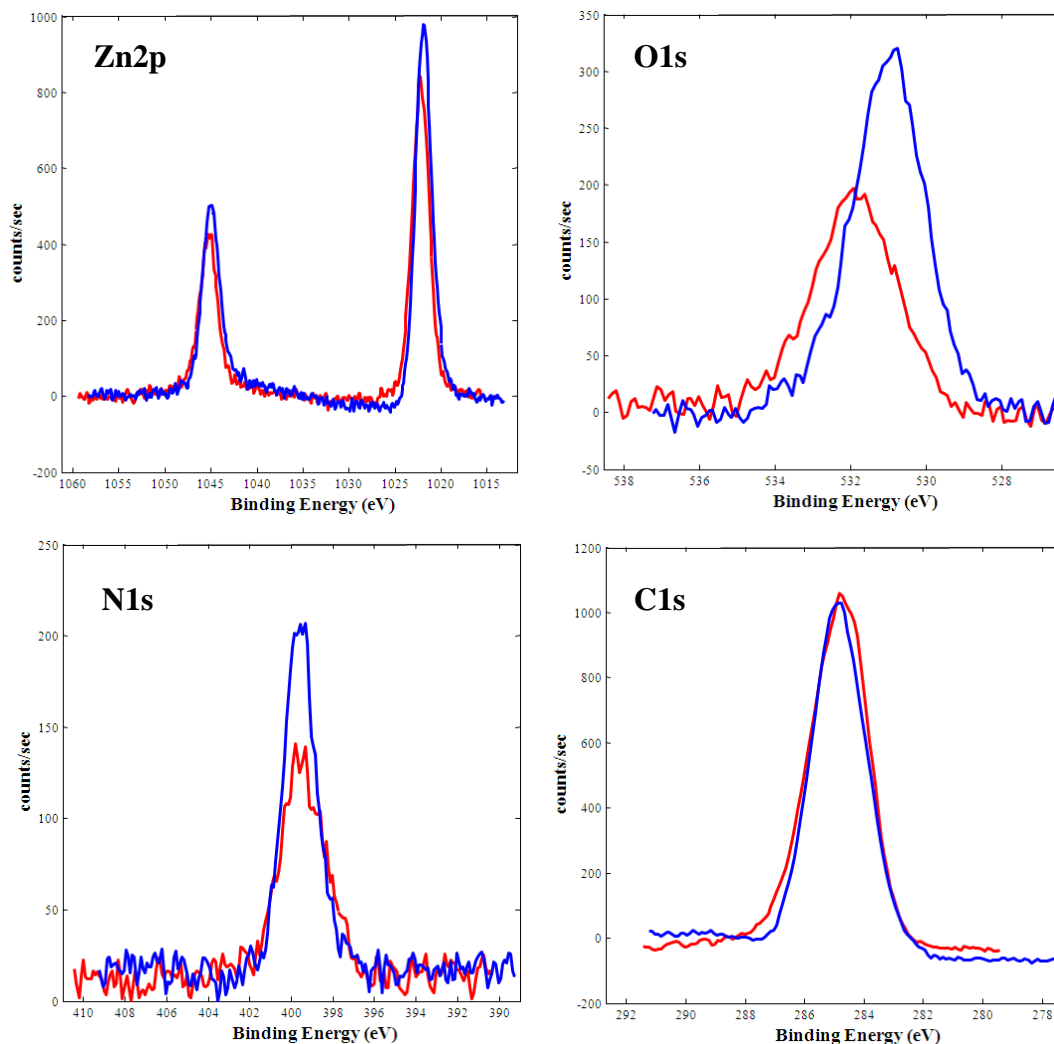


**Figure 21: Comparison of the high resolution XPS peaks of Znq<sub>2</sub> before (red) and after (blue) degradation.**

Figure 22 shows the fitted XPS peaks of the high resolution scans of Zn2p, O1s and N1s. The fitted peaks for Zn2p at 1021.9 eV and 1045.0 eV correspond to the O-Zn-O bond. Three peaks are fitted for the O1s peak. The peak at 530.8 eV corresponds to the C-O-Zn bond and the one at 531.5 eV is attributed to chemisorbed species [9]. The intensity of the C-O-Zn is higher than that of the chemisorbed species, indicating that most of the chemisorbed species have left the surface. The third peak at 532.8 eV is attributed to the carbonyl and methoxy O1s species that are present in

the degraded products [10]. Only one peak is fitted for the N1s peak at 399.6 and it corresponds to the C-N=C bond.

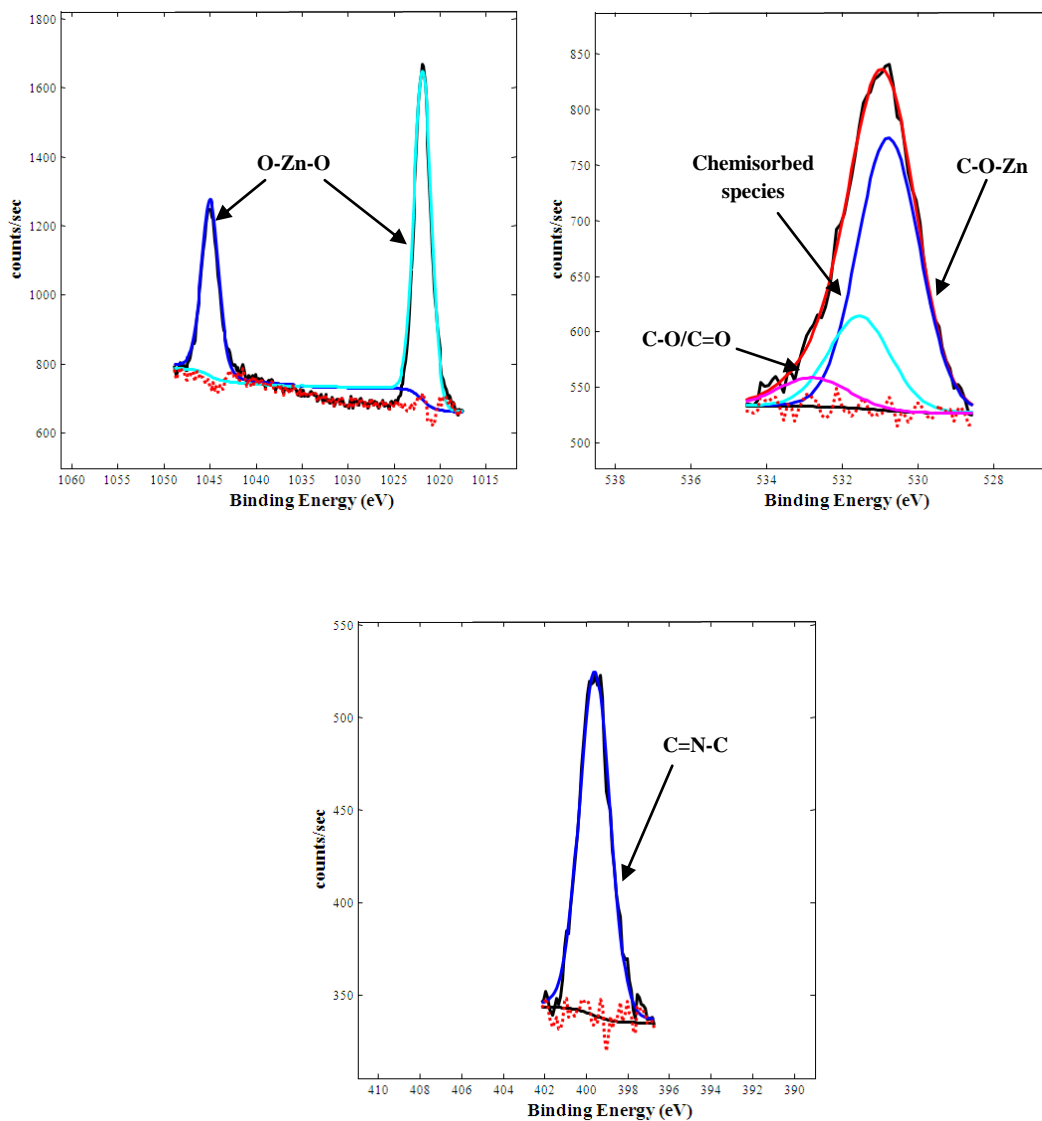


**Figure 22: High resolution XPS peaks of the degraded Znq<sub>2</sub> sample.**

Degraded Znq<sub>2</sub> can also form the four degraded products (P2 - P5) proposed by Rosseli [3] when the phenoxide ring ruptures. Figure 23 – 26 shows the fitted carbon peaks of these four products.

**Table 8: Carbon bonds for degraded Znq<sub>2</sub> (P2)**

Bond number	Carbon bond	Number of bonds
1 (283.9 eV)	$\begin{array}{c} \text{O} = \text{C} - \text{C} \\   \\ \text{O} \end{array}$	4
2 (285.75 eV)	$\begin{array}{c} \text{HC} = \text{C} - \text{N} \\   \\ \text{C} \end{array}$	2
3 (284.7 eV)	$\begin{array}{c} \text{HC} - \text{C} - \text{CH} \\    \\ \text{C} \end{array}$	2
4 (284.9 eV)	$\begin{array}{c} \text{HC} = \text{C} - \text{C} \\   \\ \text{H} \end{array}$	8
5 (284.5 eV)	$\begin{array}{c} \text{HC} - \text{C} - \text{H} \\    \\ \text{N} \end{array}$	2

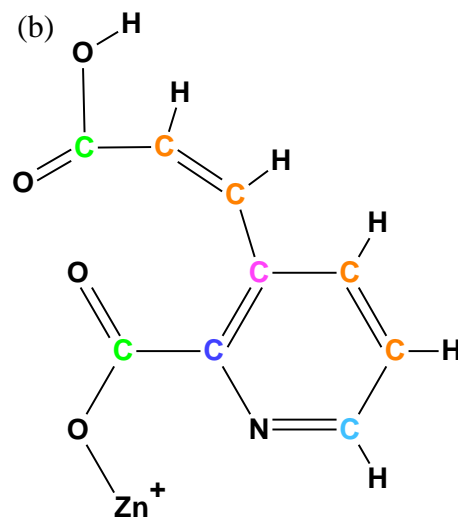
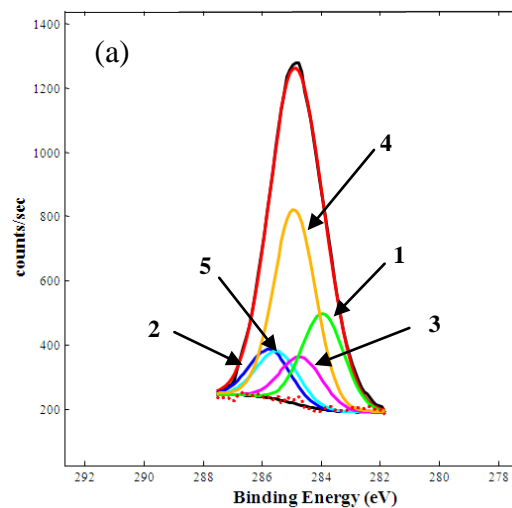


**Figure 23: (a) High resolution C1s XPS peak of P2 and (b) part of the degraded Znq<sub>2</sub> molecule (P2) showing the different carbon bonds.**

**Table 9: Carbon bonds for degraded Znq<sub>2</sub> (P3)**

Bond number	Carbon bond	Number of bonds
1 (284.2 eV)	$\begin{array}{c} \text{O} = \text{C} - \text{C} \\   \\ \text{H} \end{array}$	2
2 (284.8 eV)	$\begin{array}{c} \text{HC} = \text{C} - \text{C} \\   \\ \text{H} \end{array}$	8
3 (284.85 eV)	$\begin{array}{c} \text{HC} - \text{C} - \text{CH} \\    \\ \text{C} \end{array}$	2
4 (285.5 eV)	$\begin{array}{c} \text{HC} - \text{C} - \text{H} \\    \\ \text{N} \end{array}$	2
5 (285.9 eV)	$\begin{array}{c} \text{HC} = \text{C} - \text{N} \\   \\ \text{C} \end{array}$	2
6 (283.7 eV)	$\begin{array}{c} \text{O} = \text{C} - \text{C} \\   \\ \text{O} \end{array}$	2

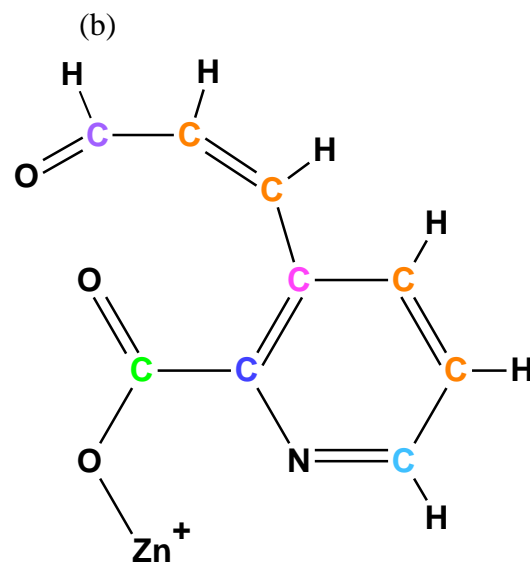
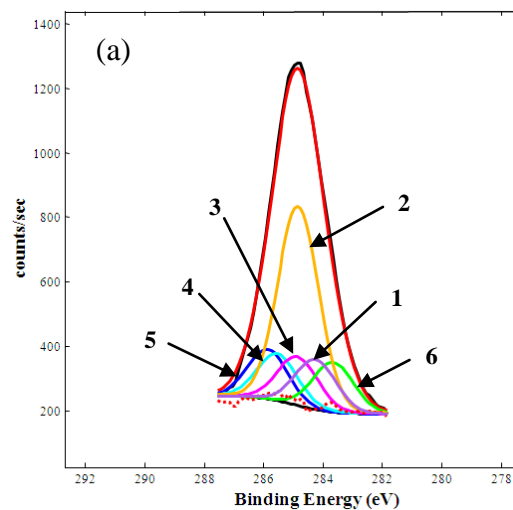


**Figure 24: (a) High resolution C1s XPS peak of P3 and (b) part of the degraded Znq<sub>2</sub> molecule (P3) showing the different carbon bonds.**

**Table 10: Carbon bonds for degraded Znq<sub>2</sub> (P4)**

Bond number	Carbon bond	Number of bonds
1 (285.0 eV)	$\begin{array}{c} \text{O} = \text{C} - \text{C} \\   \\ \text{O} \end{array}$	4
2 (285.8 eV)	$\begin{array}{c} \text{HC} = \text{C} - \text{N} \\   \\ \text{C} \end{array}$	2
3 (283.8 eV)	$\begin{array}{c} \text{HC} - \text{C} - \text{CH} \\    \\ \text{C} \end{array}$	2
4 (284.45 eV)	$\begin{array}{c} \text{HC} = \text{C} - \text{C} \\   \\ \text{H} \end{array}$	4
5 (285.3 eV)	$\begin{array}{c} \text{HC} - \text{C} - \text{H} \\    \\ \text{N} \end{array}$	2

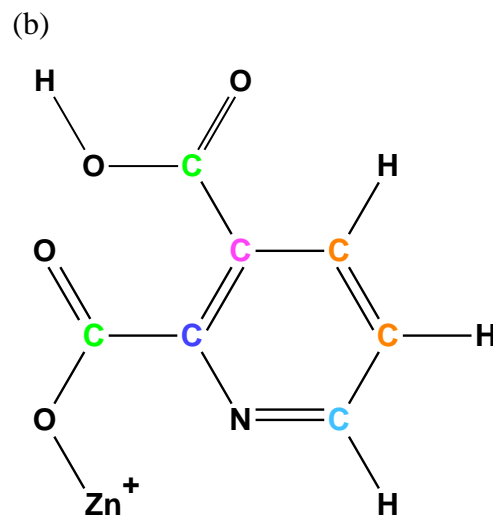
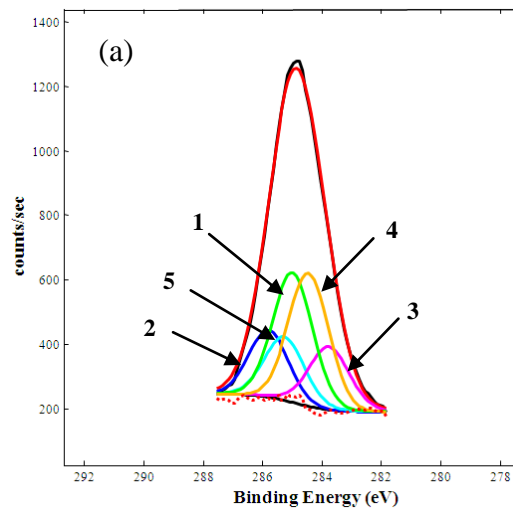


**Figure 25: (a) High resolution C1s XPS peak of P4 and (b) part of the degraded Znq<sub>2</sub> molecule (P4) showing the different carbon bonds.**

**Table 11: Carbon bonds for degraded Znq<sub>2</sub> (P5)**

Bond number	Carbon bond	Number of bonds
1 (284.8 eV)	$\begin{array}{c} \text{O} = \text{C} - \text{C} \\   \\ \text{H} \end{array}$	2
2 (284.9 eV)	$\begin{array}{c} \text{HC} = \text{C} - \text{C} \\   \\ \text{H} \end{array}$	4
3 (283.7 eV)	$\begin{array}{c} \text{HC} - \text{C} - \text{CH} \\    \\ \text{C} \end{array}$	2
4 (285.2 eV)	$\begin{array}{c} \text{HC} - \text{C} - \text{H} \\    \\ \text{N} \end{array}$	2
5 (285.8 eV)	$\begin{array}{c} \text{HC} = \text{C} - \text{N} \\   \\ \text{C} \end{array}$	2
6 (284.4 eV)	$\begin{array}{c} \text{O} = \text{C} - \text{C} \\   \\ \text{O} \end{array}$	2

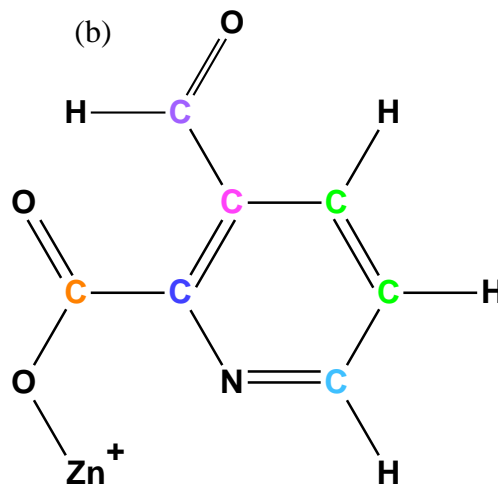
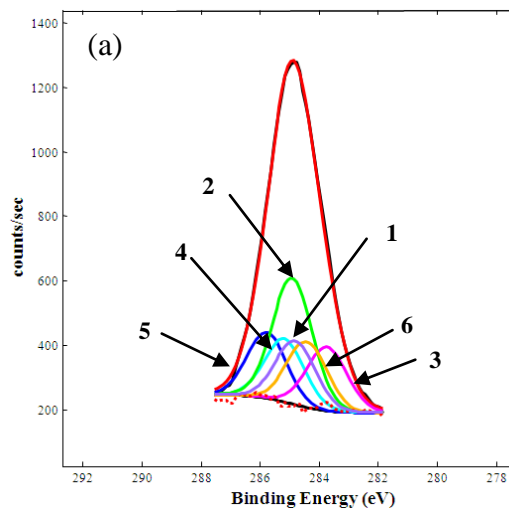


**Figure 26: (a) High resolution C1s XPS peak of P5 and (b) part of the degraded Znq<sub>2</sub> molecule (P5) showing the different carbon bonds.**

#### 4. The effect of SiO<sub>2</sub> encapsulation on the degradation of Alq<sub>3</sub>.

Alq<sub>3</sub> was encapsulated with SiO<sub>2</sub> as described in chapter 5. Freshly prepared Alq<sub>3</sub>:SiO<sub>2</sub> showed a higher PL intensity than as-prepared Alq<sub>3</sub>. The Alq<sub>3</sub>:SiO<sub>2</sub> powder sample was exposed to 365 nm UV light and the change in intensity of the PL peak at 520 nm was monitored over time. The evolution of the PL peak with time is shown in figure 27 (a) and figures 27 (b) shows how the PL intensity decreased with time. It can be seen that the intensity decreased rapidly and after 10 hours it had decreased by 50%. It continued to decrease and after 120 hours the intensity was barely detected by the spectrometer. Reisfeld et al. [14] reported the same behaviour in Alq<sub>3</sub>/SiO<sub>2</sub> thin films and proposed that the SiO<sub>2</sub> shell decompose during UV exposure into Si and O<sub>2</sub> species. Alq<sub>3</sub> reacts with the O<sub>2</sub> species, causing the phenoxide ring to rupture. Non-luminescent molecules were formed.

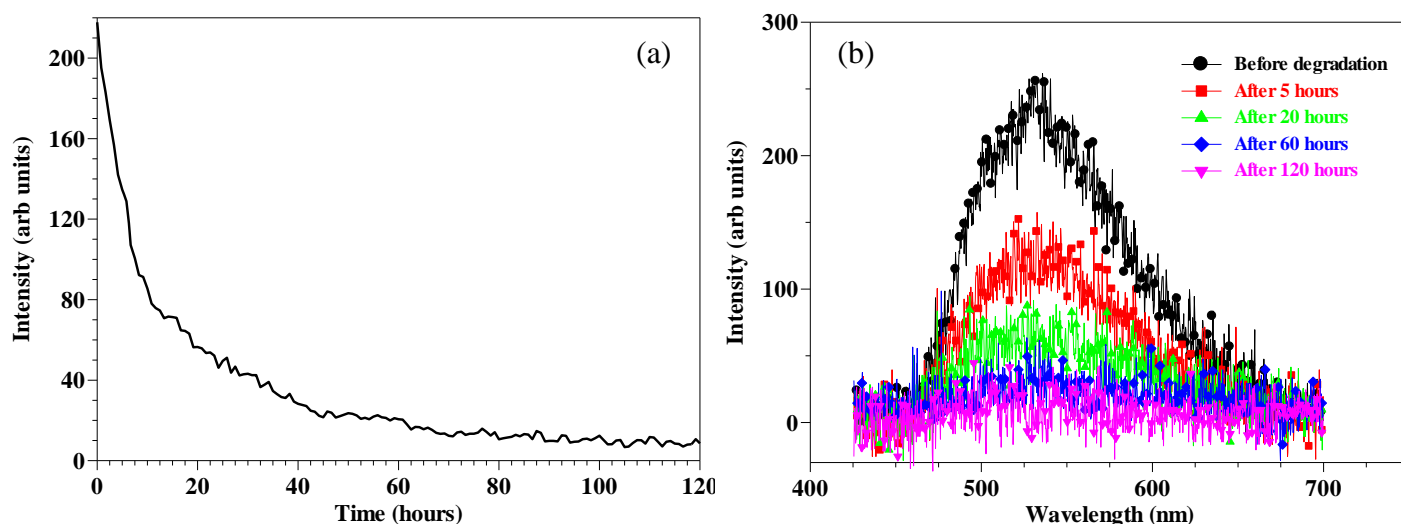


**Figure 27: Degradation of Alq<sub>3</sub>:SiO<sub>2</sub> under UV exposure ( $\lambda = 365$  nm). (a) Evolution of the emission band with time and (b) PL intensity versus time.**

#### 5. Effect of PMMA on the degradation of Alq<sub>3</sub>.

A PMMA thin film that was mixed with 1% of Alq<sub>3</sub> was exposed to UV light for 400 hours. Figure 28 shows the decrease in luminescence intensity with exposure time. A rapid decrease in intensity of 70 % is observed for the first 80 hours of exposure. After that there is only a slight

decrease in the intensity and for the last 100 hours the intensity is almost stable. Wochnowski et al. [15] showed that PMMA that was subjected to UV illumination degraded into  $\text{CO}_2$ ,  $\text{CH}_4$ ,  $\text{CO}$  and  $\text{HOCH}_3$ . These groups might react with the phenoxide ring of the  $\text{Alq}_3$  causing it to degrade.

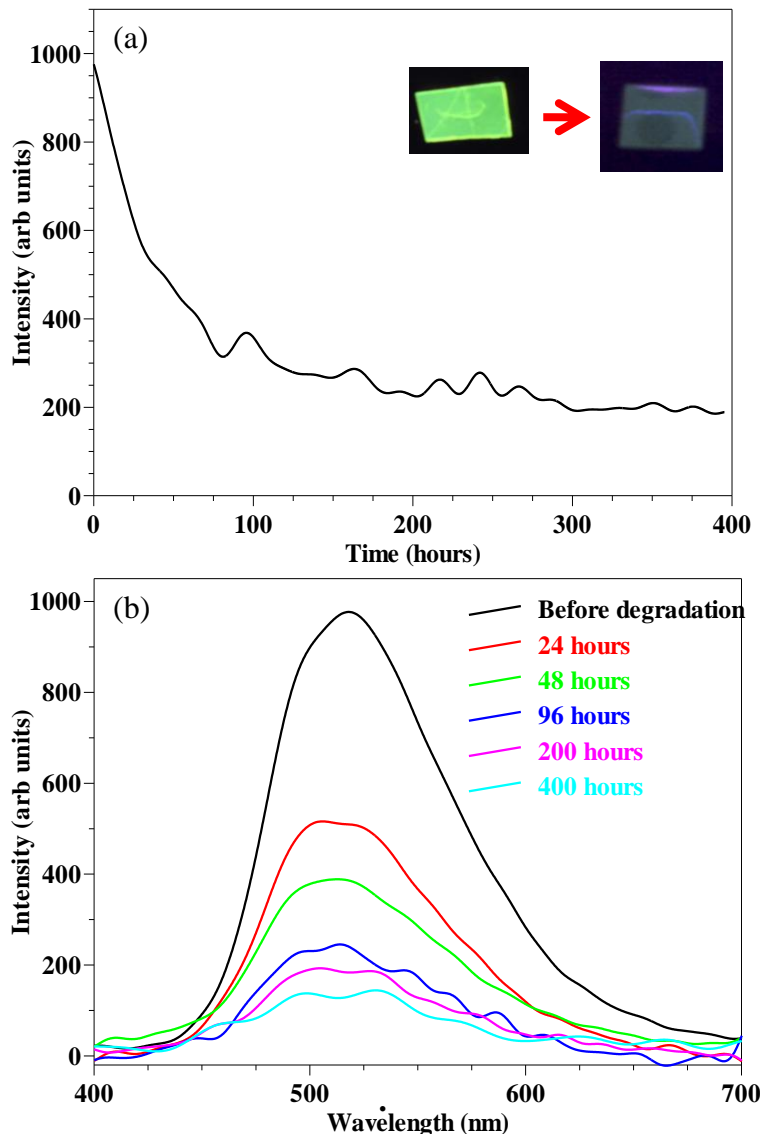


**Figure 28: Degradation of  $\text{Alq}_3$ :PMMA under 365 nm UV exposure.**

XPS was performed on the degraded sample and compared to the as-prepared films. The results of the high resolution XPS scans are shown in figure 29 (red – as prepared and blue - degraded). Peaks for  $\text{O}1s$ ,  $\text{N}1s$ ,  $\text{C}1s$  and  $\text{Al}2p$  are observed that correspond to  $\text{Alq}_3$  and PMMA. Two additional peaks for  $\text{Cl}2p$  and  $\text{Si}2p$  are observed. The  $\text{Si}2p$  peak is contributed to contamination inside the PMMA powder used to prepare the films and the  $\text{Cl}2p$  peak is due to trapped solvent

molecules (chloroform) inside the film. The N1s and Al2p peak's intensities are lower after degradation. This might be due to the degradation of the Alq<sub>3</sub> inside the PMMA film. The Cl2p peak is also lower showing that the trapped solvent molecules left the surface during degradation. This might be due to slight heating of the sample under the UV irradiation. The shape of the O1s peak changed and the intensity of the C1s peak is lower. Peak fitting was done to these peaks and compared with the as-prepared films (figure 30).

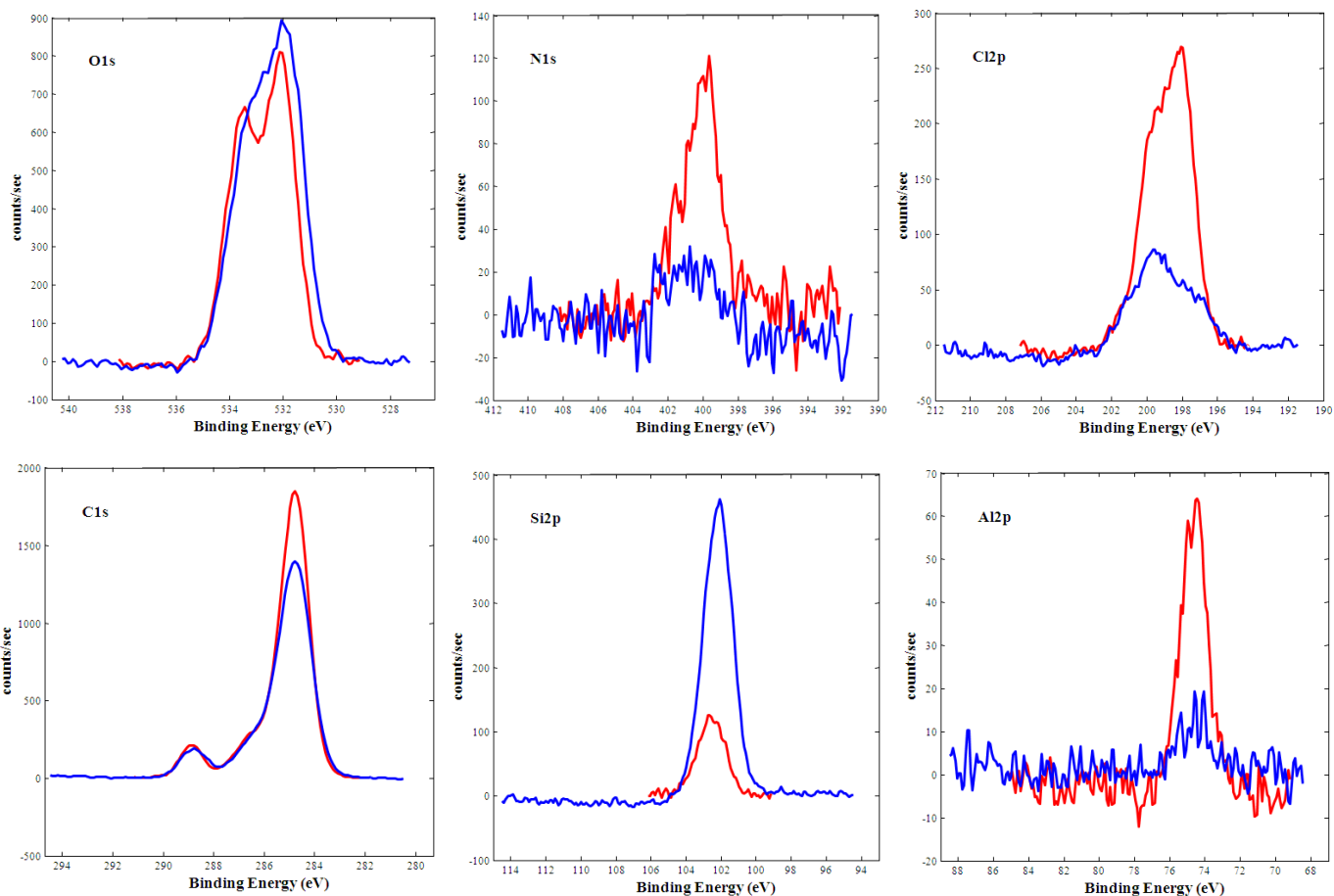


**Figure 29: High resolution XPS scans of as-prepared (red) and degraded (blue) Alq<sub>3</sub>:PMMA films.**

Figure 30 shows the fitted peaks for C1s and O1s before and after degradation. Four peaks are fitted for the as-prepared C1s and they correspond to the O-C=O (288.8 eV), C-O (286.7 eV), C-C (285.4 eV) and C-H (284.7 eV) bonds. The same four peaks are present in the degraded C1s

peak, but have shifted. The O-C=O, C-O and C-H bonds have shifted with 0.1 eV to 288.7 eV, 286.8 eV and 284.8 eV. The C-C peak has shifted by 0.7 eV to 286.1 eV. These shifts might be due to the existence of methyl radicals in the degraded film [15]. Three peaks are fitted for the as-prepared O1s peak at 532.1 eV (O-C=O) 533.40 eV (C-O-C) and 534.00 eV (chemisorbed species). For the degraded film the energy gap between the two oxygen peaks is very small and they have moved towards each other almost merging into one. This indicates the formation of carbon monoxide (CO – 531.75 eV) and carbon dioxide (CO<sub>2</sub> – 533.2 eV) during degradation [15].

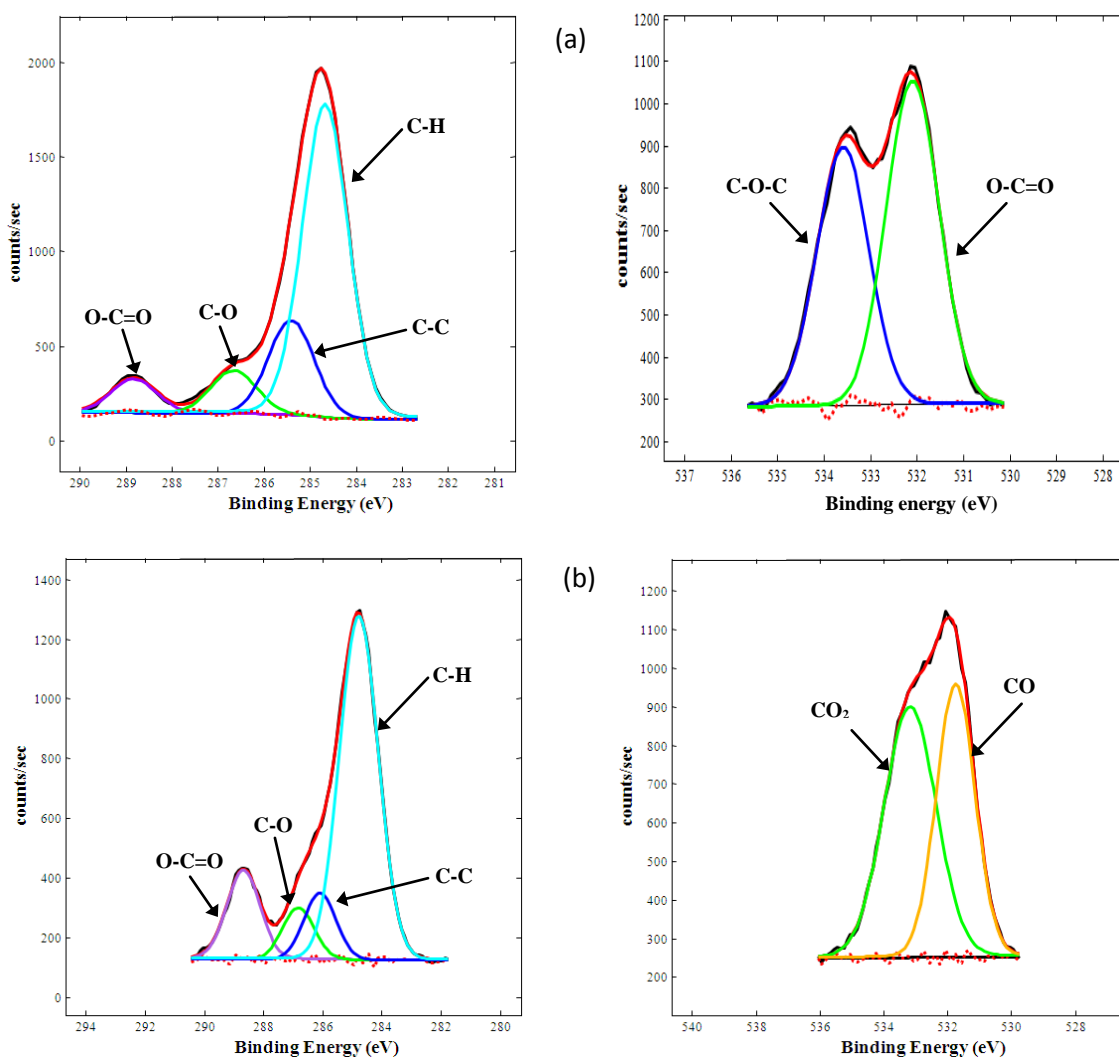


**Figure 30: Fitted XPS peaks of C1s and O1s before (a) and after (b) degradation.**

## 6. Effect of substituents on the phenoxide ring on the photon degradation.

$\text{Alq}_3$ , 5,7Me- $\text{Alq}_3$  and 5Cl- $\text{Alq}_3$  were synthesized as described in chapter 3. Figure 31 shows the normalized photon degradation curves for the three  $\text{Alq}_3$  samples. The spectra were obtained over a period of 24 hours of continuous photon irradiation. A decrease of 35% of the PL intensity was observed for the  $\text{Alq}_3$  sample and a decrease of 50% for the 5Cl- $\text{Alq}_3$  sample. In the case of the 5Cl- $\text{Alq}_3$  sample the PL intensity decreased rapidly at the beginning and reached one half of its original intensity after 4 hours and then the rate of decrease slowed down for longer exposure times. The samples were fully exposed to oxygen and moisture in the open air, which are known to destroy the molecular structure at the C-7 position [3, 6, 16-17]. In the case of 5,7Me- $\text{Alq}_3$  there was no decrease in the PL intensity. It is believed that the methyl group at position 7 protects the phenoxide ring from O and OH groups to form C=O, C-O-H and O=C-O-H bonds.

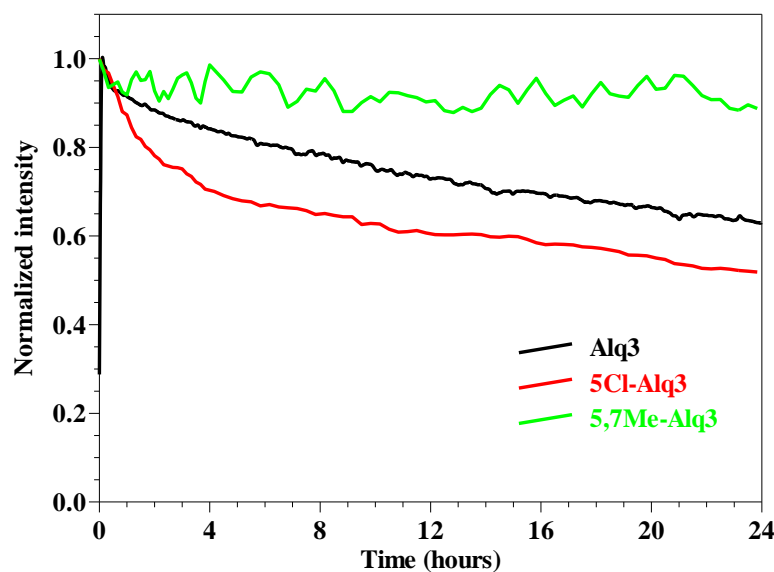


**Figure 31: Normalized photon degradation spectra of the three  $\text{Alq}_3$  compounds under UV exposure ( $\lambda = 365$  nm).**

## 7. Conclusion

Alq<sub>3</sub> powder was successfully synthesized using the co-precipitation method. Under prolonged UV exposure it was observed that the luminescence intensity decreased with time. This can be attributed to two degradation mechanisms. First oxygenation and ozonolysis, which form quenchers, cause dark spots to form on the surface. Secondly the Alq<sub>3</sub> powder reacts with H<sub>2</sub>O to form 8-Hq. The 8-Hq further reacts with O<sub>2</sub> to form a dark non-emissive polymer. Oxygenation and ozonolysis were most probably responsible for the fast degradation at the beginning, while the reaction with H<sub>2</sub>O would result in slower degradation rates with time. With time the whole sample would become non luminescent.

FTIR and XPS studies done on the degraded Alq<sub>3</sub> samples showed that the Al-O and Al-N bond stayed intact and that the phenoxide ring ruptured. This was in agreement with the oxygenation model proposed for the degradation. XPS fittings of the C1s peak suggested that all four proposed degradation products involving the rupture of the phenoxide ring were present after degradation.

When Al<sup>3+</sup> was substituted with Zn<sup>2+</sup> a higher PL intensity was observed for the samples. The Znq<sub>2</sub> sample also showed less degradation than Alq<sub>3</sub>. This might be due to the fact that Znq<sub>2</sub> only has two phenoxide rings per molecule, causing it to crystallize in a different form than Alq<sub>3</sub>. This might protect the phenoxide ring from O<sub>2</sub> and H<sub>2</sub>O. XPS studies also suggested that all four the degradation products proposed by Rosseli [3] are present after degradation.

By encapsulating the Alq<sub>3</sub> with SiO<sub>2</sub> a high PL intensity was initially observed, but it decreased drastically upon exposure to UV irradiation. It is suggested that the SiO<sub>2</sub> degraded into Si and O<sub>2</sub> species that reacted with the Alq<sub>3</sub> to form non-emissive products.

A mixture of 1% Alq<sub>3</sub> with PMMA had an emission intensity that was comparable with Alq<sub>3</sub> powder. Upon exposure to UV irradiation the PL intensity decreased for the first 80 hours, but stabilised after ~ 100 hours. PMMA degrades under UV irradiation to form products like CO<sub>2</sub>, CH<sub>4</sub>, CO and HOCH<sub>3</sub>. These products react with the Alq<sub>3</sub> to form non-emissive products. The

PMMA only degrades up to a point and after that it acts as a protective layer around the Alq<sub>3</sub> molecules protecting them from O<sub>2</sub> and H<sub>2</sub>O.

The Alq<sub>3</sub> and 5Cl-Alq<sub>3</sub> samples' luminescence intensity decreased under UV exposure. This decrease was attributed to oxygen and moisture induced destruction of the molecule. The 5,7Me-Alq<sub>3</sub> sample showed a relatively slow rate of degradation and this might be due to the methyl group protecting the carbon bond at position 7.

## References

- [1] V.K. Shukla, S. Kumar and D. Deva, *Synth. Met.* **156** (2006) 387-391.
- [2] G. Baldacchini, T. Baldacchini, A. Pace and R.B. Pode, *Electrochem. Solid-State Lett.* **8** (2005) J24-J26.
- [3] F.P. Rosseli, W.G. Quirino, C. Legnani, V.L. Calil, K.C. Teixeira, A.A. Leitao, R.B. Capaz, M. Cremona and C.A. Achete, *Org. Electron.* **10** (2009) 1417-1423.
- [4] Z.D. Popovic, H. Aziz, A. Ioannidis, N. Hu and P. N. M. Dos Anjos, *Synth. Met.* **123** (2001) 179-181.
- [5] O. Legrini, E. Oliveros and A. M. Braun, *Chem. Rev.* **1093** (1993) 671-698.
- [6] F. Papadimitrakopoulos, X.M. Zhang, D.L. Thomsen and K.A. Higginson, *Chem. Mater.* **8** (1996) 1363-1365.
- [7] M. Cölle, S. Forero-Lenger, J. Gmeiner and W. Brüttingy, *Phy. Chem. Chem. Phys.* **5** (2003) 2958-2963.
- [8] V. Kumar, H.C. Swart, O.M. Ntwaeaborwa, R.E. Kroon, J.J. Terblans, S.K.K. Shaat, A. Yousif and M.M. Duvenhage, *Mater Lett.* **101** (2013) 57-60.
- [9] L.L. Yang, Q. Zhao, M. Willander, X. Liu, M. Fahlman and J.H. Yang, *Appl. Surf. Sci.* **11** (2010) 3592-3597.
- [10] L.P. Buchwalter and G. Czornyj, *J. Vac. Sci. Technol. A*, **8** (1990) 781-784.
- [11] D. Datta, V. Tripathi, C.K. Suman, V.K. Shukla and S. Kumar, *Proc. of ACID*, (2006) 206-209.
- [12] X. Bing-she, H. Yu-ying, W. Hua, Z. He-feng, L. Xu-guang and C. Ming-wei, *Solid State Commun.* **136** (2005) 318-322.
- [13] X. Wang, M. Shao and L. Liu, *Synth. Met.* **160** (2010) 718-721.
- [14] V.K. Shukla and J. Maitra, *J. Mater.* **2013** (2013) 1-5.
- [15] R. Reisfeld, E. Zigansky and T. Saraidarov, *Opt. Mater.* **30** (2008) 1706-1709.
- [16] C. Wochnowski, M.A. Shams Eldin and S. Metev, *Polym. Degrad. Stabil.* **89** (2005) 252-264.
- [17] P.E. Burrows, Z. Shen, V. Bulovic, D.M. McCarty and S.R. Forrest, *J. Appl. Phys.* **79** (1996) 7991-8006.

- [18] M.M. Duvenhage, O.M. Ntwaeaborwa and H.C. Swart, *Physica B-Condensed Matter* **407** (2012) 1521-1524.

# Chapter 7

## Synthesis, crystal structure, luminescent properties and photon degradation of *mer-tris(8-Hydroxy-quinolinato-N, O)-indium(iii) hydrate 0.5 methanol solvate*.\*

### 1. Introduction

Since the first discovery of tris-(8-hydroxyquinoline) aluminium ( $\text{Alq}_3$ ) as a source of efficient electroluminescence, organic light emission diodes (OLEDs) have attracted the attention of researchers and industry alike.  $\text{Alq}_3$  especially, finds wide application in OLEDs as electron transport materials, a source of green light and as host material for red-emitting dopants [1 - 4]. The development of new OLEDs that might replace traditional lighting devices will have a huge environmental and financial impact, but is hampered by several practical issues, including the availability of stable materials with high emitting quality and good structural stability [5 - 7]. The last decade has seen the development of numerous different hosts and emitters comparable to  $\text{Alq}_3$ . However, the need to understand structure-property relationships in detail is also important since these materials can undergo many changes including isomerisation, phase changes and even photon degradation when deposited as thin films under different conditions which may affect device properties [8, 9].

The effect of solvent molecules in the solid state crystal lattice can have marked effects on the photoluminescence (PL) properties [10] of these types of materials, but strangely enough limited reports in the literature suggest that this has not been explored extensively. There are several crystal structure reports of the  $\text{In}(\text{qn})_3$  moiety in the literature, none of which have water and methanol included in the crystal lattice [11 - 14]. In order to explore this avenue of research we synthesized *mer-tris(8-Hydroxy-quinolinato-N, O)-indium(iii) hydrate 0.5 methanol* (*mer*- $[\text{In}(\text{qn})_3]\cdot\text{H}_2\text{O} \cdot 0.5 \text{CH}_3\text{OH}$ ), which have water and methanol solvent molecules in the crystal lattice, and present here its PL properties, photon degradation mechanism, crystal structure, high resolution x-ray photoelectron spectroscopy (XPS) and spectral properties.

\*M.M. Duvenhage, H.C. Swart, O.M. Ntwaeaborwa and H.G. Visser, *Optical Materials*, **35** (2013) 2366-2371.

## 2. Synthesis of mer-[In(qn)<sub>3</sub>].H<sub>2</sub>O. 0.5 CH<sub>3</sub>OH (compound 1)

Compound 1 was synthesized using the method described by Ohkaku et al. [15]. A methanol solution (20 ml) of 8-hydroxyquinoline (1.96 g, 1.36 mmol) was slowly added to a water solution (20 ml) of indium trichloride (0.1 g, 0.45 mmol) with stirring at room temperature. Stirring was continued overnight after which a yellow precipitate was filtered off and washed with cold methanol to remove excess 8-hydroxyquinoline. The filtrate was recrystallized in a water/methanol mixture (10:90 %) by slow evaporation at room temperature. Yellow, plate-like crystals, suitable for single crystal X-ray diffraction were obtained after one week. The yield was 0.228 g (87 % based on In). Some of the powder was also annealed in air at 130 °C for 2 hours.

## 3. Results

### 3.1 Crystal structure and x-ray crystallography.

#### 3.1.1 Experimental and calculations

Single crystal diffraction data were collected at 100 K on a Bruker X8 ApexII 4K diffractometer using monochromated Mo K $\alpha$  radiation ( $\lambda = 0.71073 \text{ \AA}$ ). The cell parameters were refined by the SAINT-Plus program [16] while SADABS [17] was used for the absorption corrections. Structures were solved with direct methods using SIR97 [18] and were refined by full-matrix least-squares methods on  $F^2$  with SHELXL-97 [19] and WinGX [20]. The structure was checked for higher symmetry with the help of the Platon program [21]. The molecular graphics were obtained with DIAMOND [22]. Aromatic hydrogen atoms were placed in geometrically idealized positions (C-H = 0.95  $\text{\AA}$ ) and constrained to ride on their parent atoms with  $U_{\text{iso}}(\text{H}) = 1.2U_{\text{eq}}(\text{C})$ . Methyl hydrogen atoms were placed in geometrically idealized positions (C-H = 0.98  $\text{\AA}$ ) and constrained to ride on their parent atoms with  $U_{\text{iso}}(\text{H}) = 1.5U_{\text{eq}}(\text{C})$ . Aqua hydrogen atoms were located from Fourier difference maps and constrained with equal O-H distances (0.85(2)  $\text{\AA}$ ). Powder X-ray diffraction (XPRD) data were obtained on a Bruker D8 Advance Diffractometer equipped with a Cu K $\alpha$  source.

### 3.1.2 Crystal structure

The X-ray single crystal structure data show that compound **1** exists as a neutral 3 d chain with a basic  $[\text{In}(\text{qn})_3] \cdot \text{H}_2\text{O} \cdot 0.5\text{CH}_3\text{OH}$  unit. The asymmetric unit contains one  $\text{In}(\text{qn})_3$  molecule, half of a methanol solvent molecule and a water molecule (figure 1). The solvate water molecule is disordered over two positions (67:33 %) while the methanol solvate molecule exhibits a crystallographically imposed 50 % disorder.

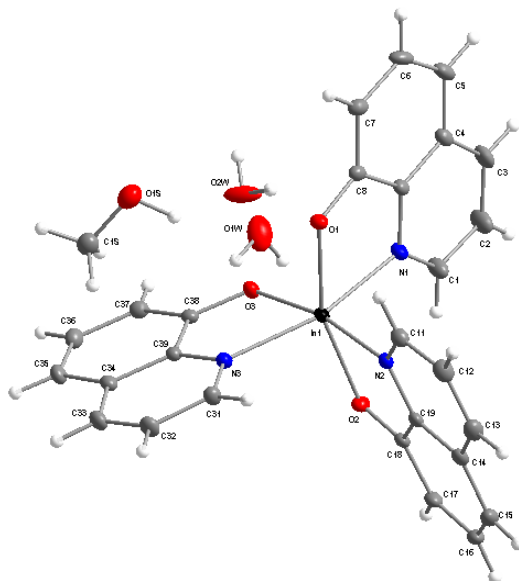
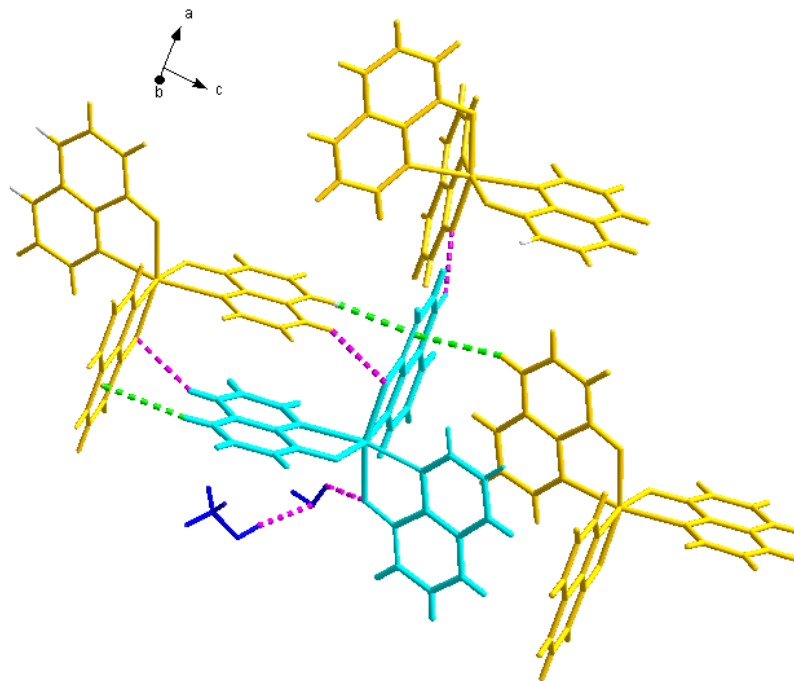


**Figure 1: Numbering scheme of compound 1.**

The structure shows that the  $\text{In}(\text{III})$  ion is coordinated to the 8-hydroxyquinoline bidentate ligands by its respective oxygen and nitrogen atoms in a meridional fashion. The octahedral geometry around the central metal ion is severely distorted as illustrated by the  $\text{O}-\text{In}(1)-\text{N}$ ,  $\text{O}-\text{In}(1)-\text{O}$  and  $\text{N}-\text{In}(1)-\text{N}$  bonding angles which range between  $76.69(7)$  and  $100.42(7)^\circ$ . The  $\text{In}(1)-\text{N}$  bonding distances vary between  $2.232(2)$  and  $2.257(2)$  Å while the  $\text{In}(1)-\text{O}$  distances vary between  $2.1164(19)$  and  $2.1410(18)$  Å. All the bonding angles and distances in the structure fall within the normal range [11, 23].

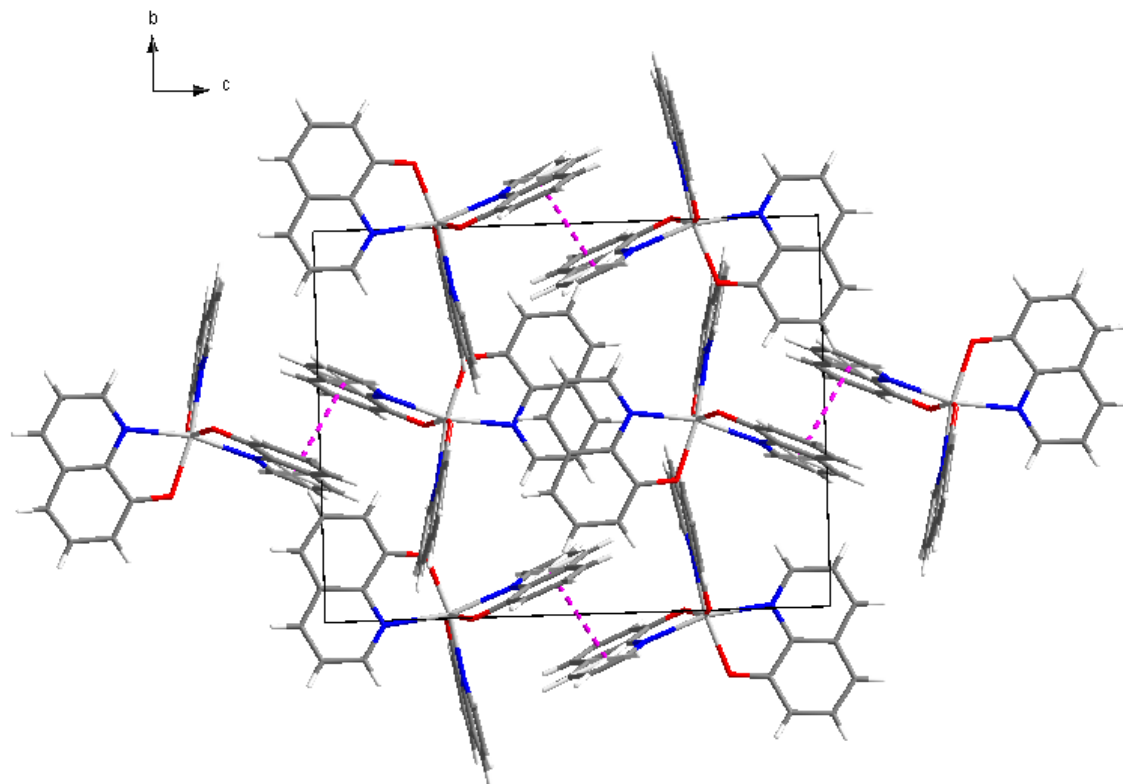
The structure is stabilized by five kinds of hydrogen bonds that involve the quinolinato ring protons of the  $\text{In}(\text{III})$  complex, the oxygen atoms of coordinated 8-hydroxyquinoline ligands and the solvent water and methanol molecules ( $\text{C}(13)-\text{H}(13) \cdots \text{O}(1s)\#3 = 3.329(5)$  Å,  $147.8^\circ$ ;  $\text{C}(15)-$

H(15) $\cdots$ O(2)#3 = 3.199(3) Å, 151.7 °; C(33)-H(33) $\cdots$ O(2)#2 = 3.371(3) Å, 150.5 °; O(1w)-H(12w) $\cdots$ (O1) = 2.849(4) Å, 119(5) °; O(1s)-H(1s) $\cdots$ O(1w) = 2.675(6) Å, 160(6) °; symmetry codes: #1  $-x + 1/2, y + 1/2, -z + 1/2$ ; #2  $-x, -y, -z$ ; #3  $x - 1/2, -y - 1/2, z - 1/2$ , illustrated in figure 2.



**Figure 2: Hydrogen bonding interactions in compound 1.**

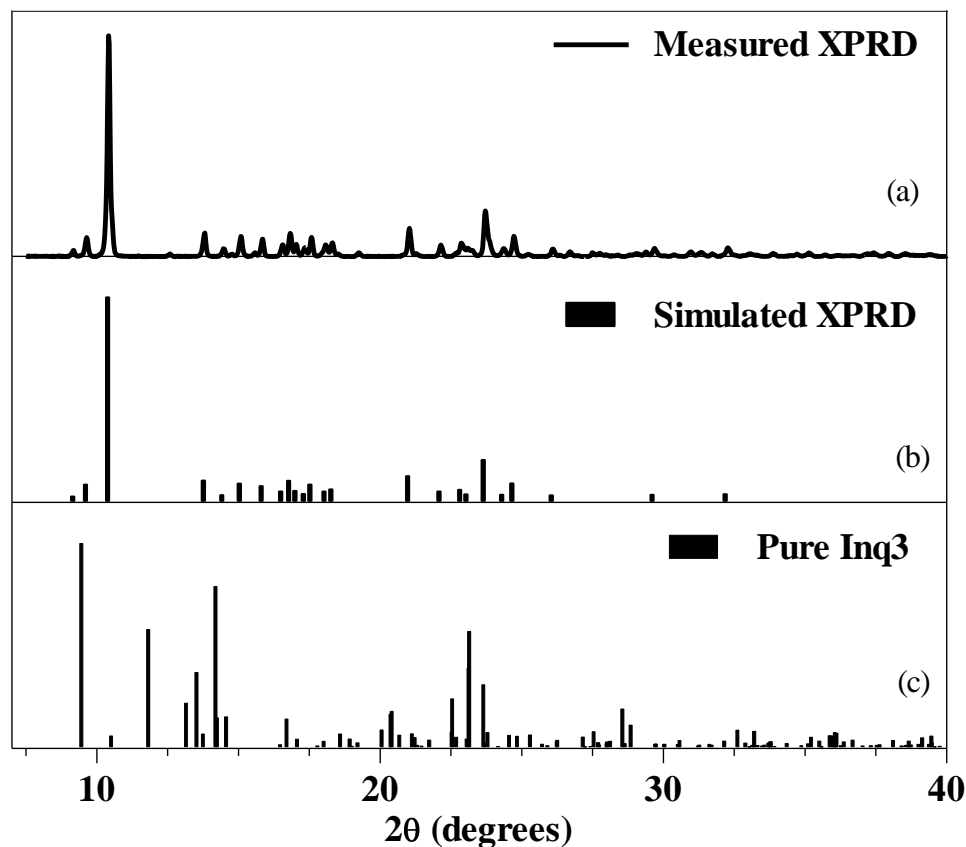
One weak  $\pi$ -stacking interaction (figure 3) is observed between the pyridine ring of one of the 8-hydroxyquinoline ligands and its symmetry equivalent of a neighboring molecule with a centroid to centroid distance of 3.694(2) Å.



**Figure 3:  $\pi$ -stacking as observed across the  $bc$ -plane.**

### 3.1.3 X-ray crystallography

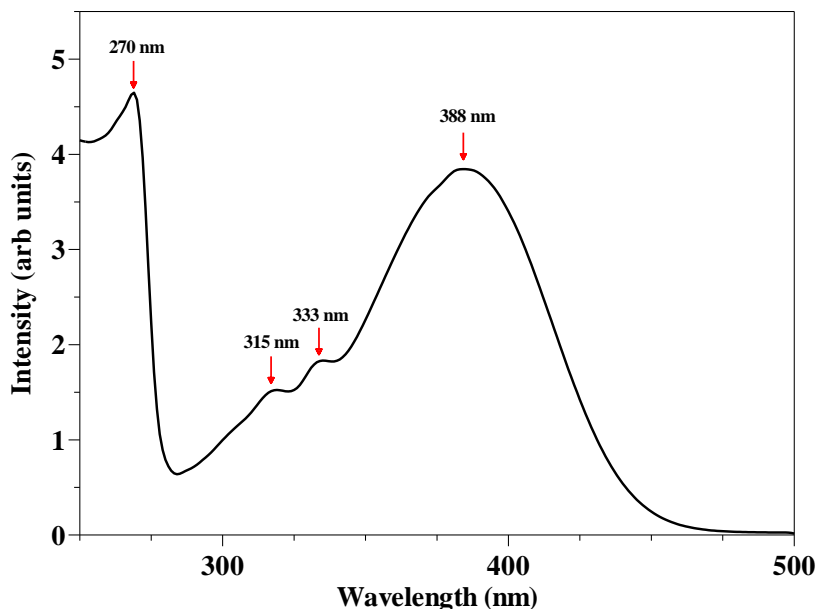
Figure 4 (a) shows the experimental XPRD pattern of compound **1**, obtained at room temperature. DIAMOND [21] was used to simulate the XPRD pattern for compound **1** from the single crystal data. These data are shown in figure 4 (b). Their peak positions are in good consistency with each other, indicating the phase purity of the as-synthesized samples. The single crystal data for pure  $\text{Inq}_3$  were obtained from the Cambridge Structural Database [24] and DIAMOND [21] was used to simulate the XPRD pattern. The XPRD of compound **1** was compared to that of pure  $\text{Inq}_3$  (figure 4 (c)) and it can be seen that there is no comparison between the two.



**Figure 4: The simulated and experimental XPRD patterns of compound 1.**

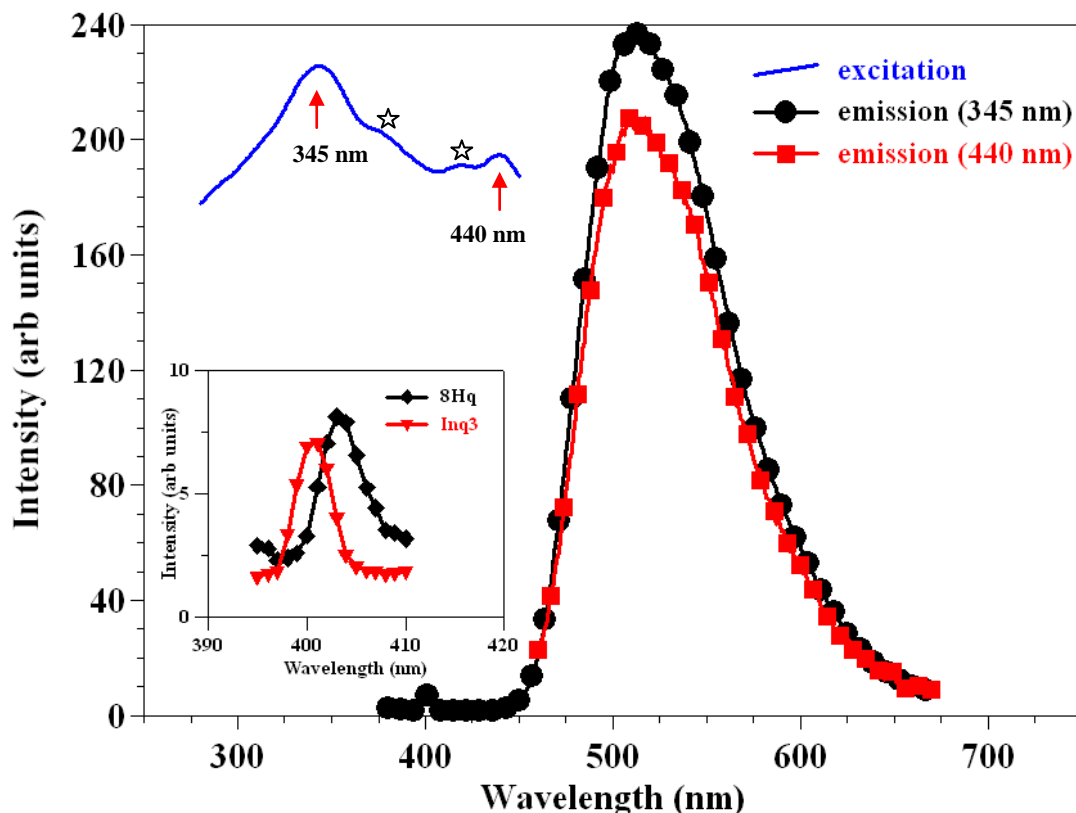
### **3.2 Luminescent properties and photon degradation**

Figure 5 shows the absorption spectrum for compound **1** dissolved in ethanol. The spectrum is dominated by two intense absorption bands at  $\sim 270$  and  $388$  nm. These bands can be assigned to ligand centered electronic transitions [25] and are broad and structureless. In addition to these intense bands, there are 2 weak absorption bands at  $315$  and  $333$  nm, which are assigned to the vibronic progression due to the ring deformation mode of an electronic transition at  $346$  nm [25].



**Figure 5: Absorption spectrum of compound 1 dissolved in ethanol.**

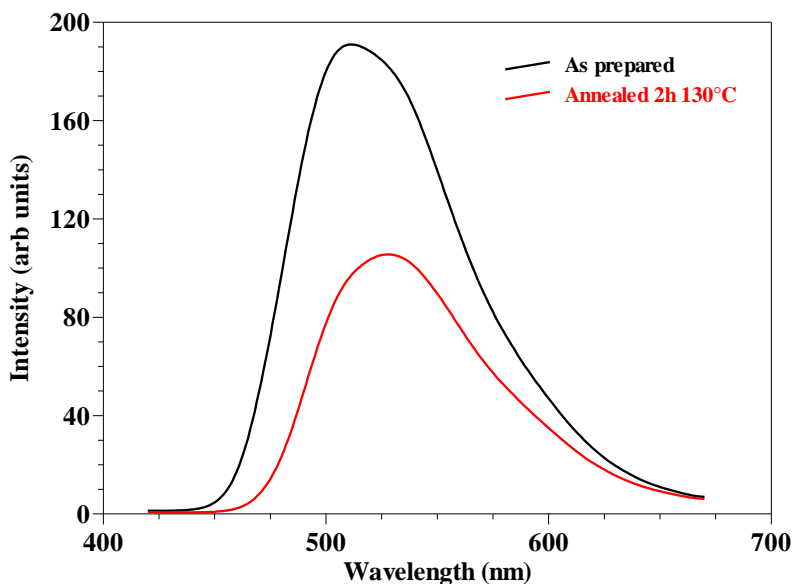
The solid state excitation spectrum of compound **1** was obtained at room temperature (Figure 6). Two main peaks at 345 and 440 nm and shoulders at 372 and 420 nm (indicated with a \* on the graph) respectively, are observed. The peak at 440 nm is assigned to the 0-0 vibronic state of  $\text{In}(\text{qn})_3$  [25]. The peak at 345 nm and the shoulder peaks at 372 and 420 nm are assigned to high energy transitions ( $S_4$  and above) [26] to the nearest-neighbor ligands of different molecules in the crystalline structure. Figure 5 also shows the emission spectra of compound **1**, which peak at 510 nm with a FWHM of 90 nm. Two wavelengths (345 and 440 nm) were used to excite the sample and both yield the same emission wavelength maxima. The intensity of the spectrum excited at 440 nm is lower than that excited at 345 nm. This is in accordance with the intensities of the excitation spectrum, since  $\text{Inq}_3$  is known to be a singlet emitter [27]. The emission is due to the relaxation of an excited electron from the  $S_1$ - $S_0$  level. The small peak at 400 nm corresponds to the emission of 8-hydroxyquinoline (inset of Figure 6). This is an indication that a small amount of unreacted 8-hydroxyquinoline is still present in the powder samples.



**Figure 6: Solid state photoluminescence excitation and emission spectra of compound 1.**

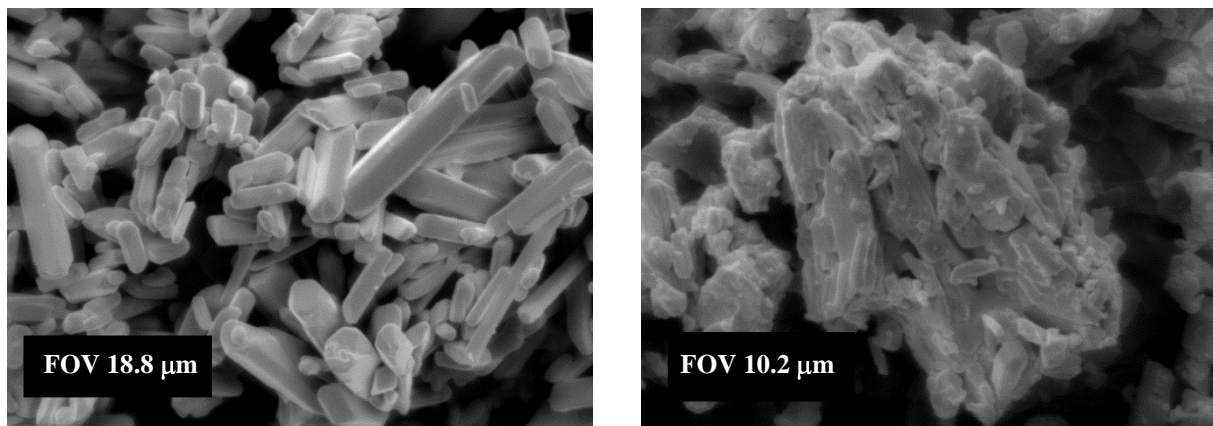
In another experiment, the photoluminescence spectrum of a powder of compound **1** was obtained as prepared after which the sample was annealed at 130 °C for two hours (Figure 7). A red shift of 16 nm is observed after annealing and the intensity was shown to decrease by 50 %. Brinkmann et al. [28] reported that in the case of  $\text{Alq}_3(\text{MeOH})$  and  $\text{Alq}_3(\text{C}_6\text{H}_5\text{Cl})$  the methanol molecules cannot lead to any  $\pi$ - $\pi$  orbital overlaps with the ligands and it will simply act as a spacer molecule, which reduces the direct intermolecular interactions between the quinoxaline moieties. Both these materials also showed a blue shift in emission spectra compared to unsolvated  $\text{Alq}_3$ . From Figure 3 it can be seen that only a weak  $\pi$  interaction is observed between one of the 8-hydroxyquinoline ligands. It can therefore be concluded that the methanol and water molecules in compound **1** also acts as optically inactive spacer molecules in the crystalline network and cause a blue shift on the emission of solid  $\text{Inq}_3$ . Some of the solvents have evaporated during annealing as can be seen from the XPRD and XPS results. The XPRD results also show that the crystal structure has changed for the annealed sample. This might lead to more

favorable  $\pi$ - $\pi$  overlaps between the facing ligands, which are reported [28] to lead to a red shift in the emission spectrum.



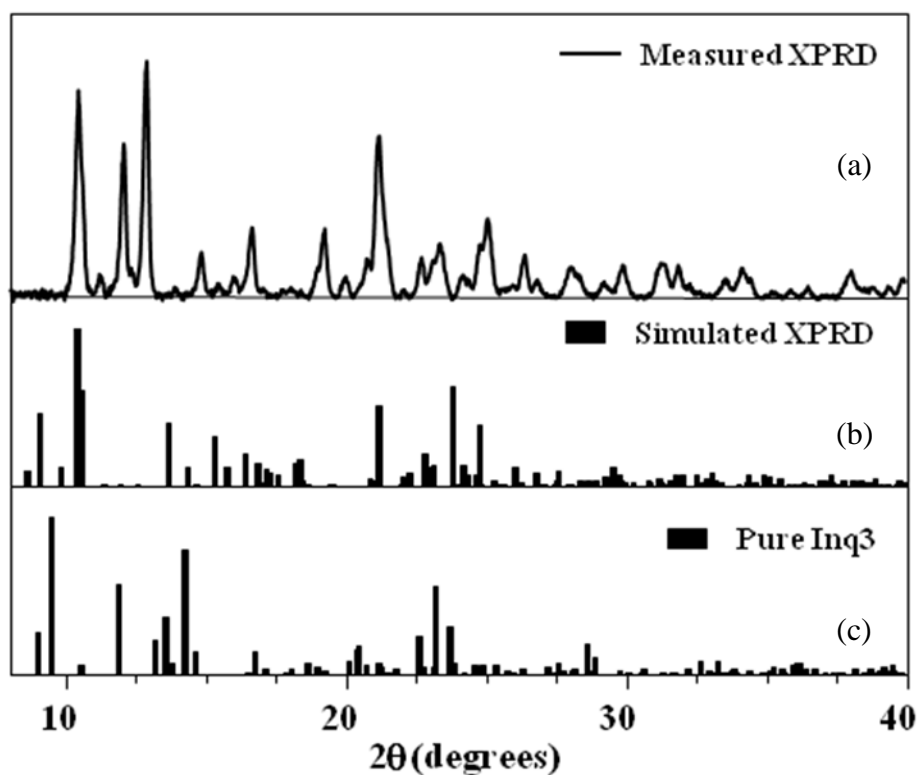
**Figure 7: Photoluminescence spectra of compound 1 as-prepared and annealed for two hours at 130 °C.**

From the SEM images in figure 8 it can be seen that for the as-prepared powder, rod-like crystals formed with lengths between 2 - 8  $\mu\text{m}$  and widths of  $\sim 1 \mu\text{m}$ . After annealing these rods melted together to form big agglomerated particles. The change in morphology contributed to the decrease in luminescence intensity of the annealed sample and could possibly be assigned to a loss of solvent species.



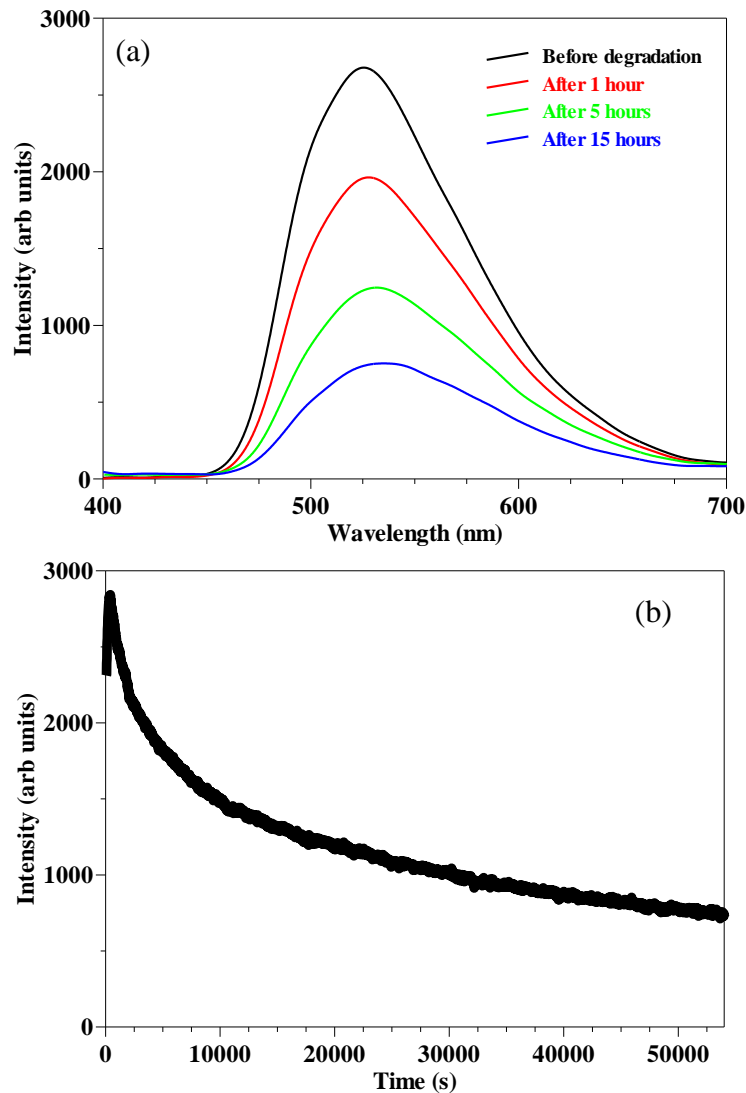
**Figure 8: SEM images of (a) as-prepared and (b) annealed Inq<sub>3</sub>.**

The XPRD pattern for the annealed sample is shown in figure 9 (a). It is not an exact match with either the simulated XPRD of (b) compound **1** or that of (c) pure Inq<sub>3</sub>. The peaks at 10.41° and 21.14° match with that of compound **1**, while the peak at 12.05° matches with pure Inq<sub>3</sub>. The XPRD of the annealed sample is an indication that there is still some solvent left in the crystal structure.



**Figure 9: XPRD spectrum of the annealed sample.**

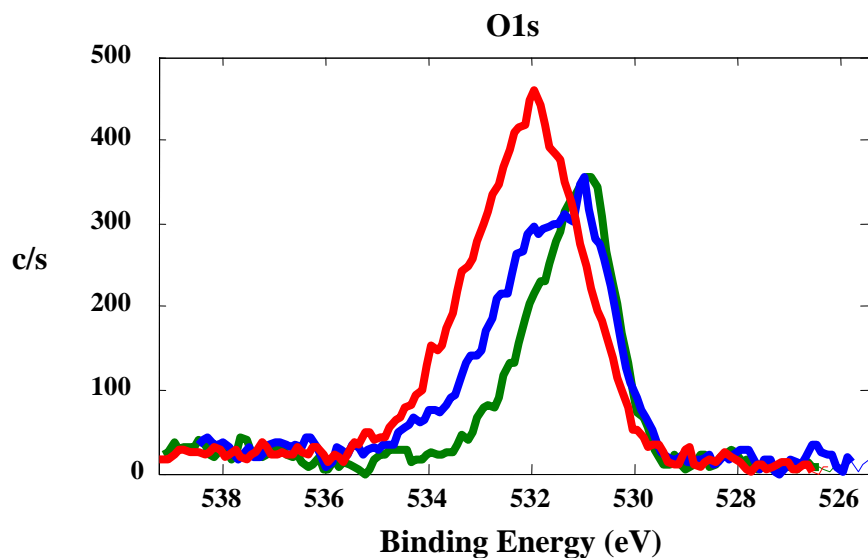
The photodegradation spectrum of compound **1** was obtained over a period of 15 hours. Figure 10 (a) illustrates the evolution of the emission band during the ~15 hours of UV exposure, resulting in a decrease in intensity. A decrease of ~ 60% is observed. This result is in correlation with results previously reported by Kumar et al. [29]. From figure 10 (b) it can be seen that the luminescence intensity decreases rapidly at the beginning and reaches one-half of its original value after five hours. The rate of decrease slowed down for longer exposure times. The sample was fully exposed to oxygen and moisture in the open air, which are known to destroy the molecular structure [30 - 33].



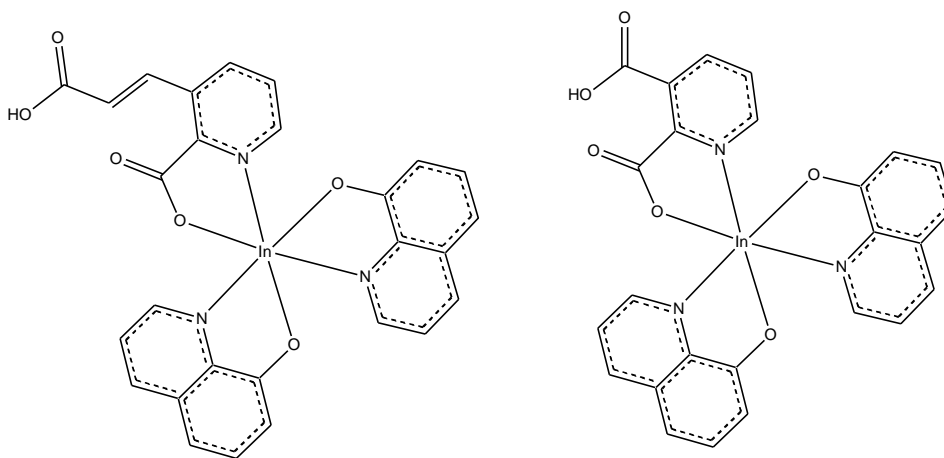
**Figure 10: Photodegradation spectra of compound 1 under UV exposure ( $\lambda = 365$  nm). (a) Evolution of the emission band with time and (b) quenching of luminescence with time.**

Figure 11 shows the high resolution XPS peaks of O-1s for the as-prepared (red), annealed (blue) and degraded (green) Inq3 samples. The as-prepared sample's peak is a combination of C-O ( $\sim 534$  eV) [34] and O in an In environment such as  $\text{In}_2\text{O}_3$  ( $\sim 532$  eV) [35]. O-H bonds from the solvents (water and methanol) trapped in the crystal lattice are found at a binding energy of  $\sim 530.5$  eV [34]. Some of the solvents have evaporated upon annealing and caused a shift to lower binding energies. In the case of the degraded sample, the oxygen and moisture in the air caused decomposition of the phenoxide ring [30]. Rosseli et al. [30] proposed that C=O ( $\sim 532.5$  eV), C-

O-H and O=C-O-H (~ 530.5 eV) bonds formed during photodegradation. Possible products that might have formed during photodegradation are shown in figure 12.



**Figure 11: High resolution XPS peaks of O-1s of the as prepared (red), annealed (blue) and degraded (green) Inq<sub>3</sub> samples.**



**Figure 12: Possible products formed after photon degradation.**

## 4. Conclusion

In summary, we synthesized a *mer*-[In(qn)<sub>3</sub>].H<sub>2</sub>O. 0.5 CH<sub>3</sub>OH complex with interesting solvent disorders in the crystal structure as well as good photoluminescent properties which makes this compound a candidate for potential photoactive materials. Photoluminescence excitation peaks were obtained at 345 and 440 nm and a broad emission peak at 510 nm. The solvent molecules were shown to increase the photoluminescent properties of the compound **1** as well as causing a red shift of 16 nm in the emission spectrum. The methanol and water molecules inside the crystal structure act as optically inactive spacer molecules which lead to a blue shift in the solid state emission. The XPRD showed a change in the crystal structure of the annealed sample. This might lead to favorable  $\pi$ - $\pi$  overlaps which are responsible for a red shift in the emission spectrum. The sample showed a 60% decrease in luminescence intensity upon UV exposure. This is an indication that oxygen and moisture in the air caused the phenoxide ring to decompose, destroying the luminescent centers in the process. XPS studies of the O-1s peak indicated that after annealing of the sample some of the solvent species were no longer present in the crystal. For the degraded sample the O-1s peak indicated that C=O, C-O-H and O=C-O-H bonds had formed.

## References

- [1] C.W. Tang and S.A. van Slyke, *Appl. Phys. Lett.* **51** (1987) 913-915.
- [2] C.W. Tang, S.A. van Slyke and C.H. Chen, *Appl. Phys. Lett.* **65** (1989) 3610-3616.
- [3] P.E. Burrows, L.S. Sapochak, D.M. McCarty, S.R. Forrest and M.E. Thompson, *Appl. Phys. Lett.* **64** (1994) 2718-2720.
- [4] C. Tai, Y. Chou and B. Wang, *J. of Lumin.* **131** (2011) 169-176.
- [5] F.P. Rosselli, W.G. Quirino, C. Legnani, V.L. Calil, K.C. Teixeira, A.A. Leitao, R.B. Capaz, M. Cremona and C.A. Achete, *Org. Electron.* **10** (2009) 1417-1423.
- [6] F. Nunez-Zarur and R. Vivas-Reyes, *J. of Mol. Struc.* **850** (2008) 127-134.
- [7] T. Tsuboi and Y. Torii, *J. Non-Cryst. Solids* **356** (2010) 2066-2069.
- [8] L.S. Sapochak, A. Padmaperuma, N. Washton, F. Endrino, G.T. Schmett, J. Marshall, D. Fogarty, P.E. Burrows and S.R. Forrest, *J. Am. Chem. Soc.* **123** (2001) 6300-6307.
- [9] S. Liao, J. Shiu, S. Liu, S. Yeh, Y. Chen, C. Chen, T.J. Chow and C. Wu, *J. Am. Chem. Soc.* **131** (2009), 763-777.
- [10] C.H. Chen and J. Shi, *Coord. Chem. Rev.* **171** (1998) 161-174.
- [11] L.S. Spaochak, A. Ranasinghe, H. Kohlmann, K.F. Ferris, P.E. Burrows, *Chem. Mater.* **16** (2004) 401-406.
- [12] Yu.A. Bankovskii, V.K. Bel'skii, L.Ya. Pech, Ya.V. Ashaks, *Zh. Neorg. Khim. Russ. J. Inorg. Chem.* **38** (1993) 1988-1992.
- [13] N. Korber, B. Achour, F. Nepveu, *J. Chem. Cryst.* **24** (1994) 685-688.
- [14] M.A. Green and J.C. Huffman, *J. Nucl. Med.* **29** (1988) 417-420.
- [15] K. Nakamoto and N. Ohkaku, *Inorg. Chem.* **10** (1971) 798-805.
- [16] SAINT-Plus, version 6.02 (including XPREP); Bruker AXA, Inc.: Madison, WI, USA, (1999).
- [17] SADABS, version 2004/1; Bruker AXS, Inc.: Madison, WI, USA, (2004).
- [18] A. Altomare, M.C. Burla, M. Camalli, G.L. Casciarano, C. Giacovazzo, A. Guagliardi, A.G.G. Moliterni, G. Polidori and R. Spagna, *J. Appl. Cryst.* **32** (1999) 115-119.
- [19] G.M. Sheldrick, *Acta Cryst.* **A64** (2008) 112-122.
- [20] L.J. Farrugia, *J. Appl. Crystallogr.* **32** (1999) 837-838.
- [21] A.L. Spek, *J. Appl. Cryst.* **36** (2003) 7-13.

- [22] K. Brandenburg and H. Putz, DIAMOND, release 3.1b, Crystal Impact GbR: Bonn, Germany, (2005).
- [23] M. Rajeswaran and V.V. Jarikov, *Acta Cryst., Sect. E* **59** (2003), m306-m307.
- [24] “The United Kingdom Chemical Database Service”, D.A. Fletcher, R.F. McMeeking and D. Parkin, *J. Chem. Inf. Comput. Sci.* **36** (1996) 746-749.
- [25] V.V.N. Ravi Kishore, A. Aziz, K.L. Narasimhan, N. Periasamy, P.S. Meenakshi and S. Wategaonkar, *Synth. Met.* **126** (2002) 199-205.
- [26] W. Stampor, J.Kalinowski, G. Marconi, P. Di Marco, V Fattori and G. Giro, *Chem. Phys. Lett.* **283** (1998) 373-380.
- [27] A.D. Walser, R. Priestley and R. Dorsinville. *Synth. Met.* **102** (1999) 1552-1553.
- [28] M. Brinkmann, G. Gadret, M. Muccini, C.Taliani, N. Masciocchi and A. Sironi, *J. Am. Chem.Soc.* **122** (2000) 5147-5157.
- [29] S. Kumar, V.K. Shukla and A. Tripathi, *Thin Solid Films* **477** (2005) 240-243.
- [30] F.P. Rosseli, W.G. Quirino, C. Legnani, V.L. Calil, K.C. Teixeira, A.A. Leitao, R.B. Capaz, M. Cremona and C.A. Achete, *Org. Electron.* **10** (2009) 1417-1423.
- [31] F. Papadimitrakopoulos, X.M. Zhang, D.L. Thomsen and K.A. Higginson, *Chem. Mater.* **8** (1996) 1363-1365.
- [32] P.E. Burrows, Z. Shen, V. Bulovic, D.M. McCarty and S.R. Forrest, *J. Appl. Phys.* **79** (1996) 7991-8006.
- [33] M.M. Duvenhage, O.M. Ntwaeaborwa and H.C. Swart, *Physica B-Condensed Matter* **407** (2012) 1521-1524.
- [34] K Kontis, 28th International Symposium on Shock Waves, Volume 1, Springer-Verlag Berlin Heidelberg (2012) 188.
- [35] V. Golovanov, M.A. Maki-Jaskari, T.T. Rantala, G. Korotcenkov, V. Brinzari, A. Cornet and J. Morante, *Sensor Actuat. B* **106** (2005) 563-571.

# Chapter 8

## Basic principles of organic light emitting diodes and their fabrication.

### 1. Introduction

Organic electroluminescence (EL) is the electrically driven emission of light from noncrystalline organic materials. The phenomenon of organic EL was first discovered by Pope in 1963 [1]. In 1987 Tang and VanSlyke, a team at the Chemistry Division of Kodak Research Laboratories, introduced a double layer organic light emitting diode (OLED). The device combined modern thin film deposition techniques with suitable materials and structure to give moderately low bias voltages and attractive luminance efficiency [2]. Their research eventually led to the discovery of the first efficient multi-layered organic EL device based on the concept of heterojunction architecture. Since then, tremendous progress has been made in the field of organic EL. The growing interest is largely motivated by the promise of the use of this technology in flat panel displays and lighting (Figure 1).



**Figure 1: An OLED television made by LG [3] and a flexible OLED lighting panel by Konica Minolta [4].**

## 2. OLED

An OLED has an organic EL medium consisting of extremely thin layers ( $< 0.2 \mu\text{m}$  in combined thickness) sandwiched between two electrodes. Some organic layers act as hole transporting layers (HTL) and the others as electron transporting layers (ETL). When a potential difference is applied between the anode and the cathode, the holes and electrons will migrate towards the opposite charged electrode. Holes and electrons then transfer to the emitting material forming tightly bound excitons which emit a photon upon relaxation. These photons are then capable of escaping the device architecture through the transparent anode and out of the glass substrate.

The heterojunction of the device should be designed to facilitate hole injection from the HTL into the ETL and also to block electron injection in the opposite direction in order to enhance the probability of the formation of an excitons and recombination near the interface region. Figure 2 shows the energy level diagram of a simple two-layer OLED. The highest occupied molecular orbital (HOMO) of the HTL is slightly above that of the ETL. Holes can therefore readily enter into the ETL. The lowest unoccupied molecular orbital (LUMO) of the ETL is significantly below that of the HTL, so that electrons are confined in the ETL. The low hole mobility in the ETL causes a buildup in hole density and this enhances the collision capture process. If this interface is spaced at a sufficient distance from the contact, the probability of quenching near the metallic surface is greatly reduced.

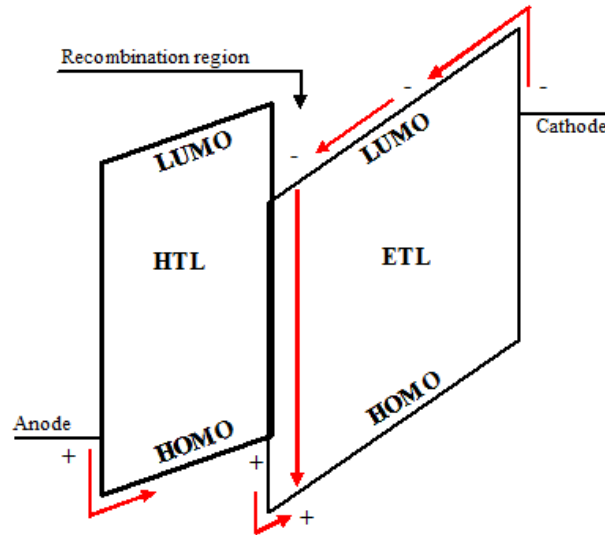


**Figure 2: Energy level diagram of a two-layer OLED [5].**

The simple structure can be modified to a three-layer structure. In this structure, an additional luminescent layer is introduced between the HTL and ETL. This layer functions primarily as the site for hole-electron recombination. In a device like this the functions of the individual organic layers are distinct and can therefore be optimized independently. The recombination layer can be chosen to have a desirable EL colour as well as high luminance efficiency. The HTL and ETL can be optimized for the carrier transport property.

### 3. OLED Materials

The advantages of organic materials over inorganic materials are their excellent colour gamut and high fluorescence efficiency. The fast decay of excited molecular states produces the light in organic materials and the colour of the light depends on the energy difference between those excited states and the molecular ground level. Many materials show intense photoluminescence (PL) with near unity quantum yield, while the EL efficiency is limited to the probability of creating non-radiative triplet excited states in the electron-hole recombination. A typical OLED device structure is shown in figure 3.

Indium tin oxide (ITO) is commonly used as the anode, while the cathode consists of a metal with a low work function (like Al or Mg) doped with LiF or Cs<sub>2</sub>CO<sub>3</sub> to help with the injection of electrons. The ETL, HTL, injection and blocking layers consist of organic layers in the order of 50 nm each.

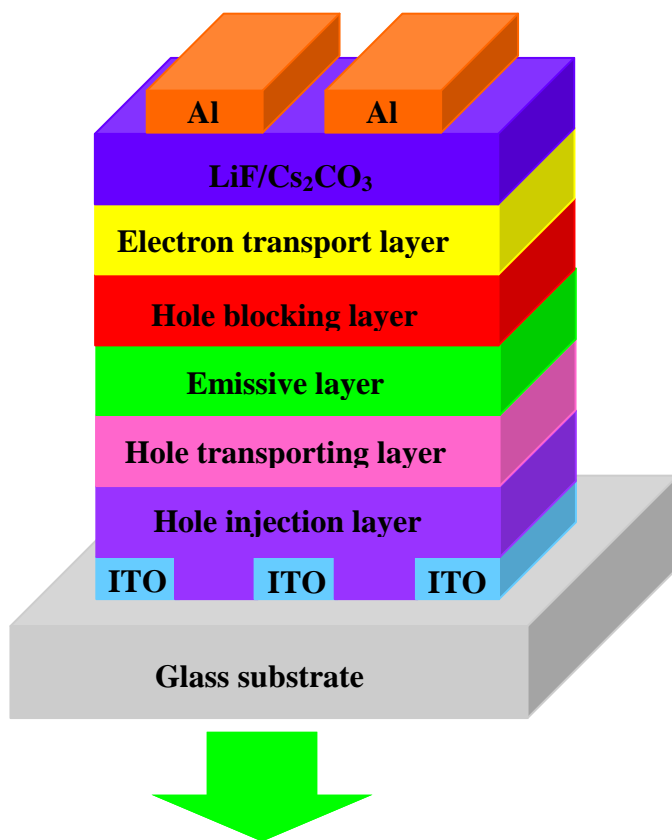


**Figure 3: Typical OLED device structure.**

### **3.1 Anode and hole-injection materials**

The hole-injecting contact requires a metal of high work function to match the HOMO of the organic material. Most OLEDs rely on the transparent and conductive indium tin oxide (ITO, or tin-doped indium oxide) as the anodic material to facilitate hole-injection while permitting light to exit the device in an effective manner. ITO is a mixture of indium(III) oxide (In<sub>2</sub>O<sub>3</sub>) and tin(IV) oxide (SnO<sub>2</sub>), typically 90% In<sub>2</sub>O<sub>3</sub> and 10% SnO<sub>2</sub> by weight. In powder form it is yellow-green in colour, but it is transparent and colourless when deposited as a thin film at thicknesses of 1000-3000 Å [6]. The work function of ITO ranges from 4.5 to 5.0 eV [5] and is strongly

dependent on the methods of surface treatment. Treatment of ITO glass substrates using UV-ozone or oxygen plasma substantially increases its work function and also enhances the hole-injection from the ITO anode into the HTL. By coating the ITO surface with hole-injection layers such as copper phthalocyanine (CuPc) and poly(3,4-ethylenedioxythiophene)–poly(styrene) (PEDOT/PSS) (Figure 4), the surface can be smoothed, reducing the probability of electrical shorts, decreasing the turn-on voltage and prolonging the operation lifetime of the device.

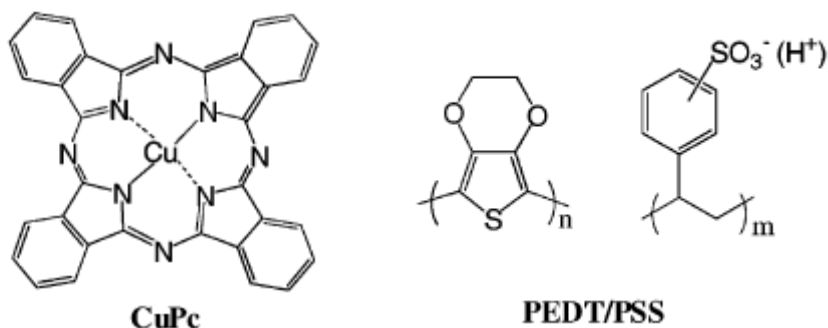


**Figure 4: Hole-injection materials [5].**

### 3.2 Hole-transport materials

Several materials have been preferred as hole-transporting materials. Among them N,N'-diphenyl-N,N'-bis(3-methylphenyl)(1,10-biphenyl)-4,40-diamine (TPD) and N,N'-bis(1-naphthyl)-N,N'-diphenyl-1,10-biphenyl-4,40-diamine (NPB) have been studied extensively (Figure 5). These materials have a glass transition temperature below 100.8 °C and a hole mobility on the range of  $10^{-3}$  to  $10^{-4}$   $\text{cm}^2/\text{Vs}$  [163]. In OLEDs, the hole current dominates the total current, owing to efficient hole-injection and sufficiently high hole mobilities.

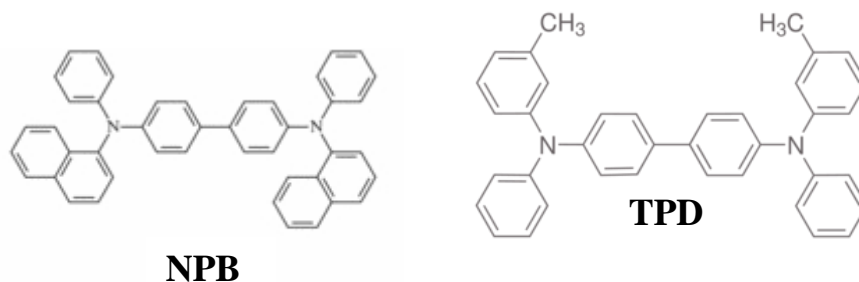


**Figure 5: Hole-transport materials [5].**

### 3.3 Electron-transport and host emitting materials

The most widely used electron-transport and host emitting material in OLEDs is tris(8-hydroxyquinolato)aluminum ( $\text{Alq}_3$ ) (Figure 6).  $\text{Alq}_3$  is morphologically and thermally stable to be evaporated into thin films, easily synthesized and purified. It is also used as an emissive material, which emits in the green region with a broad emission peaking at 520 nm. The electron mobility in  $\text{Alq}_3$  strongly depends on the electric field with a value of approximately  $10^{-6} \text{ cm}^2/\text{Vs}$  at  $4 \times 10^5 \text{ V/cm}$ . Other EL colors can be obtained by doping a small amount of specific guest molecules in  $\text{Alq}_3$  or by choosing different organic fluorescent materials as emitters. Some of the fluorescent dopant molecules are shown in Figure 7. In some cases, doping also enhances the luminance efficiency by reducing non-radiative decay. By making some structural modifications to  $\text{Alq}_3$  the quantum efficiency, thermal stability and thin film morphology can be improved (Figure 6).

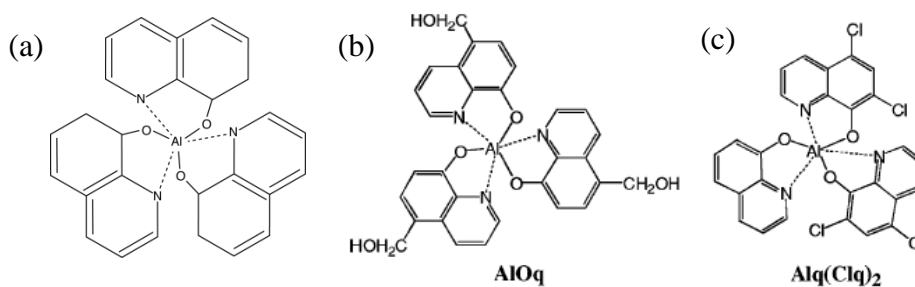


**Figure 6: (a)  $\text{Alq}_3$  and (b,c) modified  $\text{Alq}_3$  molecules [5].**

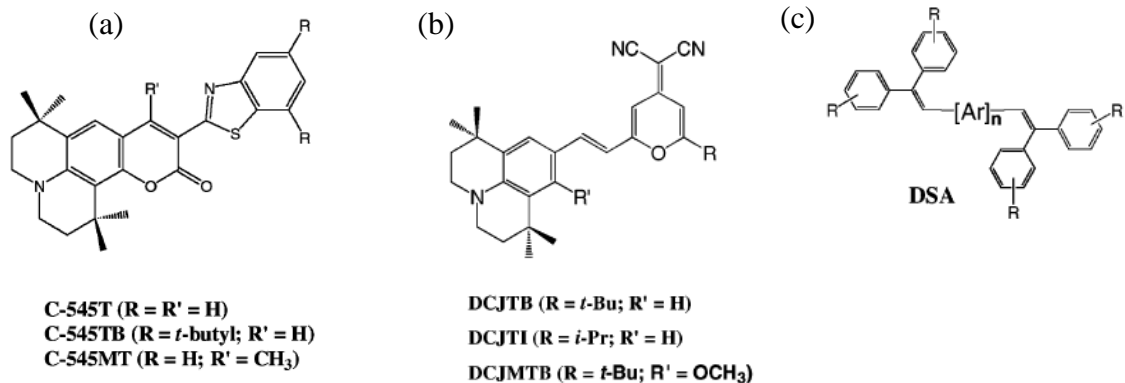


**Figure 7: Some fluorescent doping molecules: (a) green, (b) red and (c) blue [5].**

## 3.4 Cathode

### 3.4.1 Elemental metals

A barrier for electron injection is commonly present at the metal-organic contact when the work function of the metal is larger than the LUMO of the organic materials, and thus the use of a low work function metal is highly desirable to facilitate the injection of electrons. Attempts to use Ca, K and Li for effective cathode materials revealed that they exhibit poor corrosion resistance and high chemical reactivity with the organic medium. Therefore, a variety of low work function metal alloys such as Mg-Ag and Al-Li are used for cathodes. Mg has a work function of 3.66 eV [5], which is sufficiently low for it to be useful as an electron-injecting electrode. A small amount of Ag (volume ratio of 10:1) assists the Mg deposition by presumably providing nucleating sites on the alloy film during co-sublimation.

### 3.4.2 Alkali metal compounds/Al

Alkali compounds have been combined with a capping Al layer to form an efficient electron injector. Both efficiency enhancement and voltage reduction were observed in compounds like LiBO<sub>2</sub>, K<sub>2</sub>SiO<sub>3</sub> and Cs<sub>2</sub>CO<sub>3</sub>, with a thickness of 0.3 – 1.0 nm. These compounds decompose during deposition and produce LiO<sub>2</sub>, K<sub>2</sub>O and Cs<sub>2</sub>O at the Alq<sub>3</sub>/Al interface, respectively. By

using these compounds the device performance is more reproducible. The physical origin of the improved EL characteristics is not certain at present, but it is most likely due to the dissociation of alkali metal oxides at the Alq<sub>3</sub>/Al interface. The released alkali metal atoms may react with the Al to lower its work function. This will result in enhanced electron injection which will lead to more balanced charge injection and higher EL efficiencies.

### **3.4.3 LiF**

By adding a LiF layer with a thickness of 0.3 – 1.0 nm between the Al and Alq<sub>3</sub> layers, the emission efficiency is improved. Various mechanisms for this improvement have been proposed including a shift of the light-emitting zone to a region close to the HTL/ETL interface, causing constructive interference of light in the device, tunneling and reduction in gap states by aligning the Fermi level of Al with the LUMO of Alq<sub>3</sub>. That will enable direct tunneling of electrons through the thin LiF layer and by removing gap states by the use of a thin insulating layer, avoiding a direct contact between Al and Alq<sub>3</sub>.

## **4. Purification of OLED materials.**

### **4.1 Temperature gradient sublimation.**

Over the past two decades, synthetic organic, organometallic and polymeric solids have received considerable attention for their scientifically novel and potentially useful electrical, magnetic and optical properties. In order to perform meaningful physical studies on these materials, significant efforts must be devoted to material purification, crystal growth and characterization. Impurities in organic-based materials can arise for several reasons. Because the products of organic synthetic reactions are often the result of more than one reaction pathway, the questions of the presence of impurities and their potential consequences for the physical and structural properties of a given crystalline phase should be addressed. Attention should be paid to possible decomposition due to the formation of chemically reactive radicals during synthesis and introduction of impurities, especially solvent, during crystal growth. Thermal or radiation-induced reactions in organic solids can also take place [8].

One technique that can be used to purify organic materials is temperature gradient sublimation. In such a procedure, the organic material is filled into an inner quartz tube consisting of multiple segments that are lined up in an outer quartz tube. This tube is connected to a roughing and turbomolecular pump and is evacuated down to high vacuum (low  $10^{-6}$  Torr). Several heaters are placed around the outer tube whose temperatures are gently raised and individually controlled in order to obtain an almost linear gradient along the tube's long axis. Below the actual sublimation temperature of the desired organic substance, impurities start degassing from the raw material. Further warming leads to the sublimation of the target material which subsequently condenses in the closest sufficiently cold segment. Since the temperature difference between adjacent segments is rather small, each compartment contains only material of comparable sublimation temperature. After completion of a single cycle, each segment is harvested separately and the residual materials in the source as well as low temperature impurities are disposed of. Segments containing the largest crystallites are used for repeating the entire procedure (without adding new material), yielding even higher purity of the product [9].

## **5. OLED fabrication**

### **5.1 Thermal evaporation**

Thermal evaporation is a process where a material is heated until it starts to evaporate and then condensates against the cold substrate surface and the walls of the vacuum chamber. Pressures in the order of  $10^{-6}$  Torr [10] are needed to prevent a reaction between air molecules and the vapour. At these low pressures, the mean free path of the vapour atoms is of the same order as the vacuum chamber's dimensions. This causes the vapour particles to move in straight lines from the evaporation source towards the substrate. Different methods can be used to apply heat to the material. The most common techniques are either resistance heating or electron beam heating.

During resistance heating an electrical current is passed through a filament or metal boat, containing the evaporation material, until fusion takes place and the material is deposited on the

substrate. This is known as Joule heating and can be defined as follows [11]: When an electric current flows through a solid or liquid with finite conductivity, the electric energy will be converted to heat through resistive losses in the material. The heat will be generated on the micro scale when the conduction electrons transfer energy to the conductor's atoms through collisions. Evaporation filaments (Figure 8(a)) typically draw 50-100 A at 6-20 V. Only small amounts of material can be evaporated using a filament and it is not always easy to load the filament into the vacuum chamber. The filament can be replaced with a thin sheet of tungsten or tantalum with a dimple or depression to hold more material which is easier to load (Figure 8(b)). These materials have a vapour pressure of almost zero at the evaporation temperature of 1000 – 2000 °C. However, while the voltages are lower, the current can be as high as 300 - 400 A and high performance equipment is therefore needed [12]. Where there is a risk that the evaporating material might react with the filament, it can be heated indirectly in a ceramic crucible (Figure 8(c)). A great deal of power is lost through radiated heat, particularly with large surface area heaters. Baffled crucible heaters can greatly reduce these losses and allow for high temperatures to be achieved at reduced currents.

A schematic diagram of a thermal evaporator using resistive heating is shown in Figure 9.

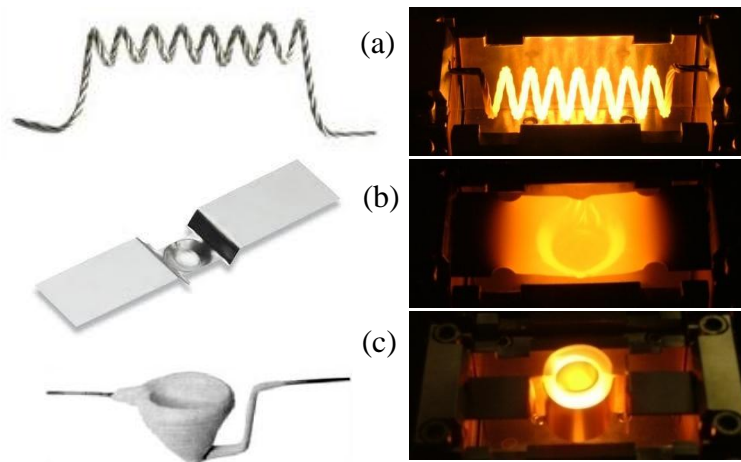


**Figure 8: Different heating sources: (a) Filament, (b) boat and (c) crucible [12, 13].**

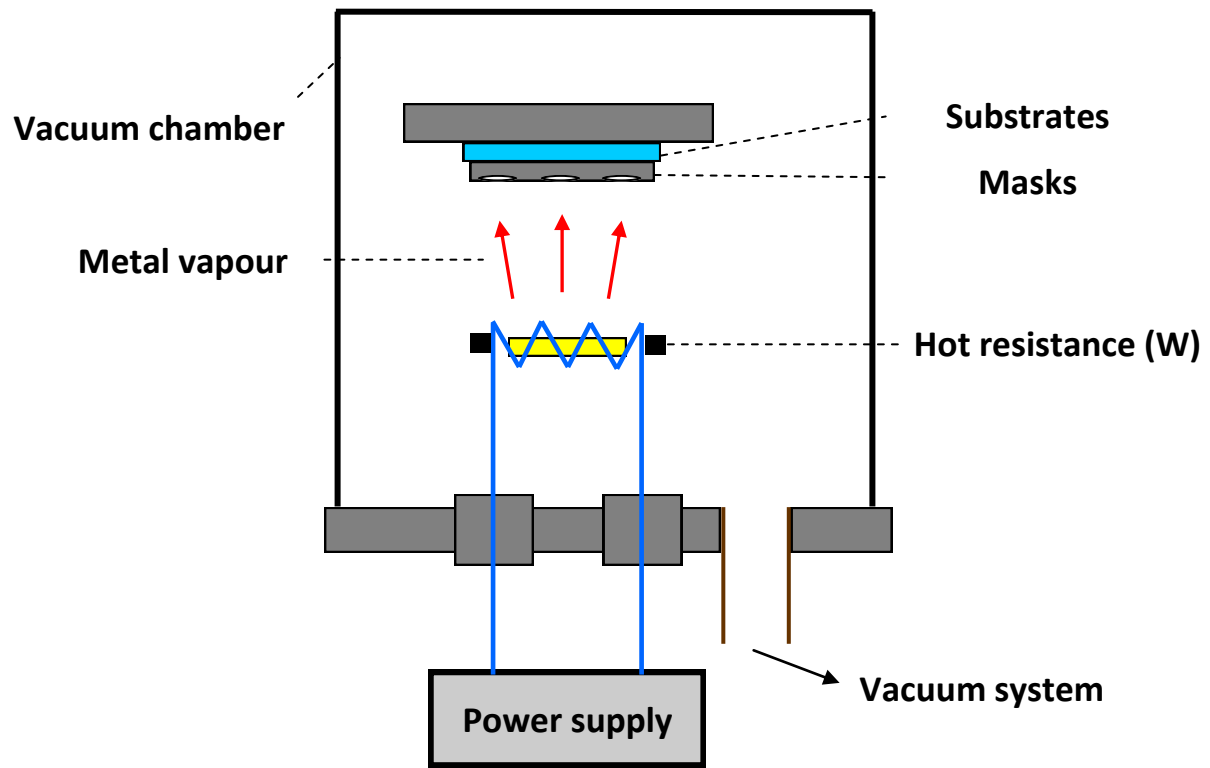


Figure 9: Schematic diagram of a thermal evaporator.

## References:

1. M. Pope, H.P. Kallmann, P. Magnante, *J. Chem. Phys.* **38** (1963) 2042-2043.
2. C.W. Tang, S.A. VanSlyke, *Appl. Phys. Lett.* **51** (1987) 913-915.
3. Perfect gadgets; accessed from: <http://www.perfect-gadget.com/lg-oled-tv-55-before-the-end-of-2012.html> (16/02/2012).
4. GE And Konica Minolta To Show Off Flexible OLED Lighting Panel; accessed from: <http://www.ubergizmo.com/2010/04/ge-and-konica-minolta-to-show-off-flexible-oled-lighting-panel/> (16/02/2012)
5. L.S. Hung, C.H. Chen, *Mater. Sci. Eng.* **R 39** (2002) 143-222.
6. Indium-Tin Oxide (ITO); accessed from <http://www.indium.com/documents/pds/97550.pdf> (21/02/2012)
7. T.M. Brown, J.S. Kim, R.H. Friend, F. Cacialli, R. Daik, W.J. Feast, *Appl. Phys. Lett.* **75** (1999) 1679-1681.
8. D.J. Sandman, *J. Cryst. Growth* **89** (1988) 111-116.
9. A.A. Levin, T. Leisegang, R. Forker, M. Koch, D.C. Meyer and T. Fritz, *Cryst. Res. Technol.* **45** No. 4 (2010) 439-448.
10. Thermal evaporation; accessed from: <http://www.icmm.csic.es/fis/english/evaporacion.html> (14/02/2012).
11. Joule heating; accessed from: <http://www.comsol.com/multiphysics/jouleheating/> (14/02/2012).
12. Thermal evaporation; accessed from: [http://www.oxford-vacuum.com/background/thin\\_film/evaporation.htm](http://www.oxford-vacuum.com/background/thin_film/evaporation.htm) (14/02/2012).
13. Product info; accessed from: <http://www.rdmthis.com/prodinfo.htm> (14/02/2012).

# Chapter 9

## The effect of synthesised Alq<sub>3</sub> on the external quantum and power conversion efficiencies of OLEDs.

### 1. Introduction

An organic light emitting diode (OLED) [1] device consists of an electroluminescent (EL) medium of thin organic layers (<0.2 μm) sandwiched between two electrodes. Some organic layers transport holes and others electrons. When a potential difference is applied between the anode and the cathode the holes and electrons will migrate towards the oppositely charged electrode. Holes and electrons will then be transferred to the emitting material forming tightly bound excitons which emit photons upon relaxation. These photons are then capable of escaping from the device architecture through the transparent anode and the glass substrate.

In this study we have synthesized nano-sized Alq<sub>3</sub> for use in fabricating OLEDs by a thermal evaporation process. Thermal evaporation utilizes high vacuum and direct heating of materials to deposit nanoscale layers of material onto a desired substrate and is an ideal technique for the deposition of organic small molecules due to the fine control and relatively gentle method of deposition. A description of this method and the tools necessary are presented.

In this study Alq<sub>3</sub> was used as both the ETL and emitting layer (EML) of the OLED, while commercial N,N'-di(naphthalen-1-yl)-N,N'-diphenyl-benzidine (NBP) was used as the hole transporting layer (HTL). Indium tin oxide (ITO) coated onto a glass substrate was used as the anode, while the Al:Cs<sub>2</sub>CO<sub>3</sub> top electrode was used as the cathode. The devices fabricated using the synthesized Alq<sub>3</sub> are compared with those fabricated using the commercially available Alq<sub>3</sub>. Furthermore, the current-voltage-luminance characteristics were also measured and the external quantum and power efficiencies of the two devices are compared.

## 2. Experimental

### 2.1 Purification of Alq<sub>3</sub>

During purification of Alq<sub>3</sub>, three quartz tubes (segments) were used. These tubes were placed in an outer quartz tube (figure 1 (a)). 0.394 g of raw material was loaded in the first segment. The outer quartz tube was sealed with quartz wool to prevent any solids from entering the vacuum pumps. The tube was connected to a roughing pump and turbo molecular pump and was evacuated to a pressure of  $2 \times 10^{-6}$  Torr. The second segment was heated to 150 °C in 90 minutes. The first segment was heated to 50 °C above this temperature and segment three was heated to 50 °C below this temperature, yielding a temperature gradient of 100 °C over the segments. The setup was left for 24 hours. Subsequently the heaters were switched off and the system was allowed to air cool back to room temperature. Impurities were left in the first segment and had a dark brown color (figure 1 (b)), while the purified Alq<sub>3</sub> crystals were collected in the second segment (bright yellow color (figure 1 (b))). Almost no material was present in the third segment. Segment two was harvested for purified material and 0.140 grams (35.53%) of the material was yielded. The impurities yielded almost 15% while 50% of the raw material was lost during the purification.

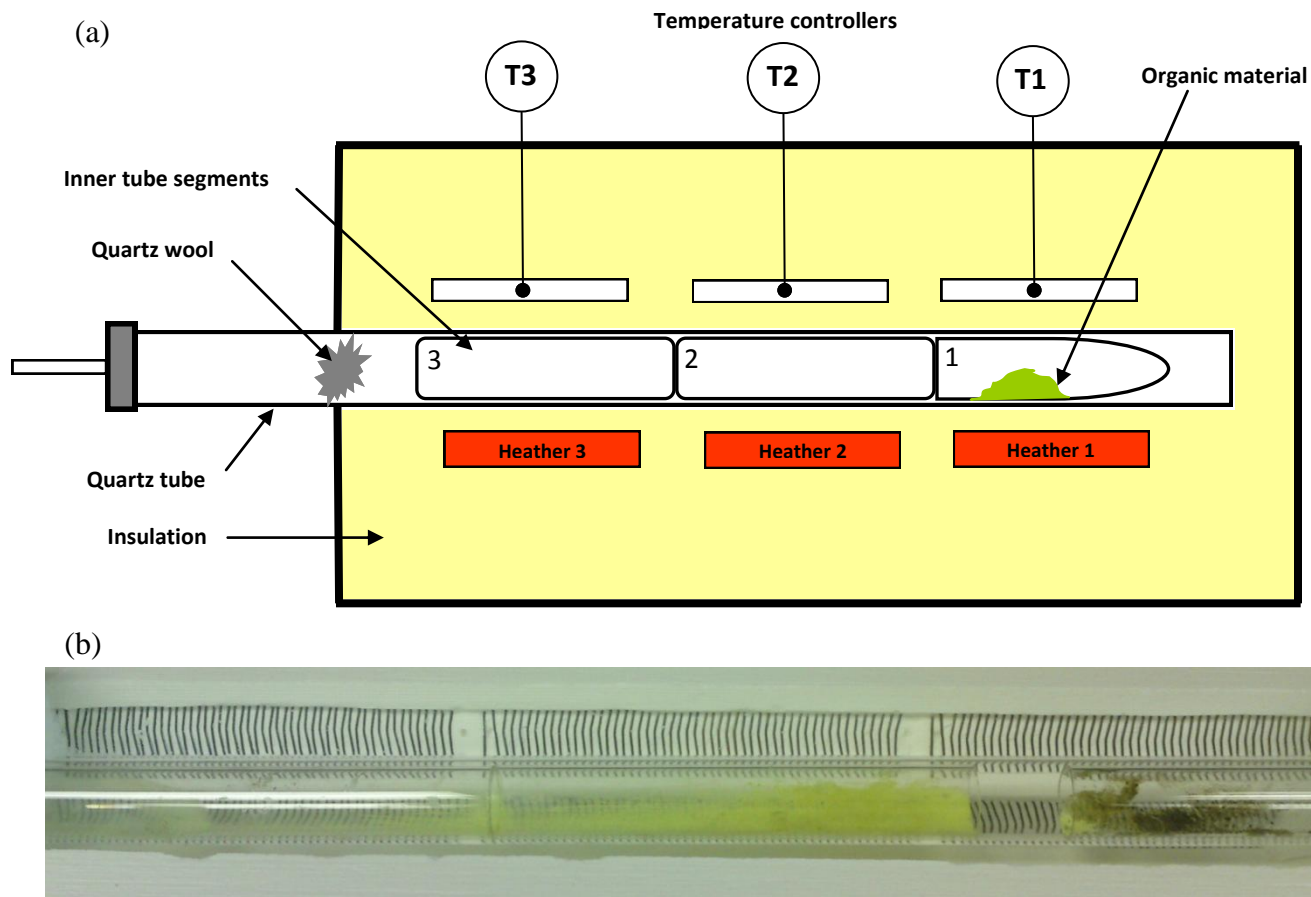


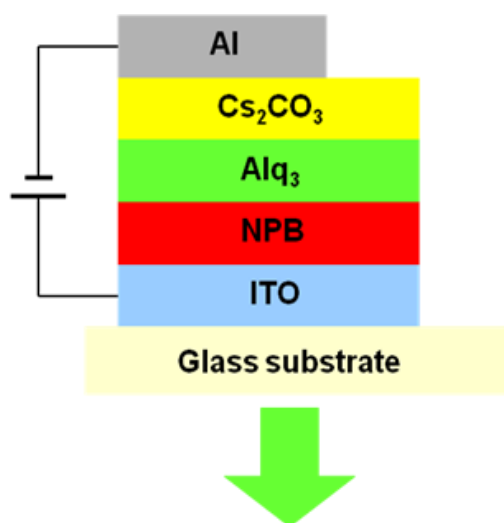
**Figure 1: (a) Schematic diagram of the experimental setup for temperature gradient sublimation and (b) the three segments showing the purified material (yellow) and impurities (brown) after sublimation.**

## 2.2 Fabrication of OLEDs

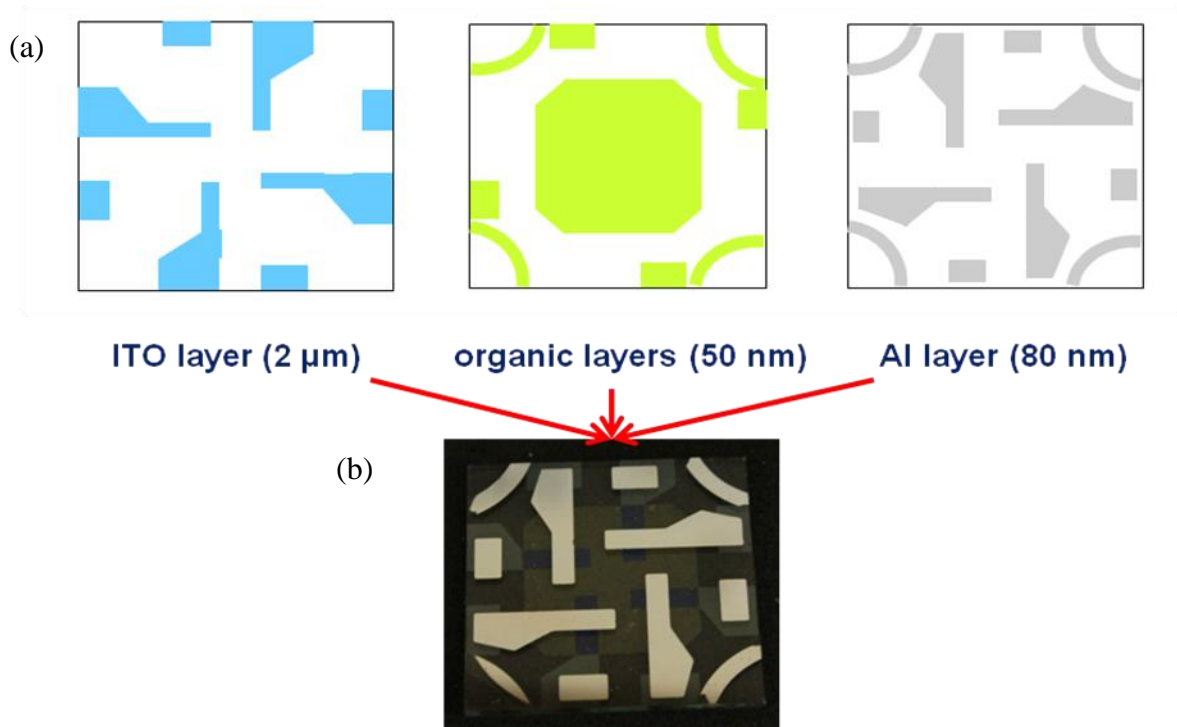
Glass substrates precoated with an indium tin oxide (ITO) anode (sheet resistance  $\sim 20 \Omega/\text{sq}$ ) were degreased in detergent and de-ionized water, and cleaned with ultrasonic baths of acetone and isopropanol consecutively for 15 minutes each. The substrates were then exposed to an ultraviolet-ozone ambient for 15 minutes (figure 2 (a)) immediately before loading into a high vacuum thermal evaporation system (base pressure  $\sim 3 \times 10^{-7}$  Torr) (figure 2 (b)). All the organic and metal layers were deposited successively without breaking the vacuum. The device structure consisted of ITO/NPB/Alq<sub>3</sub>/Cs<sub>2</sub>CO<sub>3</sub>:Al layers shown in figure 3. The NPB and Alq<sub>3</sub> layers were 50 nm thick each, the Cs<sub>2</sub>CO<sub>3</sub> layer was 1 nm and the Al layer was 80 nm thick (figure 4).



**Figure 2: (a) UV ozone system used for cleaning of ITO substrate and (b) thermal evaporator used to fabricate the OLED devices.**



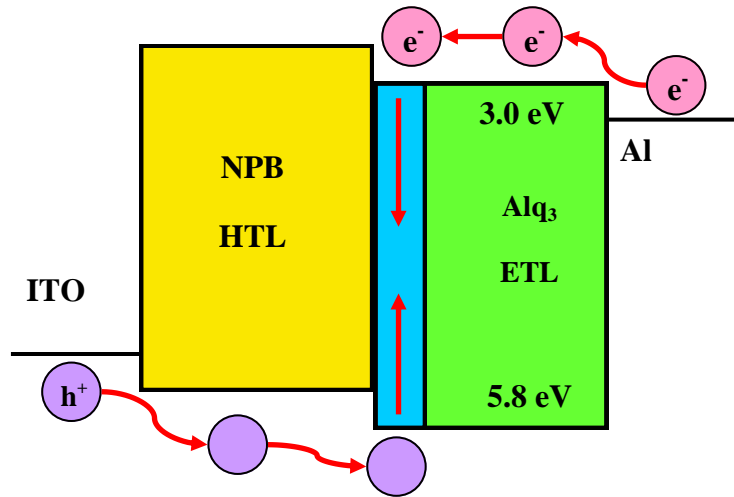
**Figure 3: Schematic illustration of the device structure.**



**Figure 4: (a) Schematic diagram showing the patterns of the different layers that were deposited and (b) a photograph of the actual device.**

Figure 5 shows the energy level diagram of the fabricated OLED device [2]. A barrier for electron injection is commonly present at the metal-organic contact when the work function of the metal is larger than the lowest unoccupied molecular orbital (LUMO) of the organic materials. The use of a low work function metal is highly desirable to facilitate the injection of electrons. By adding sub-monolayer amounts of LiF or Cs<sub>2</sub>CO<sub>3</sub> between the cathode and ETL, the work function of the metal can be decreased dramatically [3]. Electrons are injected from the cathode (Al:Cs<sub>2</sub>CO<sub>3</sub>) into the Alq<sub>3</sub> layer, which acts as the ETL. The hole-injecting contact requires a metal of high work function to match the highest occupied molecular orbital (HOMO) of the organic hole transporting layer. This contact must also be transparent to permit light to exit the device in an effective manner. Most OLEDs rely on the transparent and conductive ITO as the anodic material to facilitate the hole-injection. The work function of ITO ranges from 4.5 to 5.0 eV [4] and is strongly dependent on the methods of surface treatment. Treatment of ITO glass substrates using UV-ozone substantially increases its work function and also enhances the hole-injection from the ITO anode into the HTL. Holes are simultaneously injected from the

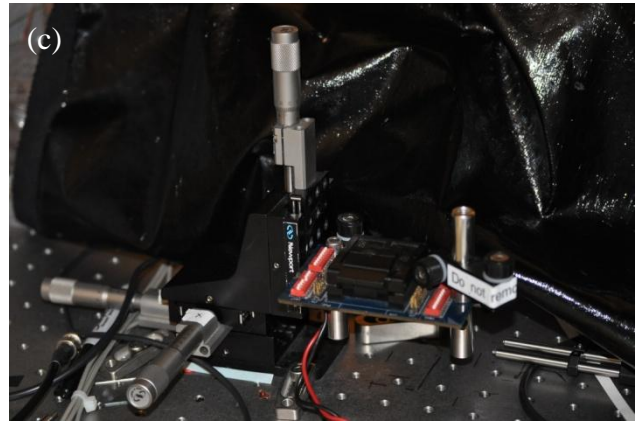
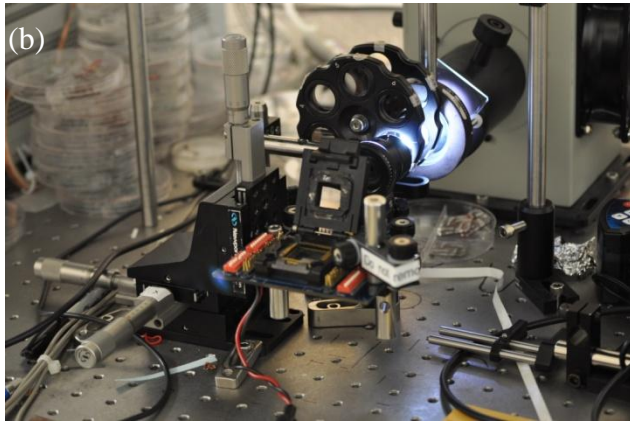
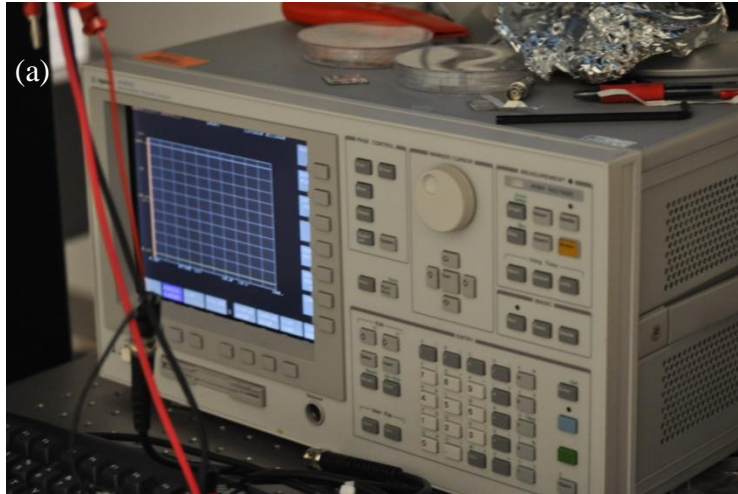
anode (ITO) into the NPB layer, which acts as a hole transporting layer. The Alq<sub>3</sub> layer acts as the emissive layer and electron-hole recombination takes place just next to the interface between Alq<sub>3</sub> and NPB on the Alq<sub>3</sub> side. During recombination photons with a wavelength of 520 nm are released.



**Figure 5: Energy level diagram of the fabricated OLED.**

### 2.3 Characterization

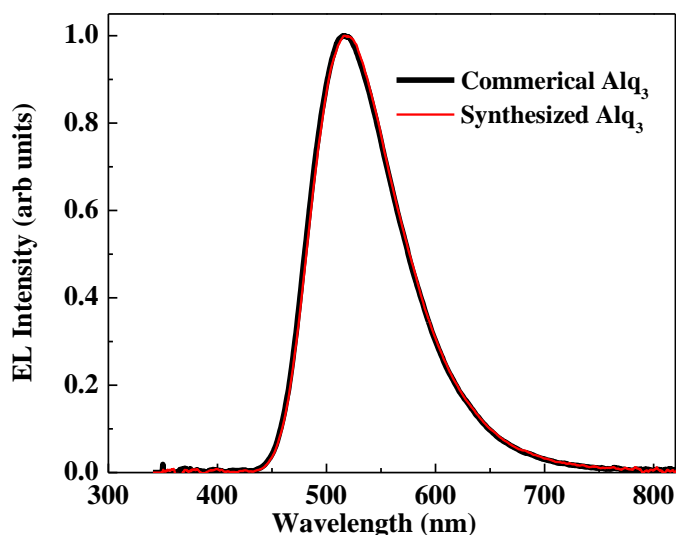
Luminance ( $L$ )–current density ( $J$ )–voltage ( $V$ ) measurements were conducted in ambient conditions using an Agilent 4155C semiconductor parameter analyzer and a Newport 818-UV photodetector (figure 6). The luminance of the OLEDs was calibrated using a Konica Minolta LS-100 luminance meter assuming a Lambertian emission pattern. Electroluminescence (EL) spectra were recorded using an Ocean Optics Jaz spectrometer.



**Figure 6: (a) The semiconductor parameter analyzer and the photodetector attached to the sample holder (b) open and (c) closed.**

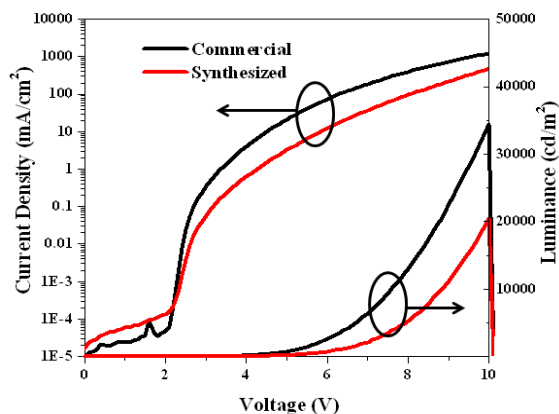
### **3. Results**

A potential difference of 4 V was applied to the OLED at a constant current of 400  $\mu$ A and the EL of the device was measured. The device's EL was compared to a device fabricated with commercial Alq<sub>3</sub>. The normalized EL curves are shown in figure 7. Both devices show emission at 520 nm. This emission is consistent with the PL data reported previously [5, 6, 7] for Alq<sub>3</sub> powder.

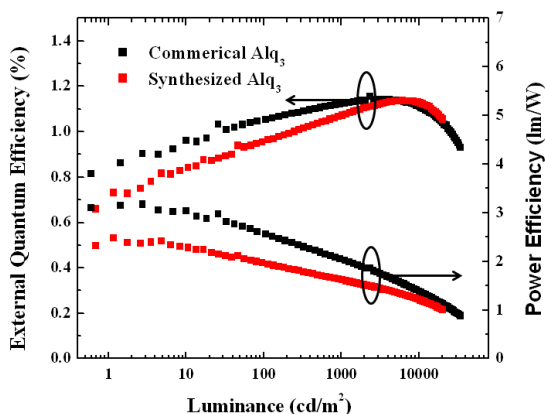


**Figure 7: The normalized EL spectra of commercial and synthesized Alq<sub>3</sub>, both showing a broad emission peak with a maximum at 520 nm.**

Figure 8 compares the  $L$ - $J$ - $V$  characteristics of OLED devices fabricated using the synthesized and commercial Alq<sub>3</sub>. Both devices were found to have a turn on voltage of  $\sim 2$  V. The current density of the device fabricated using the commercial Alq<sub>3</sub> was higher than that of the one fabricated with the synthesized Alq<sub>3</sub>. The luminance of the commercial Alq<sub>3</sub> device was  $1.5\times$  more intense than that of the synthesized Alq<sub>3</sub> device. The luminance of both devices dropped to  $0\text{ cd/m}^2$  at 10 V, pointing to a complete breakdown of the device. The external quantum efficiency ( $\eta_{EQE}$ ) and power conversion efficiency ( $\eta_P$ ) were calculated based on the methods recommended by Forrest et al. [8] and the plots of  $\eta_{EQE}$  and  $\eta_P$  versus luminance are shown in figure 9. Both devices show a maximum  $\eta_{EQE}$  of just above 1%. This is consistent with other  $\eta_{EQE}$  values reported for devices fabricated with commercial Alq<sub>3</sub> [9]. The  $\eta_P$  value at  $100\text{ cd/m}^2$ , which is an important luminance level for display devices, was about  $2.5\text{ lm/W}$  for the commercial Alq<sub>3</sub> device dropping to  $2\text{ lm/W}$  for the synthesized Alq<sub>3</sub> device. This is an indication that the synthesized Alq<sub>3</sub> layer degraded faster, especially under high voltages. This degradation might be due to some impurities such as hydroxyquinoline and Al-O compounds which were probably still present in the Alq<sub>3</sub> even after purification.

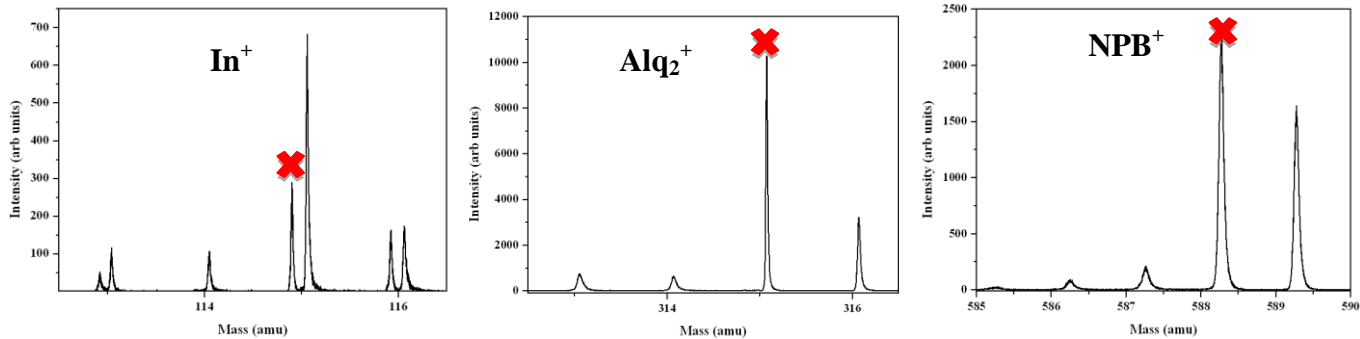


**Figure 8:  $L$ - $J$ - $V$  characteristics of the OLEDs.**

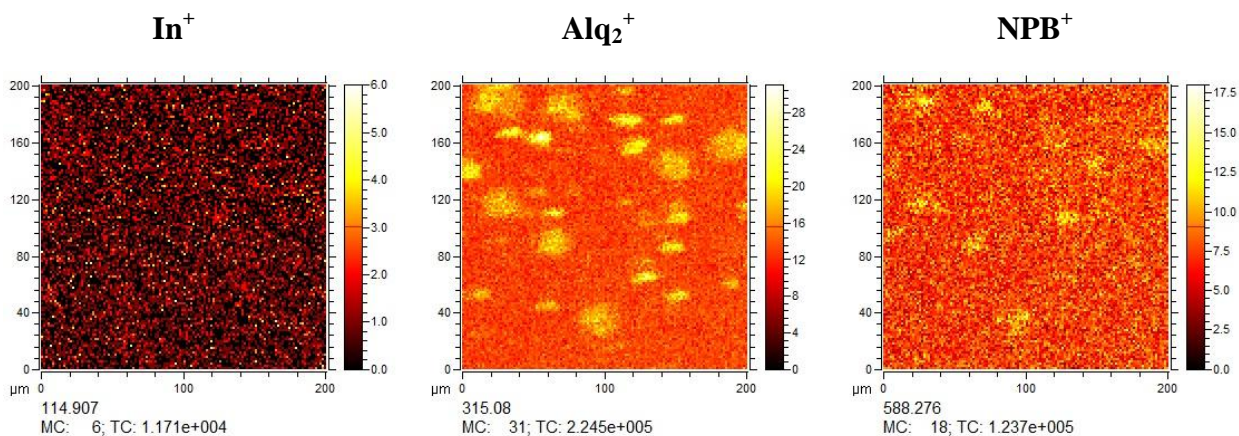


**Figure 9:  $\eta_{EQE}$  and  $\eta_P$  as a function of luminance for the two devices.**

Time of flight secondary ion mass spectroscopy (TOF SIMS) measurements were performed on the samples. A 30 kV Bi 1+ ion gun with a target current of 1 pA was used as the primary gun and an Ar<sup>+</sup> cluster gun with 1 kV 1500 Ar clusters was used as the sputter gun. The measurement was performed in spectroscopy mode and the analyser was in positive mode. The sample was sputtered for 5 seconds after which a surface scan of 200x200  $\mu\text{m}$  was done. This process was repeated until no Alq<sub>2</sub><sup>+</sup> and NPB<sup>+</sup> were visible on the surface. In<sup>+</sup> (114.907 amu), Alq<sub>2</sub><sup>+</sup> (315.08 amu) and NPB<sup>+</sup> (588.276 amu) were monitored (figure 10). Figure 11 shows the surface images of the three ions after the first 5 seconds of sputtering.

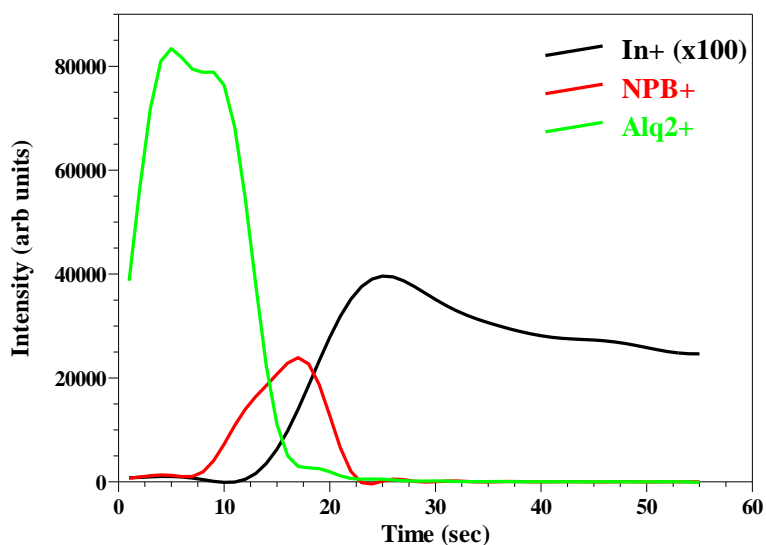


**Figure 10: TOF Sims spectra of the three ions that were monitored.**



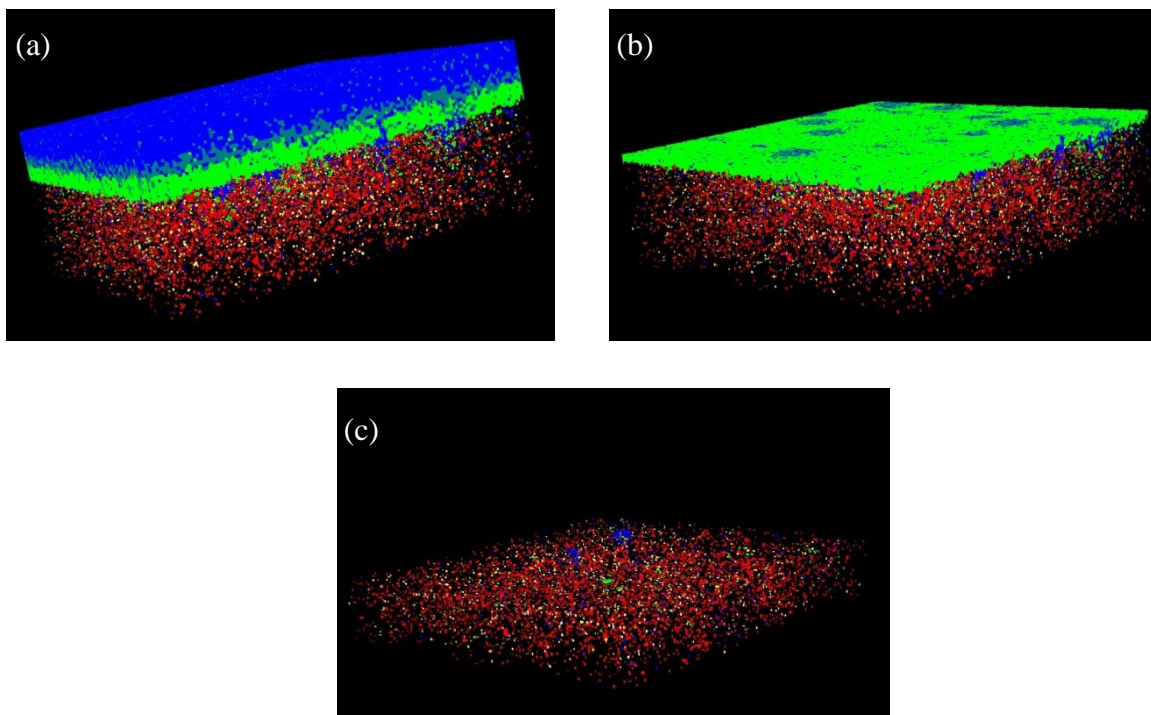
**Figure 11: Surface images of the three ions after 5 seconds of sputtering.**

Figure 12 shows the depth profile that was recorded during sputtering of the device. Note that no Al or  $\text{Cs}_2\text{CO}_3$  was observed. The  $\text{Ar}^+$  cluster gun is designed to sputter organic and therefore does not have enough energy to sputter the metal and inorganic layers. The Al layer was therefore peeled off with Scotts tape to reveal the organic layers underneath. The intensity of the  $\text{In}^+$  is also very low (100x lower than the organic layers) due to this. The depth profile clearly shows the  $\text{Alq}_2^+$ ,  $\text{NPB}^+$  and  $\text{In}^+$  layers corresponding to the  $\text{Alq}_3$ , NBP and ITO that were deposited on top of each other.



**Figure 12: Depth profile clearly showing the different layers that were deposited.**

Figure 13 shows the 3D depth profile of the device. Blue represents  $\text{Alq}_2^+$ , green  $\text{NPB}^+$  and red  $\text{In}^+$ . Figure 13 (a) shows that  $\text{Alq}_2^+$  forms a smooth cover on the top, but in figure 13 (b) it can be seen that some of the  $\text{Alq}_2^+$  diffused into the  $\text{NPB}^+$  layer. Some of the  $\text{Alq}_2^+$  is even present in the ITO layer (figure 13 (c)). There might be a few reasons for this: diffusion could have taken place upon deposition of the layers at high temperatures, the  $\text{Alq}_3$  could have diffused through the layer during the IV measurements or it could be due to device breakdown after being exposed to the atmosphere.



**Figure 13: 3D depth profile of the OLED device.**

#### **4. Conclusion**

Alq<sub>3</sub> powder was successfully synthesized using the co-precipitation method. Both devices' normalized EL spectra showed emission at 520 nm and this corresponds with reported PL results. Both devices had a turn on voltage of 2 V. The synthesized Alq<sub>3</sub> device had a lower current density, luminance and  $\eta_P$  values compared to the commercial Alq<sub>3</sub> device. These lower values were an indication that the synthesized Alq<sub>3</sub> layer degraded faster, especially under higher voltages. The reason for the degradation could be due to residual impurities that could not be removed by purification. The  $\eta_{EQE}$  and  $\eta_P$  can be increased by using Alq<sub>3</sub> just as ETL and using a host like 4,4'-bis(9H-carbazol-9-yl)biphenyl (CBP) doped with a green dopant like tris(2-phenylpyridine)iridium (Ir(ppy)<sub>3</sub>). TOF SIMS measurements confirmed the presence of Alq<sub>3</sub>, NPB and ITO in the device.

## References

- [1] C.W. Tang and S.A. Vanslyke, *Appl. Phys. Lett* **51** (1987) 913-916.
- [2] T.C. Lin, C.H. Hsiao and J.H. Lee, *Proc. of SPIE* **5937** (2005) 59371Q-1–59371Q-7.
- [3] S.E. Shabeen, G.E. Jabbour, M.M. Morrell, Y Kawabe, B Kippelen and N Peyghambarian, *J. Appl. Phys.* **84** (1998) 2324-2327.
- [4] L.S. Hung and C.H. Chen, *Mater. Sci. Eng.* **R 39** (2002) 143-222.
- [5] C.J. Mao, D.C. Wang, H.C. Pan and J Zhu, *J. Ultrason. Sonochem* **18** (2011) 473-476.
- [6] F Taylor and J Wilkins, *Chem. Soc. Dalton Trans.* **1** (1973) 87-90.
- [7] M.M. Duvenhage, O.M. Ntwaeaborwa and H.C. Swart, *Physica B-Condensed Matter.* **407** (2012) 1521-1524.
- [8] S.R. Forrest, D.D.C. Bradley and M.E. Thompson, *Adv. Mater.* **15** (2003) 1043-1048.
- [9] Y.H. Lee, W.J. Kim, T.Y. Kim, J Jung, J.Y. Lee, H.D. Park, T.W. Kim and J.W. Hong, *Curr. Appl. Phys.* **7** (2007) 409-412.

# Chapter 10

## Conclusion and future work.

This chapter contains the overall conclusion of the results obtained from  $Mq_3$  and its derivatives as well as future work regarding this research study.

### 1. Conclusion

This thesis reports on the synthesis and characterization of metal quinolates ( $Mq_3$ ) and their derivatives for use as electron transporting and emissive layer in organic light emitting diodes (OLEDs).

$Mq_3$  were synthesized and extensive research was done on their optical properties via absorption and luminescence studies. It is known that the luminescent centre of  $Mq_3$  is situated on the quinoline ring itself, with the highest occupied molecular orbital (HOMO) situated on the phenoxide ring while the lowest unoccupied molecular orbital is situated on the pyridyl ring. Emission originates from the ligand's electronic  $\pi-\pi^*$  transitions between the LUMO and HOMO and LUMO. Absorption studies revealed one major absorption band and two weaker absorption bands for  $Alq_3$ ,  $Gaq_3$  and  $Inq_3$ . The major absorption band was reported to be a ligand centered electronic transition, while the weaker bands were assigned to vibronic progressions due to ring deformation of an electronic transition at 346 nm. Only one broad emission band was observed for  $Mq_3$ .  $Mq_3$  is a known singlet emitter and the emission is assigned to the relaxation of an electron from the  $S_1-S_0$  level. The emission decreased and red shifted with an increase in atomic number of the central metal ion. It was also found that the emission maxima were independent of the excitation wavelength.

The effect of substituents on the optical band gap of  $Alq_3$  was investigated. Cl was substituted in the 5 position (5Cl- $Alq_3$ ) and methyl groups in the 5 and 7 position (5,7Me- $Alq_3$ ). Cyclic voltammetry (CV) measurements were performed to determine the HOMO and LUMO levels of the samples. The absorption onset and Tauc's relation was also used to determine the optical band gap. The obtained band gap was 0.2 eV lower than the theoretical value. This is expected as

it is known that solvents play a role in the formation of the band gap. The band gap of the substituted samples was lower than that of Alq<sub>3</sub>. This was due to the red shift in the absorption spectra of the samples. The HOMO and LUMO levels were 0.8 eV lower than the theoretical values. Care must be taken in the design of the device architecture.

Alq<sub>3</sub> was synthesized using a co-precipitation method. The crystal structure was in good agreement with the standard for Alq<sub>3</sub>. The morphology showed needle like crystals on big agglomerated particles. This crystal formed during the recrystallization process in acetone. The absorption spectrum showed a broad band at ~380 nm. When the sample was excited at 335 nm, a broad emission peak was observed at 510 nm. This emission could be ascribed to singlet emission. The Alq<sub>3</sub> sample was coated with SiO<sub>2</sub>. There was a small shift in the crystal structure indicating that the SiO<sub>2</sub> distorted the Alq<sub>3</sub> crystal. The emission was blue shifted by ~10 nm and a shoulder peak at 490 nm was observed. The shift was due to both the absence of intermolecular interactions between the Alq<sub>3</sub> molecules and the onset of new interactions if Alq<sub>3</sub> with the SiO<sub>2</sub> material. The shoulder might be due to inhomogeneous broadening that is common in glasses, meaning that each molecule acquired a slightly different position. Concentrations ranging from 0.5 – 5 % of Alq<sub>3</sub> were mixed with PMMA to obtain Alq<sub>3</sub>:PMMA thin films. The morphology showed small holes covering a smooth surface. The holes were formed when gasses escaped during the evaporation of chloroform. The samples were excited at 355 nm and a broad emission spectrum with a maximum at 515 nm was observed. The sample containing 1% of Alq<sub>3</sub> showed the highest intensity. A blue shift observed in the emission of the 0.5 % sample was attributed to changes in excitonic states. XPS studies done on the commercial powder showed traces of Al, S and Si. These were attributed to contamination during the fabrication process. The films that were prepared with chloroform as solvent showed traces of Cl. The carbon peak was fitted with four peaks and was assigned to -CH<sub>2</sub>, -CH<sub>3</sub>, the quaternary carbon of PMMA, -C-O- species and the carbonyl C 1s electrons of carbon. Two peaks which were fitted for the oxygen peak were assigned to carbonyl and methoxy O1s species. Ar sputtering was performed on the blended films. After sputtering the O-C=O and C-O peaks were combined into one peak and there was no separation observed between the C-O-C and O-C=O peaks.

An Alq<sub>3</sub> sample was irradiated with UV photons for 400 hours to study the photon degradation of the material. It was found that the intensity halved in 24 hours and continued to decrease with time. It is proposed that Alq<sub>3</sub> reacts with oxygen and moisture in the air to form non-radiative products through oxidation and hydrolysis processes. IR measurements were performed on the degraded sample and it was found that the Al-O and Al-N bonds stayed intact while there was an increase in the amount of moisture and C=O bonds. This corresponded to the rupture of the phenoxide ring. XPS studies done on the as-prepared Alq<sub>3</sub> samples showed Al2p, N1s, O1s and C1s peaks. The C1s peak was fitted with six peaks corresponding to the different carbon bonds in the quinoline ligand. XPS studies done on the degraded samples also showed that the Al-O bond stayed intact and peak fittings done on the C1s peak suggest that all four proposed degradation products had formed. Al<sup>3+</sup> was substituted by Zn<sup>2+</sup> to form Znq<sub>2</sub>. The Znq<sub>2</sub> PL peak has a maximum at 506 nm and its intensity was almost two times higher than that of Alq<sub>3</sub>. Upon UV degradation the intensity decreased with 10 % in the first few hours, but slowed down for longer exposure times. It showed an overall decrease in intensity of 30 % after 400 hours compared to Alq<sub>3</sub> that decreased by 80 % in the same time. This might be due to the fact that Znq<sub>2</sub> only has two quinoline ligands compared to the three of Alq<sub>3</sub>. Alq<sub>3</sub> was encapsulated with SiO<sub>2</sub> and exposed to UV irradiation. The intensity decreased by 50 % in the first 10 hours; after 120 hours the intensity was barely detected by the spectrometer. It is proposed that the SiO<sub>2</sub> shell decomposed during UV exposure into Si and O<sub>2</sub> species. Alq<sub>3</sub> reacted with the O<sub>2</sub> species causing the phenoxide ring to rupture and non-luminescent molecules were formed. A PMMA thin film that was mixed with 1% of Alq<sub>3</sub> was exposed to UV light for 400 hours. A rapid decrease in intensity of 70 % was observed for the first 80 hours of exposure. Afterwards, there was only a slight decrease in the intensity and for the last 100 hours the intensity was almost stable. XPS studies done on the degraded film showed that CO and CO<sub>2</sub> species had formed during degradation. These species reacted with the Alq<sub>3</sub> to form non-radiative species. It was also shown that since substituents on the 7 position protect the phenoxide ring from rupturing, almost no degradation was detected for this sample.

A *mer-tris*-8-hydroxy-quinolino- indium(III) complex (Inq<sub>3</sub>) was synthesized with interesting solvent disorders in the crystal structure as well as good photoluminescent properties which makes this compound a candidate for potential photoactive materials. Photoluminescence

excitation peaks were obtained at 345 and 440 nm and a broad emission peak at 510 nm. The solvent molecules were shown to increase the photoluminescent properties of the compound as well as causing a red shift of 16 nm in the emission spectrum. The methanol and water molecules inside the crystal structure acted as optically inactive spacer molecules which led to a blue shift in the solid state emission. The XPRD showed a change in the crystal structure of the annealed sample. This might have led to favorable  $\pi$ - $\pi$  overlaps which were responsible for a red shift in the emission spectrum. The sample showed a 60% decrease in luminescence intensity upon UV exposure after 15 hours. This was an indication that oxygen and moisture in the air caused the phenoxide ring to decompose, destroying the luminescent centers in the process. XPS studies of the O-1s peak indicated that after annealing of the sample some of the solvent species were no longer present in the crystal. For the degraded sample the O-1s peak indicated that C=O, C-O-H and O=C-O-H bonds had formed.

Synthesised Alq<sub>3</sub> powder was used to fabricate organic light emitting diodes (OLEDs) with a device structure of ITO/NPB/Alq<sub>3</sub>/Cs<sub>2</sub>CO<sub>3</sub>:Al. The NPB and Alq<sub>3</sub> layers were 50 nm thick, the Cs<sub>2</sub>CO<sub>3</sub> layer 1 nm and the Al layer 80 nm thick. Both devices' normalized EL spectra showed emission at 520 nm corresponding with reported PL results. Both devices have a turn on voltage of 2 V. The synthesized Alq<sub>3</sub> device has lower current density, luminance and  $\eta_P$  values compared to the commercial Alq<sub>3</sub> device. These lower values are an indication that the synthesized Alq<sub>3</sub> layer degrades faster, especially under higher voltages. The reason for the degradation could be residual impurities that could not be removed by purification. The  $\eta_{EQE}$  and  $\eta_P$  can be increased by using Alq<sub>3</sub> only as the electron transporting layer and using a host like 4,4'-bis(9H-carbazol-9-yl)biphenyl (CBP) doped with a green dopant like tris(2-phenylpyridine)iridium (Ir(ppy)<sub>3</sub>). TOF SIMS measurements confirm the presence of Alq<sub>3</sub>, NPB and ITO in the device.

## 2. Future work:

1. The effect of different electron donating (EDG) and withdrawing groups (EWG) on the emission of  $Mq_x$  samples must be studied. These groups must be placed in the favourable position to have the highest impact on the electron cloud of the sample. By finding the right substituents the colour of  $Mq_x$  can be tuned from blue to red and many new applications can be found for these materials.
2. Studies have shown that by adding a substituent to the 7 position of the quinoline ligand almost no photon degradation takes place. However, the methyl group placed at this position decreased the intensity of  $Alq_3$ . By finding the right substituent that protects the phenoxide ring and also increases the intensity, a very stable organic phosphor can be made to be used in OLED devices.
3.  $Znq_2$  showed promising results as the intensity is higher than that of  $Alq_3$  and it does not degrade at such a rapid tempo as  $Alq_3$ . By synthesizing more  $Mq_2$  samples like  $Mnq_2$ ,  $Caq_2$  and  $Mgq_2$  and characterizing them, a more stable replacement for  $Alq_3$  may be found.
4. Thin films can easily be made by spin coating them onto glass or silicon substrates. The thickness of the films can easily be controlled by using solutions of different concentrations. These thin films can be used to measure ultraviolet photon spectroscopy (UPS). UPS gives valuable information about the HOMO and LUMO levels of the material as well as information about the interface between different layers. Before an OLED device can be made, the HOMO and LUMO levels of the different components used in the device must be known. If new material is synthesized it is very important to determine the HOMO and LUMO levels before proceeding to device manufacturing. By using techniques such as UPS and comparing it with results obtained from CV and absorption measurements, the HOMO and LUMO level can be determined more accurately.

5. Infra-red spectroscopy (IR) gives valuable information about the different vibration modes in a sample. If combined with XPS results the formation or breaking of certain bonds can be determined. By doing both XPS and IR on as-prepared and degraded samples a better understanding of the degradation process of specific materials can be obtained.
6. Molecular orbital (MO) calculations give information about the HOMO and LUMO levels of the material as well as the electron cloud surrounding the central metal and different ligands. These MO calculations can determine the favourable positions for substituents. Performing these calculations before a certain material is synthesized can save a lot of time when one wants to obtain a certain result, like colour tuning or making a material with a certain HOMO and LUMO value.
7. One can synthesize and characterize a lot of materials, but in the end the best way to determine if the materials will work for OLED devices is to manufacture these devices and test their electroluminescence (EL), electrical properties (I-V and J-V curves) and efficiencies ( $n_{EQE}$  and  $n_P$ ). By using simple physical vapour deposition (PVD) techniques a number of devices can be made and characterized within hours.

# Appendix A

## PUBLICATIONS – M.M. (Biggs) Duvenhage

- [1] L.F. Koao, H.C. Swart, E. Coetsee, M.M. Biggs and F.B. Dejene, The effect of  $Mg^{2+}$  ions on the photoluminescence of  $Ce^{3+}$ -doped silica Physica B, **404** (2009) 4499-4503.
- [2] M.M. Biggs, O.M. Ntwaeaborwa, J.J. Terblans, and H.C. Swart, Characterization and luminescent properties of  $SiO_2:ZnS:Mn^{2+}$  and  $ZnS:Mn^{2+}$  nanophosphors synthesized by a sol-gel method Physica B, **404** (2009) 4470-4475.
- [3] V. Kumar, V. Mishra, M.M. Biggs, O.M. Ntwaeaborwa and H.C. Swart, Luminescence investigations of  $Ce^{3+}$  doped CaS nanophosphors, Journal of Alloys and Compounds, **492** (2010) L8-L12.
- [4] J.J. Dolo, O.M. Ntwaeaborwa, J.J. Terblans, E. Coetsee, B.F. Dejene, M.M. Biggs and H.C. Swart, The effect of oxygen pressure on the structure, morphology and photoluminescence intensity of pulsed laser deposited  $Gd^{2+}O^{2-}S:Tb^{3+}$  thin film phosphor, Applied Physics A, **101** (2010) 655-659.
- [5] M.M. Biggs, O.M. Ntwaeaborwa and H.C. Swart, 'n Oorsig van verskillende tipes luminessensie en verskillende tipes fosfors: gebruike en karakterisering, Die Suid-Afrikaanse Tydskrif vir Natuurwetenskap en Tegnologie, **29** (2010) 145-146.
- [6] V. Kumar, V. Mishra, M.M. Biggs, I.M. Nagpure, O.M. Ntwaeaborwa, J.J. Terblans and H.C. Swart, Electron beam induced green luminescence and degradation study of CaS:Ce nanocrystalline phosphors for FED applications, Applied Surface Science, **256** (2010) 1720-1724.

- [7] F.B. Dejene, A.G. Ali, H.C. Swart, J.R. Botha, K. Roro, E. Coetsee and M.M. Biggs, Optical properties of ZnO nanoparticles synthesized by varying the sodium hydroxide to zinc acetate molar ratios using a Sol-Gel process, *Central European Journal of Physics*, **9** (2011) 1321-1326.
- [8] D.B. Bem, H.C. Swart, A.S. Luyt, M.M. Duvenhage and F.B. Dejene, Characterization of Luminescent and Thermal Properties of Long Afterglow  $\text{SrAl}_x\text{O}_y:\text{Eu}^{2+},\text{Dy}^{3+}$  Phosphor Synthesized by Combustion Method, *Polymer Composites*, **32** (2011) 219-226.
- [9] M.M. Duvenhage, O.M. Ntwaeaborwa and H.C. Swart *Physica B-Condensed Matter* **407** (2012) 1521.
- [10] I.M. Nagpure, M.M. Duvenhage, Shreyas S. Pitale, O.M. Ntwaeaborwa, J.J. Terblans and H.C. Swart, Synthesis, thermal and spectroscopic characterization of  $\text{Caq}_2$ (calcium 8-hydroxyquinoline) organic phosphor, *Journal of Fluorescence*, **22** (2012) 1271-1279.
- [11] H.A.A. Seed Ahmed, M.M. Duvenhage, O.M. Ntwaeaborwa, R.E. Kroon, Luminescence from rare-earth doped sol-gel silica, SAIP/2011 Proceedings accepted October 2011.
- [12] M.M. Duvenhage, O.M. Ntwaeaborwa and H.C. Swart, Blended thin films of tris-(8-hydroxyquinoline) aluminium ( $\text{Alq}_3$ ) embedded in polymethyl methacrylate (PMMA), SAIP/2011 Proceedings accepted October 2011.
- [13] M.M. Duvenhage, O.M. Ntwaeaborwa, E. Wrzesniewski, J. Xue and H.C. Swart, The effect of nano sized  $\text{Alq}_3$  on the external quantum and power conversion efficiencies of OLEDs, SAIP/2012 proceedings, submitted July 2012.
- [14] A.K. Bedyal, V. Kumar, V. Sharma, S.S. Pitale, E. Coetsee, M.M. Duvenhage, O.M. Ntwaeaborwa and H.C. Swart, Spectral and surface investigations of  $\text{Mn}^{2+}$  doped  $\text{SrZnO}_2$  nanocrystalline phosphors, *Journal of Material Science*, **48** (2013) 3327 - 3333.

- [15] M.M. Duvenhage, H.C. Swart, O.M. Ntwaeaborwa, H.G. Visser, Synthesis, crystal structure, luminescent properties and photon degradation of *mer-tris*(8-Hydroxyquinolinato-*N, O*)-indium(iii) hydrate 0.5 methanol solvate, *Optical Materials*, **35** (2013) 2366-2371.
- [16] V. Kumar, H.C. Swart, O.M. Ntwaeaborwa, R.E. Kroon, J.J. Terblans, S.K.K. Shaat, A. Yousif and M.M. Duvenhage, Origin of the red emission in zinc oxide nanophosphors, *Materials Letters*, **101** (2013) 57-60.
- [17] M.M. Duvenhage, H.G. Visser, O.M. Ntwaeaborwa and H.C. Swart, The effect of electron donating and withdrawing groups on the morphology and optical properties of Alq<sub>3</sub>, *Physica B – Condensed Matter*, <http://dx.doi.org/10.1016/j.physb.2013.11.049>.
- [18] M.M. Duvenhage, O.M. Ntwaeaborwa, H.G. Visser, P.J. Swarts, J.C. Swarts and H.C. Swart, The effects of EWG and EDG on the HOMO and LUMO of Alq<sub>3</sub>, SAIP/2013 proceedings, submitted July 2013.

## CONFERENCES

- [1] M.M. Biggs, O.M. Ntwaeaborwa, J.J. Terblans and H.C. Swart, Mechanism of luminescence of nanoparticulate and commercial ZnS:Mn<sup>2+</sup> phosphors, Limpopo conference, SAIP UL, 9 -11 July 2008.
- [2] M.M. Biggs, O.M. Ntwaeaborwa, J.J. Terblans en H.C. Swart, Luminessensie meganisme van gesintetiseerde nanodeeltjies en kommersiële ZnS:Mn<sup>2+</sup> fosfor, Afrikaanse studente simposium, SAAWK UJ, 31 Oktober 2008
- [3] M.M. Biggs, O.M. Ntwaeaborwa, J.J. Terblans and H.C. Swart, Characterization and luminescent properties of SiO<sub>2</sub>:ZnS:Mn<sup>2+</sup> and ZnS:Mn<sup>2+</sup> nanophosphors synthesized by a sol-gel method, 3rd South African Conference on Photonic Materials, 23 - 27 March 2009.
- [4] L.F. Koao, H.C. Swart, E. Coetsee, M.M. Biggs and F.B. Dejene, The effect of Mg<sup>2+</sup> ions on the Photoluminescence of Ce<sup>3+</sup> doped silica, 3rd South African Conference on Photonic Materials, 23 - 27 March 2009.
- [5] A.G. Ali, H.C. Swart, J.R. Botha, E. Coetsee, M.M. Biggs and F.B. Dejene, Structural and optical properties of ZnO, SiO<sub>2</sub>:Ce<sup>3+</sup> and ZnO:SiO<sub>2</sub>:Ce<sup>3+</sup> nanoparticles prepared by a Sol-Gel process. International Conference on Nanotechnology and Advanced Materials 2009. (ICNAM 2009), University of Bahrain, 4 - 7 May 2009.
- [6] M.M. Biggs, O.M. Ntwaeaborwa and H.C. Swart, Characterization and luminescent properties of ZnS:Mn<sup>2+</sup> nanophosphor synthesized by a sol-gel method, Durban conference, SAIP UKZN, 7 - 10 July 2009.

- [7] L.F. Koao, H.C. Swart, E. Coetsee, M.M. Biggs and F.B. Dejene, The effect of temperature on the photoluminescence characteristics of Ce;Al or Ce;Mg doped SiO<sub>2</sub>. Durban conference, SAIP UKZN, 7 - 10 July 2009.
- [8] D.B. Bem, H.C. Swart, A.S. Luyt, M.M. Biggs, F.B. Dejene. Synthesis and Characterization of Long Persistence Strontium and Barium Aluminate Phosphors. Durban conference, SAIP UKZN, 7 - 10 July 2009.
- [9] J.J. Dolo, O.M. Ntwaeaborwa, J.J. Terblans, E.Coetsee, B.F. Dejene, M.M. Biggs and H.C. Swart, The effect of oxygen pressure on the structure, morphology and photoluminescence intensity of pulsed laser deposited Gd<sub>2</sub>O<sub>2</sub>S:Tb<sup>3+</sup> thin film phosphor. Durban conference, SAIP UKZN, 7 - 10 July 2009.
- [10] H.C. Swart, J.J. Terblans, E. Coetsee, V. Kumar, O.M. Ntwaeaborwa and M.M. Biggs. Auger Electron Spectroscopy and X-ray Photoelectron Spectroscopy study of the electron stimulated surface chemical reaction mechanism for phosphor degradation. Ecasia09, 13th European Conference on Applications of Surface and Interface Analysis, Antalya, Turkey, 18-23 October 2009.
- [11] M.M. Biggs, O.M. Ntwaeaborwa en H.C. Swart, 'n oorsig van verskillende tipes luminessensie en verskillende tipes fosfors; hulle gebruike en karakterisering, Afrikaanse studente simposium, SAAWK UOVS, 30 Oktober 2009.
- [12] M.M. Biggs, O.M. Ntwaeaborwa, J.J. Terblans, and H.C. Swart, Characterization and luminescent properties of SiO<sub>2</sub>:ZnS:Mn<sup>2+</sup> and ZnS:Mn<sup>2+</sup> nanophosphors synthesized by a sol-gel method, SAIP CSIR, 27 September - 1 October 2010.
- [13] M.M. Biggs, O.M. Ntwaeaborwa en H.C. Swart, Verbetering van die luminessensie van Alq<sub>3</sub> poeiers, Afrikaanse student symposium, SAAWK Pretoria, 27-28 Oktober 2010.

- [14] M.M. Biggs, O.M. Ntwaeaborwa and H.C. Swart, UV exposure and photon degradation of Alq<sub>3</sub> powders, 4th South African Conference on Photonic Materials, Kariega Game Reserve, 2-6 May 2011.
- [15] M.M. Biggs, O.M. Ntwaeaborwa and H.C. Swart, UV exposure and photon degradation of Alq<sub>3</sub> powders, SAIP Unisa, 12-15 July 2011.
- [16] M.M. Duvenhage, O.M. Ntwaeaborwa en HC Swart, Fotondegradasie van Alq<sub>3</sub> poeier, Afrikaanse studente simposium, SAAWK Unisa, 27-28 Oktober 2011
- [17] M.M. Duvenhage, O.M. Ntwaeaborwa, E. Wrzesniewski, J. Xue and H.C. Swart, The effect of nano sized Alq<sub>3</sub> on the external quantum and power conversion efficiencies of OLEDs, 4th International Conference on Nanoscience and Nanotechnology University of the Free State, 1-4 April 2012
- [18] M.M. Duvenhage, O.M. Ntwaeaborwa, E. Wrzesniewski, J. Xue and H.C. Swart, The effect of nano sized Alq<sub>3</sub> on the external quantum and power conversion efficiencies of OLEDs, SAIP University of Pretoria, 9-13 July 2012
- [19] M.M. Duvenhage, H.G. Visser, O.M. Ntwaeaborwa and H.C. Swart, The effect of electron donating and withdrawing groups on the morphology and optical properties of Alq<sub>3</sub>, 5th South African Conference on Photonic Materials, Kariega Game Reserve, 29 April - 3 May 2013.
- [20] M.M. Duvenhage, O.M. Ntwaeaborwa, H.G. Visser, P.J. Swarts, J.C. Swarts and H.C. Swart, The effects of EWG and EDG on the HOMO and LUMO of Alq<sub>3</sub>, SAIP University of Zululand, 8 - 12 July 2013.